

https://dspace.org/

Understanding the Sadiola Hill oxide zone (Mali), its geochemical complexities and alternation signatures

Daouda, Traore

2019
https://hdl.handle.net/10539/29543

Downloaded from a DSpace repository. https://dspace.org/

UNDERSTANDING THE SADIOLA HILL OXIDE ZONE (MALI), ITS GEOCHEMICAL COMPLEXITIES, AND ALTERATION SIGNATURES

Mr TRAORE Daouda

A Dissertation submitted to the Faculty of Science, University of the Witwatersrand, Johannesburg in fulfilment of the requirements for the degree of Master of Science

November 2019

Declaration

I declare that this dissertation is my own, unaided work. It is being submitted for the Degree of Master of Science at the University of Witwatersrand, Johannesburg. It has not been submitted before for any degree or examination at any other University.



…….

13th day of November 2019 in Johannesburg

Abstract

The Sadiola goldfield is located in the eastern Kédougou Kéniéba Inlier of the West African Craton. The study area is located in the western region of the Republic of Mali close to the international border between Mali and Senegal, and approximately 75 km south of the regional capital of Kayes in the sub-Sahelian region of West Africa.

The goals of this research are to study the different geological relationships: oxide and unaltered rock (calc-silicate, siltstone-shale-greywacke); oxide and structure; oxide and mineralisation; supergene alteration and mineralisation; supergene alteration and structure.

To achieve the Sadiola Hill oxide zone geochemical complexities and alteration signatures study, many research studies were conducted such as lithological and oxide 2D mapping, lithological and oxide 3D modelling. The oxide profiles were sampled for gold analysis, XRF, and XRD analysis. The found minerals were separated into light and heavy.

The key minerals identified by XRD are alunite (K_2A_{l6} $(SO_4)_4(OH)_{12}$) and jarosite (K_2Fe_{63}+ $(SO_4)_4(OH)_{12}$). The mineral association suggests a highly acidic environment and acidic supergene conditions. The examination of oxides also allowed distinguishing the different ferricrete horizons in the Sadiola goldfield. Significant gold mineralisation is hosted in the oxide profile (weathered calc-silicate) in the Sadiola Hill opencast pit.

Sadiola gold plant at Sadiola gold mine is fed oxide ore mined from the oxidation profile in the weathered rock. The oxide ore fed into the Sadiola gold plant includes laterite, transitional oxide and saprolitic oxide. The age of oxide saprolite and oxide transitional zones is assumed to have formed during recent weathering by deeply penetrating meteoric waters. In general, the geology of the oxide feed is assumed to be derived from weathering and decomposition of rocks of the Birimian Supergroup. The need of oxide-feed to sustain Life of Mine of the Sadiola goldfield mean that exploration for oxide ore is critical but understanding the geology and geochemistry of the oxide is also vital, particularly in terms of ore optimization.

Five main lithologies are identified from mapping the Sadiola Hill area and these include calc-silicate, siltstone-shale-greywacke, metasandstone, diorite and quartz-feldspar porphyry. Furthermore, six calc-silicate sub-facies are identified as (1) thick-bedded (more than 0.5-1 cm) marble with an alternation of white and black layers, (2) thin-bedded (3-5 mm), (3) massive marble, (4) slump-folded marble, (5) carbonaceous siltstone and (6) pure marble. Oxide mapping in the Sadiola Hill opencast pit identified three oxide profiles and three distinct alteration types as follows (Type 1) decarbonated calc-silicate alteration, (Type 2) Fe alteration (oxide-jarosite-siderite), and (Type 3) potassic clay alteration. The Fe-oxide and potassic clay alteration profile are related to the gold mineralisation at the Sadiola goldfield.

3D lithological modelling conducted in the Sadiola goldfield has established a significant relationship between gold mineralisation and the calc-silicate unit. The 3D oxide profiles and hard

rock modelling defined three types of gold mineralisation according to the age of the host. Young gold is found in the ferricrete of Eocene-Miocene age, the second type of gold is found in the oxide profile (oxide saprolite and transitional) of unknown age and the third type is found in the hard rocks of Birimian age. Gold mineralisation is associated with the (1) lithological contacts, (2) north-south trending structure (Sadiola Fracture Zone), (3) northeast trending faults, while it is proportionally with iron (Fe) and potassium (K) alteration.

The three-oxide development has been sampled individually to characterise the oxide geochemistry and alteration signature. The geochemistry study of the oxide zone of the opencast mine identified the following minerals (1) Silica or quartz (SiO_2), (2) Goethite (Fe+ 3O.OH), (3) Muscovite ($KAl_3Si_3O_{10}$ (OH) $_2$), (4) Siderite ($FeCO_3$), (5) Biotite $KFeMg_2$ ($AlSi_3O_{10}$) (OH) $_2$, (6) Bernalite (Fe (OH) $_3$), (7) Orthoclase ($KAlSi_3O8$), (8) Alunite (K_2Al_6 (SO_4)4$(OH)_{12}$) and (9) Jarosite (K2Fe63+ (SO_4)4$(OH)_{12}$). The presence of jarosite and alunite are an indicator of an acidic pH condition. The XRF analysis results established the relationship between the gold grade and silica, potassium, and iron.

The presence of alunite and jarosite highlight a highly acidic environment and acid supergene conditions. The oxidation of the calc-silicate rock caused the diminution of volume and subsequent concentration of the gold mineralisation in the decarbonated calc-silicate mainly along the structures. This diminution of volume also caused the collapse of the contact between the siltstone-shale-greywacke in the west of the Sadiola Hill opencast pit and the decarbonated calc-silicate rock in the east. This contact is known as Sadiola Fracture Zone. The collapses of the decarbonated calc-silicate is associated with the flexure of the Sadiola Fracture Zone, a number of discontinuous bodies of diorites and quartz-feldspar porphyry units, and possibly produced the soft sediment deformation in the Sadiola Hill opencast pit.

Sadiola goldfield can be classified as an oxide gold enrichment deposit.

Acknowledgments

All my thanks to the Société d'Exploitation des Mines d'Or de Sadiola S.A. (SEMOS), AngloGold Ashanti and IAMGOLD for their financial support to make my MSc dream a reality. Special thanks to Exploration Manager, Geology Manager and the SEMOS SA General Manager for believing in me and all the staff of SEMOS.

Special thanks to my supervisors, Dr Asinne Tshibubudze and Professor Robert Bolhar for their support and Professor Kim Hein who gave me the self-confidence. I just want to say, 'God bless you'. In the same way, I thank the University of the Witwatersrand, Johannesburg and all the staff of Geosciences, Professor Roger Gibson, Dr Musa Manzi, and Kgothatso Nhlengetwa, Joe Aphane, Marlin Patchappa, Professor Dave Billing and Aarif Ellemdeen from School of Chemistry.

I thank, Eybers Heinrich, Hlabangana Sitshengiso, Samuel Tessougué, Siguia Traoré, Eric Imbeah, Geoffrey Gushee, Tom Gell, and Andre Strydom (SEMOS SA. Management Director) for their support.

I thank Mamadou Sidibé, Cheick Omar Sissoko, Sekou Samaké and all the Human Resources staff.

I thank Kaiba Keita, Sory I Goita, Mamadou A Traore, Adama Diombana, Zoumana Traoré, Soumaila Doulla, Bakary Ballo, Kefa Traoré and all Mining staff.

I would like to thank all my colleagues, Yaya Singaré, Fousseyni Samaké, Yacouba S Koné, Fousseini Magassouba, Monzon Traoré, Cheick O Baby, Baguiya Boulkadre, Cheickna Cissé and grade control staff, Amadou Traoré and Hydrogeology staff, Daouda Fofana, Wadiou Traoré, and Bassirou Traoré.

I would like to thank all the sampler staff for their collaborations in each field work with me. Thanks to Mamadou Yossi and all our promotion of Ecole Nationale d'Ingénieurs, Abderhamane Baba Touré de Bamako (ENI-ABT) promotion 2007.

I thank the Malian community present in South Africa especially in Johannesburg and Free State through Moussa Dagnoko.

Special thanks to my family; my wife Mariam Diarra, my dad Mamadou Traoré, my mom Kadidia Sacko, my aunties Nana Touré, Nana Sacko, and all my uncles and children Bany, Mohamed, Mariétou and Kadidia. Nephew Binké, Basidiki, Bamoye, nieces Fatoumata Nandy Keita, Mamy, and Awa are also thanked for their support. Also, all my friends Moustapha, Nouhoum, Moussa, Adama and brothers and sisters Moulaye, Fatoumata, Oumou and Tanti, for their support and encouragement.

Table of Contents

	Page
Abstract	*3*
Acknowledgements	*5*
Table of Contents	*6*
List of Figures	*8*
List of Tables	*17*
List of Appendices	*18*
Chapter 1 - Introduction	
1.1. Preamble	19
1.2. Location and physiography	23
1.3. Exploration and Mining History	26
1.4. Aims and Program	27
1.5. Acronyms and Abbreviations	28
1.6. Thesis Organisation	28
Chapter 2 – Literature Review	
2.1. Introduction	30
2.2. Geology of the Kédougou-Kéniéba Inlier (KKI)	30
2.3. Magmatism	35
2.4. Metamorphism	36
2.5. Structure and Tectonics	36
2.6. Mineralisation	37
2.7. Sadiola 3D gold mineralisation model	37
2.8. Alteration in the Sadiola goldfield	38
2.8.1. Hydrothermal alteration	*38*
2.8.2. Supergene alteration	*38*
Chapter 3 – Methodology	
3.1. Introduction	40
3.2. Mapping	40
3.3. Modelling	40
3.4. Sampling	41
3.5. XRF analysis	58
3.6. XRD analysis	58
3.7. Minerals separation	59
3.8. Geophysical character of the Sadiola goldfield	59
3.8.1. Sadiola gravity data	*59*
3.8.2. Sadiola magnetic data	*61*
3.8.3. Sadiola radiometric data	*63*
Chapter 4 - Results	
4.1. Sadiola mine scale and regional 2D mapping	**65**
4.1.1. Introduction	65
4.1.2. Lithologies	67
4.1.3. Alteration mapping	77
4.1.4. Structural mapping	85
4.1.5. Reverse Circulation (RC) and diamond borehole results	88
4.1.5.1. Sadiola Hill opencast pit	*88*
4.1.5.2. FN3 RC Results	*89*

4.1.5.3. Tambali diamond drillhole results *90*
4.1.6. Sadiola regolith mapping results 91
4.1.7. Sadiola termite mounts sampling results 92
4.1.8. Gold mineralisation distribution 94
4.1.8.1. Gold mineralisation distribution *94*
4.1.8.2. Relationship between gold mineralisation and oxide phases *95*
4.1.8.3. Relationship between gold mineralisation and calc-silicate sub-facies *99*
4.1.8.4. Relationship between structures and lithologies *99*

4.1.9. Summary 102

4.2. 3D modelling of Sadiola goldfield lithologies and oxide profiles 106
4.2.1. Introduction 106
4.2.2. Lithology modelling 106
4.2.3. Oxide modelling 107
4.2.4. Summary 112

4.3. Geochemical analysis Results 113
4.3.1. Introduction 113
4.3.2. Gold assays 114
4.3.3. XRF results 116
4.3.4. XRD results 126
4.3.5. Minerals Separation 157
4.3.6. Summary 157

Chapter 5 - Discussion
5.1. Oxide profile development 159
5.2. Genetic model hypothesis 163

Chapter 6 – Conclusions and Recommendation 165

Reference List 166

Appendices 172
Appendix A: University of Witwatersrand XRF laboratory procedure 172

Appendix B: University of the Witwatersrand minerals separation laboratory procedure 173

Appendix C: Field Mapping data and station point descriptions 174

Appendix D: Field notebook copy 204

Appendix E: Sadiola Hill opencast pit northwest RC drilling data 301

List of Figures

Figure 1: Location of the Kédougou Kéniéba Inlier (KKI) in the West Africa Craton (WAC). Modified after Hein et al. (2012).

Figure 2: Sadiola goldfield with ancillary opencast pits. Each pit is indicated by its name. The pits shapes were plotted in the ArcGIS to represent their position in the Sadiola district.

Figure 3: The laterite road in blue linking Kayes, Sadiola and Kéniéba while the red line is a tar road linking Bamako-Kayes-Dakar.

Figure 4: Position and name of artisanal mining in the Sadiola goldfield. The names of artisanal mines indicate their location, while the light blue colour represents the waste dump and the dark yellow colour represent the opencast pits. Each artisanal mine was contoured with a GPS.

Figure 5: The inserted map shows the position of the WAC in Africa. A- Presentation of the study area in Sadiola goldfield. B- Location of the different goldfield in the Kédougou-Kénieba Inlier. In the KKI the SMSZ (Sénégalo-Malian Shear Zone) is located in the east and the MTZ (Main Transcurrent Zone) at the west (after Hein et al., 2012).

Figure 6: Sadiola goldfield local geological map, this map is established by a compilation of the field mapping and drilling data.

Figure 7: Photograph of the samples according to the alteration profile.

a. Photograph of the sample DTMS-012, showing very fine-grained sand with strong oxidized profile and Fe alteration red colour (quartz 35%, clay 55% sericite 10%).
b. Photograph of the sample DTMS-013 showing fine-grained decarbonated calc-silicate alteration (quartz 35%, clay 60%, sericite 5%).
c. Photograph of the sample DTMS-014 presents potassic and decarbonated alteration. The rock is bedded with slump folds (Hein and Tshibubudze, 2007).
d. Sample DTMS-015 comprises Fe alteration with red-brown colour (quartz 45%, clay 45% sericite 10%).
e. Sample DTMS-016 fine grain clayey sand (quartz 40% clay 50% sericite 10%. Fe alteration.
f. Sample DTMS-017 of quartz 30%, clay 55%, sericite 10%, and biotite 5%.

Figure 8: Photograph of the samples according to the alteration profile.

a. Sample DTMS-018 quartz 30% clay 55% sericite 5% biotite 5% Potassic alteration fine grain, clayey sand.
b. Sample DTMS-019 quartz 40% clay 55% sericite 5% Fe alteration fine grain, clayey sand.
c. Sample DTMS-021 quartz 35% clay 55% sericite 5% biotite 5% fine grain potassic alteration, name clayey sand.
d. Sample DTMS-022 quartz 45% clay 55% fine grain potassic alteration bedded, clayey sand
e. Sample DTMS-023 quartz 45% clay 55% fine grain Fe alteration, clayey sand

f. Sample DTMS-024 quartz 30% clay 65% sericite 5% fine grain decarbonated calc-silicate massive, clayey sand

Figure 9: Photograph of the samples according to the alteration profile.

a. Sample DTMS-025 quartz 45% clay 50% sericite 5% fine grain, bedded to massive with weak Fe alteration, clayey sand.
b. Show the sample DTMS-026 with quartz 40% clay 55% sericite 5% fine grain with decarbonated calc-silicate alteration and the sample DTMS-027 quartz 45% clay 50% sericite 5% fine grain with Fe alteration, clayey sand.
c. Sample DTMS-028 quartz 40% clay 55% sericite 5% fine grain Fe alteration, clayey sand.
d. Sample DTMS-029 quartz 35% clay 55% sericite 5% biotite 5% fine grain strong potassic alteration, clayey sand.
e. Sample DTMS-030/031 duplicated sample as composition there are quartz 45% clay 55% fine grain with strong Fe alteration brown colour, clayey sand.
f. Sample DTMS-032 quartz 45% clay 55% fine grain, Fe alteration, clayey sand.

Figure 10: Photograph of the samples according to the alteration profile.

a. Sample DTMS-033 quartz 40% clay 55% biotite 5% fine grain strong Fe alteration, clayey sand.
b. This photograph the following three sample DTMS-034 mineral composition is quartz 45% clay 50% sericite 5% decarbonated calc-silicate alteration; DTMS-036 presents quartz 40% clay 50% biotite 10% fine grain potassic alteration; DTMS-037 quartz 45% clay 55% fine grain Fe alteration, clayey sand.
c. This photograph shows the following sample: sample DTMS-038 presents quartz 40% clay 50% biotite 10% fine grain with strong potassic alteration, clayey sand; DTMS-039 presents quartz 40% clay 50% biotite 10% fine grain decarbonated calc-silicate alteration; DTMS-041 quartz 45% clay 55% fine grain Fe alteration, clayey sand.

Figure 11: Photograph of the samples according to the alteration profile.

a. Photograph of the sample DTMS-046, showing fine-grained sand decarbonated calc-silicate alteration, sandy clay (quartz 50%, clay 35% sericite 5% biotite 10%).
b. Photograph of the sample DTMS-047 showing fine-grained, Fe alteration clayey sand (quartz 45%, clay 50%, and sericite 5%).
c. Photograph of the sample DTMS-048, fine grain, presents Fe alteration, clayey sand (quartz 40%, clay 50%, biotite 5% and sericite 5%).
d. Photograph of the sample DTMS-049 comprises Fe alteration, fine grain with red colour clayey sand (quartz 40%, clay 55% sericite 5%).
e. Photograph of the sample DTMS-050/051 duplicated sample, fine grain with Fe alteration clayey sand (quartz 45% clay 55%).
f. Photograph of the sample DTMS-052 presents quartz 30%, clay 70%, and fine grain with Fe alteration, clayey sand.

Figure 12: Photograph of the samples according to the alteration profile.

a. Sample DTMS-053 presents quartz 40% clay 45% sericite 10% biotite 5% Fe alteration fine grain, clayey sand.
b. Sample DTMS-054 presents quartz 40% clay 60% decarbonated calc-silicate, Fe alteration fine grain, and clayey sand.
c. Sample DTMS-055 presents quartz 45% clay 55% decarbonated calc-silicate alteration, clayey sand.
d. Sample DTMS-056 presents quartz 40% clay 55% biotite 5%, fine grain strong Fe alteration, and clayey sand
e. Sample DTMS-057 presents quartz 35% clay 65% fine grain K alteration, clayey sand
f. Sample DTMS-058 presents quartz 45% clay 55% fine grain Fe alteration, clayey sand

Figure 13: Photograph of the samples according to the alteration profile.

a. Sample DTMS-059 presents quartz 55% clay 45% fine grain, Fe alteration, clayey sand.
b. Sample DTMS-061 shows quartz 45% clay 55% fine grain with decarbonated calc-silicate alteration clayey sand.
c. Sample DTMS-062 quartz 30% clay 70% fine grain K alteration, clayey sand.
d. Sample DTMS-063 quartz 45% clay 55% fine grain Fe alteration, clayey sand.
e. Sample DTMS-064 as composition there are quartz 45% clay 55% fine grain with strong Fe alteration brown colour, clayey sand.
f. Sample DTMS-066 quartz 45% clay 55% fine grain, K alteration, clayey sand.

Figure 14: Photograph of the samples according to the alteration profile.

a. Photograph of the sample DTMS-067, showing fine-grained clayey sand with Fe alteration (quartz 40%, clay 60%).
b. Photograph of the sample DTMS-068 showing fine-grained, clayey sand, with a decarbonated calc-silicate alteration (quartz 30%, clay 70%).
c. Photograph of the sample DTMS-069, showing fine-grained, clayey sand with K alteration (quartz 35%, clay 65%).
d. Photograph of the sample DTMS-070/DTMS-071 showing fine-grained, decarbonated calc-silicate alteration (quartz 30%, clay 70%).
e. Photograph of the sample DTMS-072, showing fine-grained sand, Fe alteration (quartz 35%, clay 65%) clayey sand.
f. Photograph of the sample DTMS-073 showing fine-grained, clayey sand, K alteration (quartz 30%, clay 70%).

Figure 15: Photograph of the samples according to the alteration profile.

a. Photograph of the sample DTMS-074, showing fine-grained clayey sand K alteration (quartz 35%, clay 65%).

b. Photograph of the sample DTMS-075 showing fine-grained decarbonated calc-silicate alteration (quartz 40%, clay 60%). Photograph of the sample DTMS-076, showing fine-grained clayey sand with Fe alteration (quartz 35%, clay 65%).
c. Photograph of the sample DTMS-077 showing fine-grained, K alteration, clayey sand (quartz 30%, clay 70%).
d. Photograph of the sample DTMS-078, showing fine-grained clayey sand Fe alteration (quartz 35%, clay 65%).
e. Photograph of the sample DTMS-079 showing fine-grained, with K alteration (quartz 35%, clay 65%).
f. Photograph of the sample DTMS-081 showing fine-grained, with a decarbonated calc-silicate alteration (quartz 30%, clay 70%).

Figure 16: Photograph of the samples according to the alteration profile.

a. Photograph of the sample DTMS-082, showing fine-grained clayey sand Fe alteration (quartz 30%, clay 70%).
b. Photograph of the sample DTMS-083 showing fine-grained, Fe alteration (quartz 35%, clay 65%).
c. Photograph showing a massive calc-silicate rock with micro fault.
d. Photograph showing unconformity between oxidized profile and fresh calc-silicate rock.
e. Photograph showing bedded calc-silicate rock.
f. Photograph showing the folded calc-silicate.

Figure 17: Sadiola goldfield regional gravity map. The blue colour represents low gravity, while the red the high gravity. Each open cast pit is located on area of low gravity, where oxides are mined for gold. Sadiola goldfield gravity data has been plotted in the Arc GIS. The black line on the map represents the SMSZ.

Figure 18: Regional Magnetic data and interpretation map on the Sadiola goldfield shows the shape and width of the SMSZ. The SMSZ is located on the western side of the map. This Sadiola total field is GradEnh_0p05_NEW_RTPLL_UC50_1VD.ecw.

Figure 19: The regional radiometric data across the Sadiola goldfield. The blue light colour shows the ferricrete which cover most parts of the goldfield. The red colour represents some outcrop through the goldfield.

Figure 20: Position of the forty-four RC holes drilled in the Sadiola Hill NW, the holes were logged for stratigraphic definition purposes.

Figure 21: Lithological map of the FN3 south and north pits. The pits are dominated by altered and unaltered calc-silicate rock and crosscut by quartz-feldspar porphyry.

Figure 22: Sadiola Hill opencast pit geological map. The eastern part of the pit is the altered and unaltered calc-silicate, while the western part is the siltstone-shale greywacke. The contact is

structurally defined by the SFZ. The sedimentary rocks are cross cut by a dyke and sill of diorite and quartz-feldspar porphyry dyke.

Figure 23: Lithological map of the Tambali opencast pits. The pits are composed mainly of sandstone and greywacke. The dyke of diorite and quartz-feldspar porphyry across the sedimentary rock.

Figure 24: The red sandstone mapped at the southwest of the Sadiola Hill. (A) present the photograph of the sandstone and (B) the position of the map.

Figure 25(a): Photography of the three different layers of the ferricrete on the decarbonated calc-silicate, the aeolian sand separates them. Looking east of the Sadiola Hill opencast pit. (b) Photography of layers of ferricrete on the decarbonated calc-silicate, the aeolian sand separates them. Image taken looking east, north of the Sadiola Hill opencast pit.

Figure 26: The hydrothermal alteration presents in the SFZ from the middle of the Sadiola Hill opencast pit.

Figure 27: West-east vertical cross section along a 1537775 Nm latitude line showing the Sadiola Hill opencast oxide profile. All the four domains are well depicted from the hard rock to the ferricrete horizon.

Figure 28: Photograph of ferricrete in the Sadiola Hill opencast showing the coarse pisolitic gravel and quartz which indicates weathering of transported materials.

Figure 29: A plan view of oxide map for Tambali north and south pits, composed of ferricrete in red colour, the oxide saprolite, the oxide transitional zone is the light blue colour and the hard rock is represented by the grey colour.

Figure 30: The oxide map of the Sadiola Hill opencast pit, composed of ferricrete in red colour, the oxide saprolite, the oxide transitional zone is the light blue colour and the hard rock in grey colour.

Figure 31: The oxide map for FN3 north and south pits, composed of ferricrete in red colour, the oxide saprolite, the oxide transitional zone is the light blue colour and the hard rock in grey colour.

Figure 32: Photograph of the weathering profile on the southern wall of the Sadiola Hill opencast pit. The shape is presented as a funnel of the meteoric water penetration.

Figure 33: West-east cross-sectional sketch of the Sadiola Hill genetic model for the supergene enrichment phase. The D2 deformation related to northwest-southeast compression, probably associated with the Eburnean orogeny, produced an effect on the SFZ, and north-northeast trending faults. The SFZ and north-northeast trending faults seem to be syn-genetic. The source of the gold in the Sadiola Hill opencast pit was concluded by Hein (2007) as hydrothermal.

Figure 34: Sadiola Hill opencast stratigraphic column. The column was established by the compilation of the pit mapping data and RC and diamond drilling data.

Figure 35: Tambali opencast pit stratigraphic column. The column was established by the compilation of the pit mapping data and RC and diamond) drilling data.

Figure 36: Map of termite mounds sample result in the Sadiola exploration permit. The red (high value), (2) yellow (medium), (3) green (Low) and (4) blue (zero) of gold. This value is overprinted on each open cast pit in the Sadiola goldfield.

Figure 37: The 3D Sadiola goldfield gold mineralisation model across the Tambali, Sadiola Hill open cast and FN3 pits. Compiled by SEMOS resources evaluation team.

Figure 38: The 3D laterite model plotted with the 3D gold mineralisation model for Sadiola goldfield (FN3 in the northern, Sadiola Hill open cast in the middle, and the Tambali pits in the southern).

Figure 39: The 3D oxide saprolite model plotted with the 3D gold mineralisation model for Sadiola goldfield (FN3 in the northern, Sadiola Hill open cast in the middle, and the Tambali pits in the southern part).

Figure 40: The 3D oxide transitional zone plotted with the 3D gold mineralisation model for Sadiola goldfield (FN3 in the northern, Sadiola Hill open cast in the middle, and the Tambali pits in the southern part).

Figure 41: The SFZ, northeast trending faults and west east trending faults plotted on the Sadiola Hill opencast pit geological map. The SFZ is located along the contact between the siltstone-shale-greywacke in the west and the calc-silicate in the east.

Figure 42: West-east cross-sectional sketch of the Sadiola Hill genetic model for the supergene enrichment phase. The surface water penetrated the calc-silicate rock through the SFZ and northeast trending structures. The pyrite in the presence of H_2O and O_2 can active some reactions and cause the oxidation of calc-silicate.

Figure 43: West-east cross-sectional sketch of the Sadiola Hill genetic model for the supergene enrichment phase. The decrease in the volume of the decarbonated calc-silicate caused the collapse of oxide. Then SFZ which is a lithological contact between siltstone-shale-greywacke and calc-silicate collapsed. Subsequently, aeolian sand was deposited on the ferricrete and on the decarbonated calc-silicate.

Figure 44: West-east cross-sectional sketch of the Sadiola Hill showing the results of oxidation and collapse of the oxide profile.

Figure 45: The 3D Sadiola goldfield lithology model. The green at the west represents the siltstone-shale-greywacke, while the calc-silicate is located mostly in the east with the blue colour.

Figure 46: The 3D laterite model for Sadiola goldfield (FN3 in the northern, Sadiola Hill open cast in the middle, and the Tambali pits in the southern part).

Figure 47: The 3D oxide saprolite model for Sadiola goldfield (FN3 in the northern, Sadiola Hill open cast in the middle, and the Tambali pits in the southern).

Figure 48: The 3D oxide transitional zone for Sadiola goldfield (FN3 in the northern, Sadiola Hill open cast in the middle, and the Tambali pits in the southern part).

Figure 49: The 3D hard rock model for Sadiola goldfield (FN3 in the northern, Sadiola Hill open cast in the middle, and the Tambali pits in the south).

Figure 50: The supergene alteration presents in the calc-silicate rock from the southern area to north of the Sadiola Hill opencast pit.

Figure 51: The three-oxide facies developed in the Sadiola Hill opencast pit. The blue colour is decarbonated calc-silicate rocks, crosscut by the red Fe-oxide alteration zones, which are in turn crosscut by zones of pink colour potassic clay alteration.

Figure 52: Diagram of SEMOS XRF "Mining Plus" showing silica (Si), potassium (K), calcium (Ca), and the iron (Fe) with gold result. There is a strong correlation, between gold and iron alteration and a second correlation with Au and potassium K, while no correlation with calcium (Ca) was examined due to the absence or weakness of Ca due to the oxidation.

Figure 53: Diagram of the XRF result analysed in the Earth laboratory of the University of the Witwatersrand, Johannesburg. On the chart, concentrations in ppm are shown on the vertical axis, while the samples are given along the horizontal axis.

Figure 54: The result of sample DTMS-012 contains silica, goethite, muscovite, siderite and biotite minerals.

Figure 55: The result of sample DTMS-013 contains silica, goethite, muscovite, siderite and biotite minerals.

Figure 56: The result of sample DTMS-014 contains silica, goethite, muscovite, siderite and biotite minerals.

Figure 57: The result of sample DTMS-015 contains silica, goethite, muscovite, siderite, bernalite and biotite minerals.

Figure 58: The result of sample DTMS-016 contains silica, goethite, muscovite, siderite and biotite minerals.

Figure 59: The result of sample DTMS-017 indicates the presents of silica, goethite, muscovite, siderite and biotite minerals.

Figure 60: The result of sample DTMS-018 indicates the presents of silica, goethite, muscovite, siderite and biotite minerals.

Figure 61: The result of sample DTMS-019 indicates the presents of silica, goethite, muscovite, siderite and biotite minerals.

Figure 62: The result of sample DTMS-021 indicates the presents of silica, goethite, muscovite, siderite and biotite minerals.

Figure 63: The result of sample DTMS-025 indicates the presents of silica, goethite, muscovite, siderite and biotite minerals.

Figure 64: The result of sample DTMS-026 indicates the presents of silica, goethite, muscovite, siderite and biotite minerals.

Figure 65: The result of sample DTMS-027 indicates the presents of silica, goethite, muscovite, siderite and biotite minerals.
Figure 66: The result of sample DTMS-028 indicates the presents of silica, goethite, muscovite, siderite and biotite minerals.
Figure 67: The result of sample DTMS-029 indicates the presents of silica, goethite, muscovite, siderite and biotite minerals.
Figure 68: The result of sample DTMS-030 indicates the presents of silica, goethite, muscovite, siderite and biotite minerals.
Figure 69: The result of sample DTMS-033 indicates the presents of silica, goethite, muscovite, siderite and biotite minerals.
Figure 70: The result of sample DTMS-034 indicates the presents of silica, goethite, muscovite, siderite and biotite minerals.
Figure 71: The result of sample DTMS-036 indicates the presents of silica, goethite, muscovite, siderite and biotite minerals.
Figure 72: The result of sample DTMS-037 indicates the presents of silica, goethite, muscovite, siderite and biotite minerals.
Figure 73: The result of sample DTMS-038 indicates the presents of silica, goethite, muscovite, siderite and biotite minerals.
Figure 74: The result of sample DTMS-039 indicates the presents of silica, goethite, muscovite, siderite and biotite minerals.
Figure 75: The result of sample DTMS-041 indicates the presents of silica, goethite, muscovite, siderite and biotite minerals.
Figure 76: The result of sample DTMS-048 indicates the presents of silica, goethite, muscovite, siderite and biotite minerals.
Figure 77: The result of sample DTMS-050 indicates the presents of silica, goethite, muscovite, siderite and biotite minerals.
Figure 78: The result of sample DTMS-053 indicates the presents of silica, goethite, muscovite, siderite and biotite minerals.
Figure 79: The result of sample DTMS-056 indicates the presents of silica, goethite, muscovite, siderite and biotite minerals.
Figure 80: The result of sample DTMS-062 indicates the presents of silica, goethite, muscovite, siderite and biotite minerals.
Figure 81: The result of sample DTMS-074 indicates the presents of silica, goethite, muscovite, siderite and biotite minerals.
Figure 82: The result of sample DTMS-077 indicates the presents of silica, goethite, muscovite, siderite and biotite minerals.

Figure 83: The result of sample DTMS-082 indicates the presents of silica, goethite, muscovite, siderite and biotite minerals.

List of Tables

Table 1 - Samples descriptions and related gold grades

Table 2 - Orientation, Assay and composition results of samples from Sadiola Hill opencast pit southwest sample data

Table 3 - Gold assay results in grams per tonne

Table 4 - SEMOS portable handheld XRF result in Soil Mode

Table 5 - SEMOS portable handheld XRF analysis in Mining Plus Mode

Table 6 - University of the Witwatersrand XRF analysis results

List of Appendices

Appendix A University of the Witwatersrand XRF laboratory procedure.

Appendix B University of the Witwatersrand mineral separation laboratory procedure

Appendix C Field Mapping data and station point descriptions

Appendix D Field notebook copy

Appendix E Sadiola Hill opencast pit northwest RC drilling data

Chapter 1
Introduction

1.1. Preamble

The Sadiola goldfield is located in the eastern Kédougou Kéniéba Inlier (KKI) of the West African Craton (WAC) (Figure 1). The Sadiola gold deposit is mined in several opencast pits including the Sadiola Hill opencast pit, Tambali, FE3, FE4, Timbougouni, FND, Farabakouta North BC (FNBC), FNA, FN3 and FN2 pits (Figure 2). The Sadiola gold mine is operated and mined by the Société d'Exploitation des Mines d'Or de Sadiola SA (SEMOS) through a joint venture partnership between AngloGold Ashanti (AGA), IAMGOLD and the Malian government. Since December 1996, SEMOS has mined oxide gold (saprolite, transitional) from the Sadiola Hill opencast pit, but the resource is almost exhausted and the Sadiola Hill deposit has reached its Life of Mine. The Sadiola Deep Sulphide Project now known as the Sadiola Sulphide Project (SSP), which is focused on hard rock sulphide ore below the oxide zone, is a focus of exploration for future development. The challenge for SEMOS is to develop or discover new oxide gold deposits, while developing the hard rock Sadiola Sulphide ore. There is a need to further understand the distribution of gold in the oxide zone, while exploring the relationship between hard rock sulphide ore and the dispersion of gold in the oxide. The oxide zone is gradational from transition zone rocks to saprolitic oxide; the saprolitic oxide is associated with alteration sub-facies of decarbonation, sulphidation, kaolinisation and lateritization, as observed during field studies early in 2015.

The aims of this research are to study the different geological relationships: oxide and unaltered rock (calc-silicate, siltstone-shale-greywacke); oxide and structure; oxide and mineralisation; supergene alteration and mineralisation; supergene alteration and structure.

The lithologies in the Sadiola goldfield are dominated by rocks of the Birimian Supergroup of the Dialé-Kofi Formation. Hein and Tshibubudze (2007) classified the lithologies of the Sadiola goldfield into greywacke, volcaniclastic, volcaniclastic-greywacke, carbonaceous siltstone, marble, carbonaceous greywacke, BIF, shale and graphitic shale. The sedimentary textures observed indicate that shallow marine deltaic processes and turbidite activity were operating conjointly during deposition. The units have been metamorphosed to at least upper greenschist facies and locally, to amphibolite facies adjacent to diorite and granodiorite dykes. The rock units are thus altered to quartzite, calc-silicate, and metapelitic rocks.

The Sadiola Fracture Zone (SFZ) is exposed in the Sadiola Hill opencast pit. It forms the tectonic boundary between hanging-wall greywacke on the western high-wall of the opencast and footwall calc-silicates on the eastern high wall. The SFZ generally trends north-south and dips steeply west to vertical. Gold mineralisation is hosted in and along the SFZ and along northeast trending

faults. The SFZ is brittle-ductile in character and ranges in thickness from 10 m to over 60 m (Cameron, 2010).

In the Sadiola goldfield there are two reported gold mineralisation styles: 1) Placer gold in palaeochannels and screes; 2) gold in breccia and stockwork veins (Hein and Tshibubudze, 2007). Masurel et al. (2017) established that gold mineralisation can be correlated to the disseminated sulphides along hydrothermal-tectonic shear zone hosted in breccia and biotite-calcite-tourmaline-quartz vein. Around 50% of the ore minerals are comparatively different, but their volumetric proportions are typically low in each rock type, ranging from approximately 0.5 to 3% sulphides.

Gold can also be found in reworked laterite above the saprolitic oxide that is locally interpreted as Tertiary in age; in saprolite and transitional oxide facies, and unweathered Birimian host rock. The oxide ore fed into the Sadiola gold plant includes laterite, transitional oxide and saprolitic oxide.

The age of oxide formation in the Sadiola goldfield is assumed to be modern and related to deep weathering of the host Birimian rocks. However, at the Yatela gold mine, north of Sadiola, oxide formation is associated with the development of karst residuum that formed over a considerable period of time, perhaps 2.0 Ga ago, but principally during the Neoproterozoic and Cretaceous (Hein et al., 2015), which may mean that the oxide at Sadiola formed over a long period of time.

This research project used mapping and characterisation of the various phases of oxide in the oxide zone that is exposed in the opencast pit of the Sadiola goldfield. The temporal relationship of gold in the oxide zone, with respect to the age of oxide formation, was investigated. Another research focus was to establish the relationship between oxide formation and gold dispersion in the oxide zone and sulphide ore in calc-silicate rocks.

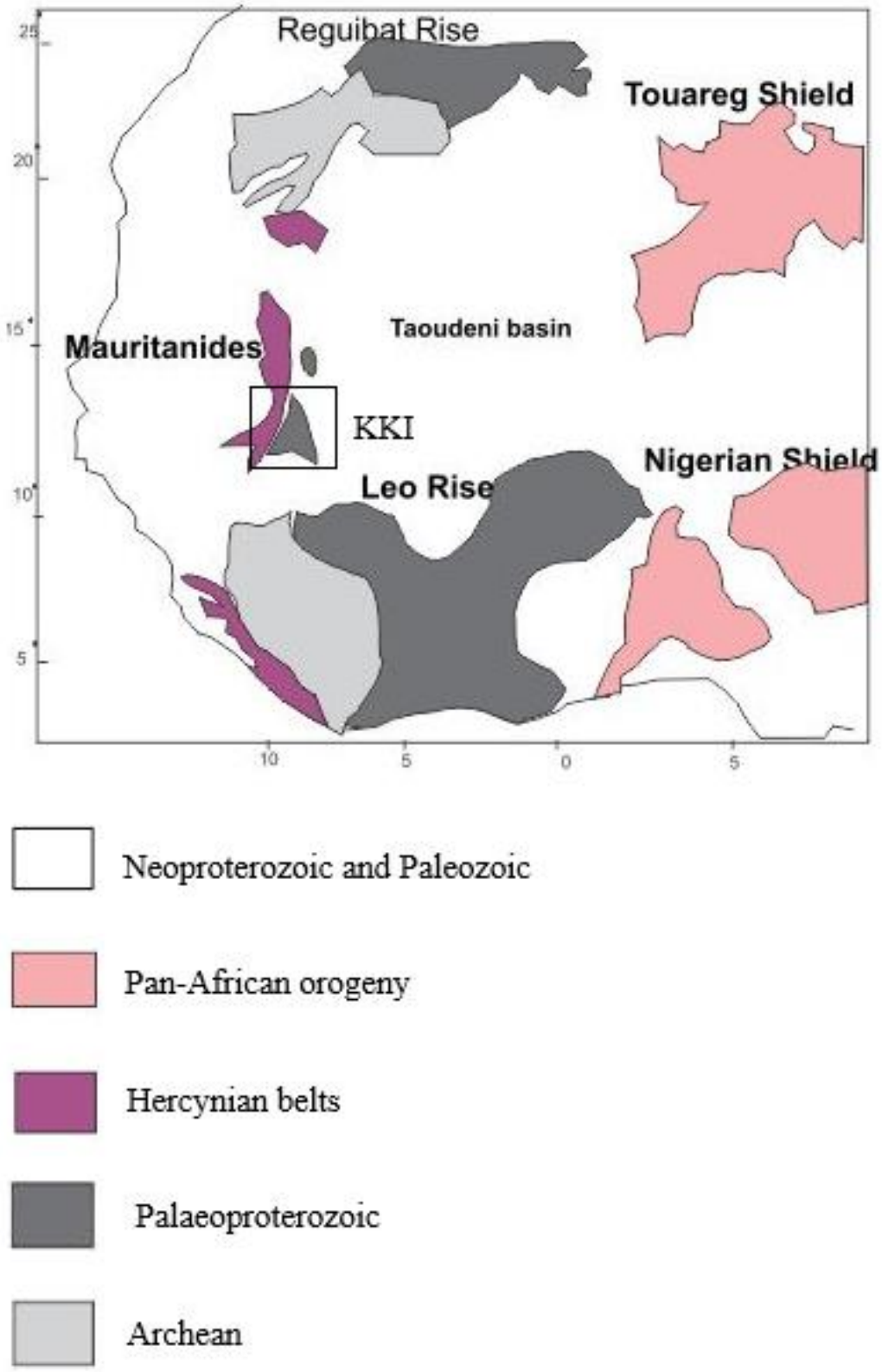

Figure 1: Location of the Kédougou Kéniéba Inlier (KKI) in the West Africa Craton (WAC). Modified after Hein et al. (2012).

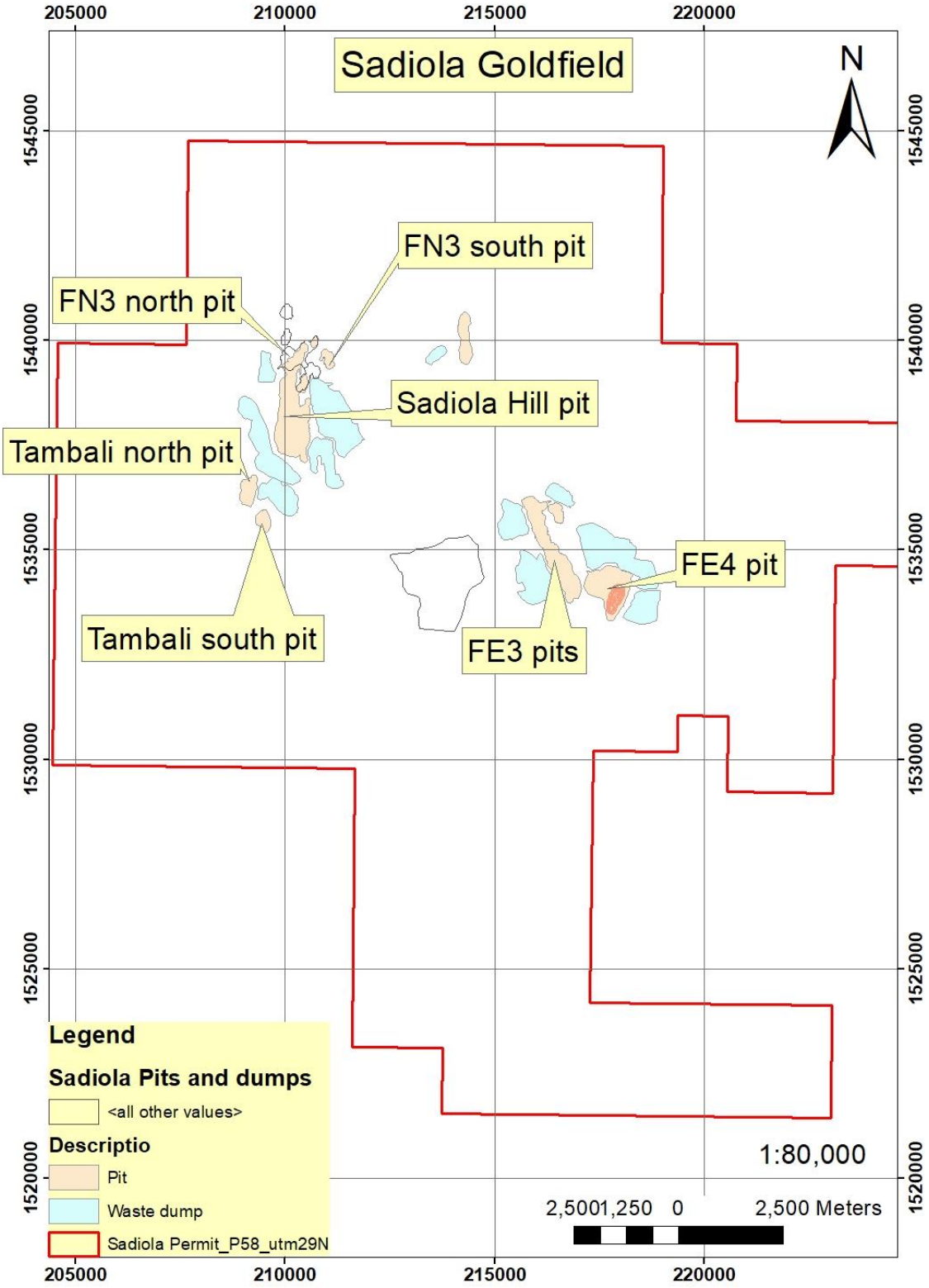

Figure 2: Sadiola goldfield with ancillary opencast pits. Each pit is indicated by its name. The pits shapes were plotted in the ArcGIS to represent their position in the Sadiola district.

1.2. Location and physiography

The study area is located in the Kayes region around 600 km from Bamako capital of Mali and 740 km from Dakar (Senegal). The Sadiola goldfield is located in the western region of the Republic of Mali close to the international border between Mali and Senegal, and approximately 75 km south of the regional capital of Kayes (Figure 3) in the sub-Sahelian region of West Africa. Sadiola is a rural commune in the municipality of the Kayes region. Covering an area of 3,050 km^2, it encompasses 46 villages and 50 hamlets. It has about 23,000 inhabitants. The city of Kayes is accessible by railway (Bamako-Kayes-Dakar), a paved road (Bamako-Kayes) as well as using an international airport.

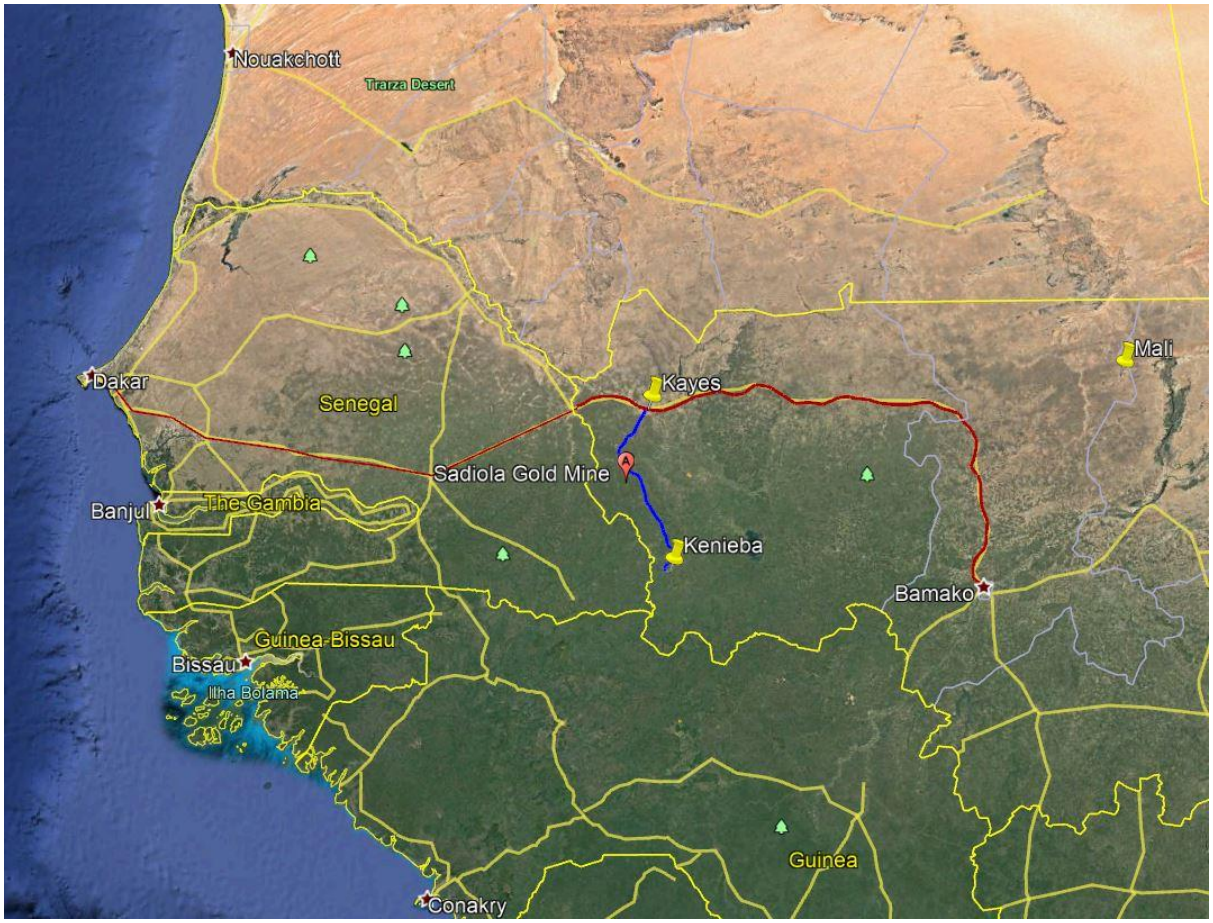

Figure 3: The laterite road in blue linking Kayes, Sadiola and Kéniéba while the red line is a tar road linking Bamako-Kayes-Dakar.

The Sadiola commune can be accessed by a domestic flight via Bamako airport linking Bamako-Kayes-Sadiola-Dakar. There is also a laterite road linking Kayes, Sadiola and Kéniéba. The mine is named after the place where it was discovered. Its geographical coordinates are 13°53'00" north, 11°42'0" west and east by the Souroukoto cliff. The region is characterized by a Sudano-Sahelian climate with three (3) seasons: (1) dry season (March to May); (2) rainy season (June to

October); (3) cold season (December to January). The climate is sub-humid in the south with rainfall of about 1000mm / year, and increasingly more arid towards the north with rainfall of about 600mm / year. The minimum and maximum temperatures during the year vary from 10° to 27° and from 25° to 45°C respectively. The vegetation, north of the Senegal River (semi-arid to sub-desert), is sparse and monotonous with fairly common baobabs and thorny trees. To the south, it is much denser and varied and is of the shrub or forest savannah type. The human population consists of Malinké, Sarakolé of Fulani and Moors. In addition, there are persons of other nationalities employed at the Sadiola gold mine. The main activities are agriculture (millet, groundnuts and sometimes maize), livestock (cattle, sheep, goats) and gold panning. Hydrography consists of temporary streams that flow only in the rainy season and dry up after the rainy season. Written records of mining at Sadiola reportedly date back 250 years and the extent of the old workings suggests that the mining could have occurred over 1,000 years ago (http://www.iamgold.com, 2015). Artisanal mining for gold was practised for centuries and especially at Farabakouta and Timbabougouni; artisanal mining continues today at Diagounté and Kantéla. Evidence for ancient and recent artisanal mining is widespread in western Mali; this is also the case at Sadiola goldfield (Figure 4). In the 7th to 14th century, the trade in gold across the Trans-Saharan trade routes was important for the Mediterranean economies. The gold together with iron and slaves was traded for salt (AAOA, 2000).

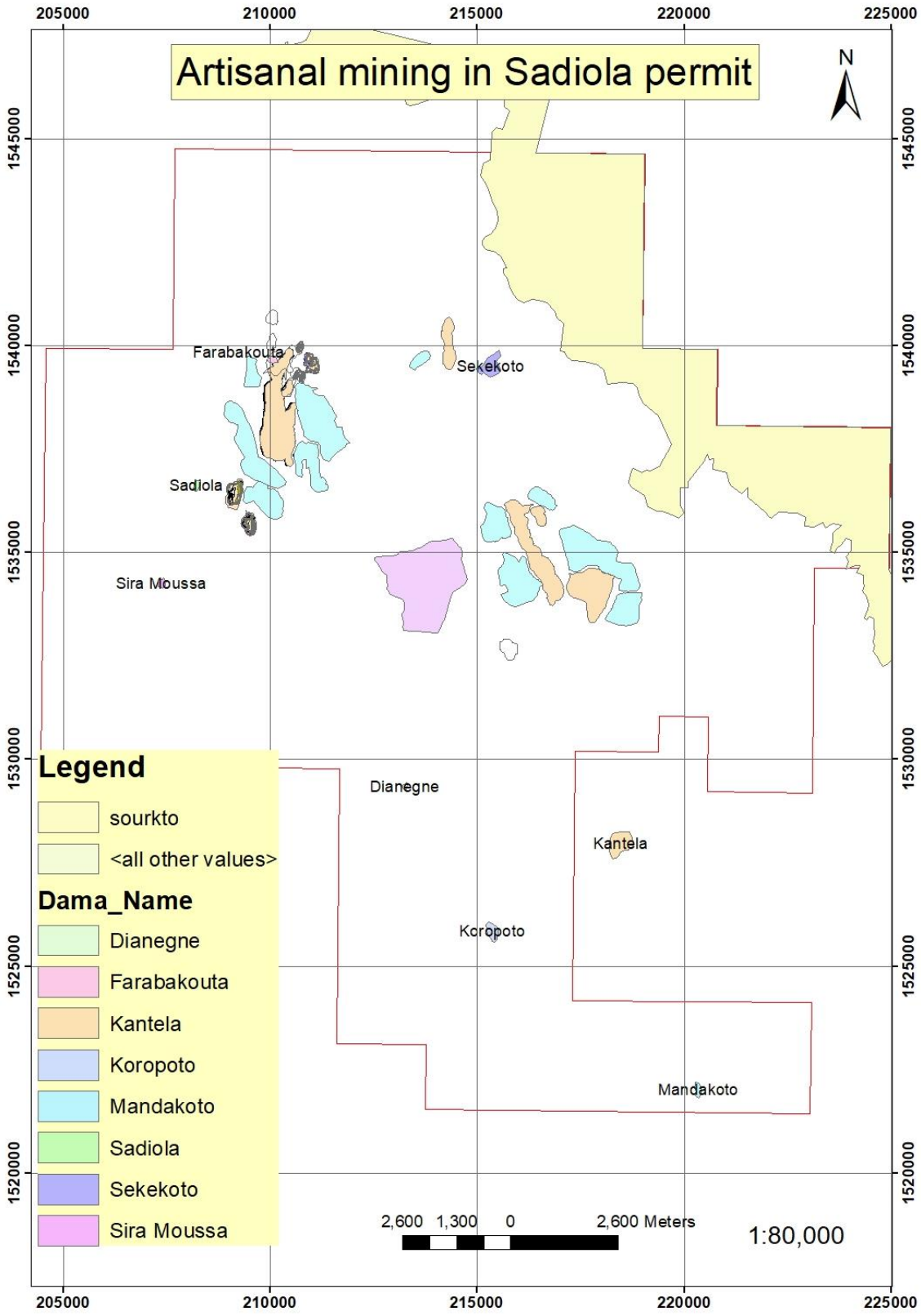

Figure 4: Position and name of artisanal mining in the Sadiola goldfield. The names of artisanal mines indicate their location, while the light blue colour represents the waste dump and the dark yellow colour represent the opencast pits. Each artisanal mine was contoured with a GPS.

1.3. Exploration and Mining History

The first major studies in the Sadiola goldfield began in the early twentieth century, mainly including the work of Hubert in 1909 to 1919 who presented the first geological map of the Afrique Occidentale Française (AOF) at 1:5,000,000. Skawych in 1913 established a first geological map at 1:500,000.

From 1979 to 1985, the Unions Gold Diamond company, COGEMA Uranium and other companies conducted regional research work. In 1987, Mali-West I, which was financed by the European Development Fund (EDF), undertook a study of the geology and geochemistry (1000m x 250 m grid) of the Kayes Inlier and KKI. In 1989, under the direction of Klöckner Industrie, the Mali-West I project investigated soil geochemistry of the Sadiola anomaly, as confirmed in 1987-1988 by Mali-West I project at its first reconnaissance campaign of Sadiola Hill, discovering high 5 g/t gold at the surface.

From 1990 to 1992, Klöckner Industrie and IAMGOLD (AGEM) conducted the first evaluation surveys of the Sadiola goldfield. In 1992, IAMGOLD and Anglo-American signed an agreement to undertake exploration, which included a systematic core drilling program and feasibility study of the Sadiola goldfield. Commercial mine development of the Sadiola goldfield began in 1992 and was based on proven and probable reserves amounting to 49.2 Mt of oxide and partly oxidized ore with an average grade of 2.86 g/t Au, representing some 4.5 Moz of contained gold at an average depth of 140 m (Boshoff et al., 1998).

During 1994 to 1998, the Australian company ELTINE (ELTINE Mali) discovered the Yatela gold deposit north of the Sadiola Hill deposits; the Yatela gold deposit was transferred to SADEX-SA (Sadiola Mining) and ANSER (Anglo Services, now known as SEMOS SA) undertook feasibility studies of the deposit. During 1998-1999, a 200 m x 50 m regolith and soil geochemistry campaign was completed on the exploration permit. From 1999 to 2009, ANSER discovered gold anomalies using detailed soil geochemistry, which additionally resulted in the discovery of several satellite deposits. From 2009 to 2015, SEMOS SA Exploration explored and mined the gold resources in both the Sadiola and Yatela goldfields, including satellite deposits at Alamoutala (Masurel et al., 2014), FE3, FE4 and Yatela.

Several Sadiola deposit genesis models have been proposed by a number of consultants, which has complicated a full understanding of the deposits in the goldfield. The Sadiola deposit has been variously classified as:

1) Carlin-style (Voet, 1996)
2) Intrusion-related style (Anonymous, 1994; Voet, 1996; Theron 1997)
3) Mesothermal Lode style
4) Greisen style
5) Skarn (distal to proximal deposit) (Sillitoe, 1994; Boshoff et al., 1998)

6) Thermal Aureole Gold Deposit or TAGD (Hein et al., 2007)

7) Carbonate-hosted Au-As-Sb mineralisation (Masurel et al., 2014; 2016).

According to Masurel et al. (2017), the structural setting and fluid flux were critical factors dictating gold mineralisation processes, although the source of fluid and metals for the Sadiola Hill hydrothermal system remains uncertain.

1.4. Aims and program

At Sadiola goldfield there are several forms of gold mineralisation, including detrital gold in Tertiary sediments, gold in oxidized rock and gold as calc-silicate hard-rock sulphide ore. The Sadiola operation currently mines detrital and oxide gold, but the future development of the goldfield may focus on hard-rock sulphide potential that exists at depth beneath the Sadiola Hill opencast pit. The hard-rock sulphide ore has been extensively studied and reported by Cameron (2010) and Masurel et al. (2017), but the character of gold ore in the oxide zone has not been systematically studied.

The aims of this project are to study the relationships between the oxides and calc-silicate; oxides and structures; oxides and mineralisation; alteration and structures as well as structure and mineralisation. Therefore, this research can be subdivided into three themes:

Theme 1: Modelling – To build a 3D Datamine model of the various oxide/hard rock phases in Sadiola and Tambali opencast pits and cross-correlate these with the gold grade.

a) The Sadiola goldfield geology, including weathering and supergene profile and the structure, was mapped. The pits forming the subject of this study are the Sadiola Hill opencast, FN3 north and south and Tambali north and south pits. The Reverse Circulation (RC) and Diamond Drill (DD) boreholes in the northwest of the Sadiola Hill opencast pit, and to the north of the Tambali northern pits were logged to establish the stratigraphic column. The calc-silicate sub-facies and Tertiary stratigraphy of the Sadiola goldfield were also mapped.

b) This work was correlated with borehole data across the opencast pits; validation included field studies.

c) Any sub-facies in the calc-silicate (marble) were established.

d) The distribution of gold grade from grade control drilling with respect to sub-facies variations and/or oxide phases was examined.

Theme 2 Extension into regional studies of gold grade distribution using ArcGIS:

a) This included regolith, termite and other regional map datasets in ArcGIS to build a comprehensive oxide database for the Sadiola goldfield.

b) Queries were undertaken to examine the relationship between gold grade, oxide phases; marble sub-facies, structures and lithologies.

c) A comprehensive rationale for gold grade distribution across the goldfield in the oxide zone was developed.

Theme 3 Oxide geochemistry:

a) XRD, XRF and minerals separation process of selected samples in the oxide zone were studied.
b) The character and nature of auriferous oxide were established using the software packages Excel 2013, Datamine CAE Studio 3 and Leapfrog Geo 3.1 for 3D modelling, CorelDraw v9, Arc Map® 10.2 for 2D mapping. Samples were collected as needed.

1.5. Acronyms and Abbreviations

SEMOS. S. A	Société d'Exploitation des Mines d'Or de Sadiola. Société Annonyme
WAC	West African Craton
KKI	Kédougou Kéniéba Inlier
SMSZ	Sénégal-Malian Shear zone
SFZ	Sadiola Fracture Zone
XRF	X- Ray Fluorescence
XRD	X-Ray Diffraction
CAE	Computer-Aided Engineering (Datamine)
FN3	Farabakouta North 3
Mt	Million ton
Moz	Million once
GPS	Global Positioning System
AOF	Afrique Occidentale Française
EDF	European Development Fund
SSP	Sadiola Sulphide Project.

1.6. Thesis Organisation

This thesis is organised as follow. The first sections present abstract, acknowledgements, list of Figures, list of Tables, and list of Appendices.

Chapter 1 introduces the research thesis by a preamble, then the study location and physiography, followed by exploration and mining history, the aims and program, the acronyms and abbreviation and the thesis organisation.

Chapter 2 gives a detailed review of the regional geology, including a summary of the regional geology of the West African Craton (WAC), and detailed regional geology of the Kédougou Kéniéba

Inlier (KKI) and geophysical datasets. The local geology of the Sadiola goldfield is also detailed in this chapter.

Chapter 3 describes the methodology that relates to the aims and objective of the research. These include mapping, sampling techniques, XRF and XRD analysis, and modelling using Datamine studio 3 CAE software and leapfrog Geo 3.1.

Chapter 4 presents the results of this MSc research: Section 4.1 presents the results of Sadiola mine scale and regional 2D mapping that include lithologies, alteration and structures. Mine-scale 2D mapping included FN3 south and north pits, Sadiola Hill opencast pit, and Tambali south and north pits as well as regolith data, Sadiola termite results. RC and Diamond drilling datasets were combined with the mapping datasets to establish a stratigraphic column and establish the relationship between gold grade and the marble sub-facies, oxide profile for every opencast working. Section 4.2 presents the Sadiola goldfield lithologies and oxide 3D modelling to establish the relationship between gold grade and different lithologies, oxide profiles. Section 4.3 presents the result of studies of the oxide geochemistry to establish the character of oxide in the goldfield.

Chapter 5 presents the discussion.

Chapter 6 presents the conclusions and Recommendation.

Chapter 2
Literature Review

2.1. Introduction

The WAC is composed of Réguibat Shield, Leo-Man Shield, Kayes Inlier and KKI on the western margin of the craton, and the Ansongo Inlier on the eastern margin of the craton. The WAC presents two major basement highs, the Réguibat Shield in the north of the craton and the Leo-Man Shield in the south. The geology of the craton is mainly composed of Archaean and Palaeoproterozoic rocks. The Neoproterozoic to Palaeozoic Taoudeni sedimentary basin separates the shields (Figure 1); they are surrounded by Pan African and Hercynian belts (Bassot, 1965; Pons et al., 1991, 1992, 1995; Ndiaye et al., 1997; Hirdes and Davis, 2002; Dioh et al., 2006; Diene et al., 2012).

The Palaeoproterozoic rocks of the WAC are generally composed of belts with tholeiitic and calc-alkaline lavas, and felsic volcaniclastics, wackes, argillites and chemical sediments (Hirdes and Davis, 2002). According to Hirdes and Davis (2002), these rocks can be grouped together as the Birimian Supergroup, excluding the conglomerates and sandstones of the Tarkwaian Group, which represent erosion products of the Birimian Supergroup.

2.2. Geology of the Kédougou-Kéniéba Inlier (KKI)

The KKI is situated on the western margin of the WAC and is crossed by the international border of Senegal and Mali. The Sadiola goldfield is situated in the eastern part of the KKI and straddles countries such as Senegal and Mali (Figure 5). In the Sadiola goldfield, two stratigraphic subdivisions have been identified including the Kofi Formation and the Saboussiré Formation by Klöckner Industrie (1989). They are generally assigned to the Birimian Supergroup but have not been dated. The Kofi Formation is made up of metasedimentary rocks, while the Saboussiré Formation is volcano-sedimentary and composed of interlayered mafic volcanic, fine-grained greywacke and clastic sediments.

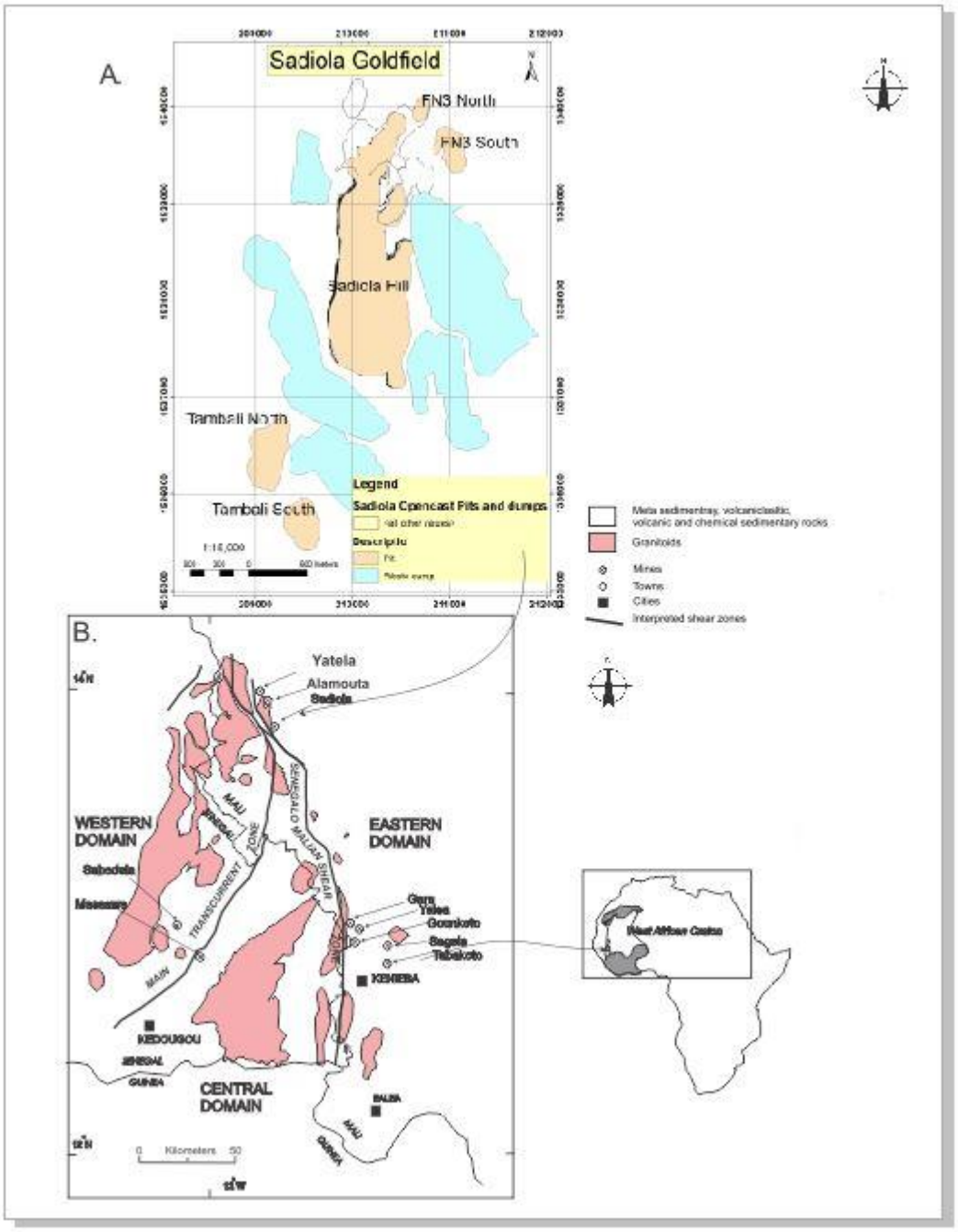

Figure 5: The inserted map shows the position of the WAC in Africa. A- Presentation of the study area in Sadiola goldfield. B- Location of the different goldfield in the Kédougou-Kénieba Inlier. In the KKI the SMSZ (Sénégalo-Malian Shear Zone) is located in the east and the MTZ (Main Transcurrent Zone) at the west (after Hein et al., 2012).

The KKI represents the western-most exposure of the Birimian in the WAC. It comprises two greenstone belts, known as the Mako Series and Falémé Series, and adjacent sedimentary basins referred to as the Dialé-Daléma Series and the Kofi Series (Hirdes and Davis, 2002).

According to Villeneuve (2008), the Hercynian Mauritanides form the western margin of the KKI. The KKI is overlain by all side by flat-lying Taoudeni basin (Masurel et al., 2014). According to

Debat et al. (1984), Bassot (1987), Ngom (1989), Pons et al. (1992), Dia (1993a, b) and Dia et al. (1993, 1997), the geology of the KKI can be divided into four (4) groups from west to east: the Mako volcanic belt, the Dialé-Daléma Series, the Falémé Belt and the Kofi Series (Figure 5B). There is no consensus as to the stratigraphic and/or paleogeographic relationship between these Series (Hirdes and Davis, 2002).

The KKI can be divided into three strato-structural domains based on the location of two regional-scale shear zones, respectively, the Main Transcurrent Zone and the Sénégalo-Malian Shear Zone. Bassot (1987) defined the Mako Series to the western domain as mainly composed of tholeiitic pillowed basalt and calc-alkaline andesite.

In the WAC, the major granitoids are divided into two groups: the "belt type", now interpreted as pre/syn-orogenic intrusive bodies (2190-2108 Ma) and the "basin-type", which is younger, with ages ranging from 2110-2080 Ma (Hirdes et al., 1992; Davis et al., 1994; Hirdes and Davis, 2002). Gueye et al. (2007) classified KKI granitoids into four generations GI-GIV. The first generation (GI) represents the oldest rocks in KKI and includes the Badon granite (2198 ± 2 Ma) and tonalitic gneisses from Tonkouto (2200-2198 Ma). The G1 generation could be correlated with an early Birimian magmatic event. The second manifestation of magmatism (GII) includes intrusion of mafic diorite, the gabbroic Sandikounda Layered Igneous Complex (SLIC), and development of the Laminia Kaourou Pluton Complex (LKPC) (2160-2130 Ma). The third major peak of magmatic activity (GIII) includes the development of the oval-shaped Diombalou and Bouroumbourou plutons. Finally, magmatism was terminated in the Mako Belt following the Eburnean Orogeny, with the emplacement of the Tinkoto and Mamakono plutons (GIV) in the east of the LKPC and continued in the Dialé-Daléma Supergroup with the syn-tectonic emplacement of the Saraya batholith. Lompo (2010) established three tholeiitic suites (PTH1, PTH2, PTH3) and two granite suites (PAG, PBG) based on the geochemical, geochronological and structural studies of Paleoproterozoic magmatic rocks in the Man-Leo Shield. The three principal events recognized by Lompo (2009) for the ca. 2.25–2.00 Ga tectonic period of evolution of the West African Craton are: Event I (ca. 2250–2200 Ma) as characterized by widespread tholeiitic volcanism in an oceanic basin setting (PTH1) to mantle plume activity, Event II (ca. 2200–2150 Ma) as characterized by a second (PTH2) and third (PTH3) generation of tholeiites in a calc-alkaline magmatic setting. The event was concomitant to widespread emplacement of amphibole-bearing (PAG) granitoids, and greenstone belt deformation. The event was facilitated by the formation of a subsiding mega-synclinorium and vertical tectonics and finally Event III (ca. 2150–2000 Ma) as characterized by the emplacement of dominant biotite ± muscovite-bearing (without amphibole) granitoids (PBG) during transcurrent tectonics illustrated in Lompo (2009).

Hirdes et al. (2002) and Dioh et al. (2006) defined the metavolcanic rocks as intercalated with immature metamorphosed sedimentary and volcaniclastic rocks. Pawlig et al. (2006) described the Dialé-Daléma Series as meta-sedimentary sequences intercalated with calc-alkaline volcanic between

the Main Transcurrent Zone (MTZ) and SMSZ in the KKI. The Dialé-Daléma Series is composed of sedimentary and volcano-sedimentary rocks (quartzite, carbonate, sandstone, conglomerate, epiclastic tuff) that were isoclinally folded and attained a schistosity during a deformation accompanying a phase of regional greenschist metamorphism **(**Hirdes and Davis, 2002). According to Ledru et al. (1991), the clastic rocks of the Dialé-Daléma Series were deposited in an intra-cratonic basin. The Dialé-Daléma Series lies beneath and are older than, the Mako Series; the former has been affected by two tectonic phases and the latter by only one phase (Ledru et al. 1991).

The Mako volcanic belt is located in the western domain of the MTZ and consists largely of basaltic, frequently carbonate-altered flow rocks intercalated with minor volcaniclastics. They are intruded by ultramafic (pyroxenitic) subvolcanic sills and numerous relatively small, massive biotite and amphibole-bearing TTG granitoids that resemble syn-volcanic, co-magmatic belt-type granitoids of Ghana and eastern Cote d'Ivoire (Hirdes and Davis 2002). The boundary of the Mako belt with the adjacent Dialé-Daléma sedimentary basin is partly transitional. Therefore, the Mako and Falémé belts volcanic, volcaniclastics and sediments of the Dialé-Daléma basin, are understood as lateral facies equivalents of almost similar relative age.

Hirdes and Davis (2002) and Schwartz et al. (2004) define the meta-sedimentary sequences of the Dialé-Daléma series as being composed of intercalations of carbonate, volcaniclastic and turbiditic units. Quartz-rich wacke from the series has been dated at 2164.7 ± 0.9 Ma ($^{207}Pb/^{206}Pb$) on the detrital zircon by Hirdes and Davis (2002) constraining the maximum age of deposition.

In contrast, the Falémé Series in the central domain is recognized as a distinct entity from the Dialé-Daléma Series. Hirdes et al. (2002) concluded that andesite and felsic lava dominant the Baoulé-Mossi domain, but volcaniclastic units, chemical sediments (e.g., chert and manganiferous shale) and metagreywacke also occur throughout the Falémé volcanic belt. They interpreted these sequences as proximal volcanic rocks. The Falémé volcanic belt is associated with major skarn type iron deposits (Schwartz et al., 2004).

The Kofi Series occurs in the eastern domain of the KKI. The Kofi Series, as first defined by Klöckner Industries (1989), crops out east of the SMSZ and is displaced sinistrally (Hirdes et al., 2002). The Kofi Series is composed of Birimian metasedimentary rocks and volcaniclastic sequences. The Kofi Series at Loulo has been dated between 2093 ± 7 and 2125 ± 27 Ma (Boher et al., 1992 quoted in Lawrence et al., 2013).

The Sadiola goldfield is situated in the Kofi Series. The Kofi Series comprises sandstones; argillites and platform carbonates; and syn-tectonic, S-type, peraluminous biotite-bearing granites (with similar compositions to the Saraya batholith) (Lawrence et al., 2013). In the KKI, the Sadiola goldfield local geology is presented in Figure 6.

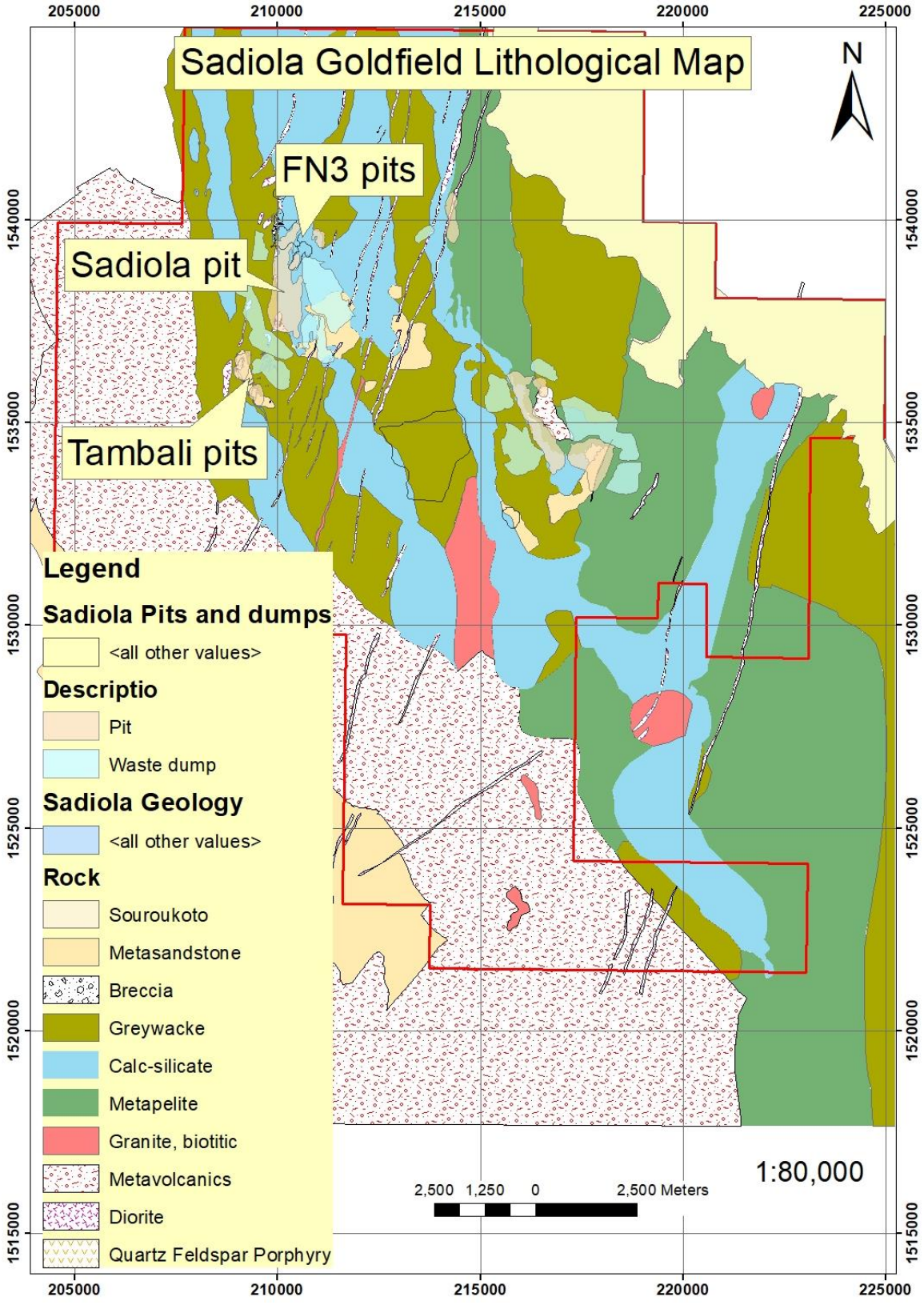

Figure 6: Sadiola goldfield local geological map, this map is established by a compilation of the field mapping and drilling data.

The KKI differs from other Palaeoproterozoic terranes in the WAC by having an abundance of carbonates, with thick sequences (>250 m) in both the Dialé-Daléma and Kofi Series, representing the most extensive carbonate exposure in the Birimian of the West Africa (Masurel et al., 2016). Sarr et al. (2012) identified four facies in sandstone, the red sandstone, white sandstone, purplish sandstone and sandstone intercalated pelites in the basin of Segou-Madina Kouta. Sarr et al. (2012) classified the Segou-Madina Kouta basin as a fragment of lower Proterozoic formations between Senegal and Guinea. The limit of this basin is on the north side by the volcanic formation of KKI, the Man ridge on the south side, on the west side by the Bassarides and the Rockellides and finally the Taoudeni basin on its eastern side. In Sadiola goldfield, the metasandstone was identified in Tambali pits, FE4 and in the southwest of Sadiola Hill opencast pit.

2.3. Magmatism

The KKI sedimentary rocks have been intruded by numerous granitoids. The granitoids of Dialé-Daléma are calc-alkaline affinity. They have been intruded with andesitic lavas that have geochemical similarities of arc magmas (Ndiaye, 1994).

The Dialé-Daléma granitoids, dated at 2008 Ma, appears to have been emplaced earlier than the Trondhjemite granitoids of the Kakadian batholith dated at 2190 Ma (Dia, 1988), and they are intrusive in the tholeiitic volcanic rocks of the Mako Supergroup.

The age of the Mako Supergroup has been dated to be 2063 ± 41 Ma (Sm-Nd on zircons; Abouchami et al., 1990) and that of the volcanic-plutonic complex has been dated at 2195 ± 118 Ma by Dia (1988).

Various intrusions were emplaced into the sedimentary rocks of the Kofi Series. According to Pons et al. (1992), biotite-muscovite and adamellite-granite make up almost 90% of the Saraya batholith (Figure 5B). Its central part, in the vicinity of the town of Saraya, contains a U-bearing episyenite. According to Hein et al. (2015), quartz-feldspar wacke was dated at 2146.6 ± 6.4 Ma, or 2106 ± 10, ($^{207}Pb/^{206}Pb$) at Yatela and intruded by diorite (dated at 2106 ± 10, $^{207}Pb/^{206}Pb$). The Alamoutala granodiorite north of the Sadiola Hill deposit has been dated at 2081 ± 6 Ma (U-Pb zircon age; Masurel et al., 2013). Masurel et al. (2013) defined many types age of diorite in the Sadiola-Yatela goldfield, namely, (1) 2116 ± 7.5 Ma for the Yatela diorite and possibly Sadiola diorite, (2) 2082 ± 8 Ma for the Alamoutala rhyodacite and (3) 2108 ± 10 Ma for the Sadiola rhyolite (Quartz Feldspar Porphyry).

According to Masurel et al. (2017), the metasedimentary rocks mapped in the Sadiola Hill opencast pit are intruded by two generations of diorite and one generation of quartz-feldspar porphyry. According to Theron (1997), in the Sadiola Hill opencast pit, the intrusions are trondhjemitic diorite-quartz dioritic to granodioritic in composition. He also reported the presence of lamprophyre dykes in the region, especially in the Dinnguilou prospect.

2.4. Metamorphism

In the KKI, the volcanic and the volcano-sedimentary rocks were subjected to greenschist-facies conditions during regional metamorphism (Taylor et al., 1992; Debat et al., 2003). In the Sadiola goldfield, metamorphic grade attained greenschist facies and hornblende-hornfels facies along contacts to tonalite-granodiorite plutons and tonalite dykes (Boshoff et al., 1998; Hein and Tshibubudze, 2007).

2.5. Structure and Tectonics

In Senegal and Mali, the geodynamic evolution of the Birimian Supergroup is characterized by several tectonic events (Ledru et al., 1991):

(1) An extensional E1 phase associated with sedimentary deposits and fissure-rupture tholeiitic volcanics;

(2) A tangential compressive deformation D1, with the tendency towards thrusting, affecting the lower Birimian successions;

(3) An extensional E2 phase associated with deposition of fluvio-deltaic deposits and calc-alkaline volcanic eruptions;

(4) A compressional D2 transcurrent tectonic phase, localized on the large north-south to southwest-northeast trending shear zones and associated with emplacement of granitoids (Dabo et al., 2010).

The two main shear zones identified in this domain are the Senegalo-Malian Shear Zone (Bassot and Dommanget, 1986) and the Main Transcurrent Zone. D1 compression in the eastern domain of the KKI is characterized by NNE to NE trending recumbent and overturned folds (F1), NW-verging thrusts, and axial planar schistosity (Milési et al., 1989; 1992; Ledru et al., 1991; Dabo et al., 2010). F1 folds are refolded by younger upright folds (F2) associated with D2 deformation. The north-south brittle-ductile SMSZ was initiated as a sinistral transpressional shear zone during the onset of D2 deformation.

According to Lawrence et al. (2013), east of the Falémé River, a third deformation (D3) is associated with transtensional displacement along D2 structures, and the development of sinistral north and north-west trending Riedel shears (third and fourth-order). Masurel et al. (2017) linked the formation of high-angle reverse shear zones and upright folds with vergence towards the west-northwest.

2.6. Mineralisation

The KKI hosts important goldfields such as the ~10 Moz Sadiola and ~2 Moz Yatela deposits, and the Loulo goldfield that includes Yalea, Gara, Gounkoto, Segala (operated and owned by Randgold Resources now known as Barrick Gold) and Tabakoto deposits (Figure 5B). The goldfields are located in different tectonic settings and show different gold mineralisation styles, including shear-hosted, disseminated sulphides, stratabound tourmaline-altered, auriferous veins-stock work, greisen style, turbidite hosted, and intrusion-related gold style (Voet, 1997; Hanssen et al., 1998; Hein and Tshibubudze, 2007; Cameron, 2010; Lawrence et al., 2013). They are close to crustal-scale shear zones, but generally occur along second-order or even lower order splay shears (Voet, 1996; Boshoff et al., 1998).

At the Sadiola Hill deposit, gold mineralisation is strongly bound to the upper part of a carbonate sequence and more particularly to the boundary between carbonate sequences and overlying greywackes. This boundary is generally interpreted as representing the SFZ. Masurel et al. (2017) linked ore minerals texturally with silicate mineral precipitation during a potassic alteration phase. Two stages of mineralisation were defined; the early As-rich sulphide (stage I), followed by an Au-Sb (stage II). Both ore stages overlap the potassic alteration event.

Robertson and Peter (2002) identified supergene or oxidised gold deposits in the WAC, e.g. at Yatela and Siguiri. This range of gold deposit types has expanded the opportunities for discovery in the WAC. Robertson and Peter (2002) identified several examples of orogenic mineralisation in the West Africa Craton including:

* Shear Zone-Hosted Vein deposits: Ashanti (Obuasi), Prestea, Poura, Belahouro
* Disseminated, Shear-Zone Hosted deposits: Bogosu, Konongo
* Breccia Disseminated: Syama, Sabodala
* Intrusive Disseminated: Ayenfuri
* Porphyry copper-gold: Diénémera; Gaoua
* Tourmaline: Loulo
* Intrusive Contact: Ity, Morila, Sadiola
* Stockwork: Bouda, Guida, Essakane, Djambaye II in the Tabakoto camp
* Extension Vein Stockwork: Kalana
* Skarn: Ity
* Paleoplacer deposits: Tarkwa (Robertson and Peter, 2002).

2.7. Sadiola 3D gold mineralisation model

A Sadiola goldfield mineralisation model has been completed by AGA evaluation team. The 3D model was used in this study to establish the relationship between gold mineralisation and the 3D oxide

phases and 3D lithological model in the Sadiola goldfield. The relationship is presented in Section 4.2. The 3D models were plotted together to show the relationship between them.

2.8. Alteration in the Sadiola goldfield

The Sadiola goldfield presents two types of alteration, namely hydrothermal and supergene. Both are visible in pits, in Reverse Circulation samples, and in the diamond core.

2.8.1. Hydrothermal alteration

Masurel et al. (2017) described a poly-phase hydrothermal alteration history at Sadiola Hill. In summary, biotite marks the fabric in host rocks within the SFZ and along the NNE-trending shear zone. The potassic alteration halo in the country rocks occurs in form of pervasive biotite and extends beyond the extent of the current Sadiola Hill open pit. The type of mica in the alteration assemblages is, at least in part, lithological controlled. Tourmaline is structurally controlled and occurs as a euhedral, rod- and heart-shaped accessory mineral (up to 2%). The reactivation of ore-hosting structures and the formation of several chlorite-calcite-pyrite veins were related to the last stage of hydrothermal alteration. According to Masurel et al. (2017), these veins postdate the potassic alteration stage and, by inference, the main mineralisation phase.

Hydrothermal gold mineralisation is generally associated with silicification in the hanging-wall (siltstone-shale-greywacke), but also closely related to a potassic alteration in the footwall (calc-silicate) called Spotty Chert Alteration (SCA) (Cameron, 2010). Boshoff et al. (1998) and Masurel et al. (2014) related the presence of gold mineralisation to potassic clay alteration. Primary calc-silicate alteration consists of a Fe-poor mineral association, including tremolite-actinolite, scapolite and vesuvianite, minor diopside, a trace of wollastonite and garnet as well as pyrrhotite. Potassic alteration consists dominantly of biotite as well as K-feldspar and sericite. Scapolite and to a lesser extent feldspar may alter to sericite (Boshoff et al., 1998).

2.8.2. Supergene alteration

At Sadiola Hill, Anonymous (1994) directly linked gold grade in the oxidized main zone to the degree of kaolinisation. Weathering /alteration are most intense along the SFZ and at depth, but otherwise follows diorite and quartz-feldspar porphyry dykes.

Decarbonation and argillisation, described as a hypogene alteration in reports dealing with the early history of the Sadiola Hill orebody, are now recognised as supergene processes, and first identified by Sillitoe (1994) and Boshoff et al. (1998). According to Voet (1996), the effects of hypogene alteration extend to 220 m in depth.

In addition to the three (3) types of alteration described, there are also other types of alteration namely biotitisation, chloritisation, sericitisation, albitisation, hematitisation, limonitisation,

kaolinitisation, scapolitisation and tourmalinisation. Jordaan et al. (1994) identified exotic weathering minerals in the saprolite profile including;

1. Alunite ($K_2Al_6(SO_4)_4(OH)_{12}$), stable in a highly acid environment.
2. Zunyite ($Al_3Si_5O_{20}(OH, F)_{18}Cl$).
3. Melanterite ($FeSO_4.7H_2O$), derived from weathering pyrite.
4. Jarosite ($K_2Fe_6^{3+}(SO_4)_4(OH)_{12}$), formed in acid supergene conditions.
5. Stibiconite ($Sb_3O_6(OH)$), a yellow oxide derived from weathering stibnite.
6. Ilsemannite ($Mo_3O_8.nH_2O$), a blue weathering product of molybdenite.
7. Azurite ($Cu_3(CO_3)_2(OH)_2$), derived from weathering copper sulphide.

Fe alteration as oxide-jarosite-siderite is linked to the gold mineralisation. Sillitoe (1994) noticed that jarosite rather than hematite is the dominant component resulting from complete sulphide oxidation.

Chapter 3
Methodology

3.1. Introduction

To understand the Sadiola Hill oxide zone, its geochemical complexities and alteration signatures, many research studies were conducted such as lithological and oxide 2D mapping, lithological and oxide 3D modelling. The oxide profiles were sampled for gold analysis, XRF, and XRD analysis. The minerals found in the samples were separated into light and heavy constituencies.

3.2. Mapping

The Sadiola goldfields pits were mapped systematically from May 2015 to February 2017 according to the mining schedule, with reference to the geology, oxidation phases, alteration profiles, and structures. Mapping took place in the FN3 south and north opencast pits, Sadiola Hill opencast pit, Tambali south and north opencast pits. The mapping was achieved only in the accessible and safe areas of the pits. The geological and oxide profiles map were achieved for each opencast pit in 2D. 2D geological and oxide profile maps were done using ArcGIS 10.3

A GPS and camera were used to georeference and take photographs of each station point across the goldfield. In the field, the data was recorded in the field notebook and then in Excel for data validation and analysis.

The results of the field mapping are presented in Section 4.1 and tabulated in Appendix A.

Pit mapping was carried out with special emphasis on the relationship between saprolite, transitional oxide, hard rock, and their structural interplay. The different kinds of alteration facies were logged and sampled, assayed for gold, analysed using XRF and XRD. Mineral separation was done to examine the different minerals from the samples.

The software packages used include Excel 2013, Datamine CAE Studio 3, Leapfrog Geo 3.1, for the 3D model, CorelDraw v9, Arc Map® 10.2 for 2D map.

3.3. Modelling

In the Sadiola goldfield, the geology and the oxide phases were modelled in 3D. The 3D geological model was achieved using Leapfrog Geo 3.1 3D software, while the oxide profiles were modelled in 3D using CAE Studio 3 3D (Datamine). The modelling were done using field mapping and drill core logged data sets. The results of the modelling are presented in Section 4.2.

In order for the 3D model to be completed, the various lithologies identified were wireframed using the Datamine software.

1. The objective of the 3D geological modelling was to investigate and establish a relationship between gold grade, lithology and lithological contacts.
2. The objectives of the oxide modelling were to investigate and establish a relationship between each oxide profile and the gold grade, to make a link with oxide phases and structure.

3.4. Sampling

The oxide phases were sampled successively in the Sadiola Hill, FN3 and Tambali opencast pits. The sampling process was conducted perpendicular to the bedding as a channel in the oxide profile. The samples were assayed for gold at Sadiola in the SEMOS laboratory.

A total of ninety-seven samples were collected. All those samples were assayed for gold mineralisation and analysed by XRF at the exploration office of Sadiola gold mine. Sixty-three samples out of the ninety-seven were selected from the three oxide profiles (Table 1). The SEMOS laboratory used fire assay as the method for gold analysis. Sample collection followed a procedure, in which the samples were split into 3 parts. To check the results of the laboratory the standard, duplicate and blank samples were inserted as quality control and quality assurance.

(1) The first part was split into two; one was sent to the SEMOS SA laboratory at Sadiola mine for gold analysis, and the second was used for XRF at the exploration office at the Sadiola Mine.

(2) The second part was crushed and sieved to obtain a fraction of < 500 μm at the University of the Witwatersrand, Johannesburg. The sieved portion was divided into three equal parts; the first powder was used for XRF analysis; the second powder was used for XRD analysis and the third sample powder was used for mineral separation.

(3) The third part sample was archived at the University of the Witwatersrand. All the samples were photographed.

According to the gold assay result, the best samples were selected and re-sampled for selecting the three identified oxide phases. Then, the sampling was also done on each identified profile, namely (1) decarbonated calc-silicate rocks unit, (2) Fe-oxide alteration zones and (3) potassic clay alteration. The second phase of sampling in the oxide profiles was used for systematical analysis of gold and subjected to XRF, and XRD for oxide geochemistry and alteration signature. Afterwards, the samples were submitted for mineral separation processing. The last process was conducted to identify and also for detrital zircon dating.

The results of XRF and XRD permitted the study of the oxide complexities and alteration signatures. The goal of sampling was to establish the relationship between gold mineralisation and oxide profiles and then establish the oxide geochemistry.

Three types of oxide alteration are observed in the field, namely the decarbonated calc-silicate rocks crosscut by Fe-oxide alteration zones, which are in turn crosscut by zones of potassic clay alteration (Figure 7 to 16).

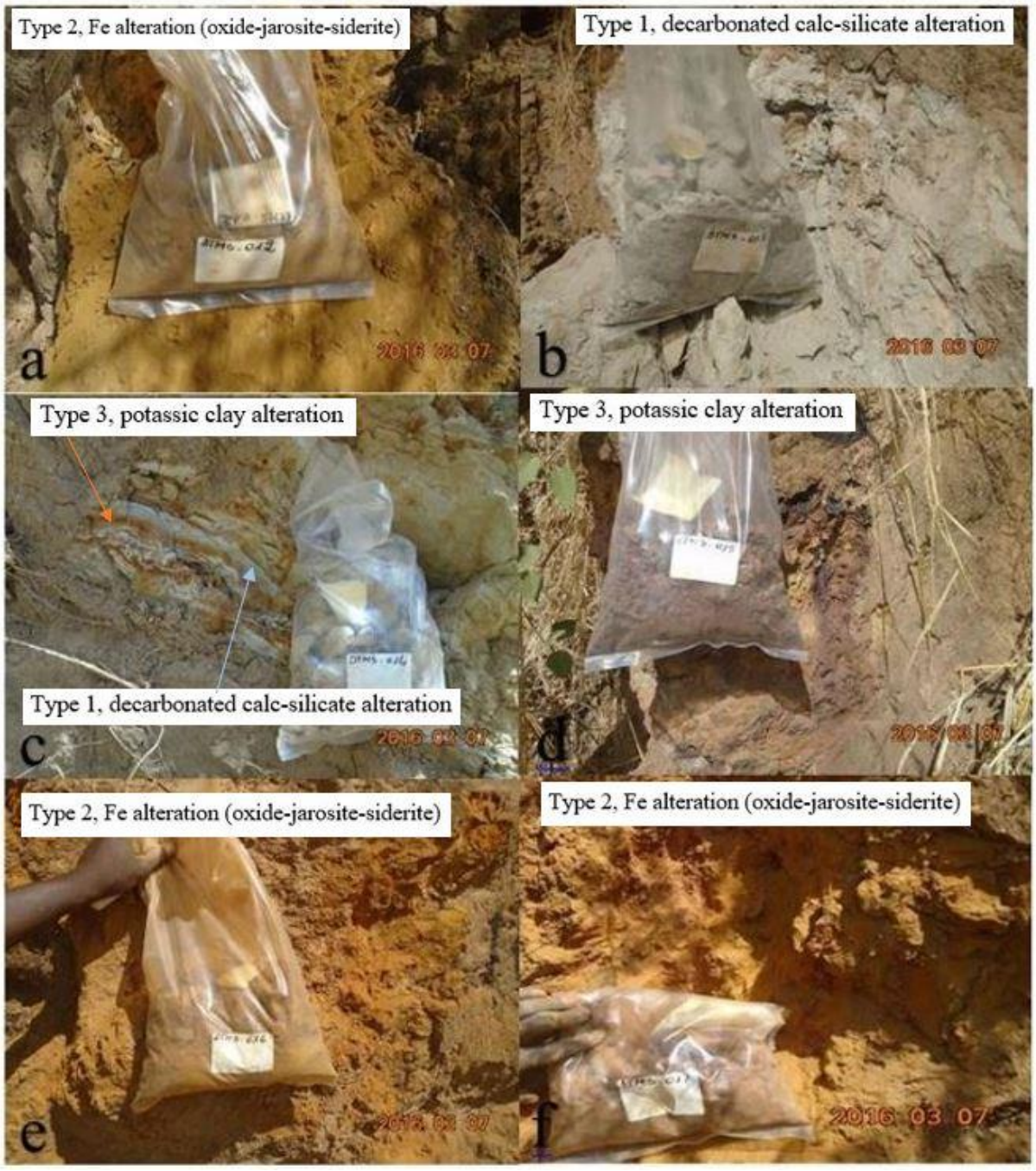

Figure 7: Photograph of the samples according to the alteration profile.

a. Photograph of the sample DTMS-012, showing very fine-grained sand with strong oxidized profile and Fe alteration red colour (quartz 35%, clay 55% sericite 10%).
b. Photograph of the sample DTMS-013 showing fine-grained decarbonated calc-silicate alteration (quartz 35%, clay 60%, sericite 5%).
c. Photograph of the sample DTMS-014 presents potassic and decarbonated alteration. The rock is bedded with slump folds (Hein and Tshibubudze, 2007).
d. Sample DTMS-015 comprises Fe alteration with red-brown colour (quartz 45%, clay 45% sericite 10%).

e. Sample DTMS-016 fine grain clayey sand (quartz 40% clay 50% sericite 10%. Fe alteration.
f. Sample DTMS-017 of quartz 30%, clay 55%, sericite 10%, and biotite 5%.



Figure 8: Photograph of the samples according to the alteration profile.

a. Sample DTMS-018 quartz 30% clay 55% sericite 5% biotite 5% Potassic alteration fine grain, clayey sand.
b. Sample DTMS-019 quartz 40% clay 55% sericite 5% Fe alteration fine grain, clayey sand.
c. Sample DTMS-021 quartz 35% clay 55% sericite 5% biotite 5% fine grain potassic alteration, name clayey sand.

d. Sample DTMS-022 quartz 45% clay 55% fine grain potassic alteration bedded, clayey sand
e. Sample DTMS-023 quartz 45% clay 55% fine grain Fe alteration, clayey sand
f. Sample DTMS-024 quartz 30% clay 65% sericite 5% fine grain decarbonated calc-silicate massive, clayey sand

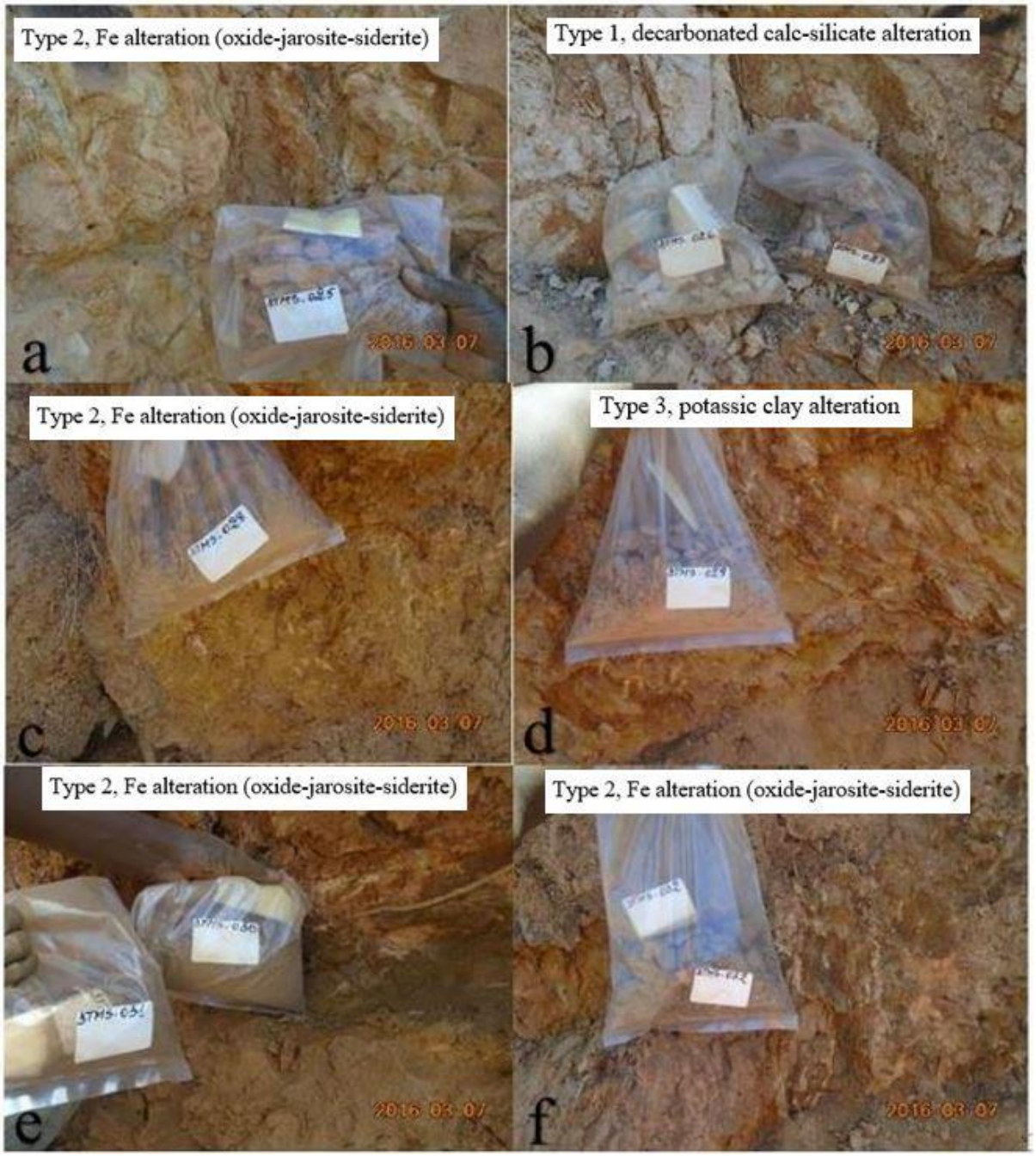

Figure 9: Photograph of the samples according to the alteration profile.

a. Sample DTMS-025 quartz 45% clay 50% sericite 5% fine grain, bedded to massive with weak Fe alteration, clayey sand.

b. Show the sample DTMS-026 with quartz 40% clay 55% sericite 5% fine grain with decarbonated calc-silicate alteration and the sample DTMS-027 quartz 45% clay 50% sericite 5% fine grain with Fe alteration, clayey sand.
c. Sample DTMS-028 quartz 40% clay 55% sericite 5% fine grain Fe alteration, clayey sand.
d. Sample DTMS-029 quartz 35% clay 55% sericite 5% biotite 5% fine grain strong potassic alteration, clayey sand.
e. Sample DTMS-030/031 duplicated sample as composition there are quartz 45% clay 55% fine grain with strong Fe alteration brown colour, clayey sand.
f. Sample DTMS-032 quartz 45% clay 55% fine grain, Fe alteration, clayey sand.



Figure 10: Photograph of the samples according to the alteration profile.

a. Sample DTMS-033 quartz 40% clay 55% biotite 5% fine grain strong Fe alteration, clayey sand.
b. This photograph shows the following three sample DTMS-034 mineral composition is quartz 45% clay 50% sericite 5% decarbonated calc-silicate alteration; DTMS-036 presents quartz 40% clay 50% biotite 10% fine grain potassic alteration; DTMS-037 quartz 45% clay 55% fine grain Fe alteration, clayey sand.

c. This photograph shows the following sample: sample DTMS-038 presents quartz 40% clay 50% biotite 10% fine grain with strong potassic alteration, clayey sand; DTMS-039 presents quartz 40% clay 50% biotite 10% fine grain decarbonated calc-silicate alteration; DTMS-041 quartz 45% clay 55% fine grain Fe alteration, clayey sand.



Figure 11: Photograph of the samples according to the alteration profile.

a. Photograph of the sample DTMS-046, showing fine-grained sand decarbonated calc-silicate alteration, sandy clay (quartz 50%, clay 35% sericite 5% biotite 10%).

b. Photograph of the sample DTMS-047 showing fine-grained, Fe alteration clayey sand (quartz 45%, clay 50%, and sericite 5%).
c. Photograph of the sample DTMS-048, fine grain, presents Fe alteration, clayey sand (quartz 40%, clay 50%, biotite 5% and sericite 5%).
d. Photograph of the sample DTMS-049 comprises Fe alteration, fine grain with red colour clayey sand (quartz 40%, clay 55% sericite 5%).
e. Photograph of the sample DTMS-050/051 duplicated sample, fine grain with Fe alteration clayey sand (quartz 45% clay 55%).
f. Photograph of the sample DTMS-052 contains quartz 30%, clay 70%, and fine grain with Fe alteration, clayey sand.



Figure 12: Photograph of the samples according to the alteration profile.

a. Sample DTMS-053 contains quartz 40% clay 45% sericite 10% biotite 5% Fe alteration fine grain, clayey sand.
b. Sample DTMS-054 comprises of quartz 40% clay 60% decarbonated calc-silicate, Fe alteration fine grain, and clayey sand.
c. Sample DTMS-055 comprises of quartz 45% clay 55% decarbonated calc-silicate alteration, clayey sand.
d. Sample DTMS-056 comprises of quartz 40% clay 55% biotite 5%, fine grain strong Fe alteration, and clayey sand

e. Sample DTMS-057 comprises of quartz 35% clay 65% fine grain K alteration, clayey sand
f. Sample DTMS-058 comprises of quartz 45% clay 55% fine grain Fe alteration, clayey sand



Figure 13: Photograph of the samples according to the alteration profile.

a. Sample DTMS-059 presents quartz 55% clay 45% fine grain, Fe alteration, clayey sand.
b. Sample DTMS-061 shows quartz 45% clay 55% fine grain with decarbonated calc-silicate alteration clayey sand.
c. Sample DTMS-062 quartz 30% clay 70% fine grain K alteration, clayey sand.
d. Sample DTMS-063 quartz 45% clay 55% fine grain Fe alteration, clayey sand.

e. Sample DTMS-064 as composition there are quartz 45% clay 55% fine grain with strong Fe alteration brown colour, clayey sand.
f. Sample DTMS-066 quartz 45% clay 55% fine grain, K alteration, clayey sand.



Figure 14: Photograph of the samples according to the alteration profile.

a. Photograph of the sample DTMS-067, showing fine-grained clayey sand with Fe alteration (quartz 40%, clay 60%).
b. Photograph of the sample DTMS-068 showing fine-grained, clayey sand, with a decarbonated calc-silicate alteration (quartz 30%, clay 70%).

c. Photograph of the sample DTMS-069, showing fine-grained, clayey sand with K alteration (quartz 35%, clay 65%).
d. Photograph of the sample DTMS-070/DTMS-071 showing fine-grained, decarbonated calc-silicate alteration (quartz 30%, clay 70%).
e. Photograph of the sample DTMS-072, showing fine-grained sand, Fe alteration (quartz 35%, clay 65%) clayey sand.
f. Photograph of the sample DTMS-073 showing fine-grained, clayey sand, K alteration (quartz 30%, clay 70%).

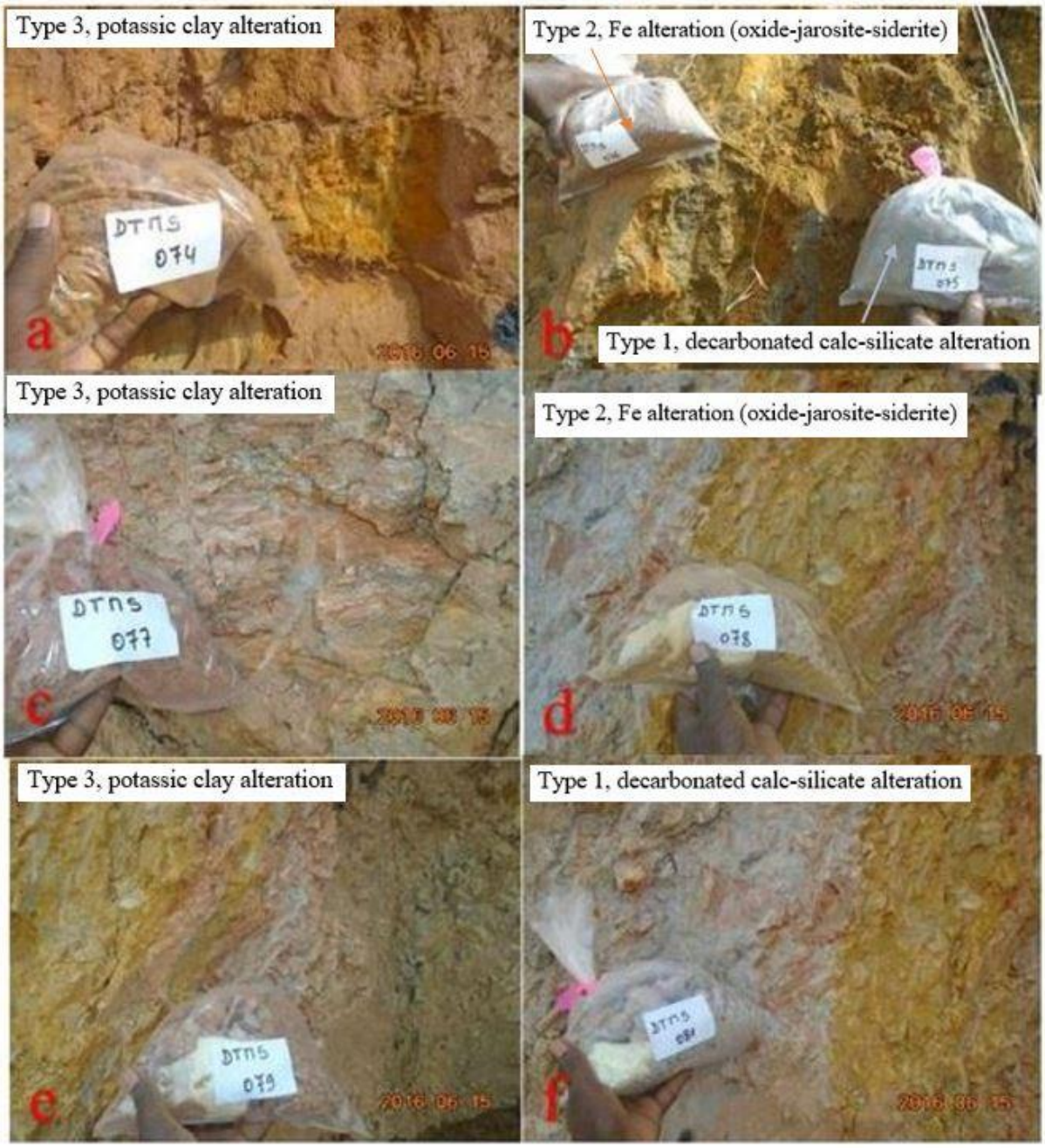

Figure 15: Photograph of the samples according to the alteration profile.

a. Photograph of the sample DTMS-074, showing fine-grained clayey sand K alteration (quartz 35%, clay 65%).
b. Photograph of the sample DTMS-075 showing fine-grained decarbonated calc-silicate alteration (quartz 40%, clay 60%). Photograph of the sample DTMS-076, showing fine-grained clayey sand with Fe alteration (quartz 35%, clay 65%).
c. Photograph of the sample DTMS-077 showing fine-grained, K alteration, clayey sand (quartz 30%, clay 70%).
d. Photograph of the sample DTMS-078, showing fine-grained clayey sand Fe alteration (quartz 35%, clay 65%).
e. Photograph of the sample DTMS-079 showing fine-grained, with K alteration (quartz 35%, clay 65%).
f. Photograph of the sample DTMS-081 showing fine-grained, with a decarbonated calc-silicate alteration (quartz 30%, clay 70%).



Figure 16: Photograph of the samples according to the alteration profile.

a. Photograph of the sample DTMS-082, showing fine-grained clayey sand Fe alteration (quartz 30%, clay 70%).
b. Photograph of the sample DTMS-083 showing fine-grained, Fe alteration (quartz 35%, clay 65%).
c. Photograph showing a massive calc-silicate rock with micro fault.
d. Photograph showing unconformity between oxidized profile and fresh calc-silicate rock.
e. Photograph showing bedded calc-silicate rock.
f. Photograph showing the folded calc-silicate.

Table 1: Sample description and related gold grades.

Sample ID	X Easting	Y Northing	Au g/t	Rock field description
DTMS-012	210074	1539445	0.46	quartz 25%, clay 45% sericite 10% very fine grain, Fe alteration
DTMS-013	210078	1539451	0.48	quartz 35%, clay 40% sericite 10% fine grain
DTMS-014	210079	1539452	0.49	quartz 35%, clay 45% sericite 5% fine grain strong potassic alteration
DTMS-015	210084	1539456	14.65	quartz 35%, clay 45% sericite 10% fine grain strong potassic/Fe alteration
DTMS-016	210110	1539466	1.02	quartz 30%, clay 50% sericite 10% fine grain strong Fe alteration
DTMS-017	210110	1539464	0.85	quartz 30%, clay 50% sericite 10% fine grain strong potassic alteration
DTMS-018	210125	1539471	2.15	quartz 35%, clay 50% sericite 5% fine grain strong potassic alteration
DTMS-019	210125	1539471	1.75	quartz 35%, clay 50% sericite 5% fine grain strong potassic alteration
DTMS-020				Standard
DTMS-021	210125	1539471	0.39	quartz 35%, clay 50% sericite 5% fine grain strong potassic alteration
DTMS-022	210148	1539470	0.11	quartz 35%, clay 55% fine grain strong potassic alteration bedded
DTMS-023	210148	1539470	0.17	quartz 35%, clay 50% fine grain strong Fe alteration
DTMS-024	210146	1539471	0.17	quartz 30%, clay 55% sericite 5% fine grain calc-silicate alteration, massive
DTMS-025	210207	1539447	0.67	quartz 45%, clay 50% biotite 5% fine grain bedded to massive strong Fe alteration
DTMS-026	210208	1539457	0.73	quartz 45%, clay 50% sericite 5% fine grain calc silicate alteration
DTMS-027	210208	1539457	0.87	quartz 45%, clay 50% sericite 5% fine grain Fe alteration
DTMS-028	210207	1539451	0.86	quartz 40%, clay 55% sericite 5% fine grain Fe alteration
DTMS-029	210207	1539449	3.09	quartz 40%, clay 55% fine grain strong potassic alteration
DTMS-030	210207	1539446	2.56	quartz 40%, clay 55% fine grain Fe alteration
DTMS-031	Field Duplicate		2.43	Field Duplicate
DTMS-032	210206	1539440	0.08	quartz 45%, clay 55% fine grain strong Fe alteration
DTMS-033	210186	1539431	0.69	quartz 40%, clay 50% fine grain strong potassic alteration
DTMS-034	210156	1539377	1.64	quartz 45%, clay 50% sericite 5% fine grain calc silicate alteration
DTMS-035				Coarse blank

DTMS-036	210156	1539377	1.03	quartz 40%, clay 50% fine grain strong potassic alteration
DTMS-037	210156	1539377	1.31	quartz 45%, clay 55% fine grain strong Fe alteration
DTMS-038	210152	1539403	0.89	quartz 40%, clay 50% fine grain strong potassic alteration
DTMS-039	210152	1539403	2.2	quartz 45%, clay 50% sericite 5% fine grain decarbonated calc silicate alteration
DTMS-040				Standard
DTMS-041	210152	1539403	0.58	quartz 45%, clay 55% fine grain strong Fe alteration
DTMS-045				Pulp Blank
DTMS-046	210711	1539267	0.12	quartz 45%, clay 35% sericite 5% biotite 5% fine grain decarbonated calc silicate
DTMS-047	210711	1539267	0.23	quartz 45%, clay 45% sericite 5% fine grain Fe alteration
DTMS-048	210711	1539267	1.03	quartz 40%, clay 55% sericite 5% biotite 5% fine grain Fe/K alteration
DTMS-049	210476	1539694	0.02	quartz 40%, clay 45% sericite 5% fine grain Fe alteration
DTMS-050	210482	1539681	0.61	quartz 45%, clay 55% fine grain Fe alteration
DTMS-051	210482	1539681	0.46	Field Duplicate
DTMS-052	210482	1539681	0.11	quartz 30%, clay 70% fine grain Fe alteration
DTMS-053	210482	1539681	0.26	quartz 40%, clay 45% sericite 10% Biotite 5% fine grain Fe alteration
DTMS-054	210497	1539686	0.08	quartz 40%, clay 60% fine grain decarbonated calc silicate/K/Fe alteration
DTMS-055	210497	1539686	0.02	quartz 45%, clay 55% fine grain decarbonated calc silicate alteration
DTMS-056	210497	1539686	0.36	quartz 40%, clay 55% Biotite 5% fine grain Fe alteration
DTMS-057	210527	1539717	0.02	quartz 30%, clay 65% fine grain K alteration
DTMS-058	210550	1539742	0.09	quartz 45%, clay 55% fine grain Fe alteration
DTMS-059	210550	1539742	0.11	quartz 55%, clay 45% fine grain Fe alteration
DTMS-060				Standard
DTMS-061	210550	1539742	0.15	quartz 45%, clay 50% fine grain decarbonated calc silicate alteration
DTMS-062	210607	1539807	0.82	quartz 30%, clay 70% fine grain K alteration
DTMS-063	210613	1539812	0.04	quartz 45%, clay 55% fine grain Fe alteration
DTMS-064	210630	1539823	0.02	quartz 45%, clay 55% fine grain Fe alteration
DTMS-065				Coarse blank
DTMS-066	210603	1539799	0.15	quartz 45%, clay 55% fine grain K alteration
DTMS-067	210545	1539778	0.02	quartz 40%, clay 60% fine grain K/Fe alteration

DTMS-068	210545	1539778	0.02	quartz 30%, clay 70% fine grain decarbonated calc silicate alteration
DTMS-069	210532	1539861	0.01	quartz 35%, clay 65% fine grain K alteration
DTMS-070	210450	1539687	0.01	quartz 30%, clay 70% fine grain decarbonated calc silicate alteration
DTMS-071	210450	1539687	0.01	Field Duplicate
DTMS-072	210450	1539687	0.02	quartz 35%, clay 65% fine grain Fe alteration
DTMS-073	210447	1539699	0.02	quartz 30%, clay 70% fine grain K alteration
DTMS-074	210458	1538509	0.4	quartz 35%, clay 65% fine grain K alteration
DTMS-075	210523	1538567	0.02	quartz 40%, clay 60% fine grain K/decarbonated calc silicate alteration
DTMS-076	210523	1538567	0.03	quartz 35%, clay 65% fine grain K/Fe alteration
DTMS-077	210542	1538417	1.05	quartz 30%, clay 70% fine grain K alteration
DTMS-078	210519	1538447	0.08	quartz 35%, clay 65% fine grain K/Fe alteration
DTMS-079	210519	1538447	0.04	quartz 35%, clay 65% fine grain K alteration
DTMS-080				Standard
DTMS-081	210519	1538447	0.09	quartz 30%, clay 70% fine grain decarbonated calc silicate alteration
DTMS-082	210359	1538366	1.62	quartz 30%, clay 70% fine grain K alteration
DTMS-083	210426	1538089	0.06	quartz 35%, clay 65% fine grain Fe alteration
DTMS-084	210169	1539774	Not Assayed	quartz 30%, clay 70% fine grain decarbonated calc silicate alteration
DTMS-085	210169	1539774	Not Assayed	quartz 35%, clay 65% fine grain Fe alteration
DTMS-086	210169	1539774	Not Assayed	quartz 30%, clay 70% fine grain Fe alteration
DTMS-087	210169	1539774	Not Assayed	quartz 30%, clay 70% fine grain K alteration

Each profile was precisely sampled and analysed for gold, and for oxide geochemistry using XRF, XRD, and minerals separation.

The samples with the significant gold result were selected for the second part of the XRF analysis and then XRD and minerals separation processing. All these analyses were conducted in the University of the Witwatersrand, Johannesburg. The results of XRF, XRD and minerals separation analysis are presented in Section 4.3.

This sampling has allowed the establishment of the relationship between gold mineralisation and oxide profile and the geochemistry of the oxide profile.

3.5. XRF analysis

The XRF analysis was done in two stages. The first stage used a portable handheld XRF model X-500 at SEMOS Sadiola mine, using "soil" and "mining plus". The soil mode is used to analyse the termite mound samples, while the mining plus mode is used to analyse the RC, diamond samples. Soil mode detect the element such as K, Ca, Ti, Cr, Mn, Fe, Ni, while mining plus mode detect Mg, Al, Si, P, K, Ca, Ti, Cr, Mn, Fe, and Ni. The program analyses the major element and the detection limit can be 0 wt %.

The second stage of XRF analysis was done at the University of the Witwatersrand, Johannesburg using Axios Max from Panalytical. For this program, the major elements were analysed using the fused method with a Li-tetraborate flux, and data reduction was carried out using SuperQ. In the result, dl (detection limits) can be taken as 0 wt %. The two stages of XRF analysis were to establish quality assurance/quality control. At the University of the Witwatersrand, XRF analytic work was done by Mr Marlin Patchappa.

The pulps of the samples for gold assay were also analysed using XRF at the SEMOS exploration office. The powder was sieved to < 500μm. The SEMOS XRF machine used 4.5 g of pulp, while the University of the Witwatersrand XRF machine used 2 g of pulp. The results of analysis of the SEMOS XRF are presented as elements, while those of the University of the Witwatersrand XRF are presented as a compound element. Both results were presented and interpreted in this research. The procedure for XRF analysis at the University of the Witwatersrand is presented in Appendix A.

3.6. XRD analysis

The sieved powders of thirty (30) selected samples were used for XRD analysis at the University of the Witwatersrand, Johannesburg in the School of Chemistry. Ten (10 g) grams of powder were sent for XRD analysis. The analysis was done by using the Bruker D2 Phaser, using a cobalt emission source, Bragg-Brantano geometry. For this program, the setting was 50-120° step size

0.26 with a total time 15 min. The results were interpreted using Diffrac Plus Eva. The XRD analysis was completed by Professor Billing. The identified minerals are presented in Section 4.3.4.

The XRD (X-ray Diffraction) is a physical process which produces an X-ray on the atoms of a crystal, an interference effect called the diffraction pattern gives information on the structure of the crystal or the identity of a crystalline substance. It is used to study the structure, composition and physical properties of materials.

3.7. Minerals Separation

Minerals separation was conducted at the University of the Witwatersrand, Johannesburg Earth Laboratory to separate light from heavy minerals. The minerals identified petrographically were used for XRD interpretation. Different minerals were used to define the alteration signature. Minerals separated were obtained using the procedure outlined in Appendix B.

To separate the light to heavy mineral, the crushed and sieved to < 500µm powder of the mineral is washed in the glass beaker with water (remove of the clay material). The acetone liquid is added to eliminate the water on the first heavy mineral obtained from water cleaning. Then the sample is dried in the oven and put it in the separator machine and bromoform liquid is added. The density of the bromoform liquid is 2.83 g/cm3, it is very heavy. After mixing the melange the light minerals will float while the heavy will sink.

The mine-scale and the regional 2D mapping were used to interpret the geology and the oxide profile, and establish the relationship between gold mineralisation, the geology and the oxide profiles. The results are presented in Section 4.1.

3.8. Geophysical character of the Sadiola goldfield

The geophysical methods helped to identify the oxide and alteration signatures present in the goldfield are presented below. The geophysical data were done by SEMOS geophysical team, the shapefiles were loaded in ArcGIS for interpreting in this research.

3.8.1. Sadiola regional gravity data

In order to investigate the oxide profile in the goldfield, gravity data was used to identify the gravel cover, hidden fault displacements, karst features and deep weathering profile.

The weathering profile in Sadiola can be attributed to many factors. Thus, the low gravity response to surface water penetration or hydrothermal fluid reaction on the ground. Alteration associated with surface water penetration is clearly visible on the southern wall of the Sadiola Hill, this is well illustrated in chapter 4. The evidence of this on the gravity data is showing by the low gravity present in the south of the opencast pit. The low gravity signature has been noticed along the

SMSZ (Figure 17). The low gravity signature follows the structures as SMSZ or northeast trending faults.

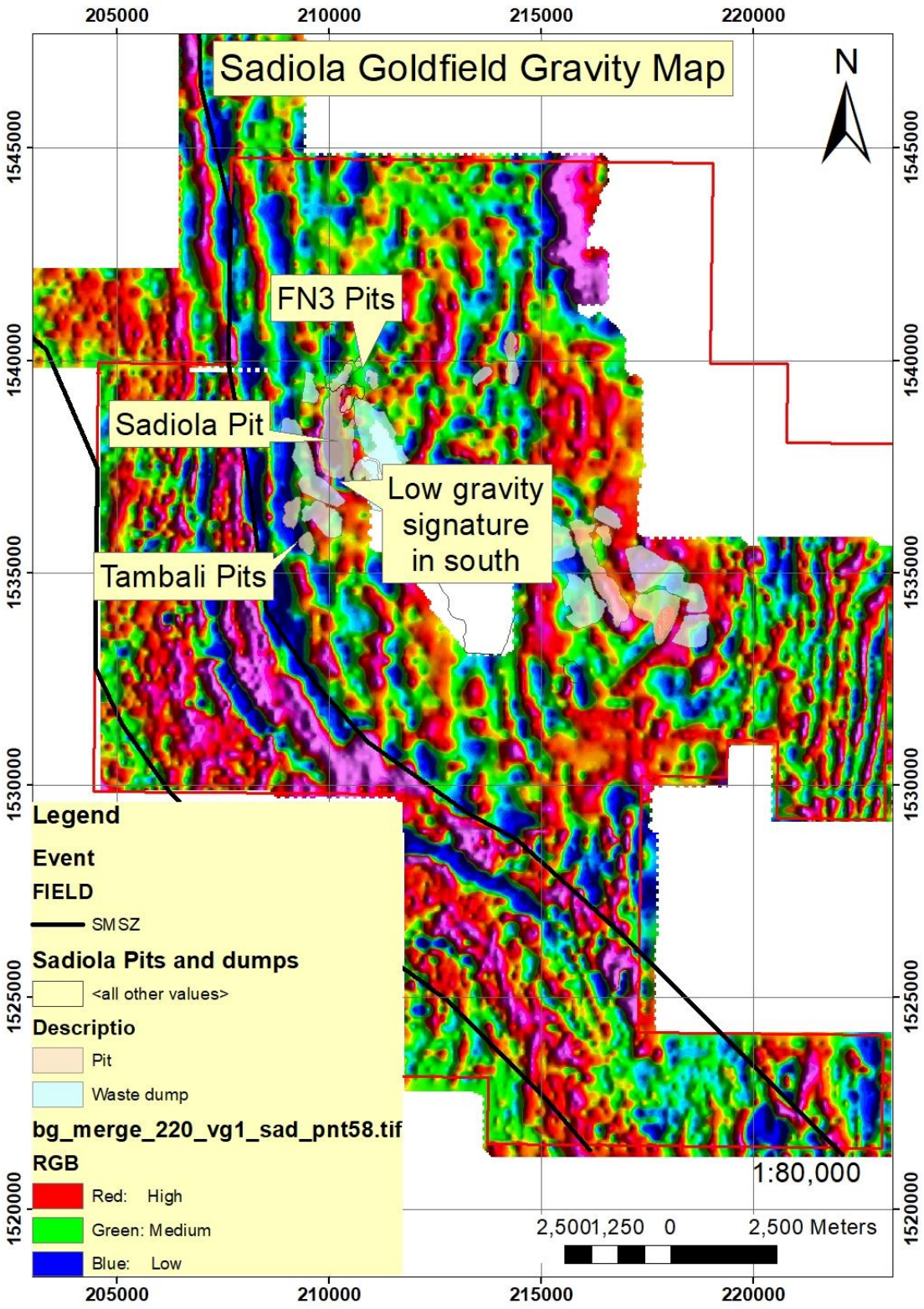

Figure 17: Sadiola goldfield regional gravity map. The blue colour represents low gravity, while the red the high gravity. Each open cast pit is located on area of low gravity, where oxides are

mined for gold. Sadiola goldfield gravity data has been plotted in the ArcGIS. The black line on the map represents the SMSZ.

3.8.2. Sadiola magnetic data

The magnetic data detects features such as igneous rocks and structures. It allows the identification and mapping of these features.

The total field magnetic image for the Sadiola goldfield is presented in Figure 18. The image shows the high magnetic response in red colour and the blue is the low magnetic response. The igneous rocks (diorite and dolerite) are visible on the image. The structures are oriented north-northeast, and the regional SMSZ is oriented north-west to north-south on the image. On the Sadiola total field magnetic image the dolerite dykes trend north-northeast and transect the SMSZ near Lakanfla prospect.

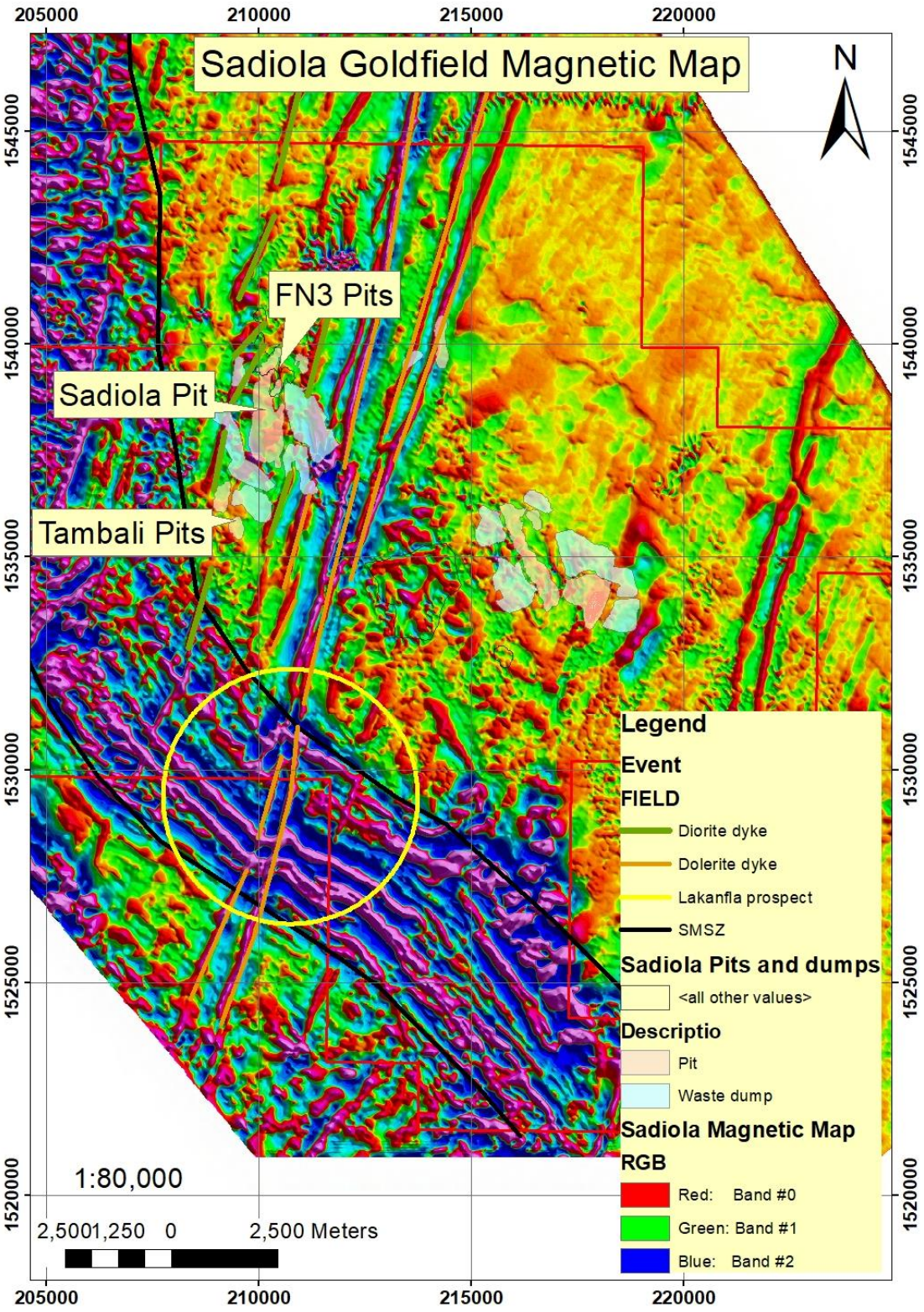

Figure 18: Regional Magnetic data and interpretation map on the Sadiola goldfield shows the shape and width of the SMSZ. The SMSZ is located on the western side of the map. This Sadiola total field is GradEnh_0p05_NEW_RTPLL_UC50_1VD.ecw.

Baratoux et al. (2016) dated the dolerite dyke in Burkina Faso as 1575 Ma, using U-Pb. The magnetic data allows us to identify the two important factors of gold mineralisation in the Sadiola goldfield, namely, the regional structures and the intrusions. The SFZ contact is a local structure and not visible in the geophysical datasets.

3.8.3. Sadiola radiometric data

The radiometric method estimates concentrations of potassium, uranium and thorium by measuring the gamma-rays (Figure 19). It was used to understand the regional geology of Sadiola goldfield. Boshoff et al. (1998), Cameron (2010) and Masurel et al. (2015) established a relationship between gold mineralisation and potassium (K) alteration. Therefore, potassium can be used as a geological mapping tool. The changes in lithology, or soil type, are often accompanied by changes in the concentration of the radiometric elements. The red shows outcropping rocks, the ferricrete is shown by the blue colour. The radiometry data provides insights into the weathering profile, palaeochannels and the ferricrete. The radiometry data contributes to geological mapping. The radiometry surveys of directly detect mineral deposits.

On the map (Figure 19) the potassium is represented by the red colour, the green colour shows the thorium, while the uranium is represented by the blue colour. A high concentration of potassium can be observed on the map in Sadiola Hill opencast pit.

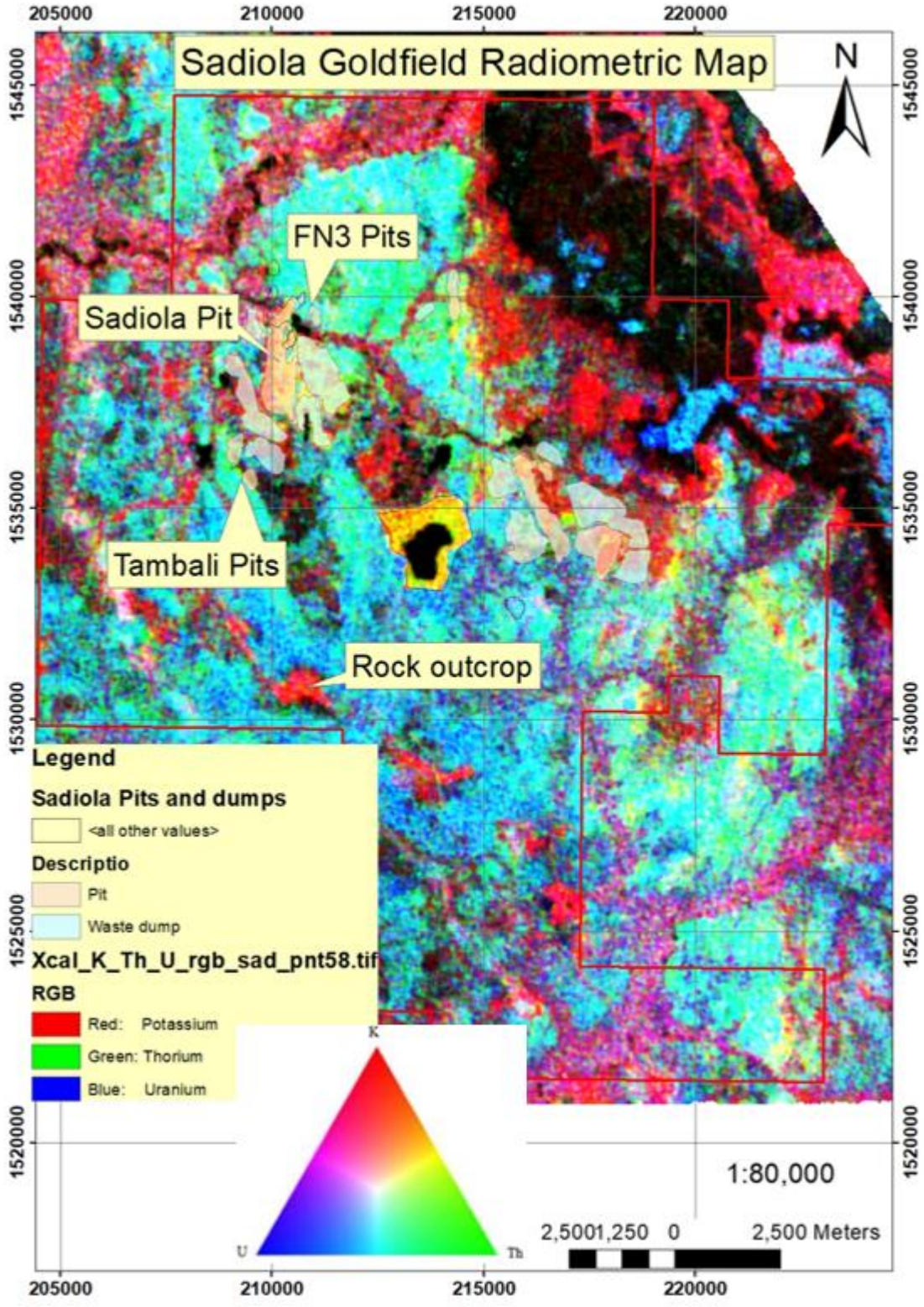

Figure 19: The regional radiometric data across the Sadiola goldfield. The blue light colour shows the ferricrete which cover most parts of the goldfield. The red colour represents some outcrop through the goldfield.

Chapter 4

Results

4.1. Sadiola mine scale and regional 2D mapping

4.1.1. Introduction

Mapping is a 2D graphical presentation of field and drill core observation and interpretation. For this purpose, the Sadiola mine scale and regional 2D mapping represent a summary of geological (lithological, oxidation, alteration and structural) observations within and also outside the exploitation pit. This chapter presents different interpreted maps created for each pit. The different types of maps produced are lithological 2D map and alteration or oxide profile 2D maps. The lithological mapping has been conducted in the three opencasts, which are Tambali, Sadiola Hill and FN3. The processes were to identify each lithology and the different lithological contacts. The description of each lithology has been conducted and presented in Table 1.

To do this lithological mapping, station point of lithological contact, structure, oxidation and alteration were recorded in a field notebook. Appendix C presents the station points descriptions and Appendix D is a copy of the field notebook. Forty-four (44) RC holes (Appendix E) and two (2) diamond holes were logged to confirm the stratigraphy of Sadiola Hill and Tambali deposits (Figure 20).

The datasets collected from pits and field mapping were imported into ArcGIS software to digitize every single lithology and oxide profile in 2D map, the examples of the lithological maps are in Figure 21, 22, and 23. The Sadiola goldfield includes Sadiola Hill opencast pit, Tambali pits south and north, and FN3 north and south opencast pits. In the oxide zone, ferricrete horizon, oxide saprolite, oxide transitional phase and hard rock phases were individually mapped. The relationship between gold mineralisation and geology, oxidation and lateritization were clarified. Gold mineralisation was correlated with each phase of alteration and oxide profile. Oxide profile mapping, 3D oxide modelling and mapping of the different types of alterations were completed for the Sadiola Hill, FN3 and Tambali opencasts pits. The objectives of those mapping study were to establish the relationship between (1) gold mineralisation distribution and the oxide phases; (2) gold mineralisation and calc-silicate sub-facies, and (3) structures and the lithologies. The stratigraphic column was established for each opencast pit across the Sadiola goldfield. The correlation between gold mineralisation and geology, oxidation and lateritization were established.

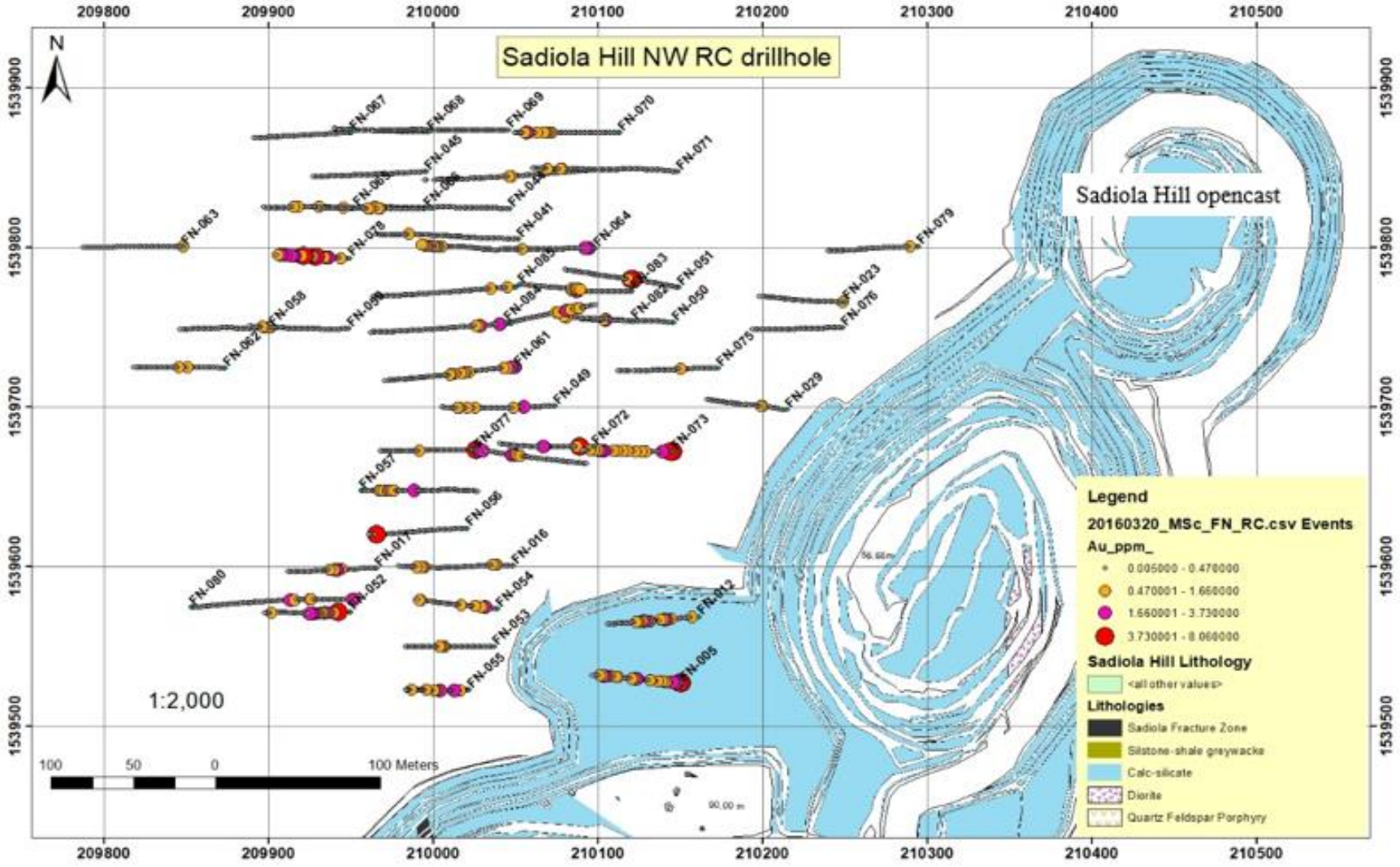

Figure 20: Position of the forty-four RC holes drilled in the Sadiola Hill NW, the holes were logged for stratigraphic definition purposes.

4.1.2. Lithologies

Lithological mapping conducted in the Sadiola goldfield allowed to establish a 2D lithological and oxide profile for Sadiola FN3 opencast, Sadiola Hill opencast and Tambali opencast pits. The FN3 opencast pits are mainly composed of weathered and unweathered calc-silicate rock and cut by quartz-feldspar porphyry. Both lithologies, calc-silicate and quartz-feldspar porphyry are covered by ferricrete. The gold mineralisation has been found in all these lithologies.

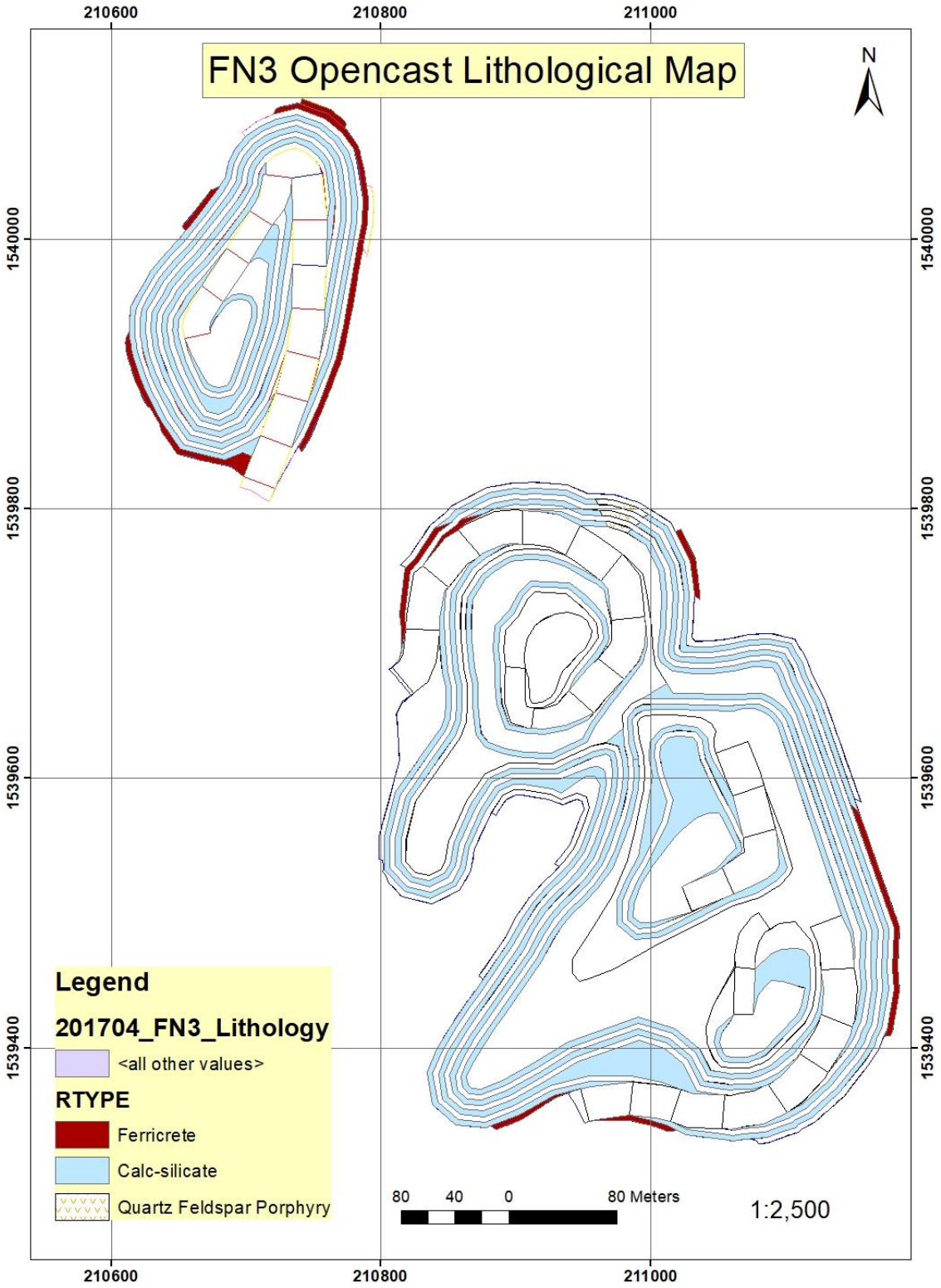

Figure 21: Lithological map of the FN3 south and north pits. The pits are dominated by altered and unaltered calc-silicate rock and crosscut by quartz-feldspar porphyry.

Lithological map of Sadiola Hill opencast is illustrated in Figure 22. Different lithologies were identified, which are mostly steeply dipping, and these are Palaeoproterozoic in age and form part of the Birimian Supergroup (Kofi Formation). However, three distinct ferricrete horizons separated by

mottled clay beds unconformably overlie the steeply dipping units. Siltstone-shale-greywacke sequence is localized on the western highwall of the Sadiola opencast pit, while calc-silicate rocks are localized on the eastern side of the pit. Diorite and quartz-feldspar porphyry crosscut all sedimentary rock units. The quartz-feldspar porphyry is crosscut by a diorite in the Tambali south pit giving a relative age for the formation of the intrusions. Diorite intrusions are present as dykes and sills. The diorite and calc-silicate are both brecciated in the northwest of FNBC pit north of the Sadiola Hill opencast pit.

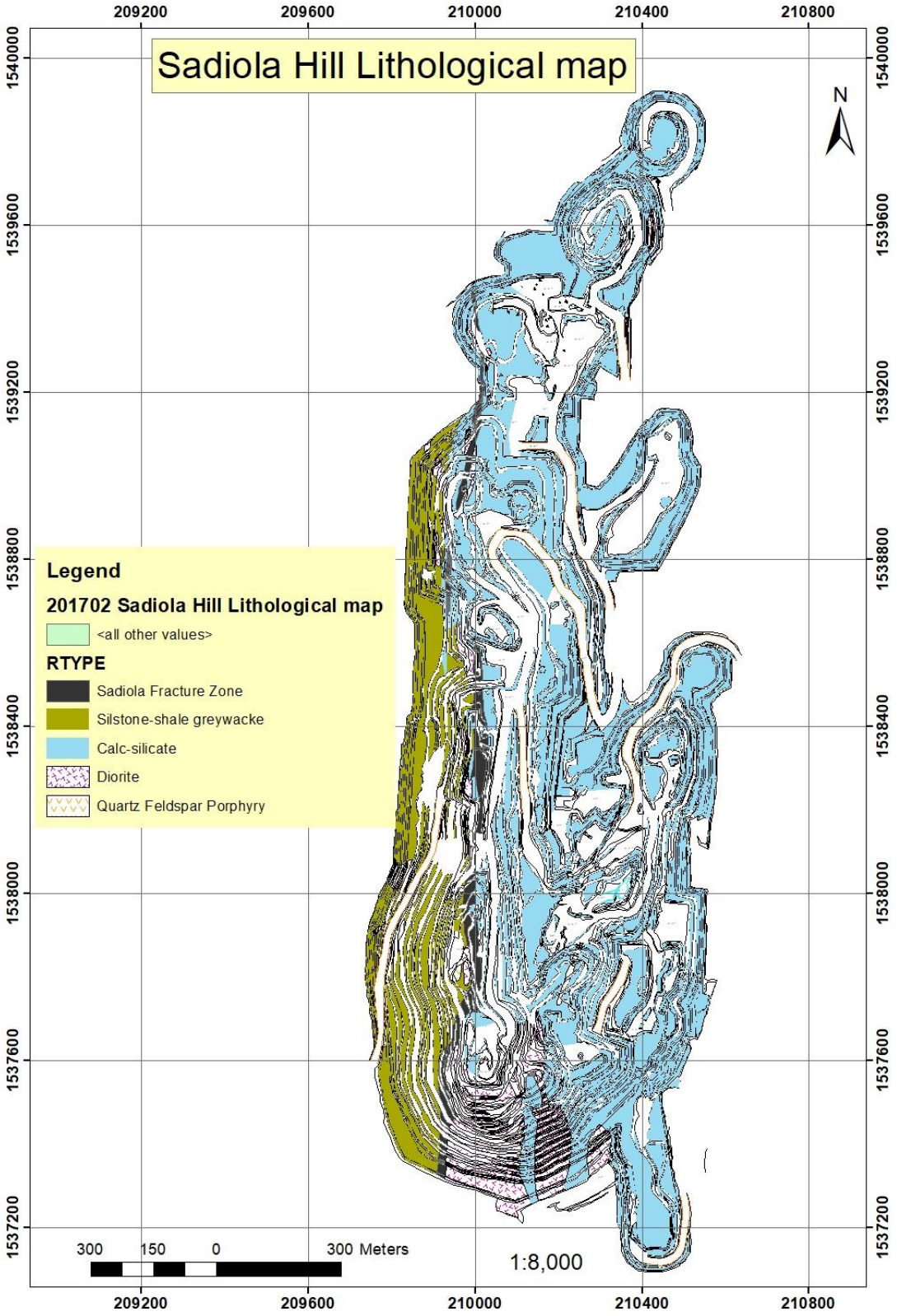

Figure 22: Sadiola Hill opencast pit geological map. The eastern part of the pit is the altered and unaltered calc-silicate, while the western part is the siltstone-shale greywacke. The contact is structurally defined by the SFZ. The sedimentary rocks are cross cut by a dyke and sill of diorite and quartz-feldspar porphyry dyke.

At Sadiola Hill opencast pit, gold mineralisation is associated with every lithology but mostly hosted in both the altered and unaltered calc-silicate units.

In the Sadiola Hill opencast pit and FN3 pits, different sub-facies of calc-silicate were observed, including (1) very thick (more than 1cm) to thick-bedded (0.5-1 cm) calc-silicate (with alternate of white and black layers, (2) thin (3-5 mm) to very thin-bedded (1-3 mm), (3) massive marble, (4) slump-folded marble, (5) carbonaceous siltstone and (6) pure marble (Figure 16 c, d, and f). In addition to these marble sub-facies Hein (2008) identified (1) massive greywacke facies, (2) carbonate greywacke-siltstone facies, (3) massive carbonate facies, (4) bedded carbonate and (5) slump to massive carbonate facies. The different intrusions present in the pit include diorite dykes and/or sills and quartz-feldspar porphyry.

The Tambali lithological map is presented in Figure 23. Tambali opencast pit lithologies include meta-sandstone, greywacke, quartz-feldspar porphyry, and diorite and these are unconformably overlain by ferricrete. In the Tambali opencast pit, diorite cuts quartz-feldspar porphyry, thus, the diorite is younger than the quartz-feldspar porphyry. The gold mineralisation is hosted in quartz-feldspar porphyry and meta-sandstones. White NE-trending quartz veins that crosscut the quartz-feldspar porphyry are mineralised.

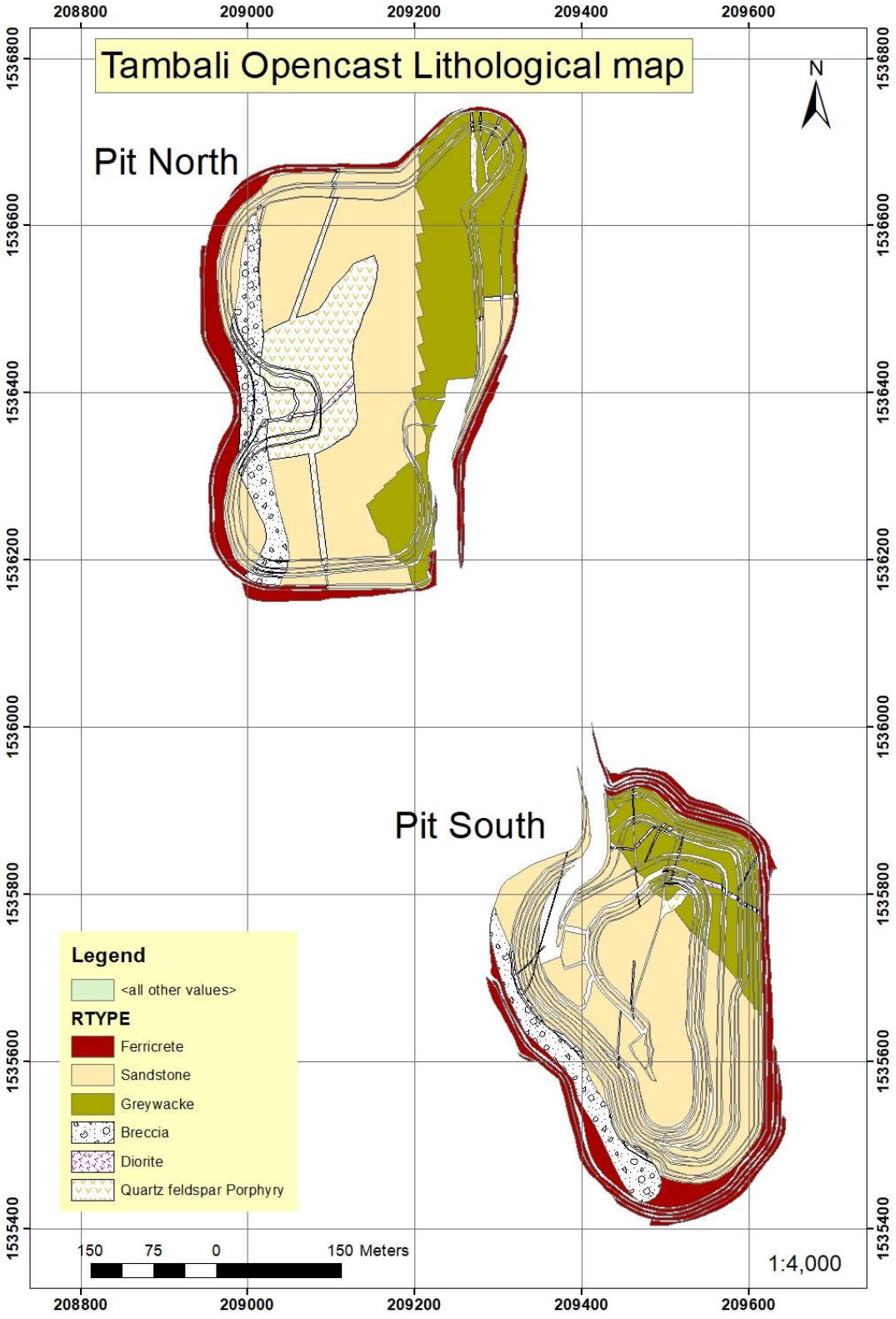

Figure 23: Lithological map of the Tambali opencast pits. The pits are composed mainly of sandstone and greywacke. The dyke of diorite and quartz-feldspar porphyry across the sedimentary rock.

A ferruginous sandstone unit exposed in the southwest of the Sadiola Hill opencast pit is folded. The sandstone trends northeast and dips steeply southeast. It is crosscut by white quartz vein. These were sampled and assayed, and the results are presented in Table 2.

Regional mapping was conducted in the south of Tambali at Lakanfla prospects and south-west of the Sadiola Hill opencast pit. Sandstone was mapped in the southwest of Sadiola Hill opencast pit (Figure 24), and also in Tambali opencast pit; the sandstones at both locations have some similarity in colour and the grain size composition but is not mineralised (Table 2).

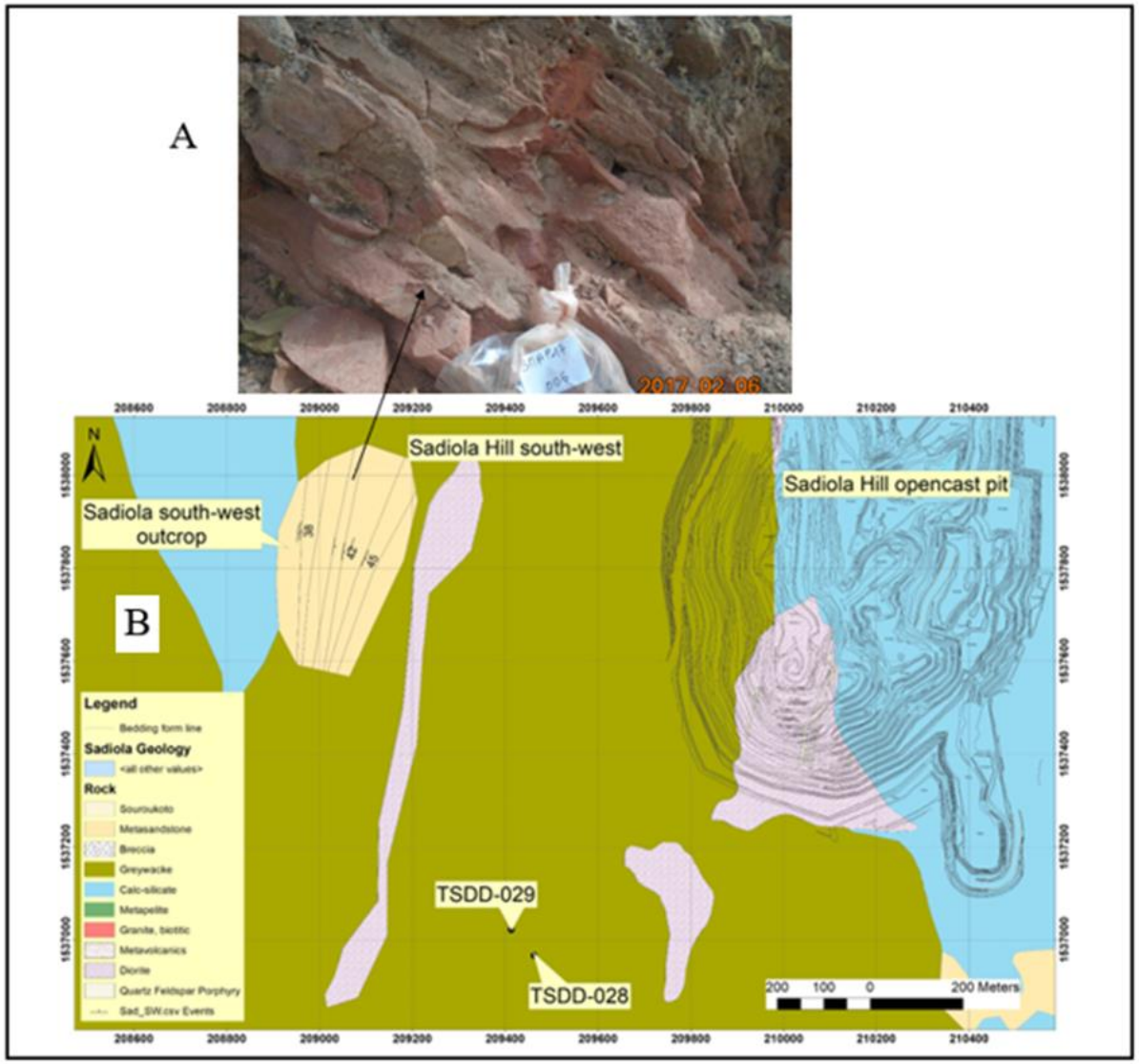

Figure 24: The red sandstone mapped at the southwest of the Sadiola Hill. (A) present the photograph of the sandstone and (B) the position of the map.

Table 2: Orientation, Assay and composition results data of samples from southwest of Sadiola Hill opencast pit.

Sample ID	XCOLLAR	YCOLLAR	ZCOLLAR	Rock type	STRUCTURE	DIP	DIP AZ	Au	COMMENT
SMAP17-001	208952	1537872	108	Meta-sandstone	Bedding	35	50	0.02	Clay 20%, quartz 80% reddish colour fine grain
SMAP17-002	208956	1537876	108	Meta-sandstone	Bedding	30	95	0.01	Clay 20%, quartz 80% reddish colour fine grain
SMAP17-003	208961	1537881	108	Meta-sandstone	Bedding	38	92	0.01	Clay 20%, quartz 80% reddish colour fine grain
SMAP17-004	209034	1537847	114	Meta-sandstone	Bedding	41	100	0.06	Clay 20%, quartz 80% reddish colour fine grain
SMAP17-005	209036	1537992	115	Meta-sandstone	Quartz Vein	60	160	0.02	White quartz vein in W-E trench 5cm width
SMAP17-006	209070	1537847	115	Meta-sandstone	Bedding	65	112	0.01	Clay 20%, quartz 80% reddish colour fine grain
SMAP17-007	209054	1537836	112	Meta-sandstone	Bedding	42	100	0.04	Clay 20%, quartz 80% reddish colour fine grain
SMAP17-008	209100	1537822	111	Meta-sandstone	Bedding	45	114	0.01	Clay 20%, quartz 80% reddish colour fine grain
SMAP17-009	209100	1537790	111	Meta-sandstone	Quartz Vein	55	160	0.01	White quartz vein 15cm width S0 50@120
SMAP17-010	209123	1537792	113	Meta-sandstone	Bedding	55	125	0.1	Clay 20%, quartz 80% reddish colour fine grain
SMAP17-011	209123	1537792	113	Meta-sandstone	Bedding	55	125	0.02	Clay 20%, quartz 80% reddish colour fine grain

Lithological mapping in the three opencast pits, FN3, Sadiola Hill opencast pit and Tambali pits identified lithologies as calc-silicate, siltstone-shale-greywacke, meta-sandstone, diorite and quartz-feldspar porphyry. Six (6) different sub-facies of calc-silicate or marble were recognised in the goldfield. The number of layers of ferricrete presents in the Sadiola Hill opencast pit has been established. Three (3) distinct ferricrete horizons were recognised overlying the calc-silicate (Figure 25a, b), while one thin horizon was observed to overlie the siltstone-shale-greywacke. The gold mineralisation was detected in every single lithology, but it is mainly hosted by altered and unaltered calc-silicate in the Sadiola Hill opencast pit. The gold mineralisation is also found in the ferricrete horizons in the Sadiola goldfield.

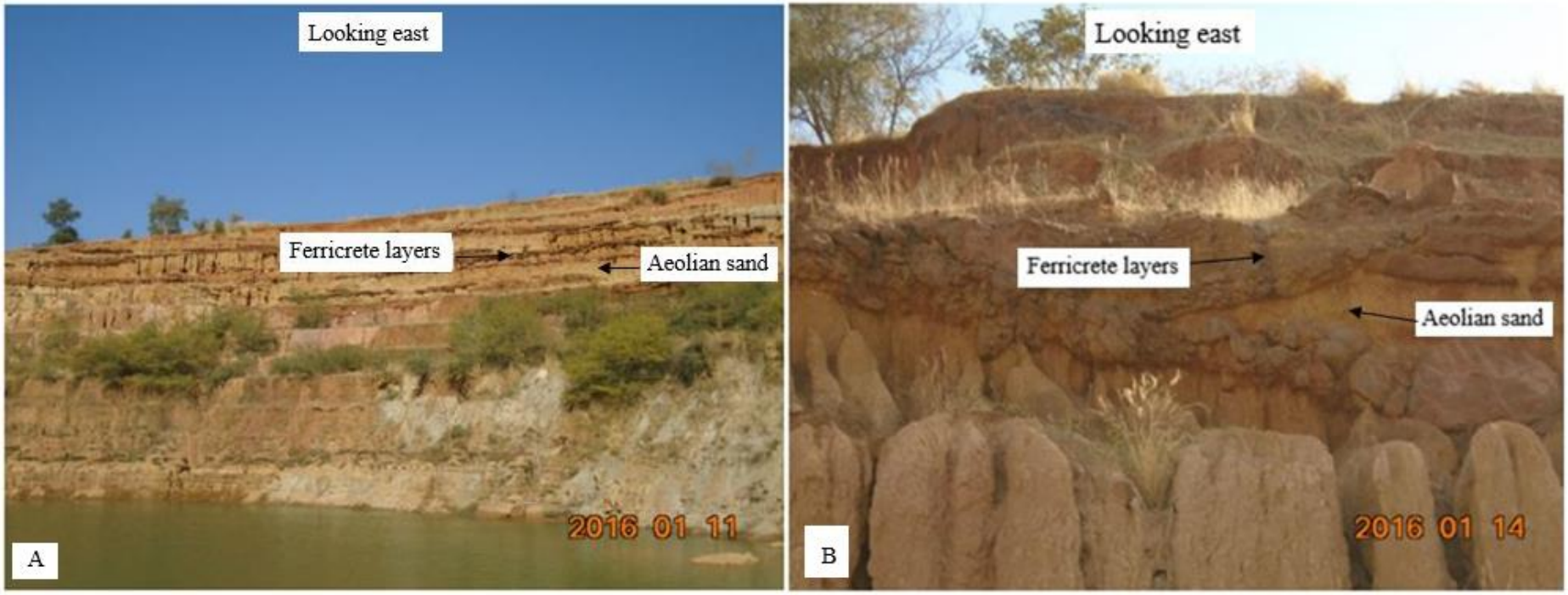

Figure 25(a): Photography of the three different layers of the ferricrete on the decarbonated calc-silicate, the aeolian sand separates them. Looking east of the Sadiola Hill opencast pit. (b) Photography of layers of ferricrete on the decarbonated calc-silicate, the aeolian sand separates them. Image taken looking east, north of the Sadiola Hill opencast pit.

4.1.3. Alteration Mapping

Alteration is the change in mineralogic composition through physical or chemical processes facilitated by hydrothermal and/ or supergene solutions. It results in two classes of alteration, namely hydrothermal and supergene (Sillitoe, 2005). Both classes of alteration were identified in the Sadiola goldfield. The hydrothermal and supergene alterations are visible along the SFZ in the Sadiola Hill opencast pit.

The supergene alteration occurred down to a depth of 220 m in the Sadiola Hill opencast pit. Supergene alteration types consist of hematitisation, kaolinitisation and limonitisation. Hematitisation is more visible in the ferricrete, while limonitisation, hematitisation and kaolinitisation are all visible in the oxide profile (saprolite and transitional). Hydrothermal alteration is associated with chloritisation, silicification, feldspathic, biotitisation, and sulfidation of calc-silicate rocks (Figure 26). The biotite alteration is spotty and follows the bedding in the calc-silicate rocks. The biotite is disseminated in the dark layer (Mg) in the calc-silicate.



Figure 26: The hydrothermal alteration presents in the SFZ from the middle of the Sadiola Hill opencast pit.

The objective of the oxide phase mapping was to identify and describe the different oxide phases and to make a link between each phase and gold mineralisation. Four domains were defined during the oxide phases mapping, namely (1) a ferricrete horizon, (2) oxide saprolite zone, (3) oxide transition zone, and (4) calc-silicate, siltstone-shale-greywacke (unweathered rock). Figure 27 is a

cross-sectional view of the Sadiola Hill opencast pit showing all four oxide domains mapped. In this supergene alteration, three-oxide development profiles are identified as decarbonated calc-silicate alteration; Fe alteration (oxide-jarosite-siderite); and the potassic clay alteration, and are related to gold mineralisation.

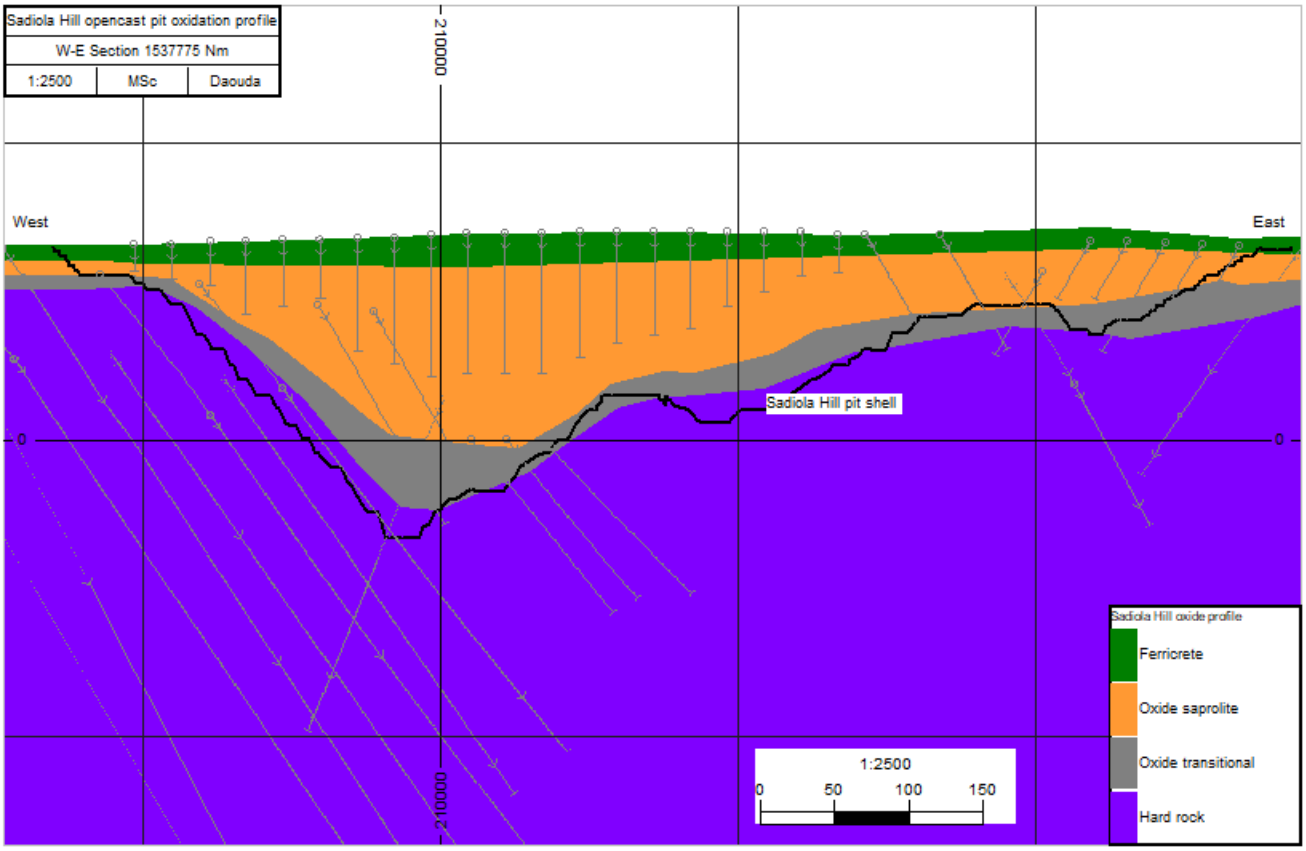

Figure 27: West-east vertical cross section along a 1537775 Nm latitude line showing the Sadiola Hill opencast oxide profile. All the four domains are well depicted from the hard rock to the ferricrete horizon.

The ferricrete horizon is interpreted as Tertiary in age (Grimaud, 2014) and overlies the oxide saprolite zone. In the oxide saprolite zone, the rock has lost its primary elements and is, by and large, replaced by secondary minerals, while in the oxide transitional zone it is possible to map primary sedimentary features and some minerals. The age of oxide saprolite and oxide transitional zones is unknown but assumed to be recent, when weathering occurred by deeply penetrating surface waters. The ferricrete represents materials which are not in-situ, but transported, as indicated by the presence of coarse pisolitic gravel and quartz (Figure 28).

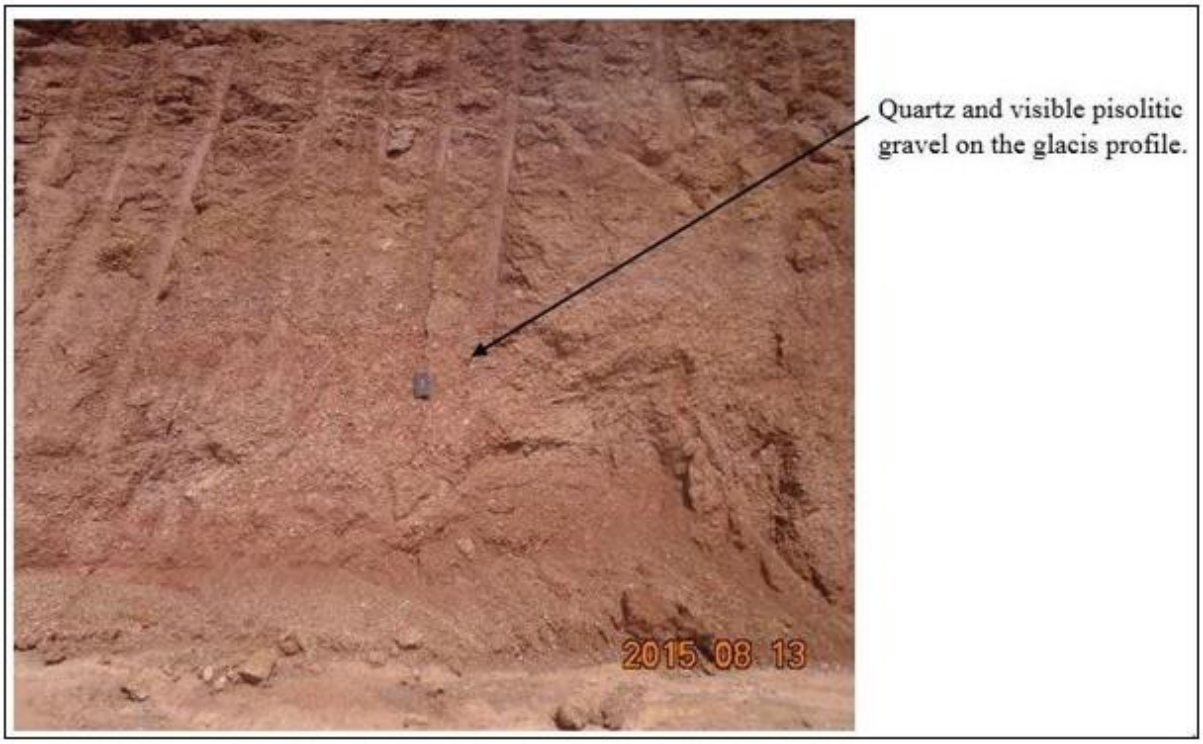

Figure 28: Photograph of ferricrete in the Sadiola Hill opencast showing the coarse pisolitic gravel and quartz which indicates weathering of transported materials.

The different oxide profiles mapped in the Tambali south and north opencast pits are shown in Figure 29, which range from ferricrete to hard rock.

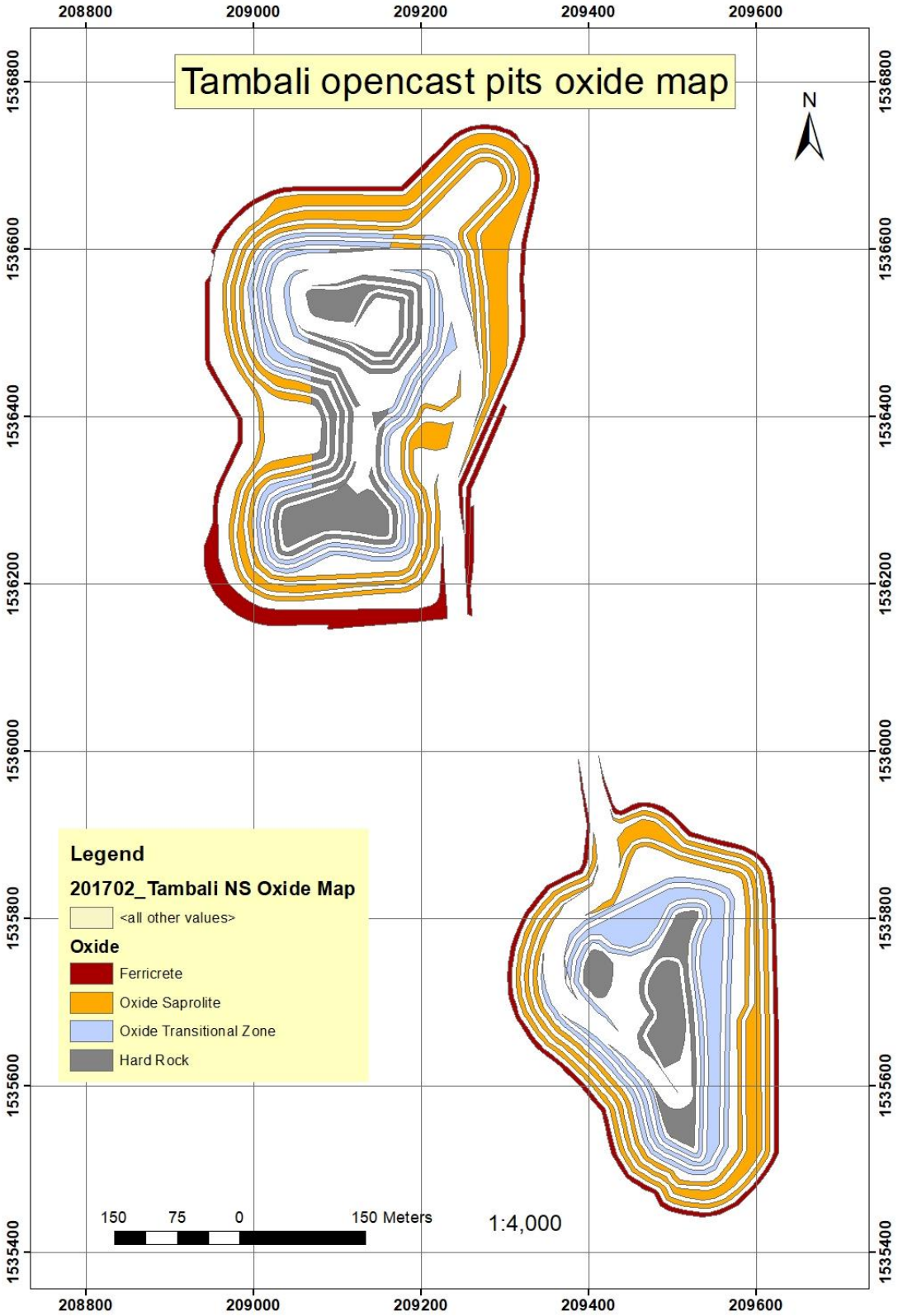

Figure 29: A plan view of oxide map for Tambali north and south pits, composed of ferricrete in red colour, the oxide saprolite, the oxide transitional zone is the light blue colour and the hard rock is represented by the grey colour.

Considering the oxide mapping results, gold mineralisation is found in the ferricrete horizon, oxide saprolite and the oxide transitional zones. In the Sadiola goldfield, the ore fed to the plant is only from the ferricrete, oxide saprolite and the oxide transitional zone ores. However, some gold in oxides and siltstone-shale-greywacke and quartz-feldspar porphyry remains in the pit as unmined due to safety or cost management issues.

The Sadiola Hill opencast pit oxide profiles mapping results are presented in Figure 30. In the Sadiola Hill opencast pit, gold mineralisation is found in the ferricrete horizon and also, hosted in the oxide saprolite and the oxide transitional zones. The gold mineralisation hosted in the hard rock should be mined in the second phase of the Sadiola Hill life, Sadiola Sulphide Project. In the Sadiola Hill opencast pit, exposures of hard rock consist of calc-silicate and siltstone-shale-greywacke.

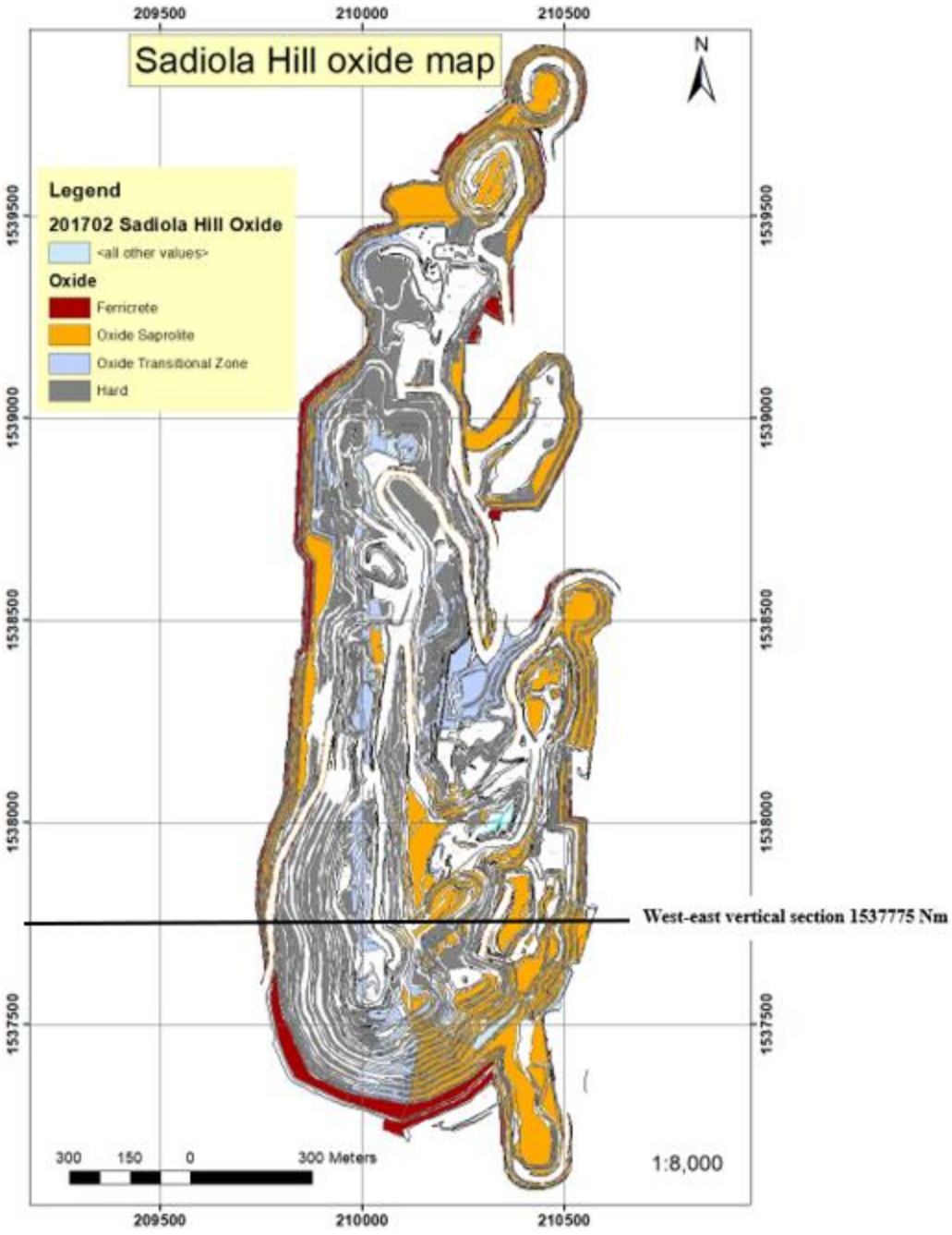

Figure 30: The oxide map of the Sadiola Hill opencast pit, composed of ferricrete in red colour, the oxide saprolite, the oxide transitional zone is the light blue colour and the hard rock in grey colour.

Based on field studies conducted in May 2015, three stages of development of the oxide profile in the Sadiola Hill opencast pit were identified. Decarbonated calc-silicate rocks are crosscut by Fe-oxide alteration zones, which are in turn crosscut by zones of potassic clay alteration. In the pit mapping process, the Fe oxide alteration has been a pathfinder for a Fe oxide-jarosite-siderite assemblage, while the decarbonation may be associated with the formation of bauxitic clay. The three stages of oxide were sampled systematically for gold, XRF, XRD analysis, and mineral separation for oxide geochemistry characterisation.

The different oxide profiles mapped in the FN3 opencast pits are shown in Figure 31. In the FN3 opencast pit, gold mineralisation is found in the ferricrete, the oxide saprolite, the oxide transitional zone, the calc-silicate, and unweathered siltstone-shale-greywacke. The thickness of the ferricrete horizon measures between 0 to 10 m; the oxide saprolite is around 10 to 20 m thick; and the oxide transitional zone extends to the base of the opencast pits and is the most important in term of volume. Gold is mined in the oxide saprolite zone, which is approximately 20 m thick, below which the oxide transitional zone is around 30 m thick. Exposures of siltstone-shale-greywacke occur at the bottom of the pits. Exposures of calc-silicates are present only at the bottom of the FN3 south pit. In the FN3 opencast pits, there are more ferricrete exposed in the northern pit than the southern pit due to the presence of the significant weathering profile in the north than south of FN3 opencast pits.

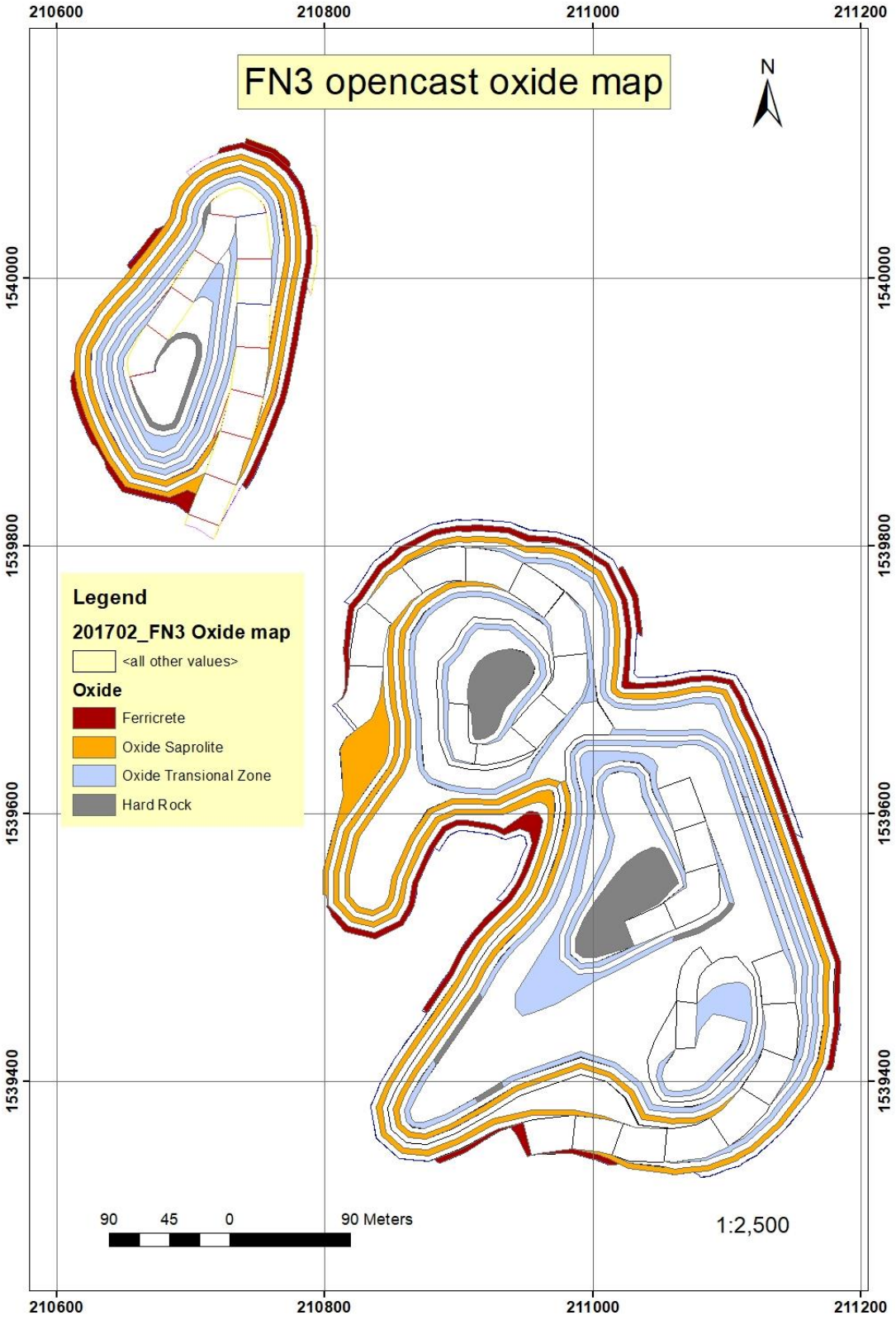

Figure 31: The oxide map for FN3 north and south pits, composed of ferricrete in red colour, the oxide saprolite, the oxide transitional zone is the light blue colour and the hard rock in grey colour.

Based on the oxide mapping completed in this study, there is more oxide by volume in the south than the north of the Sadiola goldfield (Tambali in the south, Sadiola Hill opencast pit in the middle, and FN3 pits to the north). The oxide profile is much deeper at Tambali to the south of Sadiola Hill opencast pit than FN3 opencast pits to the north. The oxide profiles are very shallow in the FN3 opencast pits. This can be explained by the fact that the SFZ was the main conduit for the circulation of meteoric water and hydrothermal fluids at Sadiola Hill, and that the structure extends to greater depths in the SSW, but terminates towards the north. In the Sadiola goldfield, the oxide profile extends to deeper levels where faults are present in the opencast pits.

In contrast, in the Sadiola Hill opencast pit, supergene alteration is largely hosted in the calc-silicate rock as karst decomposition. There is evidence of a significant surface water penetration zone on the southern highwall of the opencast pit (Figure 32). The meteoric water penetration caused the oxidation of the hard rock, then the diminution of the volume and density, after concentration of the gold in the oxide occurred.

The supergene alteration is associated with limonitisation, hematitisation, and kaolinitisation, as well as deflation of the calc-silicate leaving a brown calcium silica-sand residuum or soil. In the Sadiola goldfield, the weathered profile covers most of the structures and consists of a residuum or soil along the structure. This residuum or soil is often enriched in minerals which are not leached such as gold. Hematite, limonite and biotite alteration are related to gold mineralisation in the Sadiola goldfield.

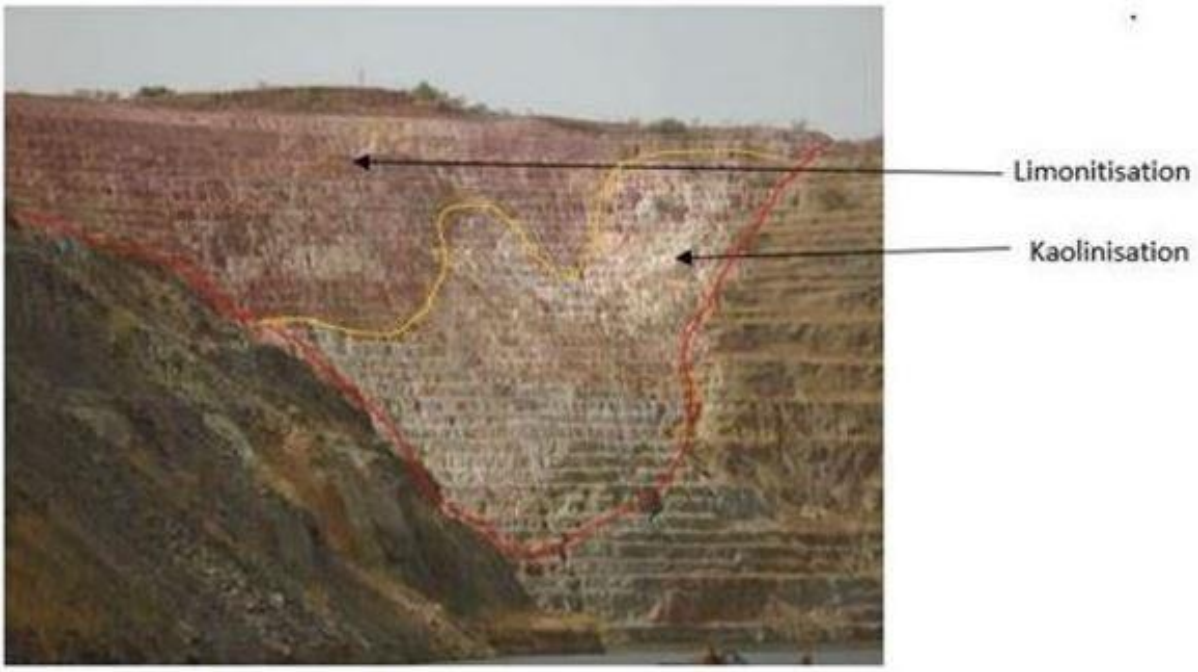

Figure 32: Photograph of the weathering profile on the southern wall of the Sadiola Hill opencast pit. The shape is presented as a funnel of the meteoric water penetration.

4.1.4. Structural mapping

Field mapping in the Sadiola goldfield indicates that syn-sedimentary structure and tectonic structures are dominant in the region. The syn-sedimentary structures are formed during the sedimentation process. They can also be related to the oxide profiles collapse. Figure 16 c, e, and f show some example of syn-sedimentary structures, all the structures were identified in the opencast pit. The pencil in figure 16 shows the sedimentary layer cut by a fault. In the calc-silicate, the bedding is generally oriented northeast and dips toward the west. Small-scale folds and intra bedding folds are present everywhere in the opencast pit.

SFZ is oriented north-south and dip west to sub-vertical. The SFZ also lies at the contact between siltstone-shale-greywacke and calc-silicate effectively making it a bedding-parallel structure (Figure 33).

The grade control data indicates that the southern part of the SFZ is gold mineralised, and the opencast workings in the northern extent show it cannot be barren - possibly just not as well mineralised. Masurel et al. (2017) indicates that the SFZ propagated and formed during D2 but experienced sinistral reactivation during D3. According to the oxide distribution established during the pit mapping, the SFZ and the northeast faults could be syn-genetic and seem to have served as the passageway/conduit of hydrothermal fluid and meteoric fluids, at least in the southern part of the pit. The SFZ is parallel to the SMSZ, without a visible relationship between them. The SFZ has exploited a lithological boundary between the siltstone-shale-greywacke (hanging wall) and the calc-silicate (footwall). The characteristic of the SFZ is due firstly to the D2 deformation and subsequently to the oxidation of the footwall (calc-silicate).

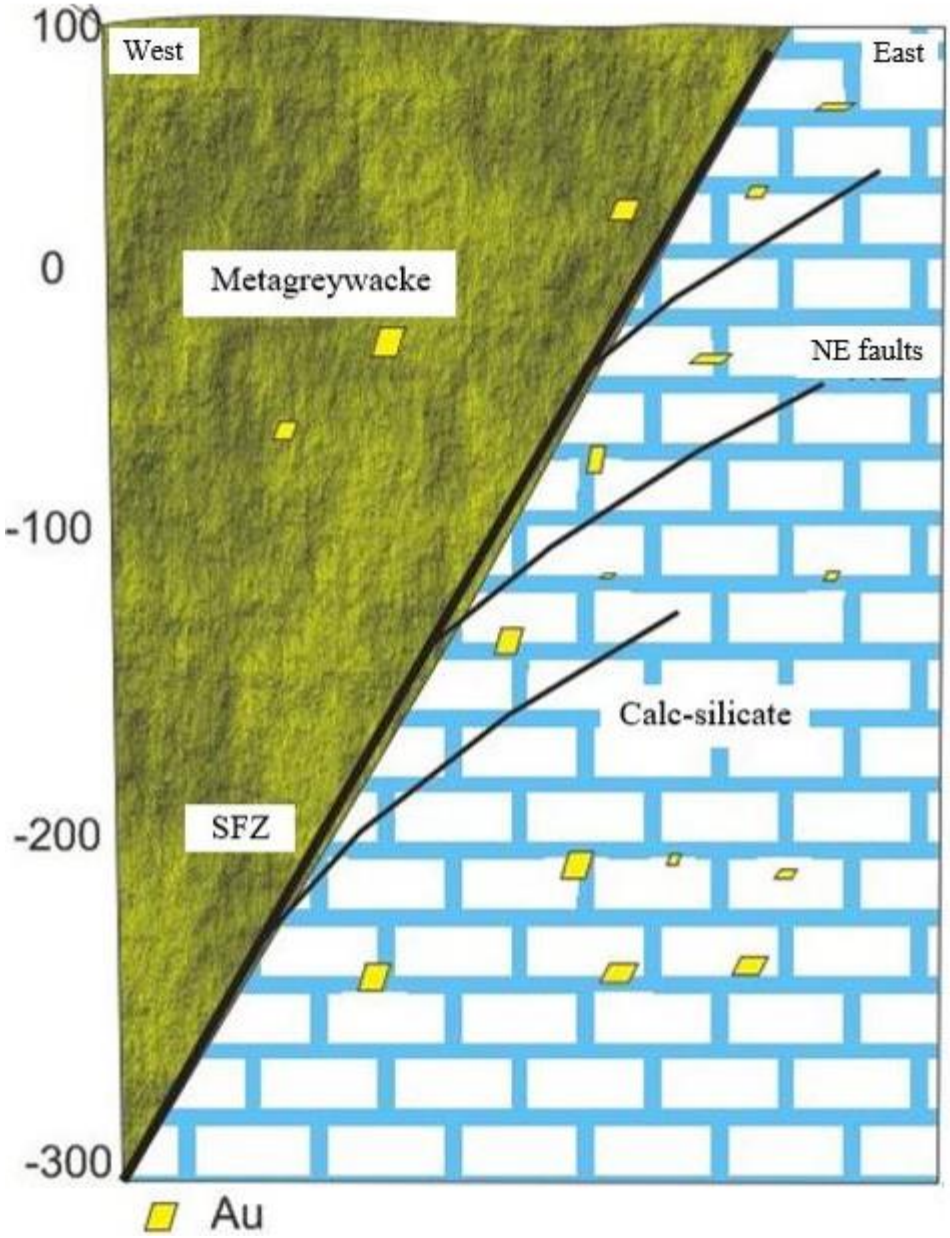

Figure 33: West-east cross-sectional sketch of the Sadiola Hill genetic model for the supergene enrichment phase. The D2 deformation related to northwest-southeast compression, probably associated with the Eburnean orogeny, produced an effect on the SFZ, and north-northeast trending faults. The SFZ and north-northeast trending faults seem to be syn-genetic. The source of the gold in the Sadiola Hill opencast pit was concluded by Hein (2007) as hydrothermal.

In contrast, the supergene alteration has penetrated the entire SFZ along its entire length creating a fault-hosted residuum or soil. As stated above, this is in part, enriched in gold, which is similar to what has been observed at the Yatela mine (Hein et al., 2015) in that pre-existing hydrothermal gold is enriched during karstification and formation of karst residuum. This seems to be the case at the Sadiola Hill gold deposit as well.

A series of west-east normal fault crosscuts the Sadiola Hill opencast and displace the SFZ and the trend of gold mineralisation.

The infiltration of the surface water into the calc-silicate through the structures has caused the oxidation of the hard calc-silicate (discordance between the oxide and hard rock). Blocks of hard rock are sporadically distributed in the oxide phases.

The oxide phases are observed to follow the structures in a north-south and north-northeast direction. The oxide phases are overprinted on the structures. To study their character, geochemistry and the alteration signatures, sampling was conducted mainly along these structures in the oxide phases. The geochemistry and the alteration signatures are presented in Section 4.3.

4.1.5. Reverse Circulation (RC) and diamond drill hole Results

Information from drill core logging was used to establish the stratigraphy and identify the oxidation profile. Stratigraphic columns were established to show the lithological sequence in every opencast pit. The oxidation profile shows the oxidation history.

4.1.5.1. Sadiola Hill opencast pit,

Sadiola Hill pit stratigraphy column is established using the pit mapping of oxide and lithologies. The different profiles from top to bottom that are well defined from pit mapping included:

1. A soil cover that is brown in colour with the significant organic material.

2. A ferricrete horizon that is red in colour with coarse pisolitic gravel and sometimes clasts of quartz. It is noted that ferricrete is present in two or three distinct levels that are separated by aeolian sand or bauxite clay.

3. Aeolian sand horizon that is very fine-grained and yellow to red in colour. The aeolian sand is yellow in colour and encrusted with kaolinite to limonite.

4. Weathered calc-silicate (decarbonated) composed of very fine-grained sandy clay. This is mixed in colour.

5. Hard calc-silicate rock that is massive to bedded and bedded siltstone-shale-greywacke that is moderately silicified (Figure 34). Calcite is present in all rock types as an alteration product. These rock types are crosscut by quartz-feldspar porphyry dykes and diorite dykes. The rock presents a strong to weak weathering profile in appearance. A diorite dyke is situated at the contact between siltstone-shale-greywacke and calc-silicate rock in the Sadiola Hill opencast pit. These dykes were emplaced after deposition of the metasedimentary rocks because they crosscut these units. Masurel et al. (2017) distinguished two dykes of diorite, one early oriented north-south and another later oriented north north-east. The brecciation associated with the SFZ affected all the lithologies.

Biotite, calcite, muscovite, sericite, quartz, and alkali feldspar and potassic feldspar minerals where identified in the calc-silicates samples or rocks cuttings derived from the RC borehole. Alteration assemblages found throughout the RC boreholes included chloritisation, skarnification, biotitisation, silicification, limonitisation, hematitisation, kaolinitisation, and calcification. The sulphides identified are pyrite, pyrrhotite, and arsenopyrite. A significant relationship has been established between biotite, pyrite and bedding.

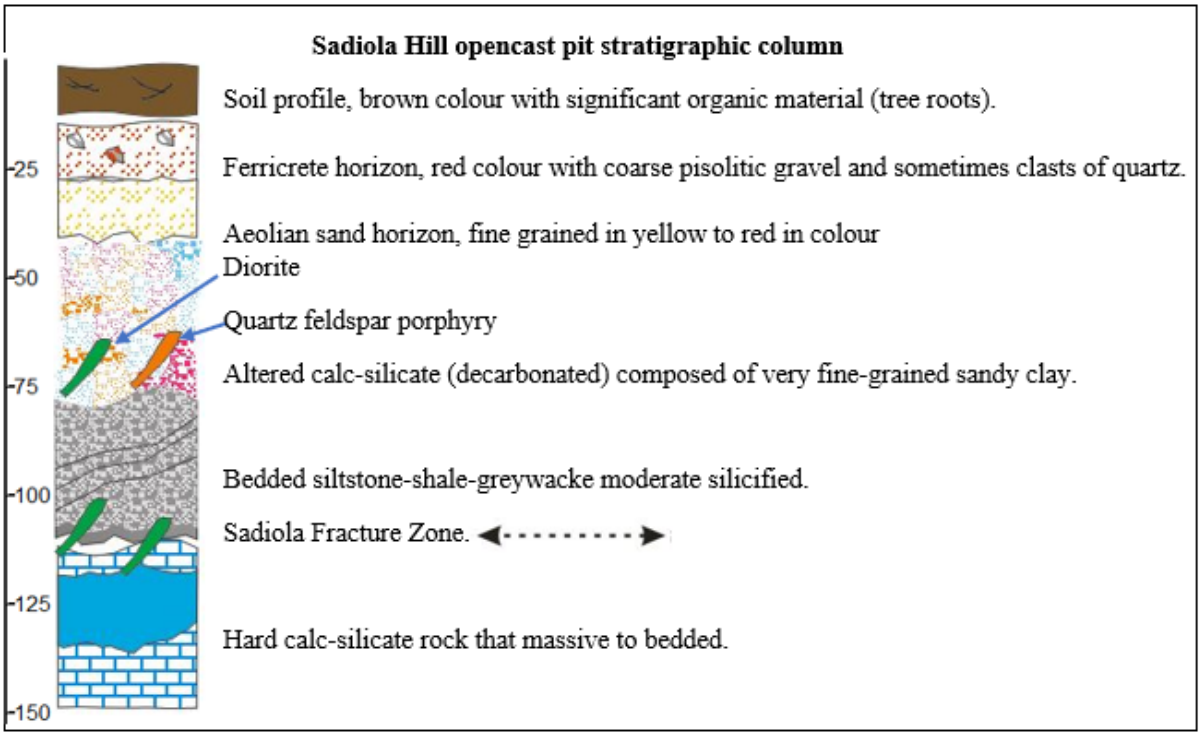

Figure 34: Sadiola Hill opencast stratigraphic column. The column was established by the compilation of the pit mapping data and RC and diamond drilling data.

4.1.5.2. FN3 RC Results

Forty-four RC boreholes drilled in the north-west of the Sadiola Hill and FN3 opencast pits were logged as part of this study to understand the oxide profile outside the pit (Appendix E). The objective of the logging is to establish a stratigraphic column for Sadiola Hill opencast pit. The pit mapping and borehole logging show a comprehensive stratigraphic column. The different lithologies downhole from top to bottom include:

1. A soil profile that is brown in colour with the significant organic material that includes tree roots.

2. A ferricrete horizon that is red in colour with coarse pisolitic gravel and sometimes clasts of quartz. It is noted that ferricrete is present in two or three distinct levels that are separated by aeolian sand or bauxite clay.

3. Aeolian sand horizon that is very fine grained and yellow to red in colour. The aeolian sand is yellow in colour and encrusted with kaolinite to limonite.

4. Weathered and decarbonated calc-silicate composed of very fine-grained sandy clay. This is mixed in colour due to the presence of the three type of oxide development.

5. Hard calc-silicate rock that is massive to bedded, and bedded siltstone-shale-greywacke that is moderately silicified. Sadiola Hill opencast pit northwest RC drilling data presented in Appendix E.

4.1.5.3 Tambali diamond drillhole results

The objective of the diamond drilling in the Sadiola goldfield was first to test the north-south mineralisation trend at Tambali, and the north to northeast mineralisation trend at Sadiola Hill opencast pit. A total of 2 diamond holes were logged. One hole at Tambali, and one at the west of Sadiola Hill opencast pit. The two were logged to confirm the stratigraphy column established during pits mapping. The detailed loggings were focused on the rock type, structures, alteration, and mineralisation.

The different lithologies downhole from top to bottom in Tambali pits (Figure 35) include the following:

1. A soil profile that is brown in colour with the significant organic material.

2. A ferricrete horizon that is red in colour with coarse pisolitic gravel and sometimes clasts of quartz.

3. Red to yellow sandstone horizon that is very fine to medium grained. This sandstone is friable and encrusted with kaolinite, limonite to hematite alteration.

4. Siltstone-shale-greywacke that is moderate to strong silicified, it is a turbidite sequence.

5. Calc-silicate rock that is massive.

6. Quartz-feldspar porphyry dykes oriented north-northeast crosscut all the sediments.

7. Diorite dykes intruded the quartz-feldspar porphyry and the sediments.

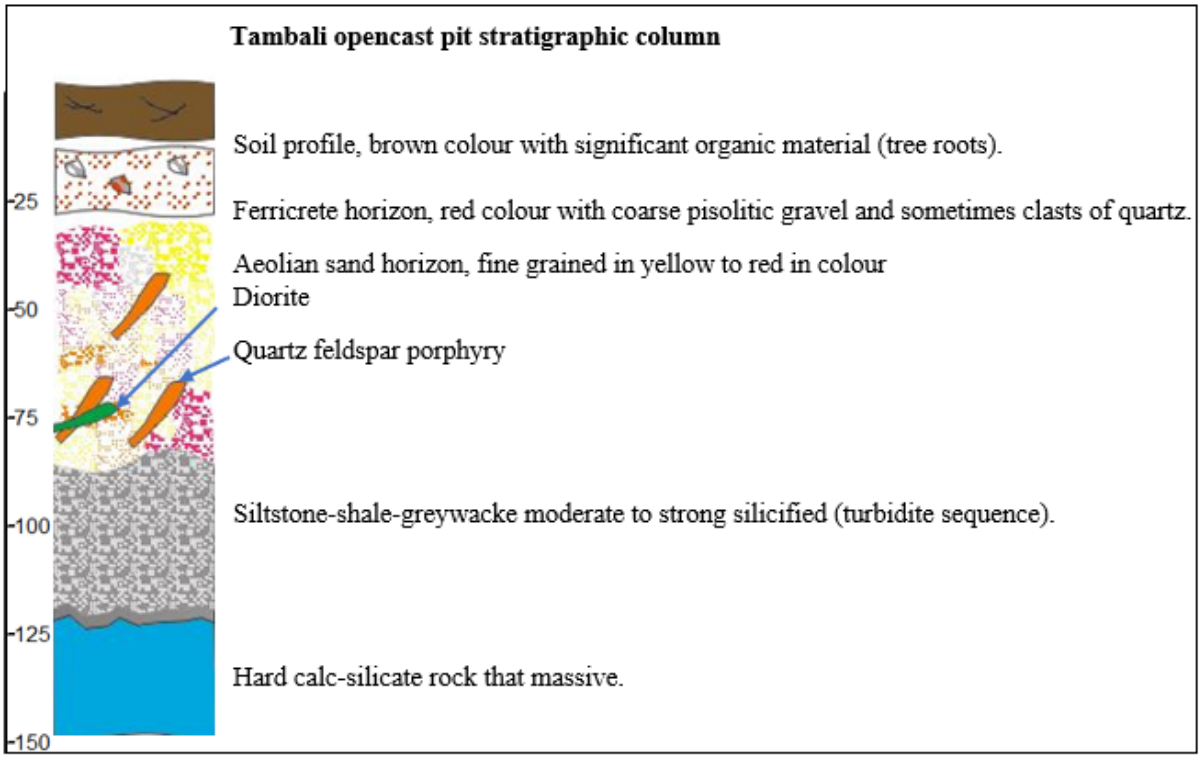

Figure 35: Tambali opencast pit stratigraphic column. The column was established by the compilation of the pit mapping data and RC and diamond). drilling data.

4.1.6. Sadiola regolith mapping results

Outcrops are limited in the Sadiola goldfield, the Sadiola area is mainly covered by ferricrete. In the KKI, the soil geochemistry is not an appropriate technique for gold exploration due to the character and profile of the ferricrete according to Chardon (2015). The Sadiola goldfield plant is fed with oxide ore material, therefore knowledge of the regolith regime related to deposition and transportation is an important factor in the exploration strategy. Gold mineralisation is found from the surface in the ferricrete to hard calc-silicate sequences and/or siltstone-shale-metagreywacke sequences of Birimian age. Hein and Tshibubudze (2007) identified two styles of gold mineralisation in Sadiola goldfield: placer gold in palaeochannels and screes, and gold in breccia and stockwork veins. Most of the goldfield is covered by ferricrete (laterite). According to Grimaud (2014), the ferricrete formation began in the Eocene-Miocene with the development of three (3) distinct glaciations across West Africa Craton. The oldest glaciation event generally caused an infill of deep palaeochannels as this can be seen in the southeast of the Sadiola Hill opencast also in the highwall adjacent to the ramp in the FE4 opencast pit.

The regolith data assisted in field mapping to indicate where there is rock outcrop and reconstitute the palaeochannels (palaeo-environment). Schwarnecki (2014) conducted regional regolith mapping in the Sadiola district. According to his compilation, there are palaeochannels, sedimentary units,

cuirasses developed in transported material, pediplain, sand and clays, and ferruginous and or lithic lag.

4.1.7. Sadiola termite mounds sampling results

In the Sadiola goldfield, the termite mounds sampling data covers all the exploration permit. The termite mounds data correspond mainly to the low gravity terrain with deep oxidation profile. The termite mounts sampling is one of the exploration strategies for gold mineralisation in the Sadiola goldfield. The entire Sadiola goldfield is covered by laterite and soil geochemistry is not an appropriate technique.

Several criteria were applied for sampling, including (1) type, (2) age and (3) colour of the termite mount. A characteristic of a good sample selection is the large mounds, with a recent age, with colour defining the type of alteration. There are three types of termite mounts (small, medium and large) in the goldfield according to the height above the surface. The colour of termite mount is an indicator of the type of alteration, the age is classified as recent (wet) or ancient (dry). The termite mound type is defined as small (0.2-0.5 m height), medium (0.5-1 m height) and large (1-2 m height). In an area of 50 m^2, a good termite mound is selected. On this large mound, the recent is sampled to avoid contamination. The last Sadiola termite mound sampling campaign was carried out in September 2012 by SEMOS exploration geologists in collaboration with AGA geochemists from Johannesburg office. The interpretation map presents four data grouping from high to low value; (1) red (high value), (2) yellow (medium), (3) green (Low) and (4) blue (zero) (Figure 36). The red represents very high value and subsequently blue represents very low assay result. Basically, the termite mounds data is the first regional data used by Sadiola exploration team. The soil geochemistry is not used to a large extent in the Sadiola exploration strategy.

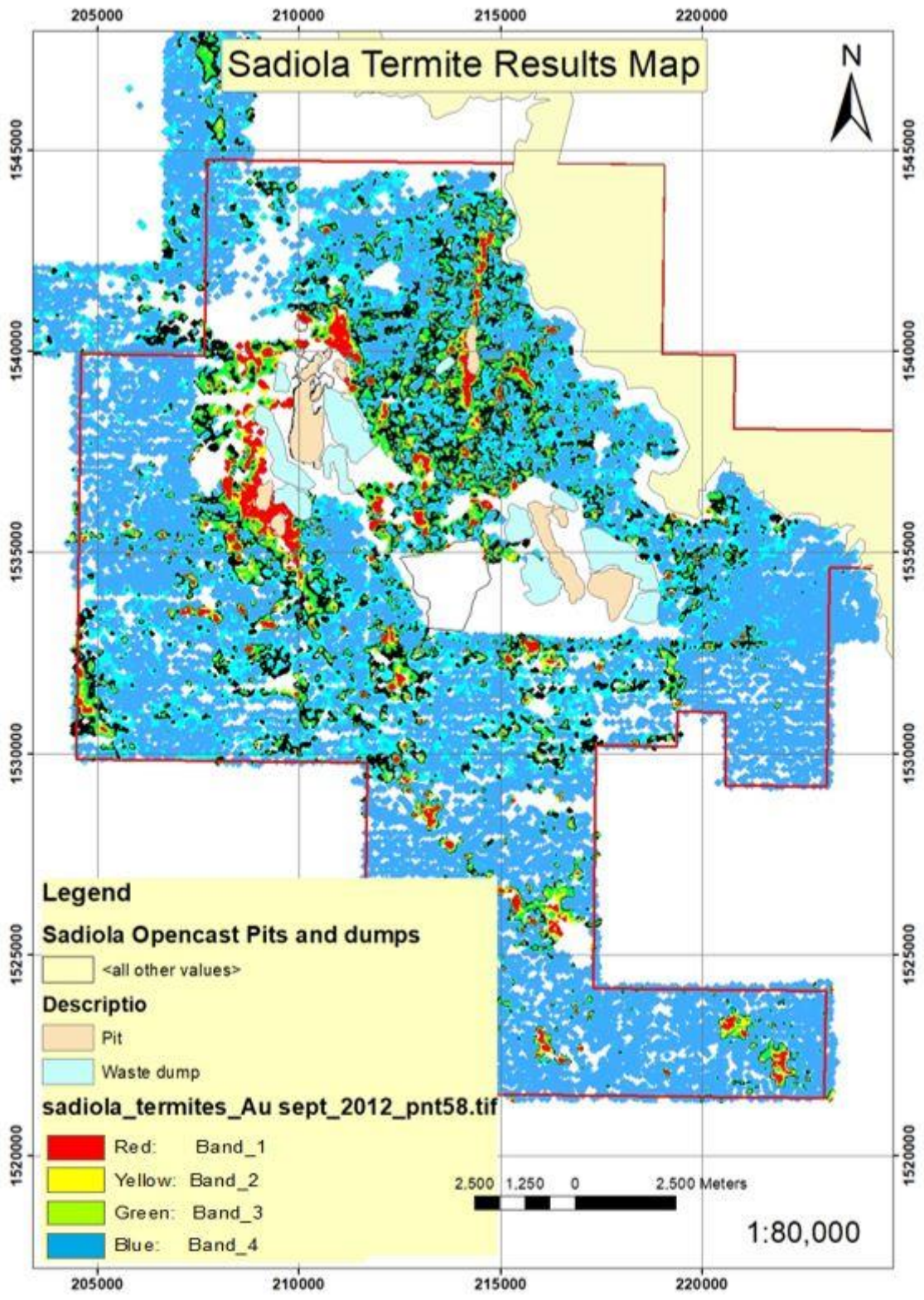

Figure 36: Map of termite mounds sample result in the Sadiola exploration permit. The red (high value), (2) yellow (medium), (3) green (Low) and (4) blue (zero) of gold. This value is overprinted on each open cast pit in the Sadiola goldfield.

4.1.8. Gold mineralisation distribution

4.1.8.1. Gold mineralisation distribution

Gold is found in three different units in the Sadiola Hill opencast. The first units are the ferricrete layers, second is the oxide units (oxide saprolite and transitional) and the third units are hard (calc-silicate, siltstone-shale-greywacke, diorite and quartz-feldspar porphyry) rock. The oxidation process was a controlling factor in the concentration of gold in the decarbonated calc-silicate rock. The shape of gold grains suggests that the source of gold mineralisation could be variable: (1) transported hosted in ferricrete, (2) hydrothermal mineralisation. Masurel et al. (2017) classified the origin of fluid and metal as unknown. At Sadiola goldfield, three types of gold have been identified and were found in unique conditions and uniquely distinguished. This has allowed the examination of the relationship between the gold mineralisation and the following factors such as (1) lithological contact, (2) SFZ, (3) northeast trending faults, (4) iron (Fe) and (5) potassium (K) alteration. The gold mineralisation has been concentrated after oxidation process into lithological contact, SFZ, and northeast trending faults, while it is proportionally associated with iron (Fe) and potassium (K) alteration. At the Sadiola goldfield, the gold mineralisation is present in all lithologies, but the significant quantity is hosted in the decarbonated calc-silicate and the calc-silicate unit. Figure 37 shows gold mineralisation distribution through the Sadiola goldfield.

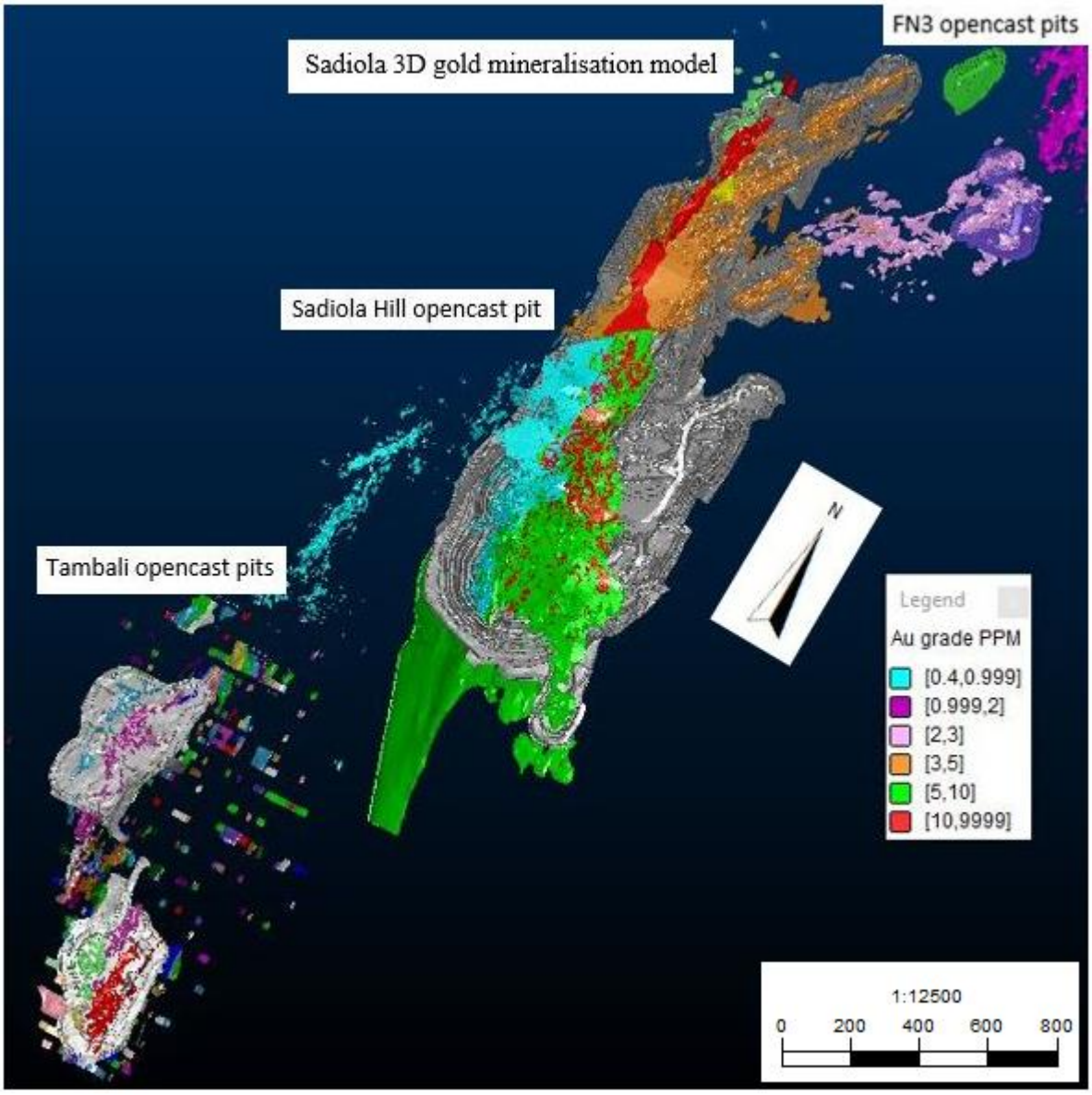

Figure 37: The 3D Sadiola goldfield gold mineralisation model across the Tambali, Sadiola Hill open cast and FN3 pits. Compiled by SEMOS resources evaluation team.

4.1.8.2. Relationship between gold mineralisation and oxide phases

Gold mineralisation in the Sadiola goldfield has been modelled in 3D model by AGA (Figure 37), while the 3D model for ferricrete, oxide saprolite and oxide transitional zone were completed in this study. To examine and establish the relationship between, gold mineralisation and the oxide phases, 3D gold mineralisation has been plotted with the following oxide profiles: ferricrete, oxide saprolite and oxide transitional. Gold mineralisation is found in the ferricrete (Figure 38), as the ferricrete has developed in transported material, it implies that the hosted gold is also transported. This can be confirmed by sub-rounded to rounded and oval shape of observed gold under the binocular microscope (Section 4.3). There is a relationship between gold mineralisation and ferricrete unit across Sadiola goldfield.

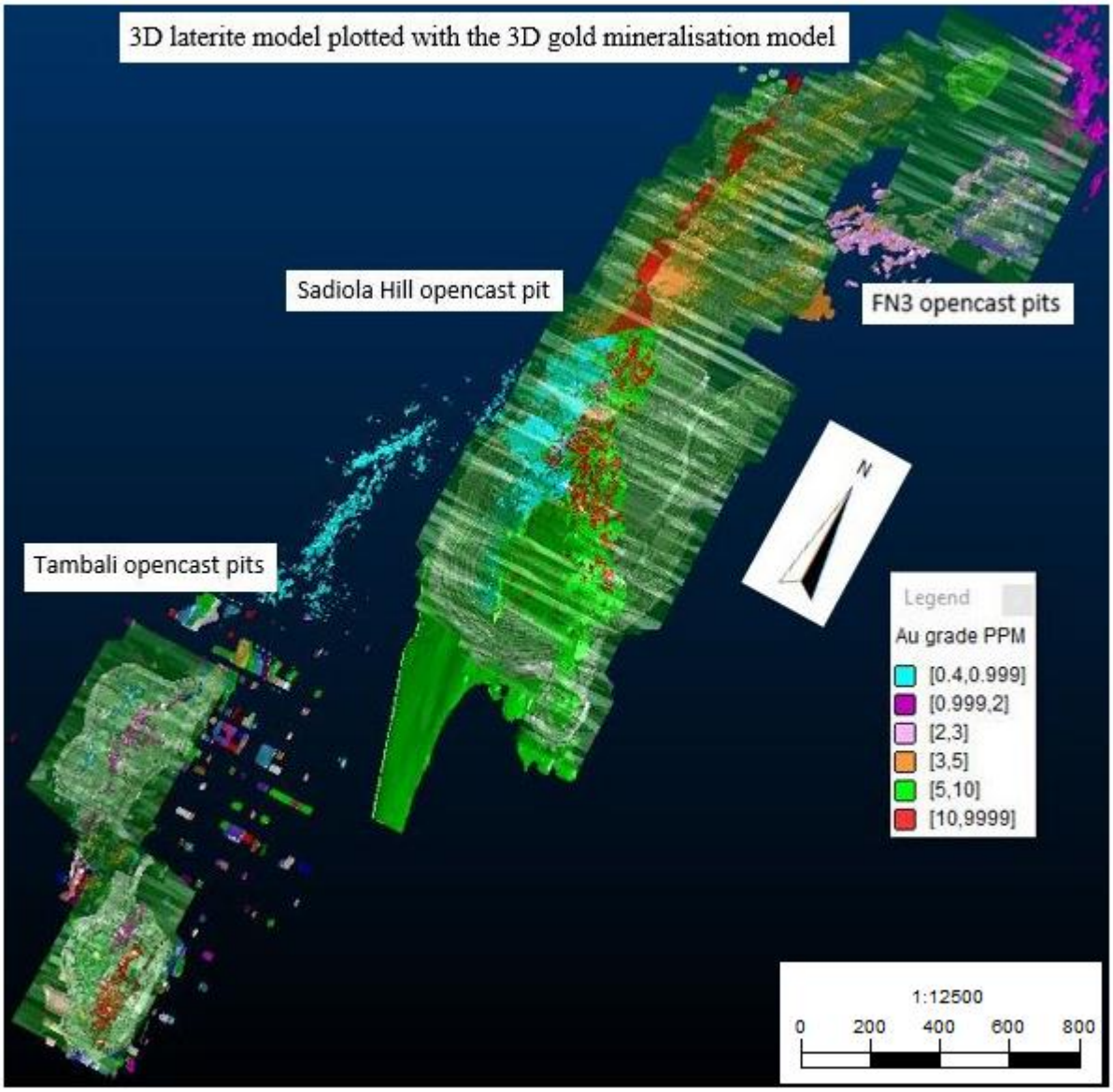

Figure 38: The 3D laterite model plotted with the 3D gold mineralisation model for Sadiola goldfield (FN3 in the northern, Sadiola Hill open cast in the middle, and the Tambali pits in the southern).

The gold mineralisation found in the ferricrete constitutes type 1 of the three-types established. Gold mineralisation is distinguished across the oxide saprolite throughout the goldfield (Figure 39). There is a strong correlation between the gold mineralisation and the oxide saprolite zone.

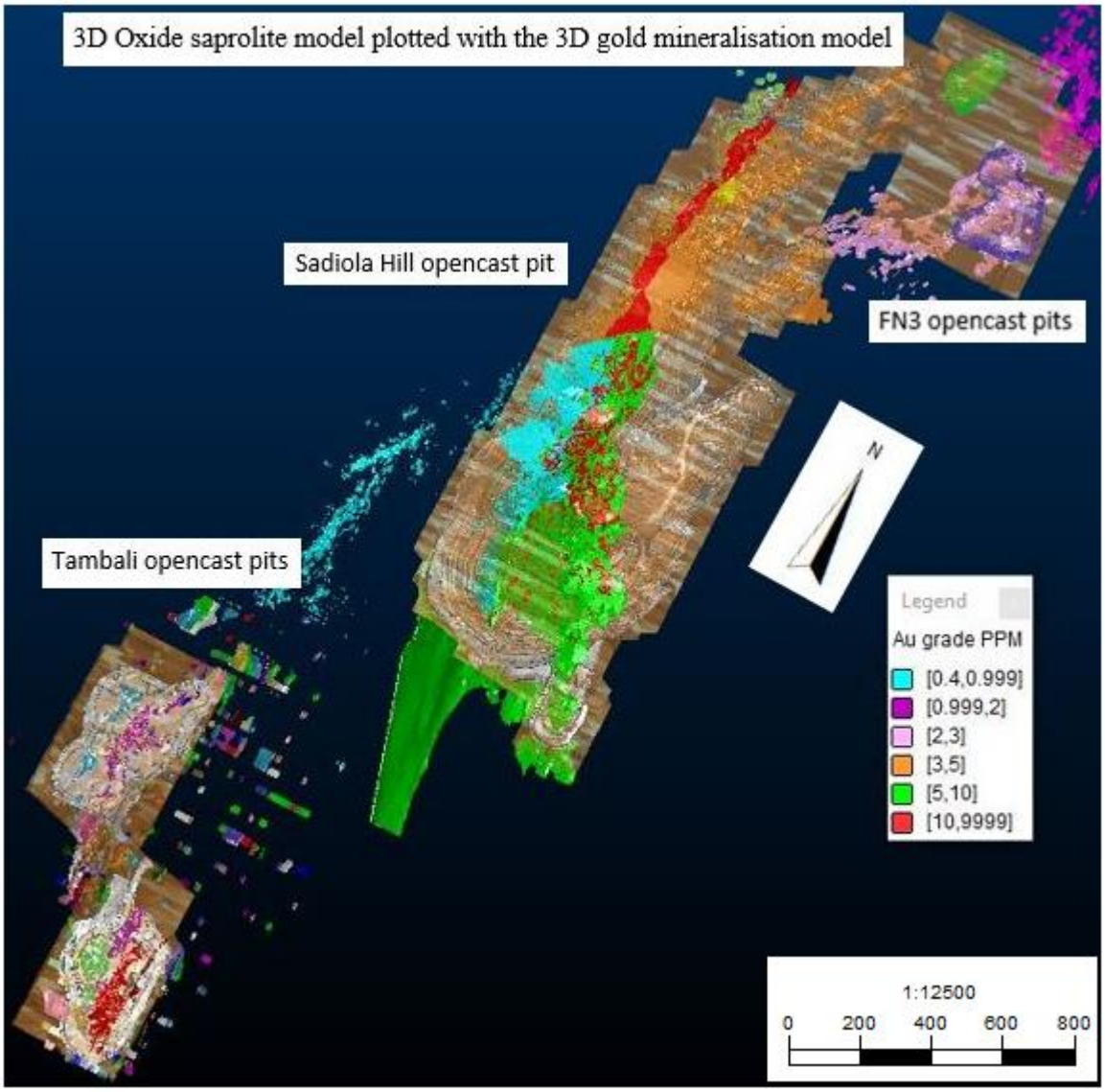

Figure 39: The 3D oxide saprolite model plotted with the 3D gold mineralisation model for Sadiola goldfield (FN3 in the northern, Sadiola Hill open cast in the middle, and the Tambali pits in the southern part).

Figure 40 shows that the Sadiola mineralisation is also hosted in the oxide transitional zones. In the oxide transitional profile, the primary features of the rocks are still distinguishable.

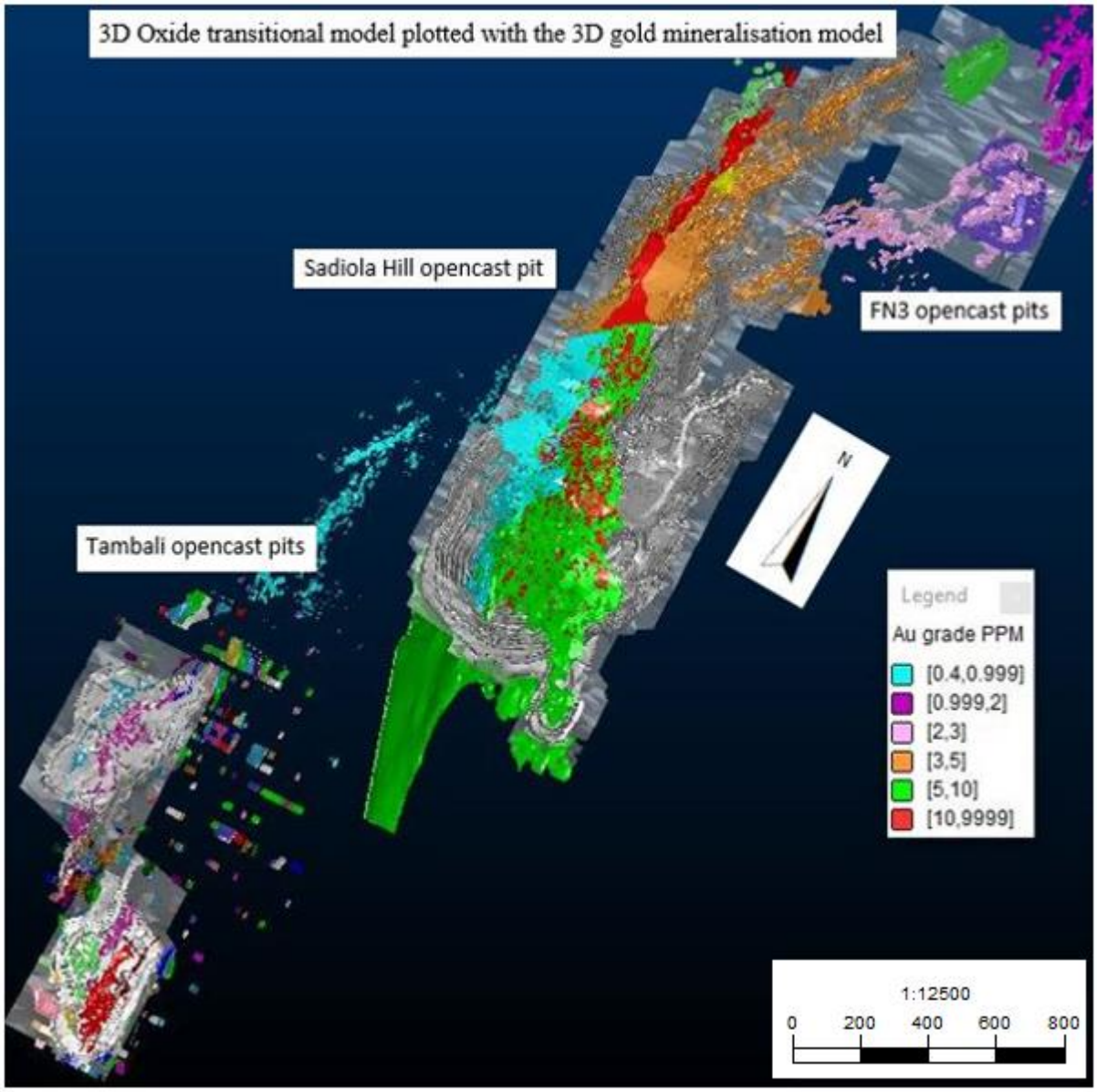

Figure 40: The 3D oxide transitional zone plotted with the 3D gold mineralisation model for Sadiola goldfield (FN3 in the northern, Sadiola Hill open cast in the middle, and the Tambali pits in the southern part).

The significant presence of the gold mineralisation in the weathered calc-silicate (oxide saprolite and oxide transitional) is the consequence of the calc-silicate weathering. The oxidation of the calc-silicate led to the diminution of volume and density with leading to concentration of the gold mineralisation. The three shapes of the gold are found in the oxide zone. The sub-rounded to oval shapes of gold (transported gold) found in the oxide phases probably comes from the ferricrete. The meteoric fluid circulation has probably facilitated the migration down in the oxide phases. At the Sadiola goldfield, gold mineralisation is hosted by the ferricrete, the oxide phases (oxide saprolite, oxide transitional zone), hard calc-silicate, and siltstone-shale-greywacke.

This relationship between gold and oxide phases study highlighted a significant correlation between them. The oxidation caused the loss of volume and diminution of the density resulting in the concentration of the gold grade in the oxide phases. This gold is the type 2 of gold mineralisation identified in the opencast. It has been proved that the oxide transitional is significantly more important than oxide saprolite in term of volume, and mineable gold quantity.

Type 3 gold mineralisation is found in hard rock. The gold mineralisation hosted in the hard rock is still present in the Sadiola opencast pit as sulphide mineralisation.

4.1.8.3. Relationship between gold mineralisation and calc-silicate sub-facies

All the six identified calc-silicate sub-facies host gold mineralisation, but a significant gold grade was found in the very thick to thick-bedded marble with alternating white and black layers, the biotite alteration related to the dark layers, the thin to very thin-bedded calc-silicate, the slump-folded marble, and the carbonaceous siltstone. It is important to note that the marble sub-facies without significant structural feature or alteration signature are not consequently mineralised. Gold mineralisation in the Sadiola goldfield is mainly located in the calc-silicate rock unit due to its chemical composition. All the lithologies are mineralised as well as the different sub-facies identified in the goldfield. The oxide profiles are significantly related to the gold mineralisation. The DD and RC drilling data from Sadiola Hill and FN3 opencast pits indicate that gold grade are mainly located in the different calc-silicate sub-facies, while the gold mineralisation is essentially in the meta-sandstone to greywacke sequence in the Tambali opencast pits. Some occurances of high grade mineralisation have been seen in siltstone-shale-greywacke in the Sadiola Hill opencast pit.

4.1.8.4. Relationship between structures and lithologies

At Sadiola goldfield there are three main faults orientations which are visible in the Sadiola Hill opencast pit: the main north-south trending structure, the northeast trending structures, and the east-west trending structures. The SFZ is oriented north-south. The SFZ is located on the lithological contact between the calc-silicate unit to the east and the siltstone-shale-greywacke unit in the west of the Sadiola Hill opencast pit (Figure 41). In general, the lithological contact corresponds to the structure. This presents a moderate to strong oxidized zone. The northeast trending faults and the SFZ are interpreted to have formed synchronously, with the northeast trending faults splaying off from the SFZ. The mineralisation is concentrated along the SFZ and northeast trending faults, while the west-east trending faults are younger than the mineralisation as they crosscut the mineralisation. All these structures are more visible in the calc-silicate rock than the siltstone-shale-greywacke due to differences in the competency of the rock. The oxidation process of the calc-silicate occurred along the north-south and northeast trending faults. The meteoric water penetrated the calc-silicate rock through the structures and caused oxidation due to the calc-silicate chemical composition. Traoré and Samaké (2010) noted that the Sadiola Hill ore body is displaced by this west-east trending faults.

According to this study, the displacement of the Sadiola Hill ore body is largely due to the collapses of the oxide unit after oxidation of the calc-silicate unit. The collapse of the oxide zone can be explained by the diminution of the volume of material. Sadiola Hill opencast pit mapping data reveals the presence of several blocks of diorite, and quartz-feldspar porphyry which can be explained by the oxide profile collapse. The loss of volume and density resulted in the concentration of the gold mineralisation in the oxide profile. The progressive collapse of decarbonated calc-silicate caused the collapse of the contact between siltstone-shale-greywacke and the calc-silicate along the SFZ.

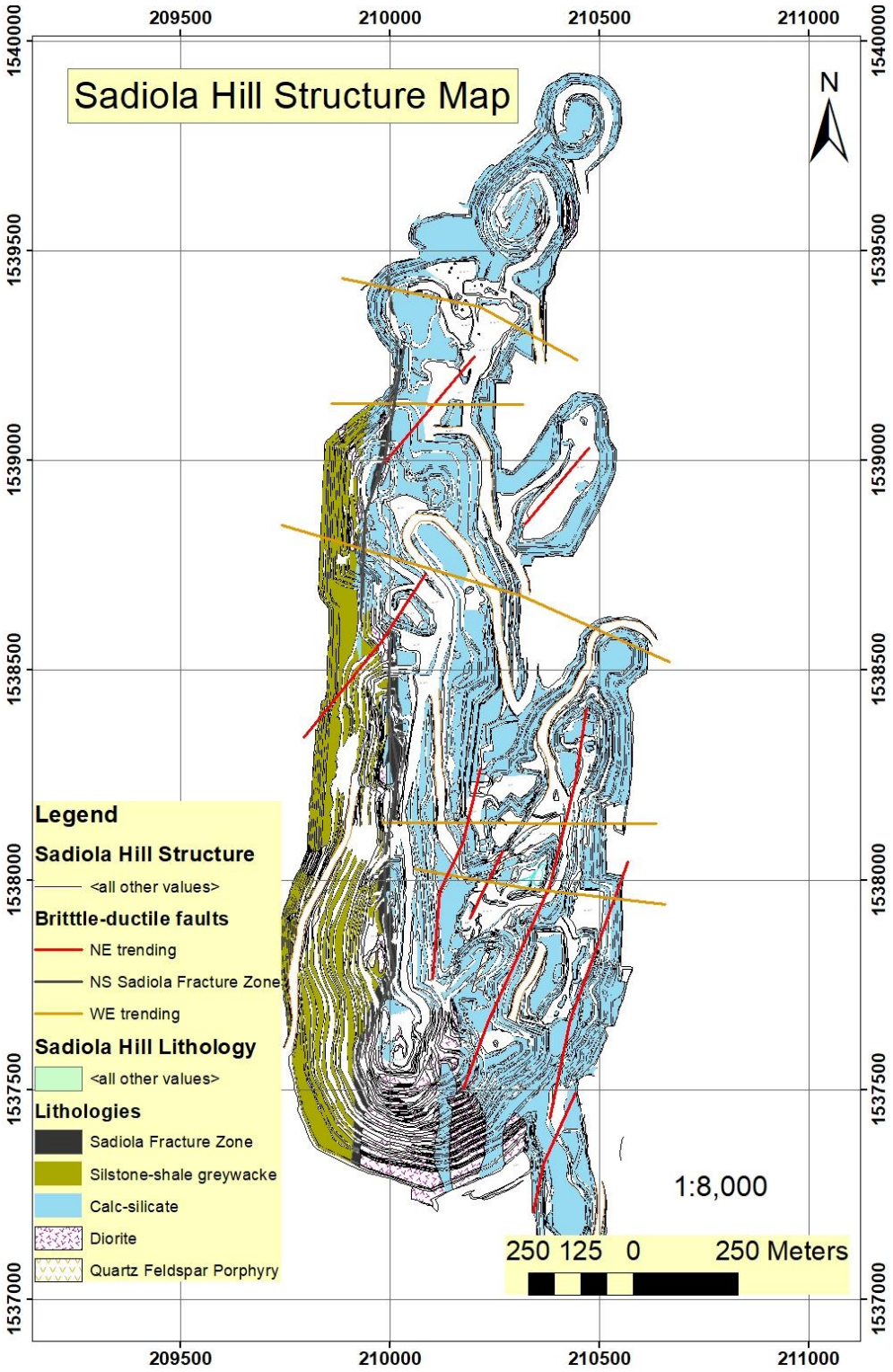

Figure 41: The SFZ, northeast trending faults and west east trending faults plotted on the Sadiola Hill opencast pit geological map. The SFZ is located along the contact between the siltstone-shale-greywacke in the west and the calc-silicate in the east.

4.1.9. Summary

Based on mapping of the Sadiola goldfield within the opencast pits and the logging of drill core (RC and DD), several lithologies can be identified, namely calc-silicate, siltstone-shale-greywacke, meta-sandstone, quartz-feldspar porphyry, and diorite. Gold mineralisation is significantly hosted in the calc-silicate sub-facies in the Sadiola Hill opencast pit, while it is hosted in the meta-sandstone to greywacke sequence in the Tambali opencast pits. There is sporadic gold mineralisation in siltstone-shale-greywacke in the Sadiola Hill opencast pit. In the Sadiola goldfield, the termite mound anomalies are an excellent indicator of gold mineralisation. There is a strong relationship between the termite mound anomaly and the oxide profile. In the goldfield, many opencast pits are located along trends of the gold anomalies in termite mounds. The regolith data assisted in field mapping and to reconstitute the palaeochannels. The meteoric water penetrated in the hard rock through the structures and caused the oxidation of the hard rock (Figure 42).

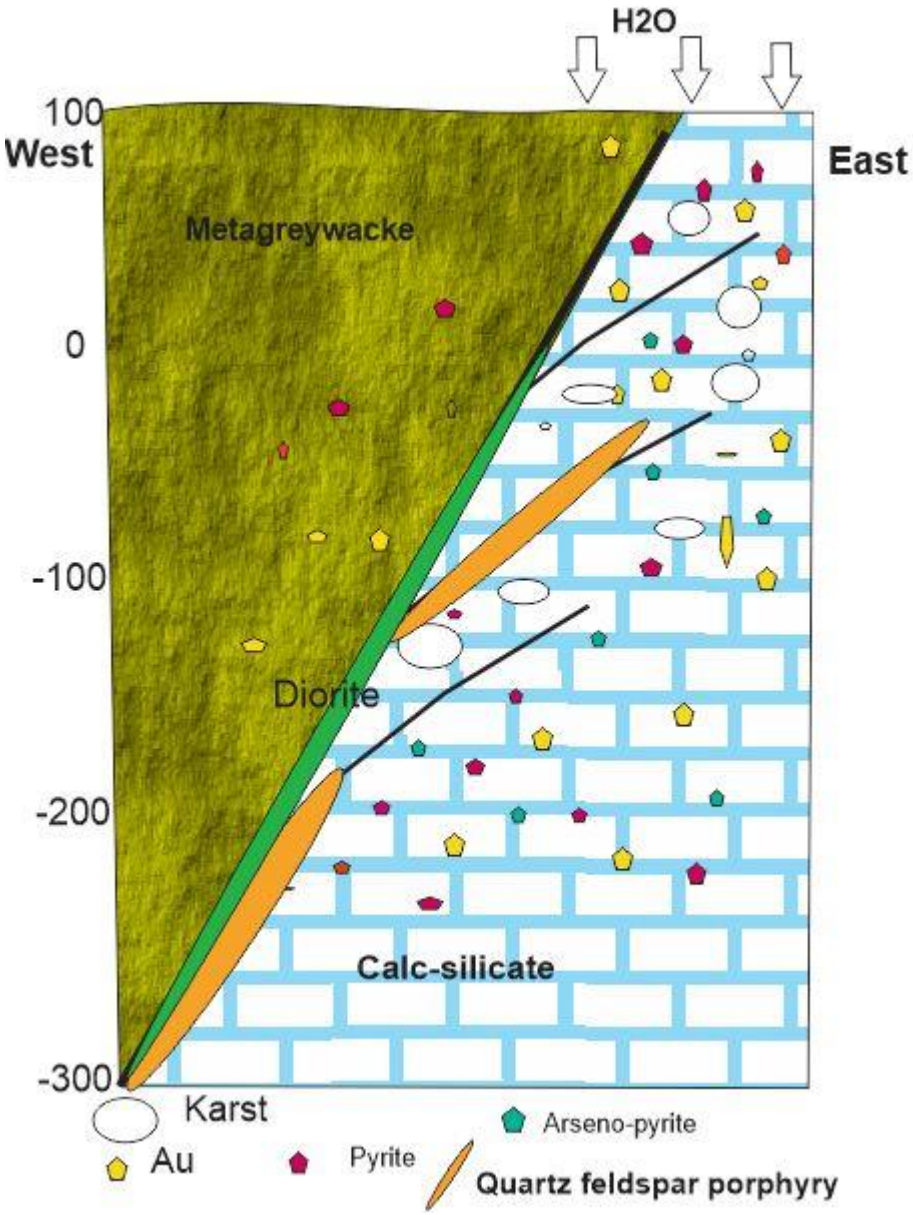

Figure 42: West-east cross-sectional sketch of the Sadiola Hill genetic model for the supergene enrichment phase. The surface water penetrated the calc-silicate rock through the SFZ and northeast trending structures. The pyrite in the presence of H_2O and O_2 can active some reactions and cause the oxidation of calc-silicate.

Note that this refers to supergene enrichment, and is not the genetic model for the primary gold mineralising event.

An increase in gold concentration is linked to a diminution of volume and density due to the formation of the oxide zone. Supergene alteration minerals are limonite, hematite, and kaolinite. Deflation of the calc-silicate has resulted in a brown calcium silica-sand residuum or soil which is often enriched in minerals that are not leached, such as gold. Hematite, limonite and biotite alteration are related to the gold mineralisation in the Sadiola goldfield. Three distinct ferricrete horizons were

identified on the calc-silicate, with one thin horizon on the siltstone-shale-greywacke. In the goldfield, every single lithology hosted the gold mineralisation. A significant part of the ore body is hosted by the weathered and unweathered calc-silicate unit in the Sadiola Hill opencast pit. At Sadiola goldfield, three units host gold mineralisation: (1) ferricrete, (2) oxide phases and (3) hard rocks (calc-silicate and/or siltstone-shale-greywacke). In the Sadiola goldfield, gold values of the oxide phase showed a significant link between the gold mineralisation and the oxide profile. The collapse of the oxide unit caused the following events (1) break down of diorite into multiple pieces in the oxide zone observed through the Sadiola Hill opencast pit, (2) break down of the quartz-feldspar porphyry in multiple pieces observed in the south-east of the Sadiola Hill opencast pit, and (3) The brittle and ductile deformations have been observed on the core drilled through the SFZ.

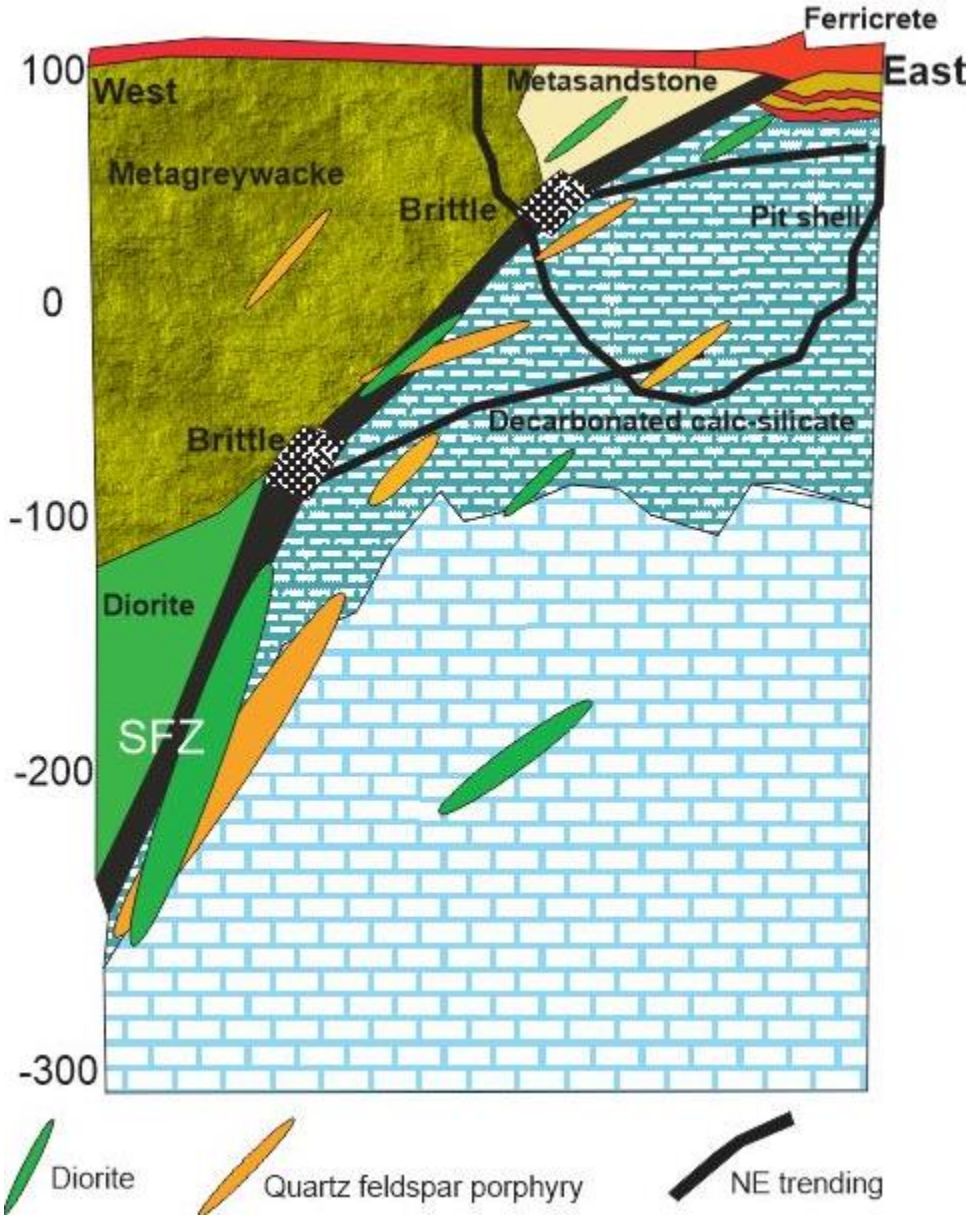

Figure 43: West-east cross-sectional sketch of the Sadiola Hill genetic model for the supergene enrichment phase. The decrease in the volume of the decarbonated calc-silicate caused the collapse of oxide. Then SFZ which is a lithological contact between siltstone-shale-greywacke and calc-silicate collapsed. Subsequently, aeolian sand was deposited on the ferricrete and on the decarbonated calc-silicate.

The Sadiola Hill opencast pit after oxidation process and collapse of the oxide profile is illustrated in Figure 44.

The Sadiola mine-scale geology and regional mapping study facilitated the building of the 3D geological model for Sadiola goldfield. The 3D lithological and oxide models are presented in Section 4.2.

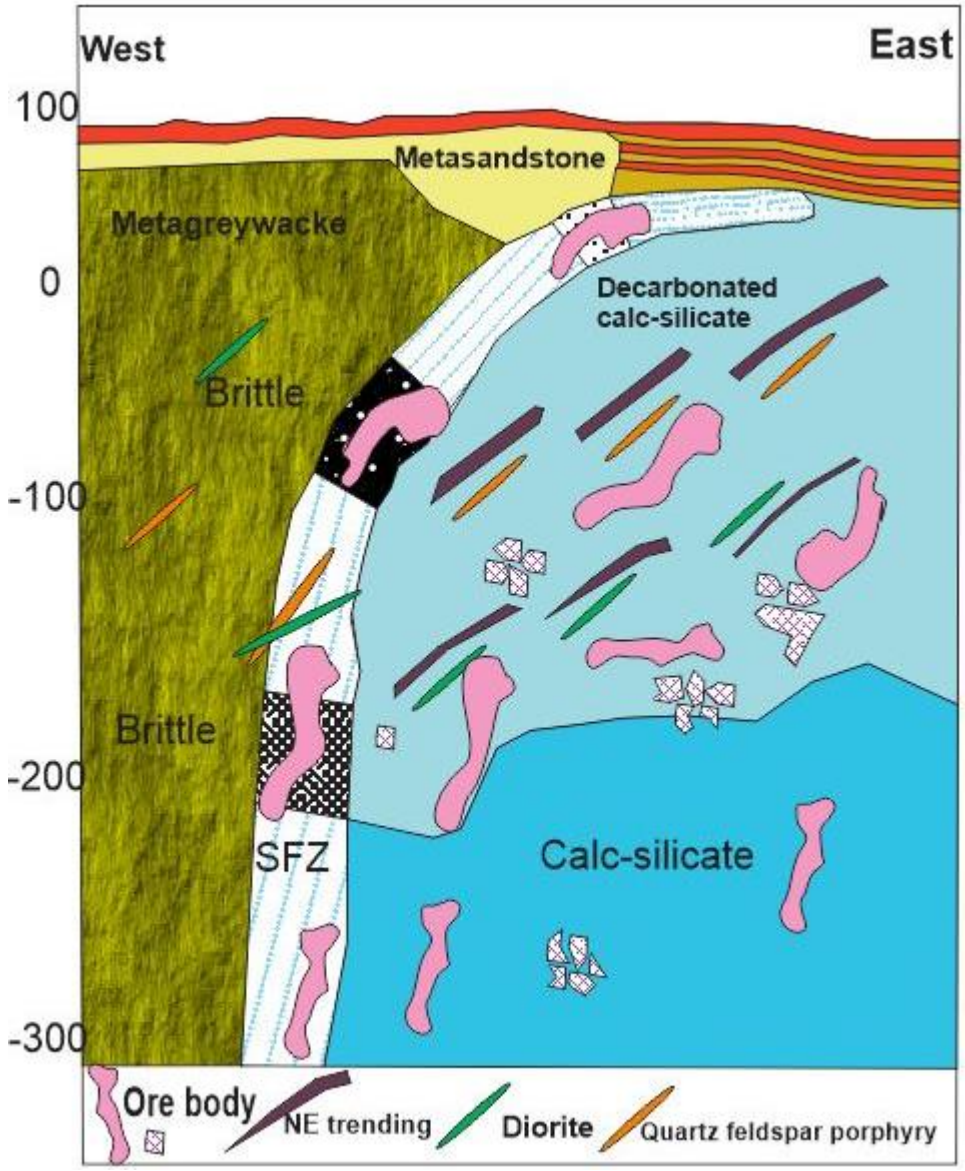

Figure 44: West-east cross-sectional sketch of the Sadiola Hill showing the results of oxidation and collapse of the oxide profile.

4.2. 3D modelling of Sadiola goldfield lithologies and oxide profiles

4.2.1. Introduction

3D modelling is a spatial representation of an object in three-dimensions (3D). The lithology and oxide profile 3D models were completed to build geometry and a stratigraphic sequence for each lithology and oxide profiles in every opencast pit, and to establish the relationship between each 3D model and gold mineralisation. 3D modelling was conducted using the 2D lithological and oxide mapping results. The mapping of the lithologies, oxide profiles and the drilling data were used to build the 3D oxide model using the CAE Studio 3 (Datamine). 3D lithological model was completed using Leapfrog Geo 3.1. To do this 3D lithological modelling, the different 2D maps were taken as reference. The west-east vertical sections were taken and then a string for each grouped lithology and oxide profile was drawn. The different grouped lithologies strings were linked as wireframe to build a 3D model. This chapter presents the building of a 3D lithological and oxide model for Sadiola goldfield, the 3D model results and interpretation. To achieve these objectives, AGA 3D gold mineralisation model was used to examine the relationship between gold mineralisation and every oxide profile, and different lithologies.

4.2.2. Lithology modelling

The models include the Tambali, the Sadiola Hill and FN3 opencast pits. The relationship between the lithologies has helped to elaborate the stratigraphic sequence for each opencast pit. The model covers the areas between the topographic surface at the top and -500 m RL depth. The geological model involves all the single lithologies present in the pit. Some lithologies were grouped to facilitate the modelling. Five units were modelled: (1) Ferricrete; (2) calc-silicate; (3) siltstone-shale-greywacke, (4) diorite and (5) quartz-feldspar porphyry. Ferricrete, laterite and overburden were grouped into a ferricrete unit; sandstone and siltstone-shale-greywacke were grouped into a siltstone-shale-greywacke unit, calc-silicate, marble, and breccia were grouped into a calc-silicate unit, diorite and granodiorite were grouped into diorite unit, and quartz-feldspar porphyry as the final unit. Figure 45 shows that a significant area in the goldfield is covered by meta-sediment (calc-silicate and siltstone-shale-greywacke). Diorite and quartz-feldspar porphyry are present in the goldfield as several discontinuous intrusions with general orientation of north-south to the northeast trend.

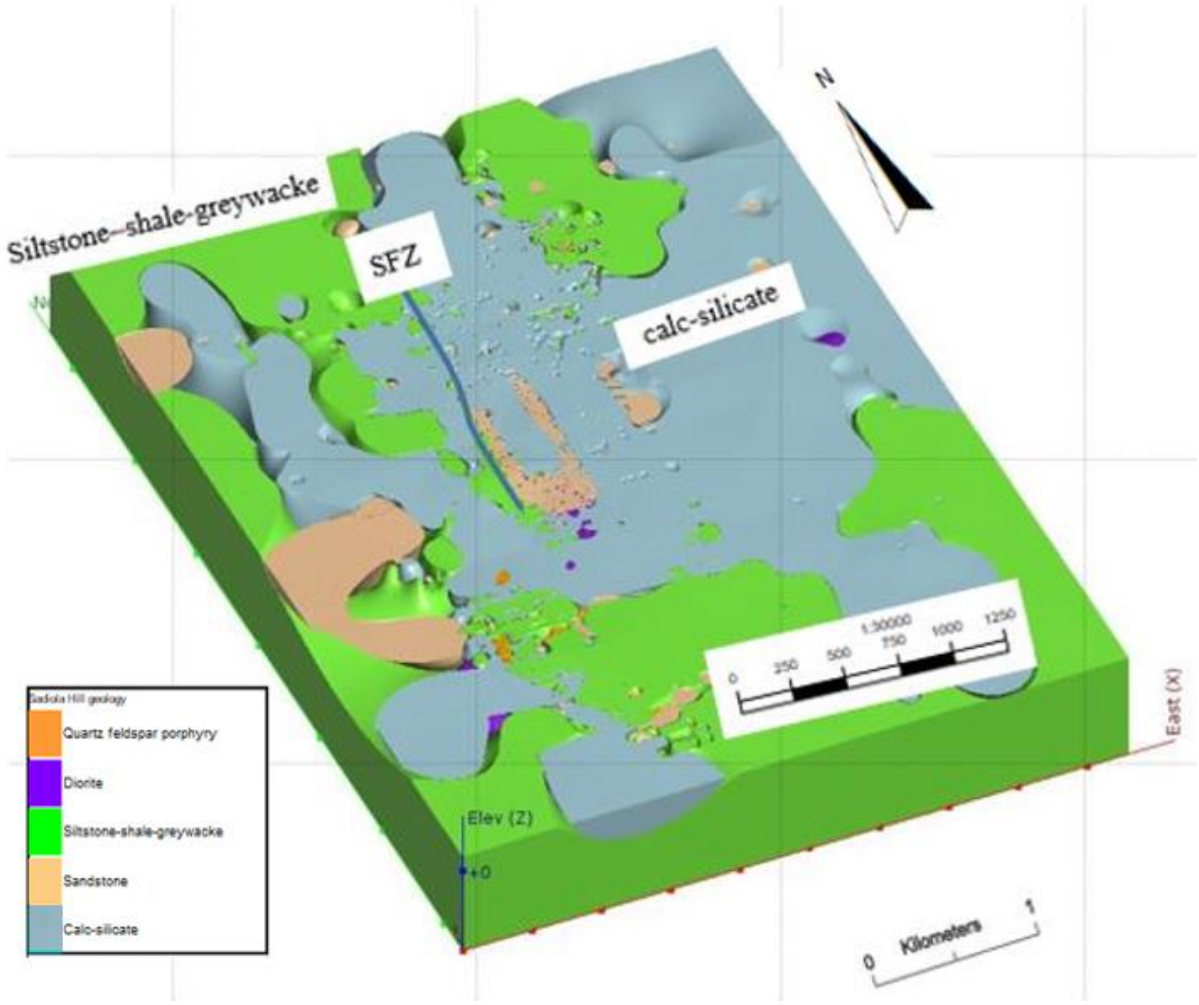

Figure 45: The 3D Sadiola goldfield lithology model. The green at the west represents the siltstone-shale-greywacke, while the calc-silicate is located mostly in the east with the blue colour.

4.2.3. Oxide modelling

The modelling was done for the four weathering profiles, i.e., (1) the ferricrete, (2) oxide saprolite, (3) oxide transitional zone, and (4) unweathered hard rocks. Each profile was modelled separately. Oxide modelling has allowed the relationship of weathered and unweathered material and the gold mineralisation to be established. It has also allowed the weathering sources and causes to be investigated and the link between oxide phases and structure. The Sadiola Hill models include structures mapped by Cameron (2010) that trend northerly and north-easterly. West-east trending structures did not resolve well in the models and are therefore not reported here (documented in Masurel et al. 2017). Sadiola Hill gold mine has produced gold since 1996 from the three oxide profiles. In the Sadiola Hill opencast pit, many supergene alterations phases are present such as limonitisation, hematitisation and kaolinisation. The 3D ferricrete model for Sadiola goldfield is presented in Figure 46. The drill hole information was used to create a ferricrete domain, section by

section from south to north. The ferricrete string domain was linked to create a ferricrete wireframe. The spacing between the sections was 25 m. There was some aeolian sand between the ferricrete layers cover the calc-silicate, as noted from pit wall mapping.

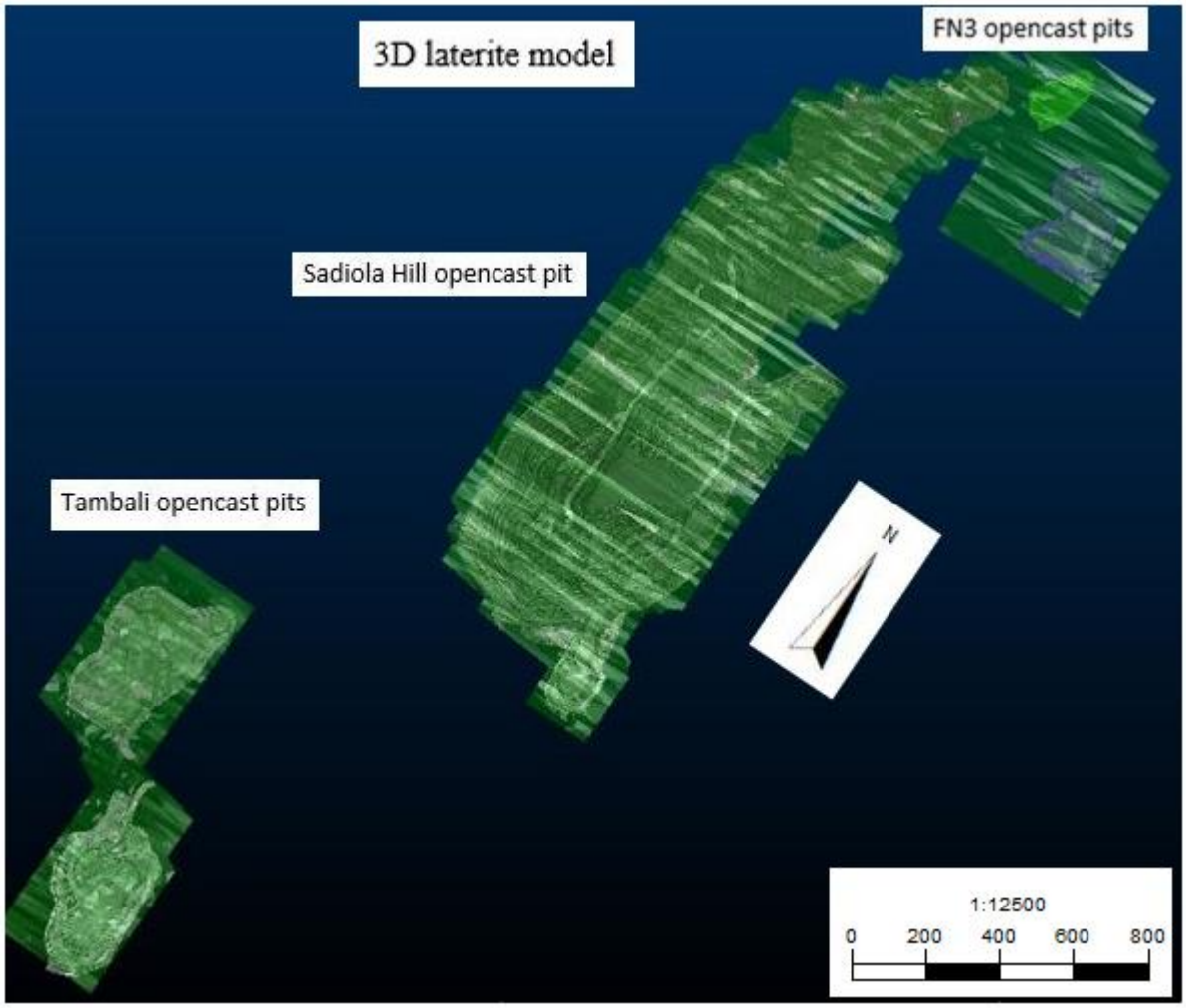

Figure 46: The 3D laterite model for Sadiola goldfield (FN3 in the northern, Sadiola Hill open cast in the middle, and the Tambali pits in the southern part).

The Sadiola goldfield 3D oxide saprolite model is presented in Figure 47. The oxide saprolite is situated between the ferricrete and oxide transitional zone. According to the pit mapping data, the oxide saprolite is significantly present in the calc-silicate than siltstone-shale-greywacke due to its chemical composition.

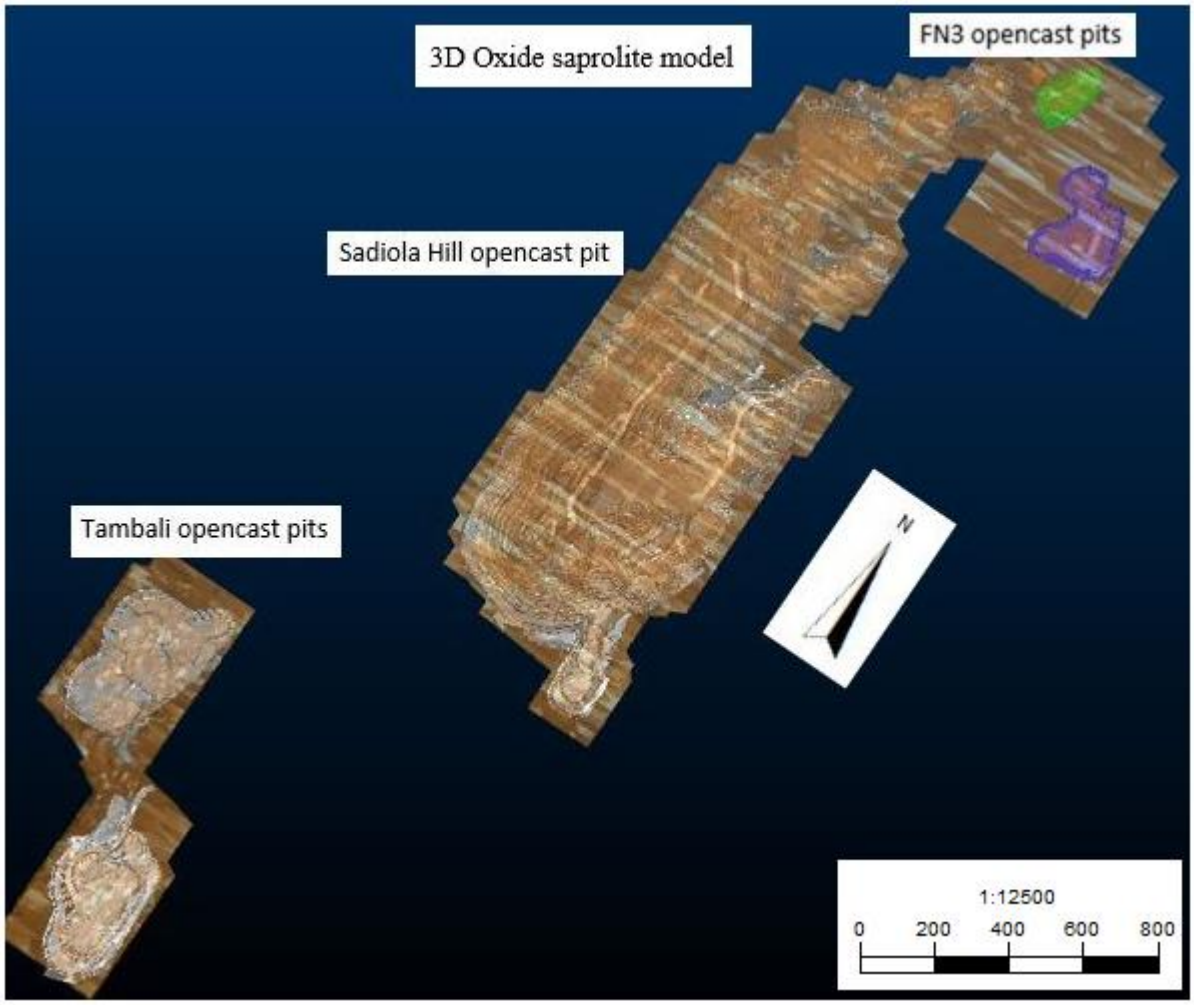

Figure 47: The 3D oxide saprolite model for Sadiola goldfield (FN3 in the northern, Sadiola Hill open cast in the middle, and the Tambali pits in the southern).

The Sadiola goldfield 3D oxide transitional model is presented in Figure 48. The oxide transitional profile is situated between the oxide saprolite profile and hard rock. The pit mapping data, and the oxide saprolite profile is more important than the oxide transitional profile.

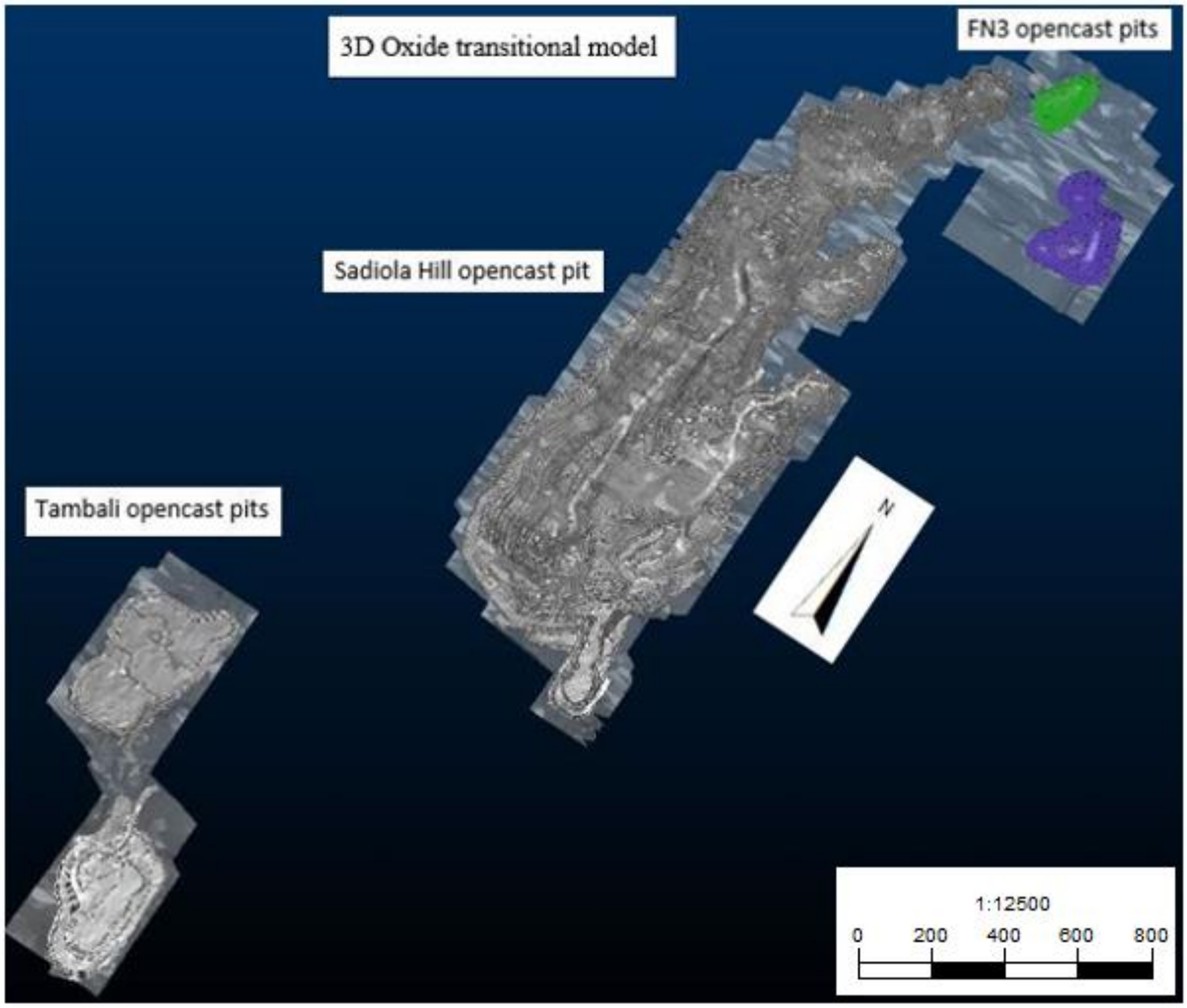

Figure 48: The 3D oxide transitional zone for Sadiola goldfield (FN3 in the northern, Sadiola Hill open cast in the middle, and the Tambali pits in the southern part).

3D modelling of the oxide saprolite and transitional zone indicates that the oxide saprolite zone is significantly more important than oxide transitional zone in terms of volume, and gold quantity.

The hard rock has been modelled in 3D (Figure 49). The hard rock profile is situated below the oxide transitional profile. The hard rock is mainly composed of calc-silicate and siltstone-shale-greywacke. The hard rock is exposed in the Sadiola Hill opencast pit (Figure 50). Hein et al. (2015) established that the Birimian supracrustal rocks are comprised of metamorphosed calcitic and dolomite marbles, which were intruded by a diorite (2106 ± 10 Ma, ^{207} Pb/^{206} Pb, zircon), and sandstone-siltstone shale sequences (youngest detrital zircon population dated at 2139 ± 6 Ma). This implies that the hard rock calc-silicate and siltstone-shale-greywacke in the Sadiola goldfield are of Birimian age.

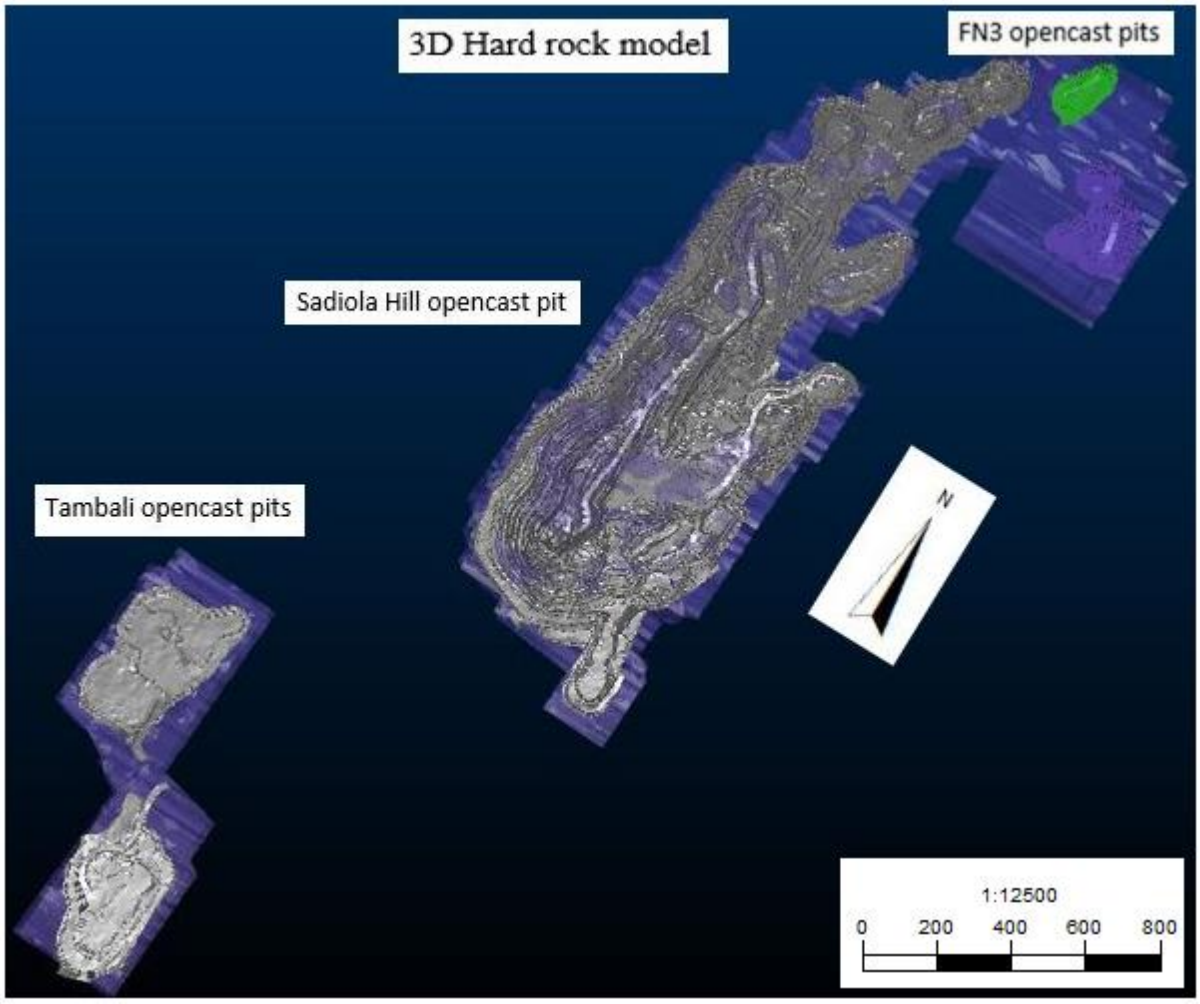

Figure 49: The 3D hard rock model for Sadiola goldfield (FN3 in the northern, Sadiola Hill open cast in the middle, and the Tambali pits in the south).

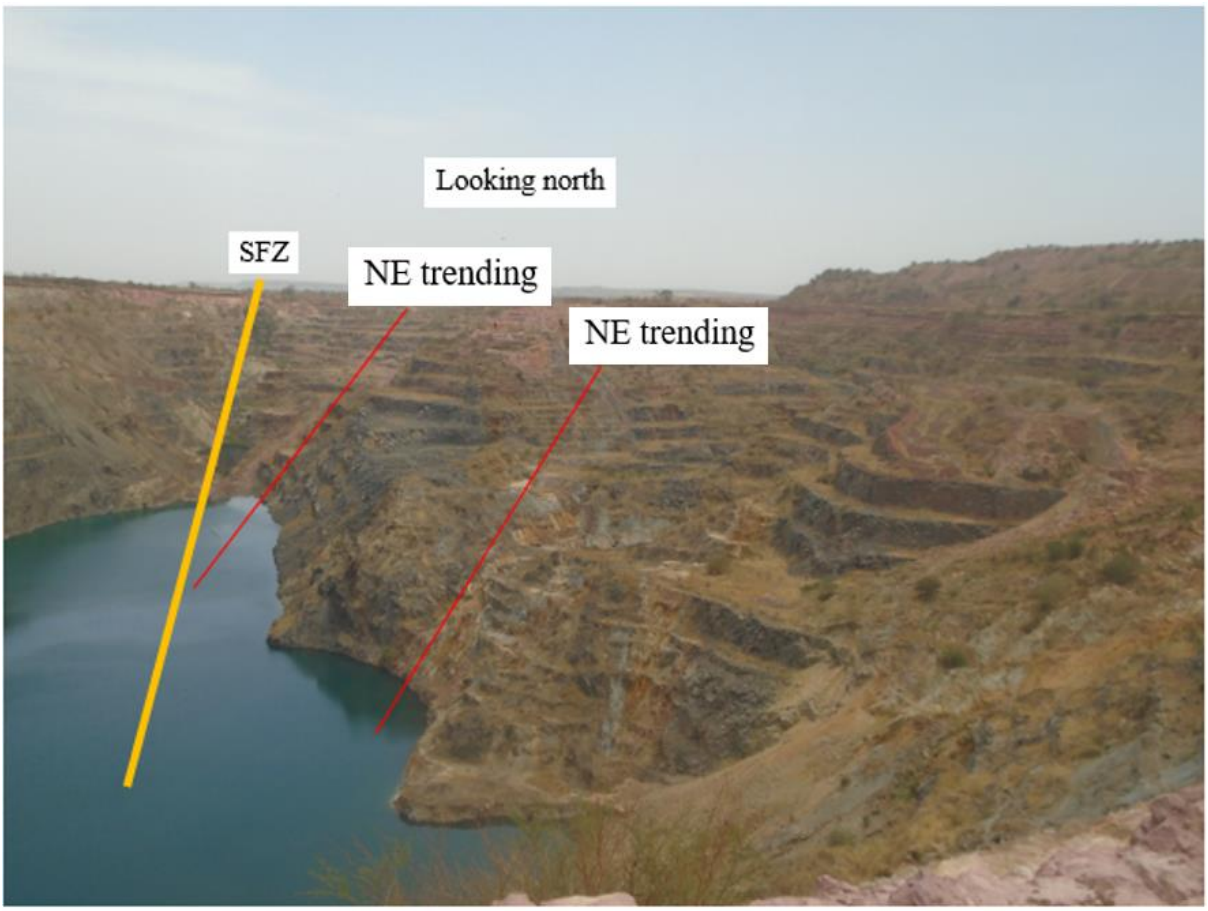

Figure 50: The supergene alteration presents in the calc-silicate rock from the southern area to north of the Sadiola Hill opencast pit.

The 3D oxide and hard rock modelling have defined three types of gold mineralisation according to the age of the host rock. The gold type 1 is found in the ferricrete of Eocene-Miocene age, the type 2 gold, in the oxide profile (oxide saprolite and transitional zone) age unknown and the type 3 gold in the hard rock, of Birimian age.

The structures include, the SFZ oriented north-south and the northeast trending fault secondary structures that splay from the SFZ. The structures allowed the circulation of meteoric and hydrothermal fluids, which caused the oxidation of the hard rock.

4.2.4. Summary

The lithological 3D model for Sadiola goldfield shows that the calc-silicate unit is significantly dominant in the goldfield followed by siltstone-shale-greywacke. Diorite and quartz-feldspar porphyry form several discontinuous pieces with a general orientation of north-south to the northeast. Three-oxide development profiles were identified. The main structures present include, the SFZ and

the northeast trending faults (Figure 50). The 3D modelling conducted in the Sadiola goldfield has allowed an examination of the relationship between the oxidation profile to the structures as SFZ and northeast trending faults. As relationship, the structures facilitated the circulation of the meteoric and hydrothermal fluids. The ferricrete hosts the coarse pisolitic gravel and quartz. The presence of the quartz in the ferricrete is an indicator of transport. To study, the oxide profile character, geochemistry and alteration signatures, sampling was conducted along these structures. The geochemistry and alteration signatures are presented in Section 4.3.

4.3. Geochemical analysis Results

4.3.1. Introduction

Geochemical data are used to study, describe and establish the alteration signature of the Sadiola oxide profiles. To achieve these objectives samples were collected during mapping and analysed for gold and by XRF and XRD. To understand the composition of the oxide facies and to establish a relationship between gold mineralisation and elemental distribution, sixty-three samples were analysed at SEMOS SA exploration office, using a portable model X-5000 XRF machine, while thirty-three samples were sent for analysis at the University of Witwatersrand, however, only thirty samples were analysed.

Additionally, minerals were separated. The separated minerals were observed under a microscope to confirm the XRD result. Geochemical data are used to determine the relationship of the gold mineralisation and the minerals, oxide profiles and alteration signature. Three-oxide zones have been recognized (Figure 51); Type 1: decarbonated calc-silicate alteration; Type 2: Fe alteration (oxide-jarosite-siderite); Type 3: potassic clay alteration was separately sampled.

Sixty-three samples were collected in the oxide zone of the various deposits to develop a fuller understanding of the geology and geochemistry, as well as gold deportment and distribution.

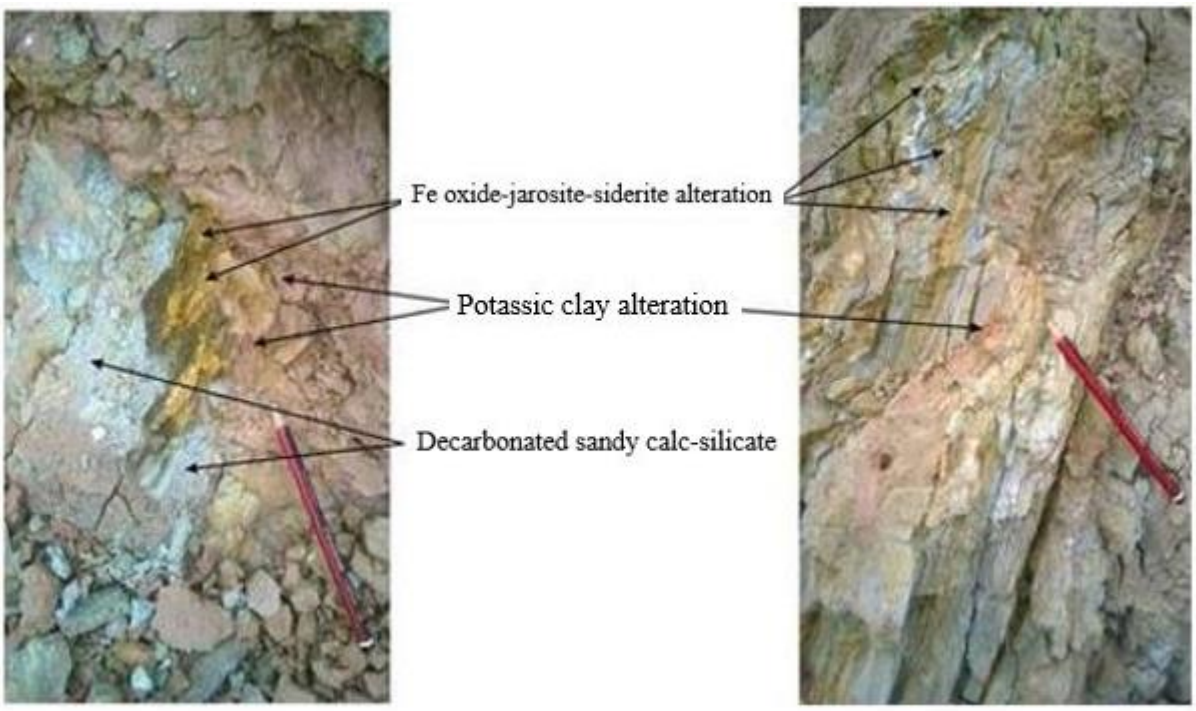

Figure 51: The three-oxide facies developed in the Sadiola Hill opencast pit. The blue colour is decarbonated calc-silicate rocks, crosscut by the red Fe-oxide alteration zones, which are in turn crosscut by zones of pink colour potassic clay alteration.

4.3.2. Gold Assays

The sixty-three oxide samples were assayed for gold at the SEMOS laboratory using the fire assay method and 30 g of sample material. The fire assay method is an analytical method of choice for gold evaluation. The method is composed of four steps as (1) fusion, (2) cupellation, (3) parting and (4) weighing the gold. The object of the fire assay fusion is to concentrate the precious metals in a button of lead, while the whole of the remainder of the ore forms a fusible slag with suitable fluxes lead sinks (Keith, 2004). The most significant gold results were found in type 2: Fe alteration (oxide-jarosite-siderite); and type 3: potassic clay alteration of the three-oxide development. The gold results are presented in Table 3 and range from 0.01 to 14.65 g/t Au. The cut-off gold grade for exploration is 0.4 g/t Au, while the mine cut-off gold grade is 0.6 g/t Au, but cut-off gold grade varies from one pit to another.

For each sample, a photo has been taken and illustrated from Figure 7 to 16.

Table 3: Gold results in grams per tonne

Sample ID	X Easting	Y Northing	Au	Comment
DTMS-012	210074	1539445	0.46	Sample
DTMS-013	210078	1539451	0.48	Sample
DTMS-014	210079	1539452	0.49	Sample
DTMS-015	210084	1539456	14.65	Sample
DTMS-016	210110	1539466	1.02	Sample
DTMS-017	210110	1539464	0.85	Sample
DTMS-018	210125	1539471	2.15	Sample
DTMS-019	210125	1539471	1.75	Sample
DTMS-020			0.93	Standard
DTMS-021	210125	1539471	0.39	Sample
DTMS-022	210148	1539470	0.11	Sample
DTMS-023	210148	1539470	0.17	Sample
DTMS-024	210146	1539471	0.17	Sample
DTMS-025	210207	1539447	0.67	Sample
DTMS-026	210208	1539457	0.73	Sample
DTMS-027	210208	1539457	0.87	Sample
DTMS-028	210207	1539451	0.86	Sample
DTMS-029	210207	1539449	3.09	Sample
DTMS-030	210207	1539446	2.56	Sample
DTMS-031	210207	1539446	2.43	Field duplicate
DTMS-032	210206	1539440	0.08	Sample
DTMS-033	210186	1539431	0.69	Sample
DTMS-034	210156	1539377	1.64	Sample
DTMS-035			0.01	Blank
DTMS-036	210156	1539377	1.03	Sample
DTMS-037	210156	1539377	1.31	Sample
DTMS-038	210152	1539403	0.89	Sample
DTMS-039	210152	1539403	2.2	Sample
DTMS-040			0.94	Standard
DTMS-041	210152	1539403	0.58	Sample
DTMS-045			0.01	Blank
DTMS-046	210711	1539267	0.12	Sample
DTMS-047	210711	1539267	0.23	Sample
DTMS-048	210711	1539267	1.03	Sample
DTMS-049	210476	1539694	0.02	Sample
DTMS-050	210482	1539681	0.61	Sample
DTMS-051	210482	1539681	0.46	Field duplicate
DTMS-052	210482	1539681	0.11	Sample
DTMS-053	210482	1539681	0.26	Sample
DTMS-054	210497	1539686	0.08	Sample
DTMS-055	210497	1539686	0.02	Sample
DTMS-056	210497	1539686	0.36	Sample
DTMS-057	210527	1539717	0.02	Sample
DTMS-058	210550	1539742	0.09	Sample

DTMS-059	210550	1539742	0.11	Sample
DTMS-060			0.9	Standard
DTMS-061	210550	1539742	0.15	Sample
DTMS-062	210607	1539807	0.82	Sample
DTMS-063	210613	1539812	0.04	Sample
DTMS-064	210630	1539823	0.02	Sample
DTMS-065			0.01	Blank
DTMS-066	210603	1539799	0.15	Sample
DTMS-067	210545	1539778	0.02	Sample
DTMS-068	210545	1539778	0.02	Sample
DTMS-069	210532	1539861	0.01	Sample
DTMS-070	210450	1539687	0.01	Sample
DTMS-071	210450	1539687	0.01	Field duplicate
DTMS-072	210450	1539687	0.02	Sample
DTMS-073	210447	1539699	0.02	Sample
DTMS-074	210458	1538509	0.4	Sample
DTMS-075	210523	1538567	0.02	Sample
DTMS-076	210523	1538567	0.03	Sample
DTMS-077	210542	1538417	1.05	Sample
DTMS-078	210519	1538447	0.08	Sample
DTMS-079	210519	1538447	0.04	Sample
DTMS-080			0.89	Standard
DTMS-081	210519	1538447	0.09	Sample
DTMS-082	210359	1538366	1.62	Sample
DTMS-083	210426	1538089	0.06	Sample

4.3.3. XRF results

The collected samples were analysed in two stages by XRF. The first has been conducted with a portable handheld XRF model X-500 at SEMOS Sadiola gold mine (Table 4 and Table 5). “Soil” and “mining plus” were the modes of analysis present in this handheld XRF. The soil mode is used to analyse the termite mound samples and soil samples, while the mining plus mode is used to analyse the RC, and diamond drill samples (Figure 52). The second analysis has been conducted at the University of the Witwatersrand, Johannesburg using Axios Max from Panalytical (Table 6) and illustrated in Figure 53. Major elements were analysed using the fused method with a Li-tetraborate flux, using the data reduction software SuperQ. In the result, dl (detection limits) can be taken as 0. The two stages of XRF analysis were to establish quality assurance/quality control. The results of XRF analysed at SEMOS are presented as elements, while those of the University of the Witwatersrand XRF are presented as oxides. The procedure for XRF analysis at the University of the Witwatersrand is presented in Appendix A.

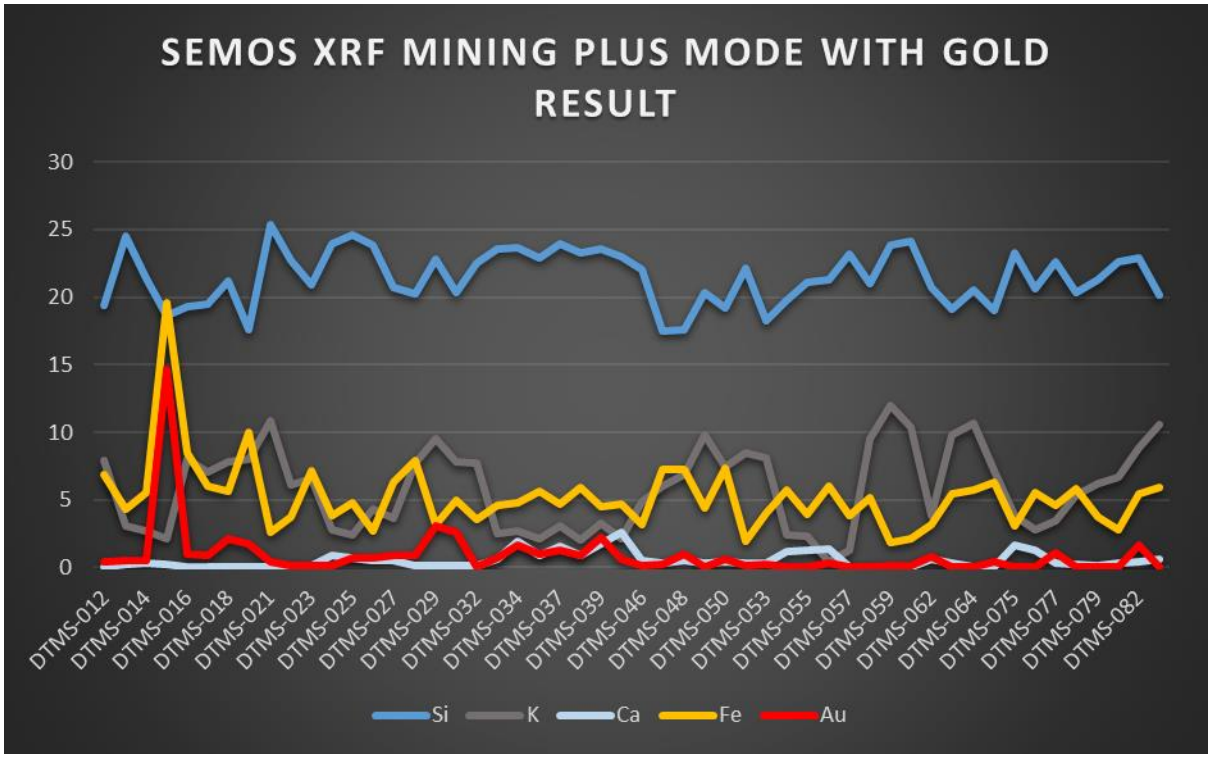

Figure 52: Diagram of SEMOS XRF "Mining Plus" showing silica (Si), potassium (K), calcium (Ca), and the iron (Fe) with gold result. There is a strong correlation, between gold and iron alteration and a second correlation with Au and potassium K, while no correlation with calcium (Ca) was examined due to the absence or weakness of Ca due to the oxidation.

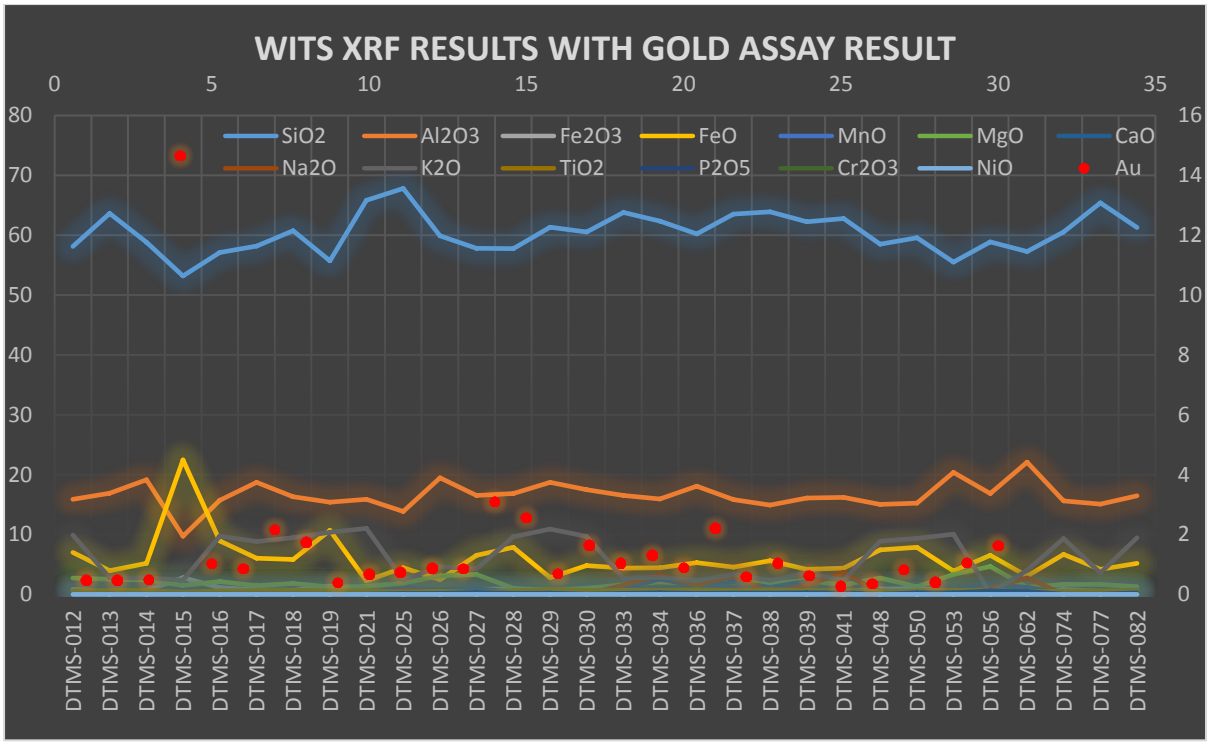

Figure 53: Diagram of the XRF result analysed in the Earth laboratory of the University of the Witwatersrand, Johannesburg. On the chart, concentrations in ppm are shown on the vertical axis, while the samples are given along the horizontal axis.

The results of the XRF analysis from SEMOS Lab are presented in Table 4 for soil mode with measurements in ppm and Table 5 for mining plus mode in % wt.

Table 4: SEMOS portable handheld XRF results in Soil Mode.

Sample ID	Mode	P	K	Ca	Ti	Cr	Mn	Fe	Ni	Unit
DTMS-012	Soil	-9711	97782	2524	3722	298	2273	67736	20	PPM
DTMS-013	Soil	-7849	25858	3709	4242	136	373	33283	-22	PPM
DTMS-014	Soil	-10058	25946	4465	4265	135	152	46612	-2	PPM
DTMS-015	Soil	-14229	29795	6425	1030	22	1577	339027	-243	PPM
DTMS-016	Soil	-5250	99243	1690	3681	103	1598	92326	7	PPM
DTMS-017	Soil	-9478	81830	1980	4061	95	231	53527	4	PPM
DTMS-018	Soil	-6213	90088	2036	4046	149	175	52159	20	PPM
DTMS-019	Soil	-10145	105214	1714	3164	77	543	118350	-10	PPM
DTMS-021	Soil	-7591	99607	965	3688	142	56	17602	1	PPM
DTMS-022	Soil	-7762	57457	1906	3337	106	1626	28588	16	PPM
DTMS-023	Soil	-12367	76838	2868	3437	124	3410	69905	7	PPM
DTMS-024	Soil	-15735	27172	9319	3818	93	641	33013	-7	PPM
DTMS-025	Soil	-8226	21809	7602	2533	86	214	40175	-14	PPM
DTMS-026	Soil	-8627	37217	5330	3261	37	375	19488	-28	PPM
DTMS-027	Soil	-9756	40379	7105	2733	70	590	60452	-59	PPM
DTMS-028	Soil	-6370	90626	3116	3343	97	201	79026	6	PPM
DTMS-029	Soil	-7917	90865	2943	4514	138	317	23252	10	PPM

DTMS-030	Soil	-7913	89047	2707	4172	101	3606	44645	-3	PPM
DTMS-031	Soil	-7480	83657	2741	4350	116	3570	47619	24	PPM
DTMS-032	Soil	-6590	80396	2728	4713	125	4300	29594	34	PPM
DTMS-033	Soil	-10425	23616	6669	4136	95	946	40160	4	PPM
DTMS-034	Soil	-23460	25468	18762	3806	113	189	40683	-25	PPM
DTMS-035	Soil	-886	4909	-195	251	139	31	2980	-7	PPM
DTMS-036	Soil	-17037	20145	9996	4625	91	333	49880	-12	PPM
DTMS-037	Soil	-17878	29786	14663	3758	393	242	41524	-13	PPM
DTMS-038	Soil	-9181	20740	9179	4635	106	520	53070	-2	PPM
DTMS-039	Soil	-22156	30645	16206	3956	119	304	36556	-14	PPM
DTMS-041	Soil	-25412	21064	24841	3677	139	199	41141	-10	PPM
DTMS-046	Soil	-9924	44352	4290	3690	201	435	25394	50	PPM
DTMS-047	Soil	-9468	80264	3612	2970	134	921	78414	56	PPM
DTMS-048	Soil	-7357	88246	4621	3165	135	534	76458	6	PPM
DTMS-049	Soil	-8562	110707	3191	3690	147	1605	37386	35	PPM
DTMS-050	Soil	-5407	90793	4487	3659	158	2952	74359	107	PPM
DTMS-051	Soil	-8077	92495	4320	3622	154	3181	90720	110	PPM
DTMS-052	Soil	-8489	76032	3991	1982	68	148	12758	47	PPM
DTMS-053	Soil	-11734	90564	3731	5011	97	481	33224	36	PPM

DTMS-054	Soil	-14135	28124	13442	3471	99	254	59054	69	PPM
DTMS-055	Soil	-16728	21558	11617	3657	197	505	32227	-1	PPM
DTMS-056	Soil	-13418	4824	16716	3809	388	1087	63138	-51	PPM
DTMS-057	Soil	-4164	10321	800	5134	186	101	30848	-8	PPM
DTMS-058	Soil	-5302	110823	786	3973	152	439	42748	58	PPM
DTMS-059	Soil	-6441	114669	475	4375	180	220	12349	67	PPM
DTMS-061	Soil	-5920	99943	952	3973	180	99	15667	45	PPM
DTMS-062	Soil	-10511	34860	6298	2128	59	89	24098	10	PPM
DTMS-063	Soil	-13583	121497	4917	4419	168	2600	49643	32	PPM
DTMS-064	Soil	-6802	122890	1245	4328	185	1006	50077	53	PPM
DTMS-065	Soil	-775	3926	-78	218	234	32	2950	-11	PPM
DTMS-066	Soil	-12406	65768	7446	1680	57	88	25674	28	PPM
DTMS-067	Soil	-17545	30467	13734	4188	209	546	46615	4	PPM
DTMS-068	Soil	-13987	60287	8456	5678	177	208	34230	68	PPM
DTMS-069	Soil	-1304	7469	626	2917	150	258	17738	23	PPM
DTMS-070	Soil	-9359	37390	5420	4383	168	352	26698	17	PPM
DTMS-071	Soil	-8681	38685	5119	4323	152	403	25375	20	PPM
DTMS-072	Soil	-12296	97706	3371	3408	132	2251	61950	15	PPM
DTMS-073	Soil	-8028	68825	3289	3315	120	740	20907	25	PPM

DTMS-074	Soil	-8123	84875	2168	3195	97	186	62671	71	PPM
DTMS-075	Soil	-15794	34266	14653	4769	181	138	23262	38	PPM
DTMS-076	Soil	-18932	29897	14475	4258	126	690	54662	7	PPM
DTMS-077	Soil	-6848	31606	4000	3556	197	90	37963	31	PPM
DTMS-078	Soil	-9349	57592	2929	3869	156	79	53686	53	PPM
DTMS-079	Soil	-8186	62339	2332	4034	177	82	29667	5	PPM
DTMS-081	Soil	-8873	62402	3402	3854	139	50	20047	1	PPM
DTMS-082	Soil	-5946	92986	4599	3799	250	150	47641	-15	PPM
DTMS-083	Soil	-8040	128451	6653	4086	134	1273	57272	22	PPM

Table 5: SEMOS portable handheld XRF analysis in Mining Plus Mode.

Sample ID	Mode	Mg	Al	Si	P	K	Ca	Ti	Cr	Mn	Fe	Ni	Unit
DTMS-012	Mining Plus	0	4.89	19.4	0	7.91	0.0797	0.309	0.0095	0.2787	6.91	0.0045	%
DTMS-013	Mining Plus	0	8.57	24.46	0	3.083	0.2788	0.3117	0	0.0375	4.3265	0	%
DTMS-014	Mining Plus	0	8.6	21.37	0	2.7458	0.335	0.3182	0	0	5.5119	0.002	%
DTMS-015	Mining Plus	0	4.19	18.62	0	2.0917	0.2726	0.1561	0	0.1661	19.54	0	%
DTMS-016	Mining Plus	0	3.07	19.28	0	8.04	0	0.3043	0	0.1985	8.48	0.0034	%
DTMS-017	Mining Plus	0	7.76	19.5	0	7.0308	0	0.3088	0	0.0253	6.0059	0	%
DTMS-018	Mining Plus	0	5.38	21.19	0	7.81	0	0.3113	0	0	5.6477	0	%
DTMS-019	Mining Plus	0	3.1	17.55	0	7.97	0	0.2657	0	0.0572	9.99	0.0039	%
DTMS-021	Mining Plus	0	5.36	25.35	0	10.84	0	0.3432	0	0	2.6015	0	%
DTMS-022	Mining Plus	0	8.51	22.71	0	6.1012	0	0.338	0	0.2407	3.7213	0.0016	%
DTMS-023	Mining Plus	0	5.19	20.94	0	6.6245	0.1273	0.2705	0	0.4147	7.13	0.0019	%
DTMS-024	Mining Plus	0	7.25	23.9	0	2.8266	0.8858	0.2609	0	0.0751	3.8398	0	%
DTMS-025	Mining Plus	0	6.22	24.57	0	2.3788	0.7137	0.1997	0	0.0231	4.7482	0	%
DTMS-026	Mining Plus	0	9.05	23.87	0	4.3167	0.5151	0.2832	0	0.0405	2.6991	0	%
DTMS-027	Mining Plus	0	6.52	20.67	0.0616	3.6494	0.5632	0.2206	0	0.0626	6.2609	0	%
DTMS-028	Mining Plus	0	6.49	20.27	0	7.77	0.1258	0.2926	0	0.0264	7.9	0.0026	%
DTMS-029	Mining Plus	0	7.78	22.82	0	9.49	0.1772	0.4465	0	0.0601	3.1857	0	%
DTMS-030	Mining Plus	0	6.58	20.3	0	7.79	0.1157	0.3785	0	0.4572	4.9756	0.0019	%
DTMS-031	Mining Plus	0	6.69	20.32	0	7.1789	0.1328	0.3692	0	0.4684	5.188	0.0018	%
DTMS-032	Mining Plus	0	6.91	22.48	0	7.77	0.1674	0.4356	0.0061	0.6068	3.5313	0.0036	%
DTMS-033	Mining Plus	0	7.5	23.54	0	2.481	0.5864	0.3524	0	0.1163	4.6232	0	%
DTMS-034	Mining Plus	0	5.92	23.67	0	2.699	1.9276	0.3291	0	0.0301	4.8035	0.0017	%
DTMS-035	Mining Plus	0	0	39.23	0	0.9067	0	0	0	0	0.5327	0	%
DTMS-036	Mining Plus	0	7.9	22.89	0	2.1169	0.9061	0.3596	0.0046	0.0298	5.6394	0	%
DTMS-037	Mining Plus	0	4.9	23.89	0	3.0767	1.5567	0.291	0.0087	0.0293	4.6512	0.0018	%
DTMS-038	Mining Plus	0	6.45	23.31	0	2.0811	0.8571	0.3323	0	0.0563	5.8845	0	%
DTMS-039	Mining Plus	0	6.46	23.54	0	3.3027	1.7215	0.3655	0	0.0325	4.5241	0.0022	%
DTMS-041	Mining Plus	0	4.93	22.97	0.0972	2.1341	2.5623	0.3143	0.0048	0.0194	4.6461	0.002	%

DTMS-046	Mining Plus	0	6.25	22.07	0	4.8891	0.5092	0.2912	0.0057	0.0502	3.1392	0.0017	%
DTMS-047	Mining Plus	0	3.94	17.47	0	6.0453	0.3363	0.2499	0.0053	0.094	7.25	0.0042	%
DTMS-048	Mining Plus	0	4.11	17.56	0	6.87	0.4777	0.2688	0.0062	0.0481	7.24	0.0034	%
DTMS-049	Mining Plus	0	5.83	20.32	0.0883	9.84	0.3423	0.358	0.0086	0.2084	4.3928	0.0027	%
DTMS-050	Mining Plus	0	4.31	19.24	0.1131	7.42	0.4156	0.3323	0.0093	0.3649	7.36	0.0062	%
DTMS-051	Mining Plus	0	4.28	18.47	0.0931	7.21	0.2912	0.3494	0.0067	0.3694	8.26	0.0057	%
DTMS-052	Mining Plus	0	10.19	22.11	0.0693	8.46	0.326	0.166	0	0	1.9304	0	%
DTMS-053	Mining Plus	0	7.47	18.23	0.069	8.12	0.3178	0.4216	0.0053	0.0584	3.9841	0.002	%
DTMS-054	Mining Plus	0	3.18	19.73	0.123	2.4273	1.1688	0.3068	0.0052	0.0231	5.7015	0.005	%
DTMS-055	Mining Plus	0	5.3	21.13	0	2.3642	1.2436	0.2644	0	0.0682	3.9177	0	%
DTMS-056	Mining Plus	0	3.89	21.26	0.3851	0.4588	1.4129	0.2551	0.0128	0.1224	6.0044	0	%
DTMS-057	Mining Plus	0	10.89	23.2	0	1.2912	0	0.3888	0	0.0167	3.8069	0	%
DTMS-058	Mining Plus	0	4.7	20.98	0	9.57	0	0.3744	0.0056	0.059	5.1858	0.0035	%
DTMS-059	Mining Plus	0	5.79	23.87	0	11.97	0	0.4434	0.01	0.0358	1.8922	0.0033	%
DTMS-061	Mining Plus	0	6.67	24.11	0	10.41	0	0.3523	0.0072	0.0222	2.1012	0	%
DTMS-062	Mining Plus	0	8.5	20.72	0.0968	3.7984	0.6097	0.1366	0	0	3.1316	0	%
DTMS-063	Mining Plus	0	4.45	19.08	0.0996	9.83	0.3603	0.3938	0.005	0.3368	5.4337	0.003	%
DTMS-064	Mining Plus	0	6.41	20.53	0.0933	10.63	0	0.3841	0.0077	0.1464	5.7675	0.0032	%
DTMS-074	Mining Plus	0	5.02	19.03	0	7.14	0.0734	0.2422	0	0.0202	6.3327	0.0035	%
DTMS-075	Mining Plus	0	6.26	23.26	0.1176	3.8809	1.6898	0.4512	0.007	0.0255	3.0445	0.0038	%
DTMS-076	Mining Plus	0	4.26	20.64	0.1128	2.8031	1.3168	0.3531	0.0057	0.0828	5.5434	0.0029	%
DTMS-077	Mining Plus	0	5.91	22.61	0	3.4339	0.3493	0.3252	0	0	4.6001	0.0024	%
DTMS-078	Mining Plus	0	5.87	20.31	0	5.345	0.2043	0.2564	0	0	5.792	0.0027	%
DTMS-079	Mining Plus	0	6.03	21.24	0	6.1759	0.1417	0.3421	0	0	3.7135	0	%
DTMS-081	Mining Plus	0	6.48	22.59	0	6.6975	0.3114	0.2825	0	0	2.7558	0	%
DTMS-082	Mining Plus	0	5.47	22.94	0	8.82	0.4015	0.2971	0.0071	0.0148	5.4911	0	%
DTMS-083	Mining Plus	0	5.05	20.12	0	10.57	0.6024	0.3605	0	0.1767	5.9383	0.0034	%

Thirty pulp samples were analysed in the XRF laboratory of the University of the Witwatersrand. The results are shown in Table 6. The XRF analysis was done according to the major oxides, which are SiO_2, AlO3, FeO_3, FeO, MnO, MgO, Cao, Na_2O, K_2O, TiO_2, P_2O_5, Cr_2O_3, NiO, and LOl. The result shows a value of SiO_2 around 60%, followed by around 6% of FeO, Fe_2O_3 then 6% of K_2O.

Table 6: University of the Witwatersrand XRF analysis results.

SID	SiO2	Al2O3	Fe2O3	FeO	MnO	MgO	CaO	Na2O	K2O	TiO2	P2O5	Cr2O3	NiO	LOI
DTMS12	58.14	15.88	0.86	7.01	0.24	2.75	0.35	0.1	9.89	0.61	0.1	0.05	0.01	4.02
DTMS13	63.65	16.91	0.49	3.98	0.05	2.51	0.5	0.04	2.8	0.72	0.03	0.02	0.01	7.74
DTMS14	58.82	19.13	0.64	5.18	0.02	2.38	0.58	0.07	2.79	0.69	0.07	0.02	0.01	9.32
DTMS15	53.2	9.72	2.77	22.48	0.19	1.5	0.61	0.06	2.37	0.35	0.1	0.02	0.01	6.29
DTMS16	57.14	15.73	1.11	8.95	0.2	2.16	0.25	0.11	9.74	0.61	0.1	0.03	0.01	3.89
DTMS17	58.2	18.7	0.75	6.05	0.03	1.45	0.3	0.09	8.85	0.63	0.09	0.02	0.01	5.47
DTMS18	60.77	16.31	0.72	5.81	0.03	1.83	0.32	0.16	9.48	0.67	0.05	0.03	0.01	4.11
DTMS19	55.74	15.38	1.32	10.68	0.07	1.22	0.29	0.28	10.35	0.57	0.12	0.02	0.01	4.01
DTMS21	65.86	15.9	0.28	2.25	0.01	1.32	0.21	0.07	11.03	0.6	0.03	0.03	0	2.61
DTMS25	67.79	13.85	0.55	4.42	0.03	1.87	0.95	0.65	2.47	0.41	0.14	0.01	0	7.02
DTMS26	59.88	19.44	0.3	2.47	0.06	3.12	0.77	0.55	4.6	0.54	0.17	0.01	0	8.21
DTMS27	57.84	16.53	0.81	6.52	0.07	3.31	0.91	0.07	4.29	0.45	0.31	0.02	0	8.09
DTMS28	57.78	16.82	0.96	7.84	0.03	0.99	0.42	0.07	9.61	0.61	0.16	0.03	0.01	4.62
DTMS29	61.32	18.74	0.35	2.78	0.04	0.69	0.49	0.16	10.89	0.78	0.23	0.03	0.01	3.48
DTMS30	60.55	17.48	0.59	4.81	0.4	0.99	0.36	0.09	9.69	0.65	0.07	0.02	0.01	4.16
DTMS33	63.83	16.55	0.54	4.36	0.12	1.62	0.9	1.54	2.67	0.69	0.16	0.02	0.01	7.15
DTMS34	62.35	15.92	0.55	4.46	0.02	2.11	2.54	3.24	2.88	0.62	0.24	0.02	0.01	4.63
DTMS36	60.21	18.1	0.65	5.28	0.04	1.74	1.33	1.52	2.29	0.75	0.17	0.02	0.01	7.96
DTMS37	63.56	15.81	0.56	4.52	0.03	2.03	2.07	3.22	3.29	0.62	0.23	0.07	0	3.68
DTMS38	63.89	14.91	0.69	5.6	0.06	1.88	1.16	0.3	2.35	0.73	0.22	0.02	0.01	8.23
DTMS39	62.25	16.08	0.51	4.16	0.04	2.31	2.19	1.48	3.6	0.65	0.24	0.02	0.01	6.63
DTMS41	62.79	16.22	0.54	4.38	0.03	1.59	3.37	3.67	2.33	0.64	0.26	0.03	0.01	4
DTMS48	58.51	15.03	0.92	7.41	0.06	2.73	0.53	0.17	8.9	0.53	0.11	0.03	0.01	4.49
DTMS50	59.58	15.25	0.97	7.88	0.32	1.26	0.56	0.21	9.35	0.55	0.29	0.03	0.02	3.53
DTMS53	55.54	20.36	0.49	3.92	0.05	3.32	0.57	0.26	10.03	0.72	0.24	0.02	0.01	4.62
DTMS56	58.91	16.84	0.8	6.51	0.11	4.66	1.61	1.09	0.24	0.65	0.6	0.06	0.01	3.42
DTMS62	57.3	22.1	0.38	3.04	0.01	1.15	1.16	2.7	4.02	0.48	0.48	0.01	0.01	7.51
DTMS74	60.55	15.62	0.82	6.67	0.03	1.67	0.29	0.04	9.32	0.55	0.11	0.02	0.02	4.64
DTMS77	65.4	15.09	0.51	4.15	0.02	1.65	0.58	0.09	3.58	0.61	0.1	0.03	0.01	8.35
DTMS82	61.28	16.45	0.64	5.2	0.02	1.28	0.71	0.09	9.46	0.64	0.25	0.04	0.01	3.38
Average	**60.421**	**16.561667**	**0.73567**	**5.959**	**0.081**	**1.96967**	**0.896**	**0.73967**	**6.10533**	**0.61067**	**0.18233**	**0.02667**	**0.009**	**5.50867**

XRF results indicate a significant relationship between the gold mineralisation and potassium and iron alteration. All the samples are totally or partially decarbonated. The XRF analytical results for Ca, K, and Fe are higher ~ 1000 %wt. The result of the XRF analysis at the Earth laboratory of the University of the Witwatersrand, Johannesburg, has been used for the interpretation of the XRD result. The XRF and XRD analysis results have facilitated the determination of the geochemistry of the oxide.

Figure 52 shows a correlation, between gold and iron alteration and a second correlation with Au and potassium K, while no correlation with calcium (Ca) was examined due to the absence or weakness of Ca due to the oxidation. Masurel et al. (2017) and Cameron (2010) established the relationship between gold mineralisation and potassium (K) in the Sadiola goldfield.

4.3.4. XRD results

XRD analysis was completed to identify the different minerals present in the types of oxides. The different minerals identified in the field by rock description have been compared to the detected minerals in the XRD results. According to Skwarnecki (2017), the XRD data has two main limitations: (i) There is a lower detection limit (even for well-crystallised minerals), generally ~5% for wavelength-dispersive systems and perhaps (10%) for energy-dispersive systems. So XRD will not detect minerals present in small quantities (Jarosite); (ii) Minerals formed during weathering are generally poorly crystalline, which means they give poor XRD patterns, so that even minerals such as goethite and hematite may be difficult to detect unequivocally.

The different minerals detected in XRD analysis are: (1) Silica or quartz (SiO_2), (2) Goethite (Fe+ 3O.OH), (3) Muscovite ($KAl_3Si_3O_{10}$ $(OH)_2$), (4) Siderite ($FeCO_3$), (5) Biotite $KFeMg_2$ $(AlSi_3O_{10})(OH)_2$, (6) Bernalite (Fe $(OH)_3$), (7) Orthoclase ($KAlSi_3O_8$). Figure 54 to 83 presents the XRD analysis results.

The alunite and jarosite alteration indicate an acidic pH condition of the formation (Hein et al., 2008). The calc-silicate skarnification produced variable minerals as diopside, actinolite, chlorite, epidote, dravitic tourmaline (Sillitoe, 1994) scapolite, vesuvianite and fluorite (Boshoff et al., 1998). According to Theron (1997), the skarnification in the Sadiola region is related to flushing of metasomatic hydrothermal fluids during contact metamorphism and emplacement of a suite of diorite intrusions. The different minerals identified helped to elucidate the condition of the oxide formation. The presence of alunite (K_2Al_6 $(SO_4)_4(OH)_{12}$) and jarosite (K_2Fe_{63}+ $(SO_4)_4(OH)_{12}$) highlight a highly acidic environment and acidic supergene conditions (Hein et al., 2008).

The mineral bernalite has been identified in the sample DTMS-0015. The bernalite mineral can be found in the surface oxidation zone. The different minerals found are all indicators of a deep oxidation zone.

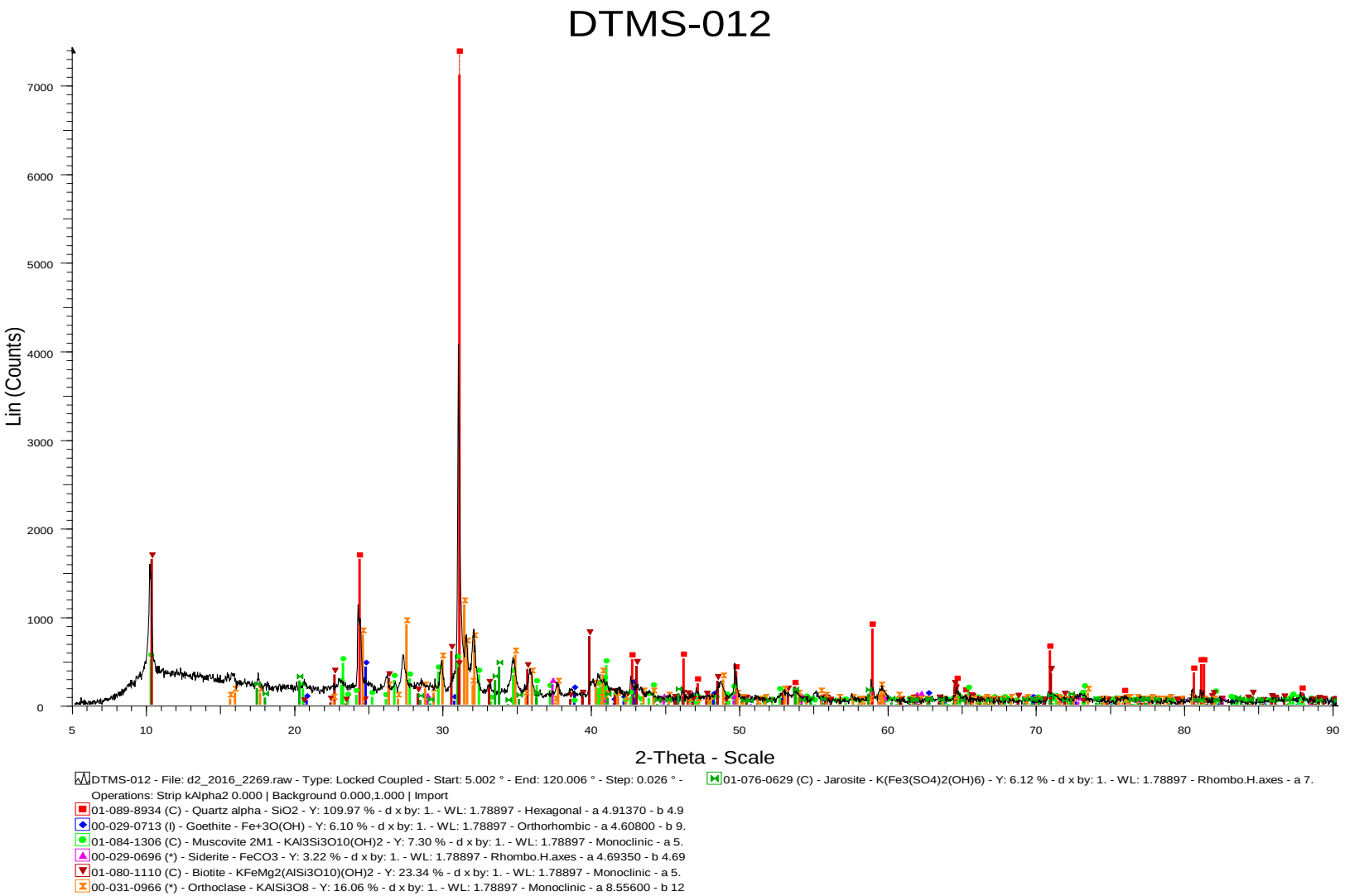

Figure 54: The result of sample DTMS-012 contains silica, goethite, muscovite, siderite and biotite minerals.

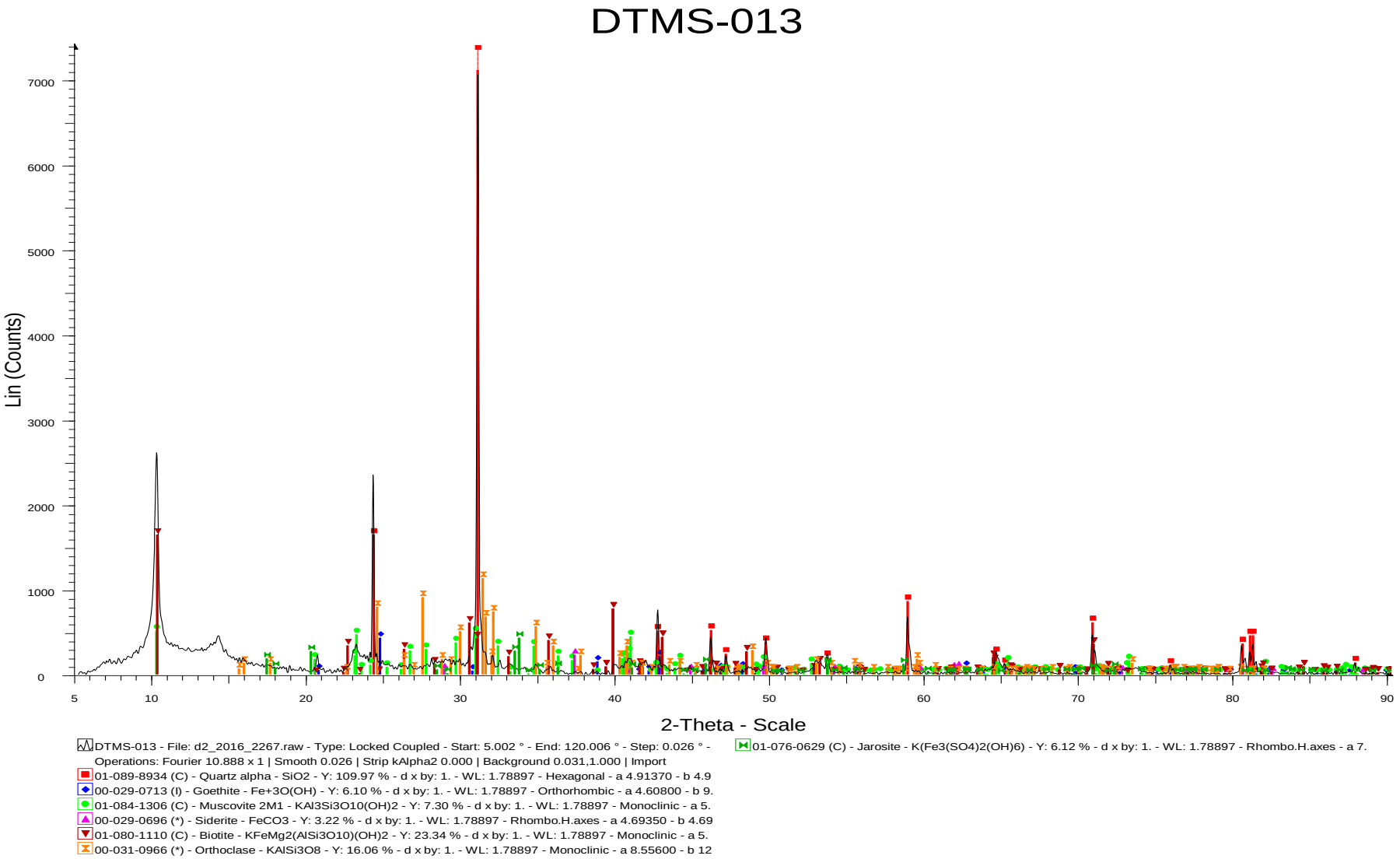

Figure 55: The result of sample DTMS-013 contains silica, goethite, muscovite, siderite and biotite minerals.

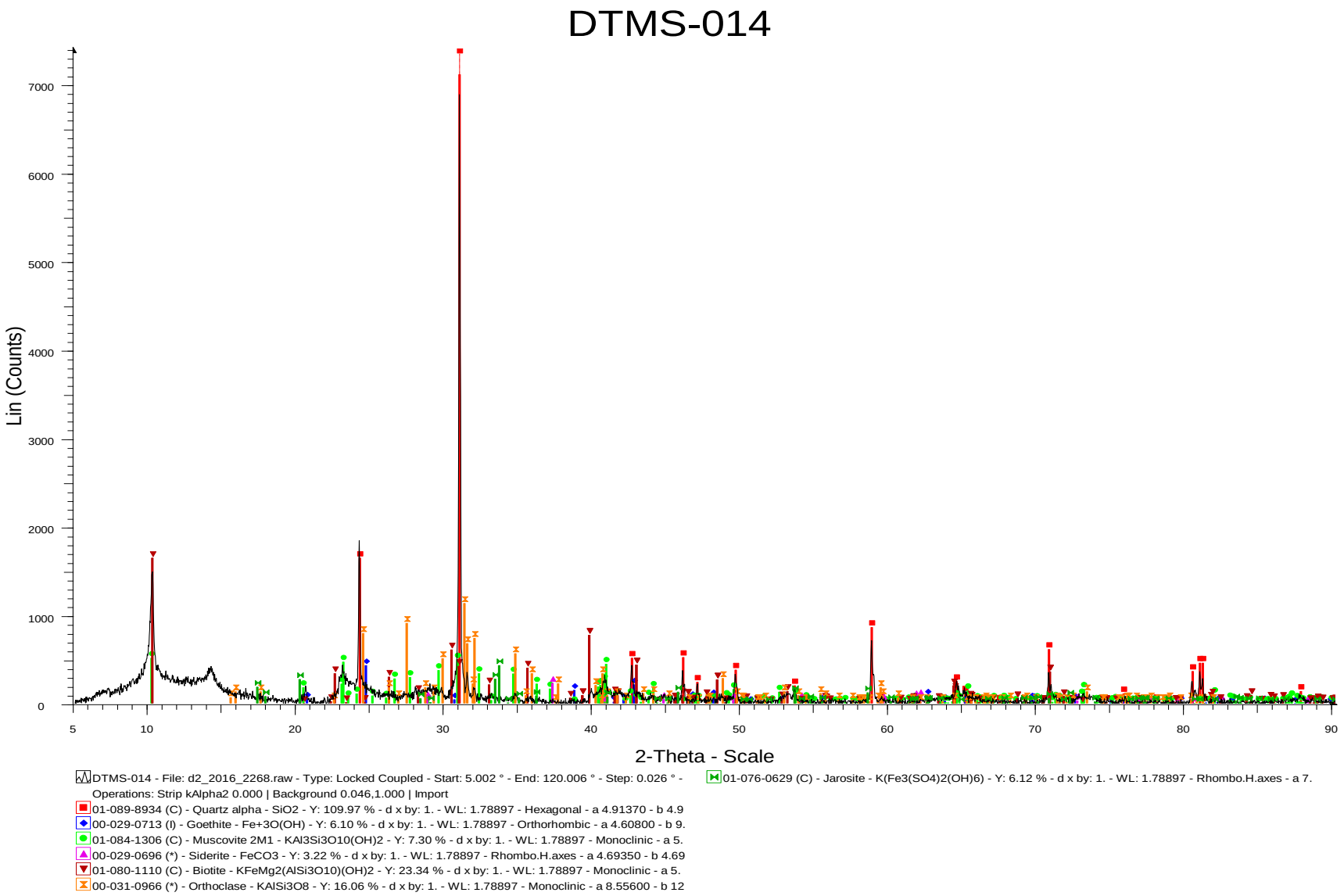

Figure 56: The result of sample DTMS-014 contains silica, goethite, muscovite, siderite and biotite minerals.

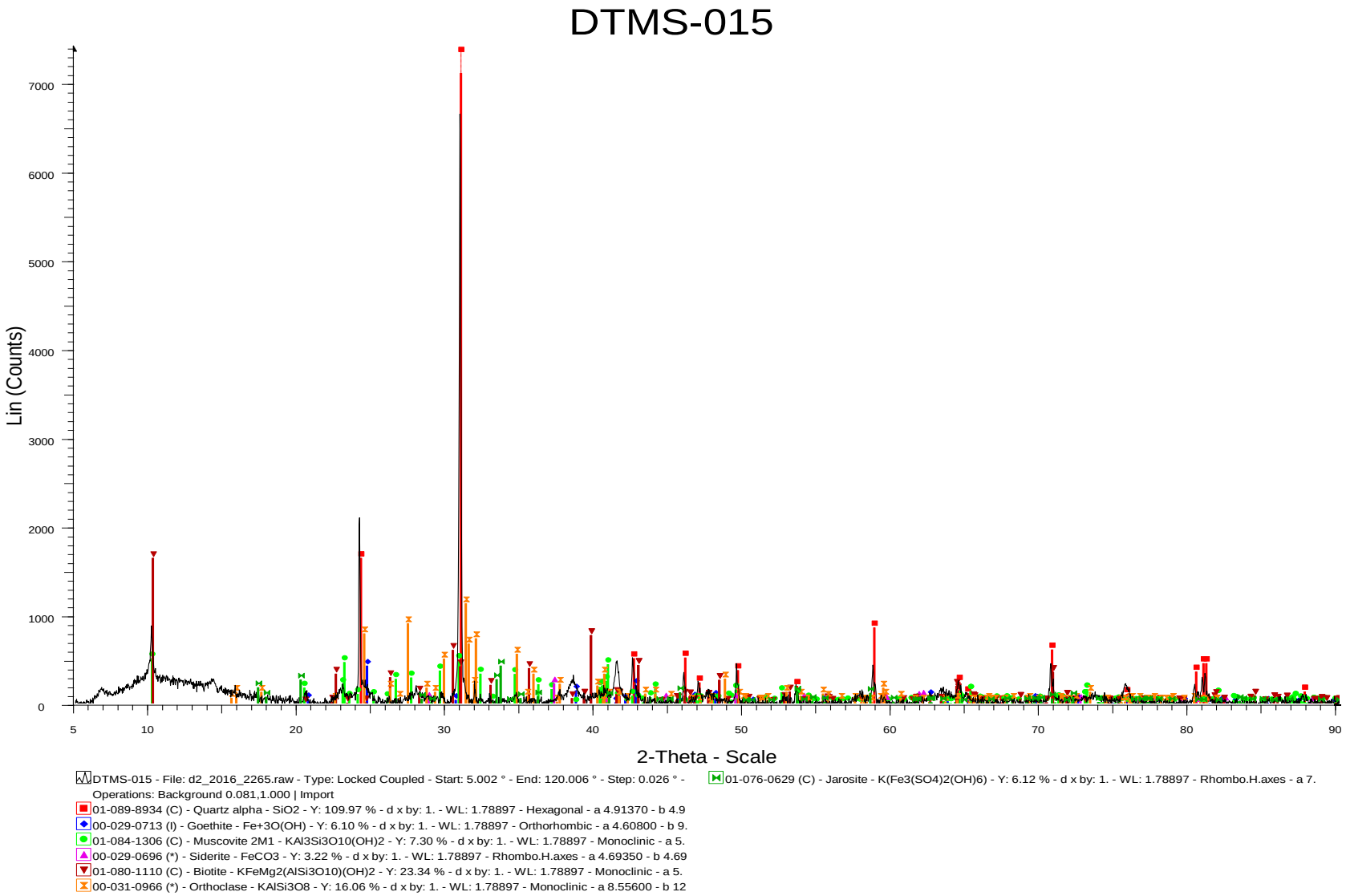

Figure 57: The result of sample DTMS-015 contains silica, goethite, muscovite, siderite, bernalite and biotite minerals.

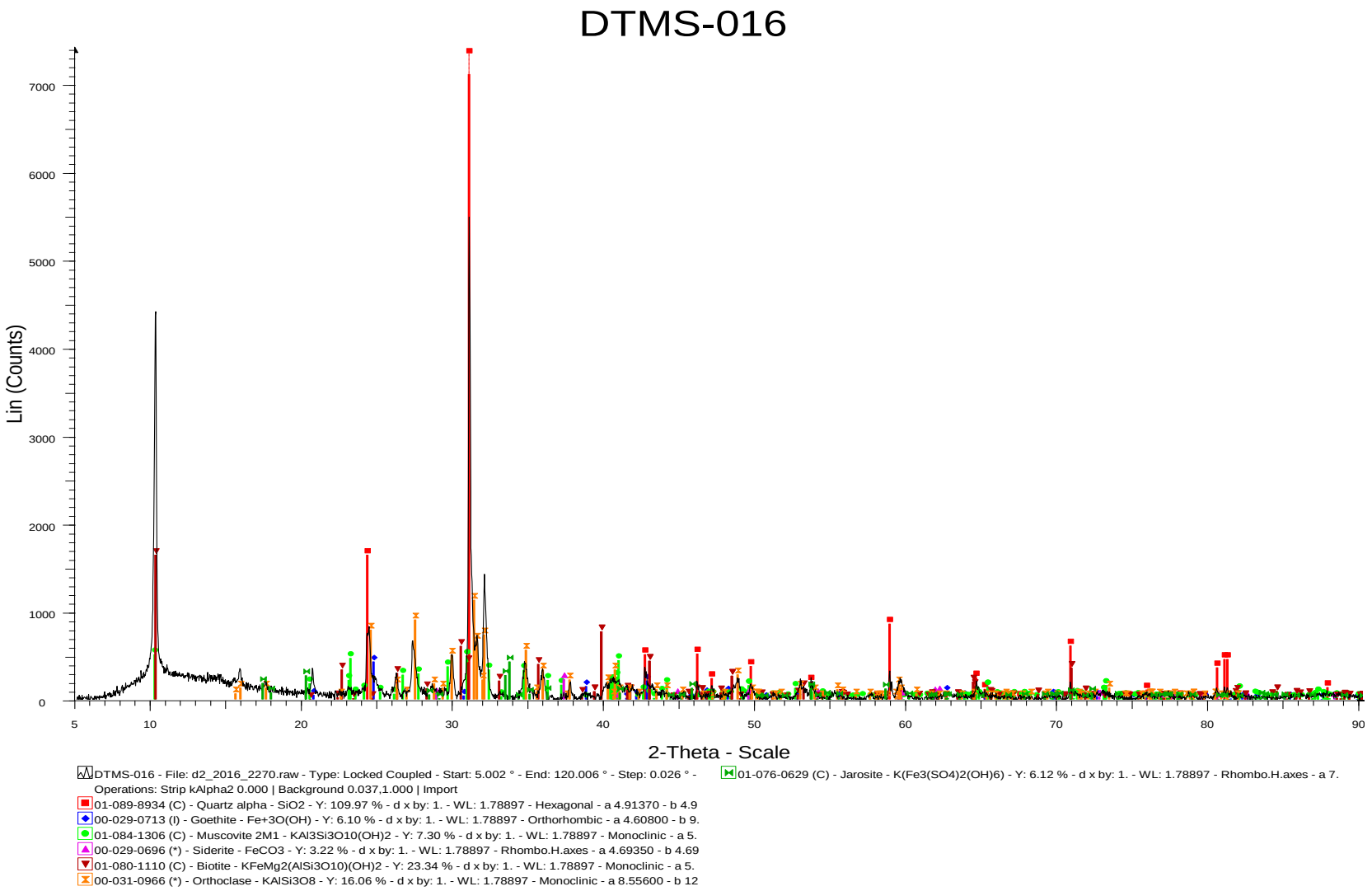

Figure 58: The result of sample DTMS-016 contains silica, goethite, muscovite, siderite and biotite minerals.

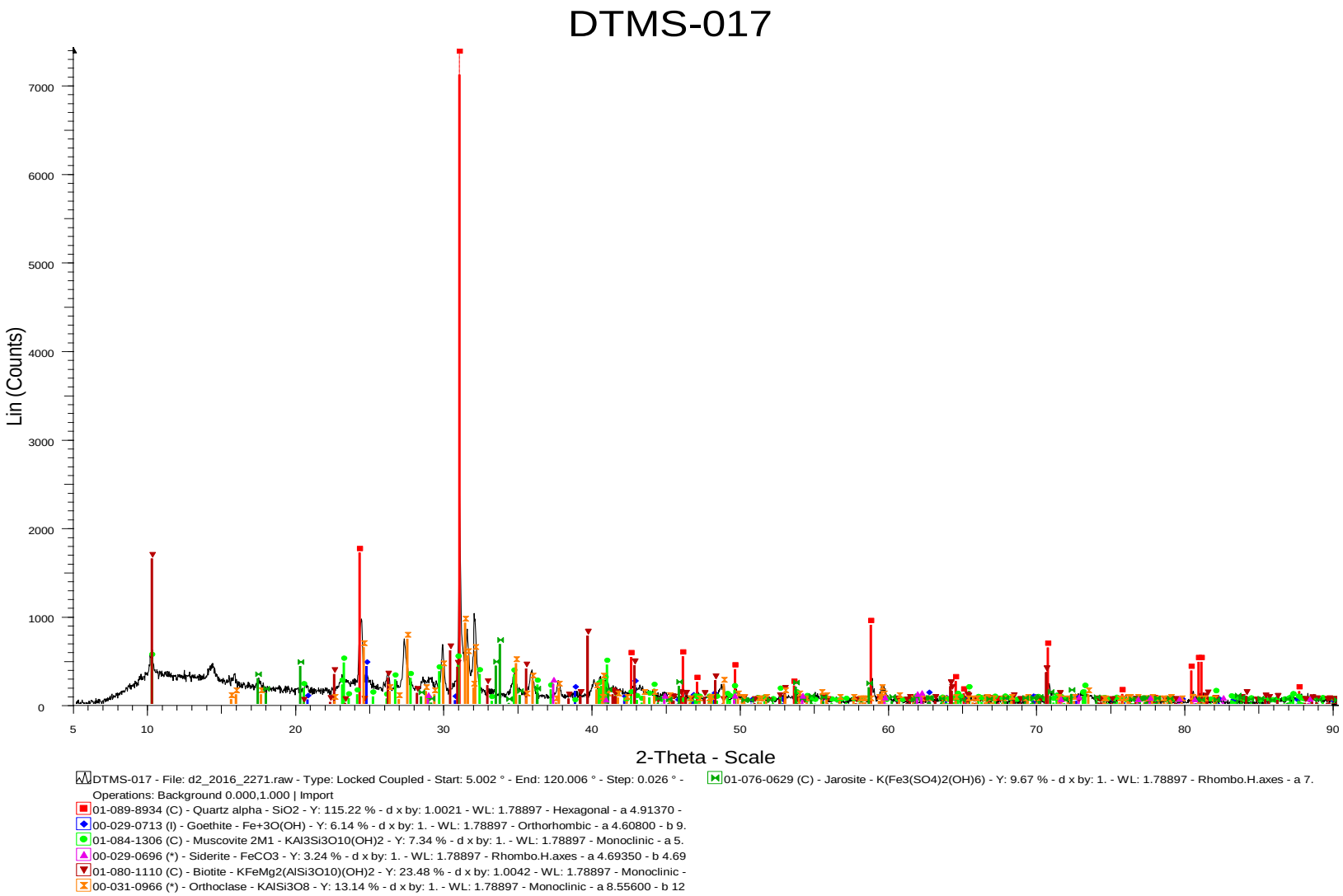

Figure 59: The result of sample DTMS-017 indicates the presents of silica, goethite, muscovite, siderite and biotite minerals.

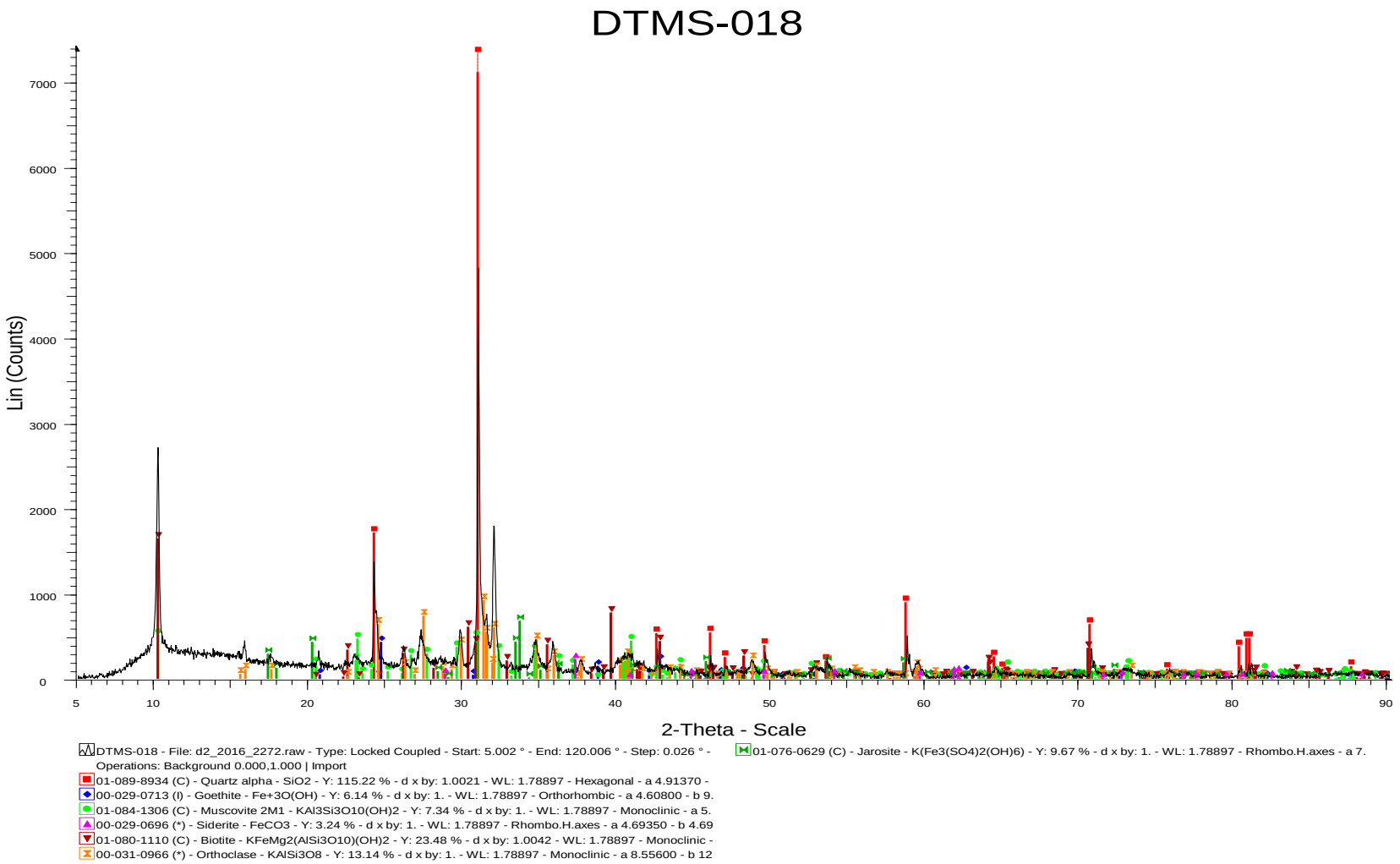

Figure 60: The result of sample DTMS-018 indicates the presents of silica, goethite, muscovite, siderite and biotite minerals.

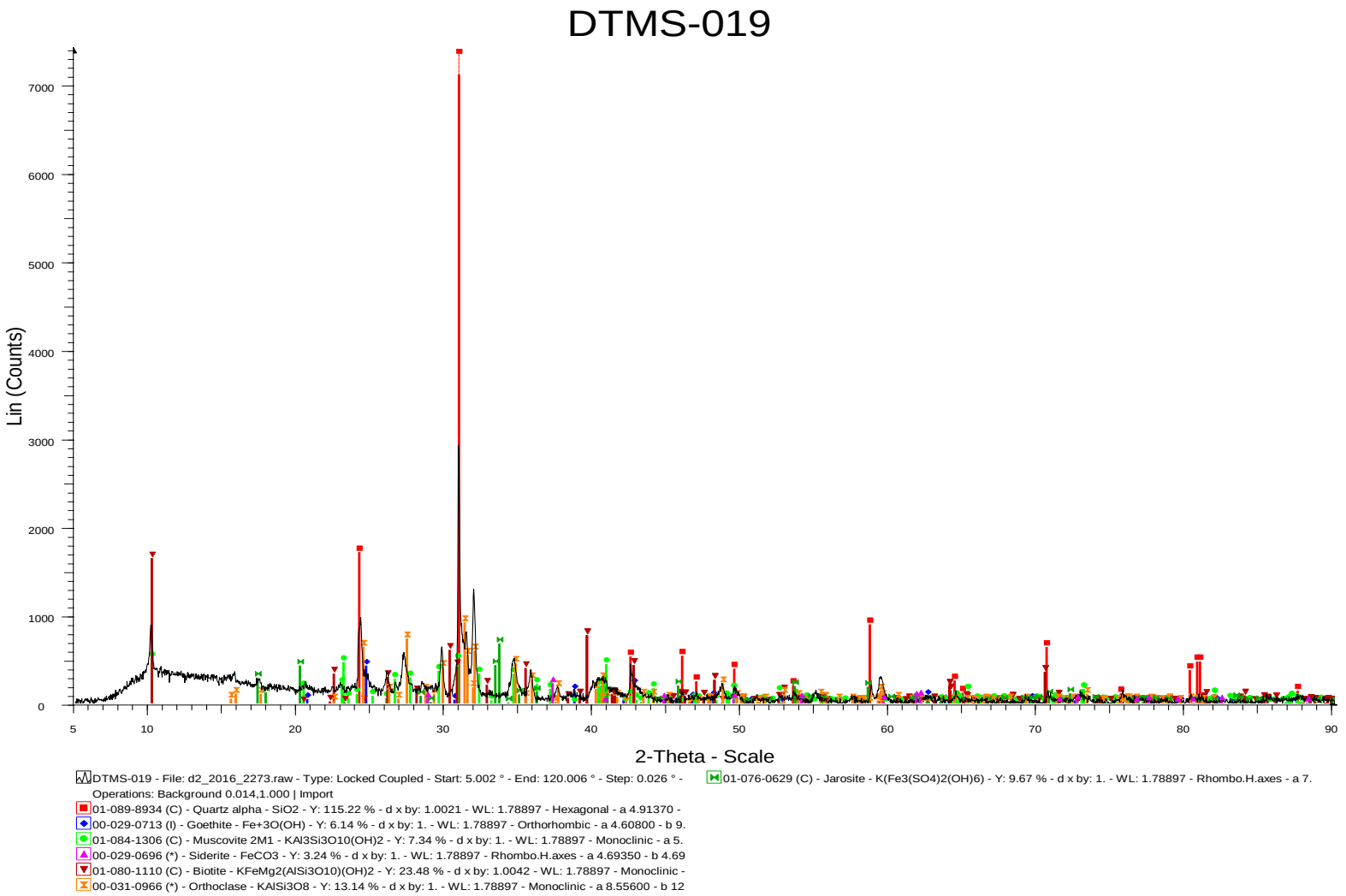

Figure 61: The result of sample DTMS-019 indicates the presents of silica, goethite, muscovite, siderite and biotite minerals.

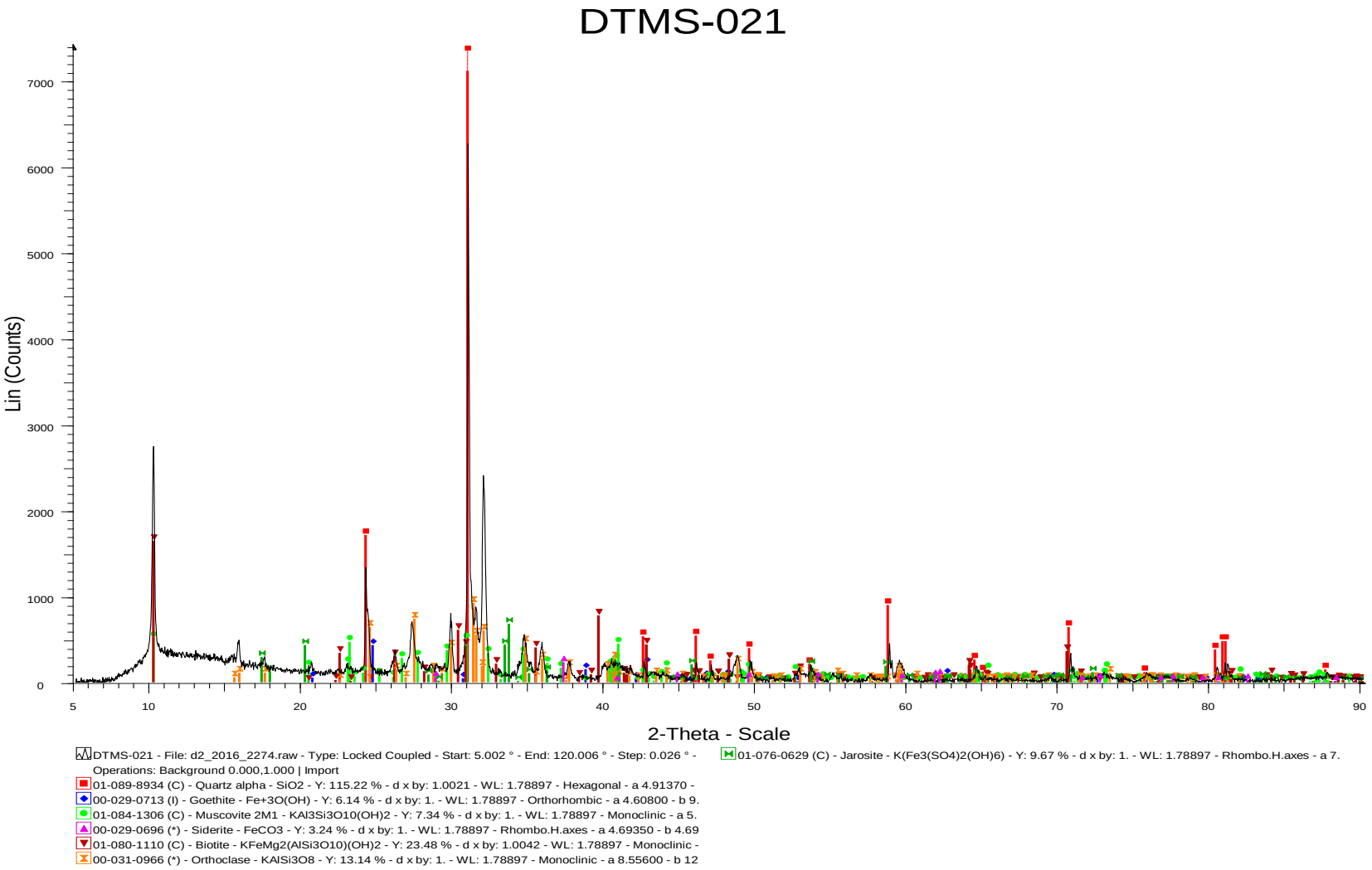

Figure 62: The result of sample DTMS-021 indicates the presents of silica, goethite, muscovite, siderite and biotite minerals.

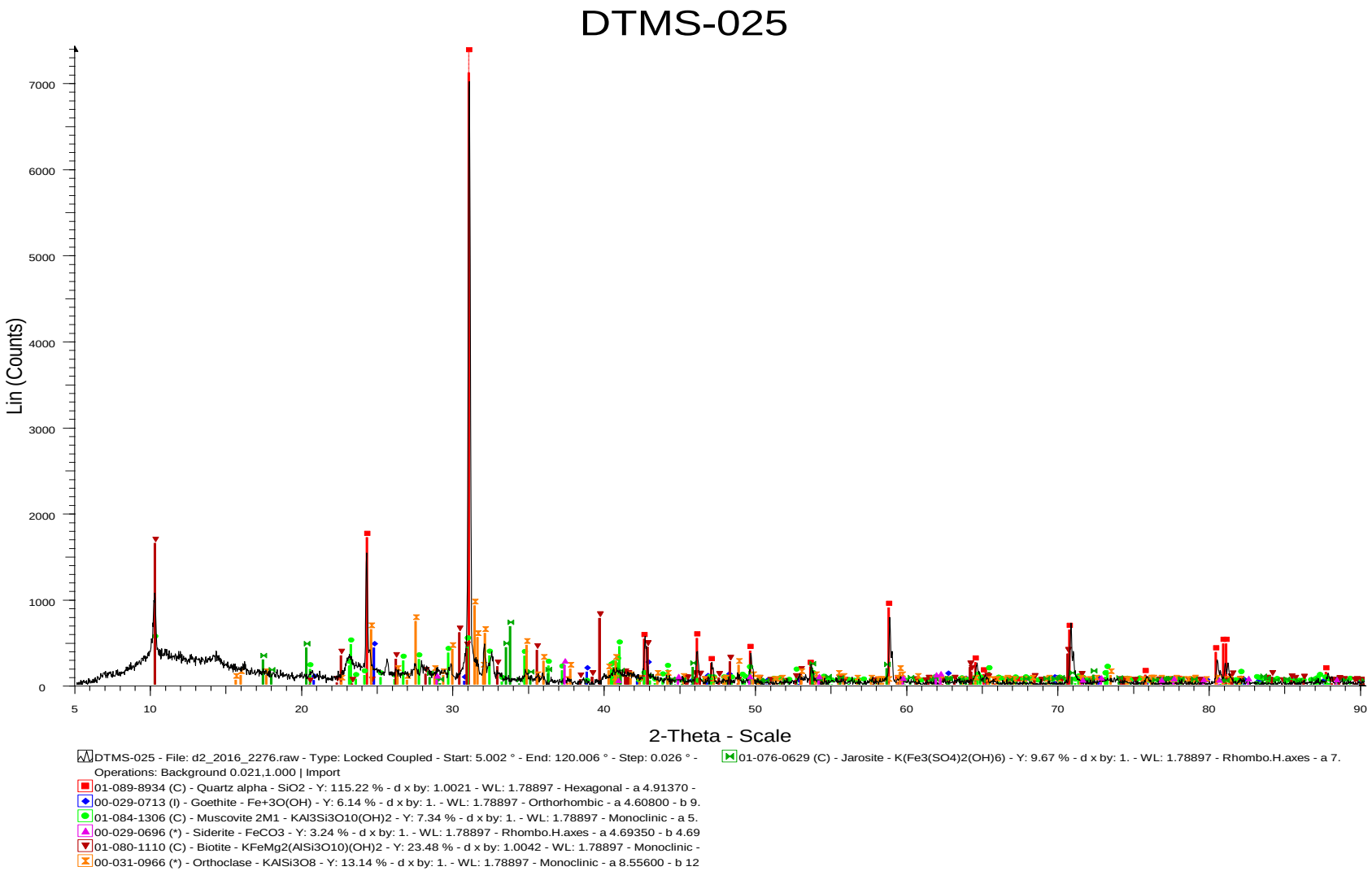

Figure 63: The result of sample DTMS-025 indicates the presents of silica, goethite, muscovite, siderite and biotite minerals.

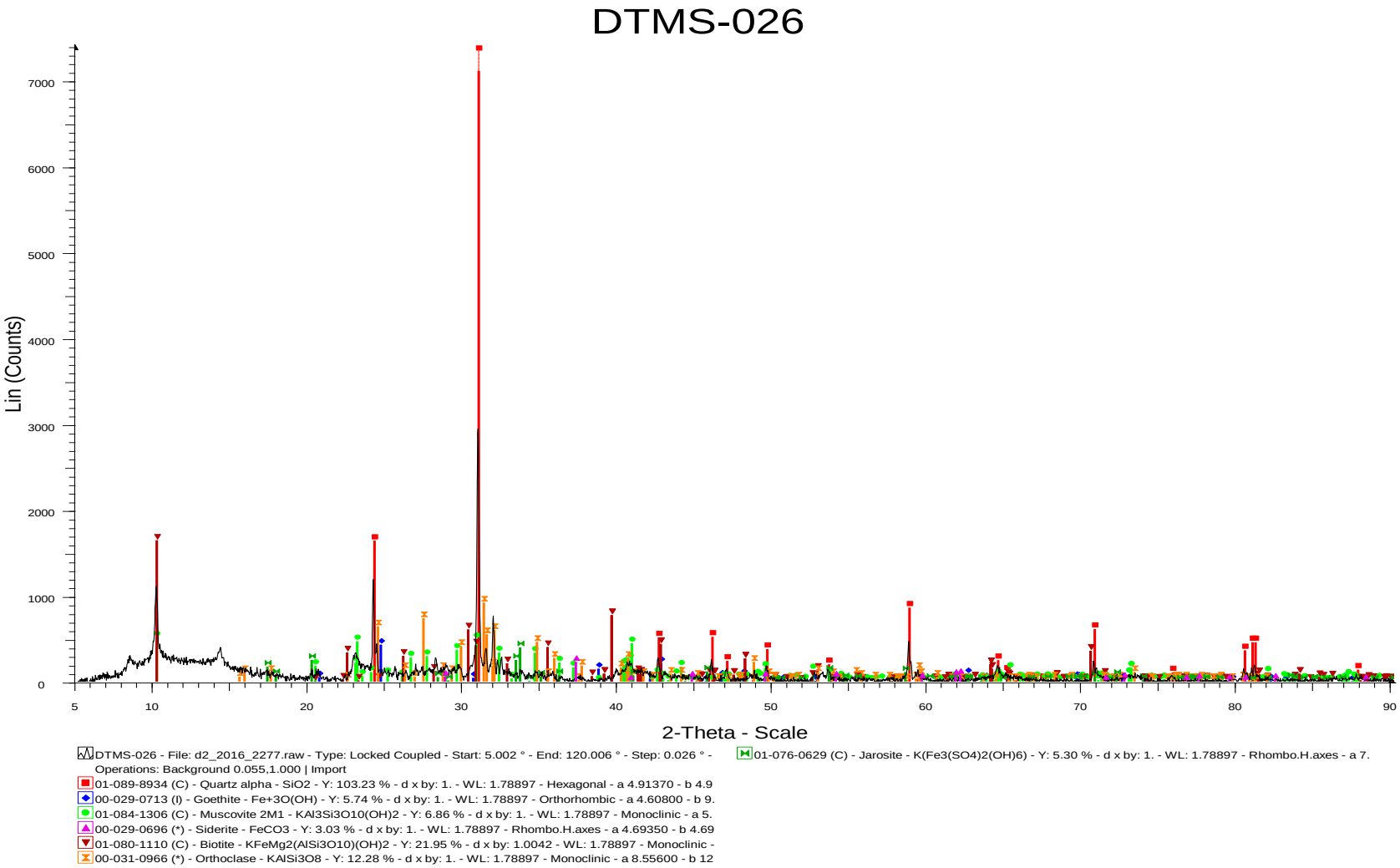

Figure 64: The result of sample DTMS-026 indicates the presents of silica, goethite, muscovite, siderite and biotite minerals.

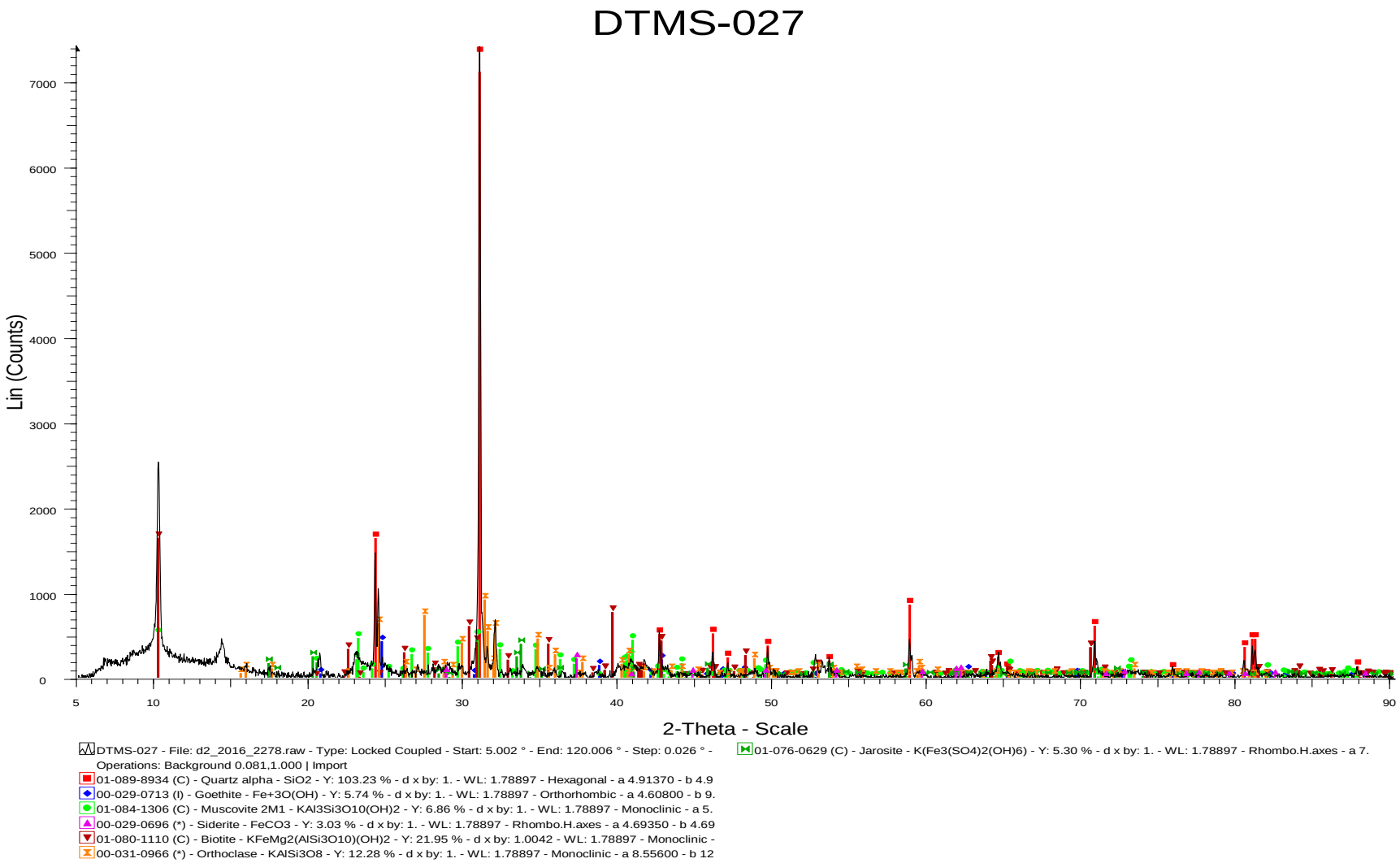

Figure 65: The result of sample DTMS-027 indicates the presents of silica, goethite, muscovite, siderite and biotite minerals.

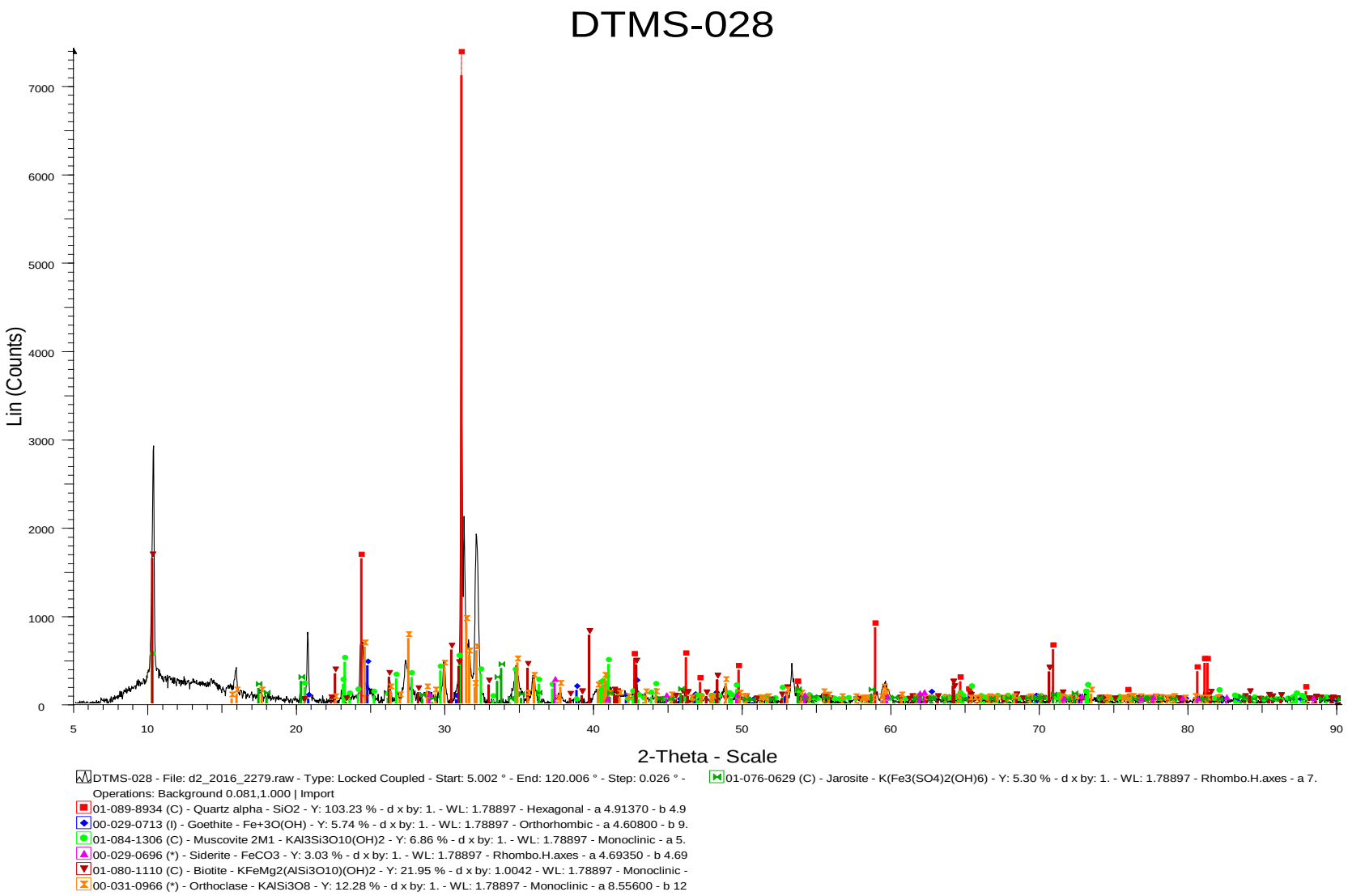

Figure 66: The result of sample DTMS-028 indicates the presents of silica, goethite, muscovite, siderite and biotite minerals.

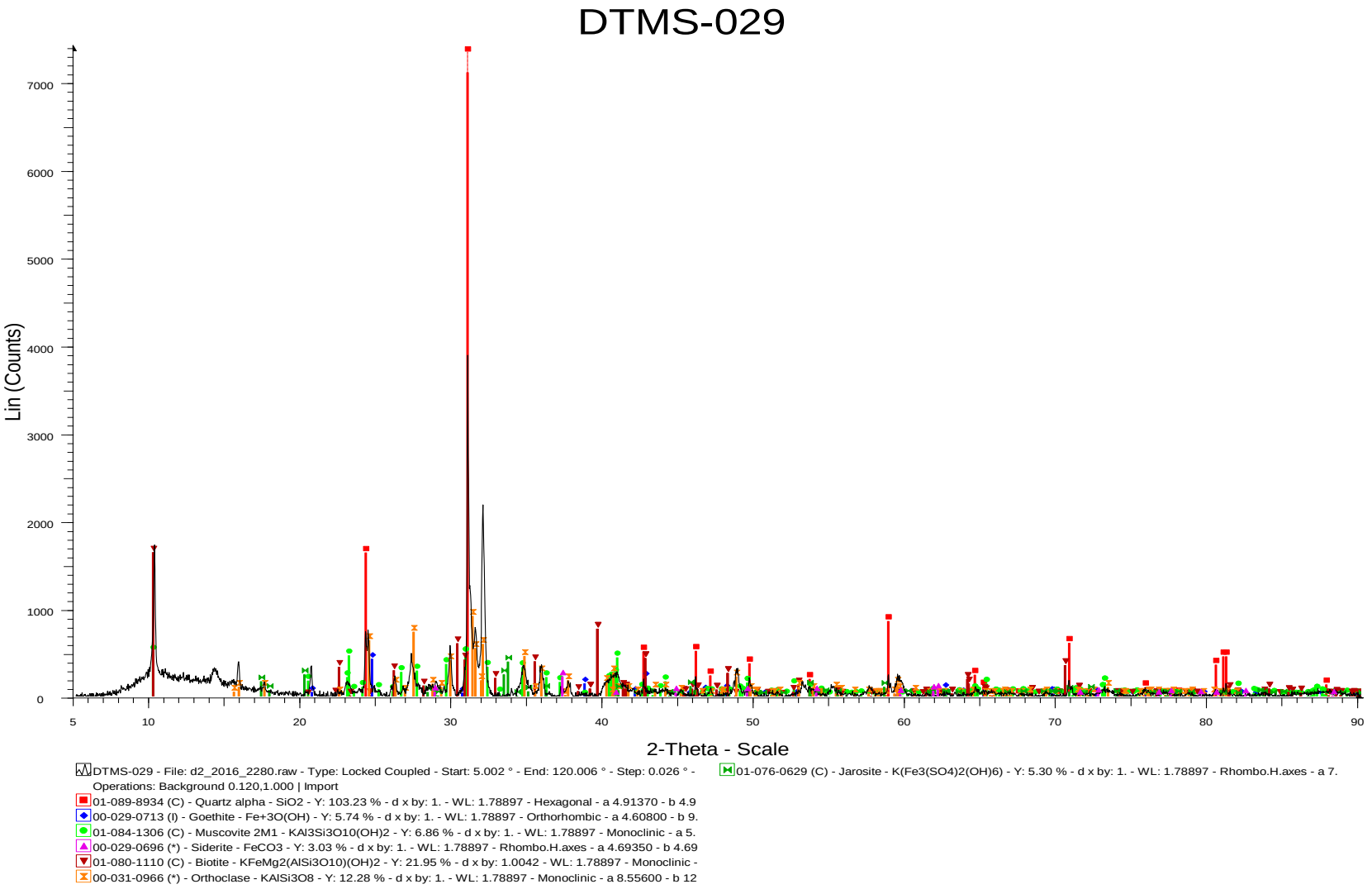

Figure 67: The result of sample DTMS-029 indicates the presents of silica, goethite, muscovite, siderite and biotite minerals.

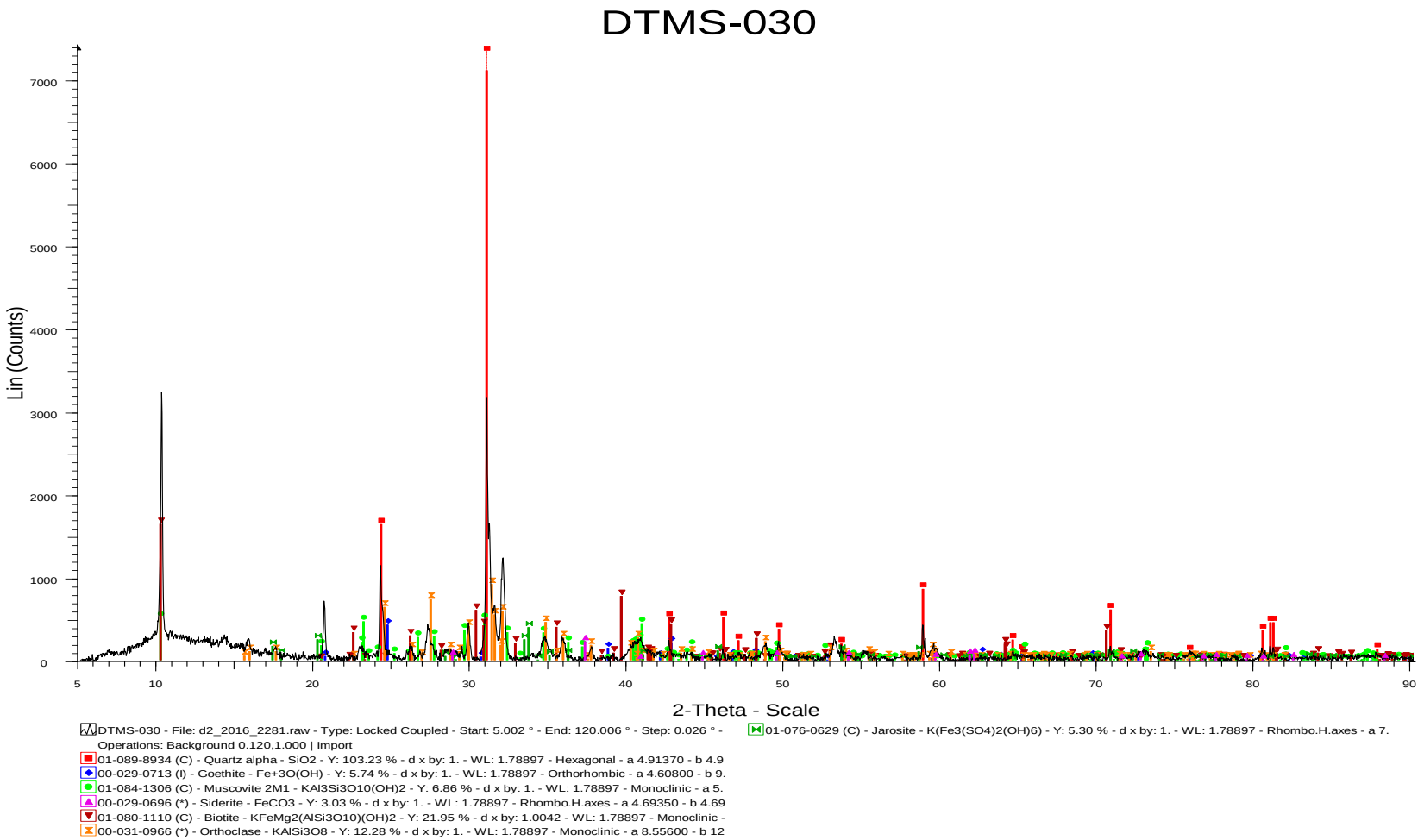

Figure 68: The result of sample DTMS-030 indicates the presents of silica, goethite, muscovite, siderite and biotite minerals.

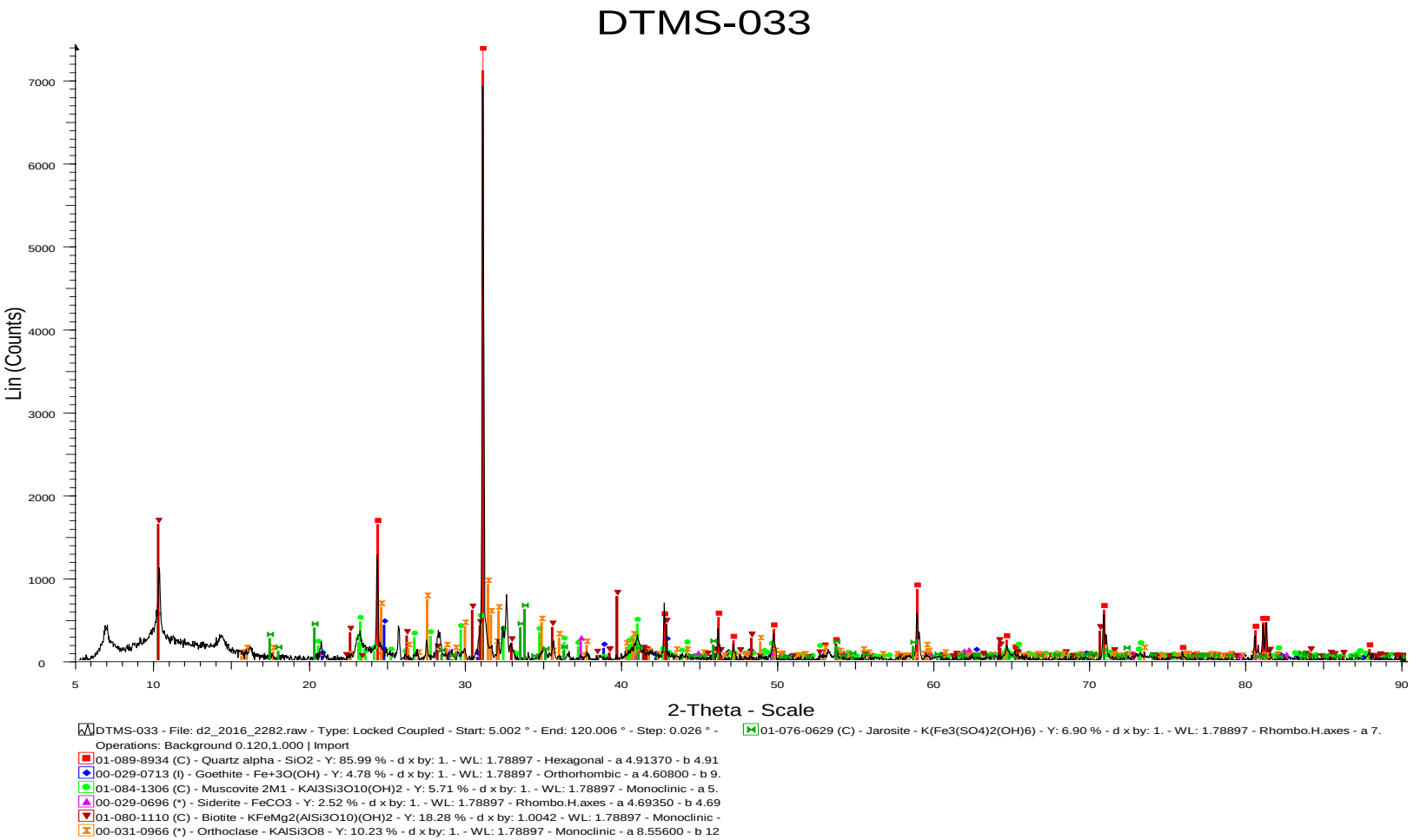

Figure 69: The result of sample DTMS-033 indicates the presents of silica, goethite, muscovite, siderite and biotite minerals.

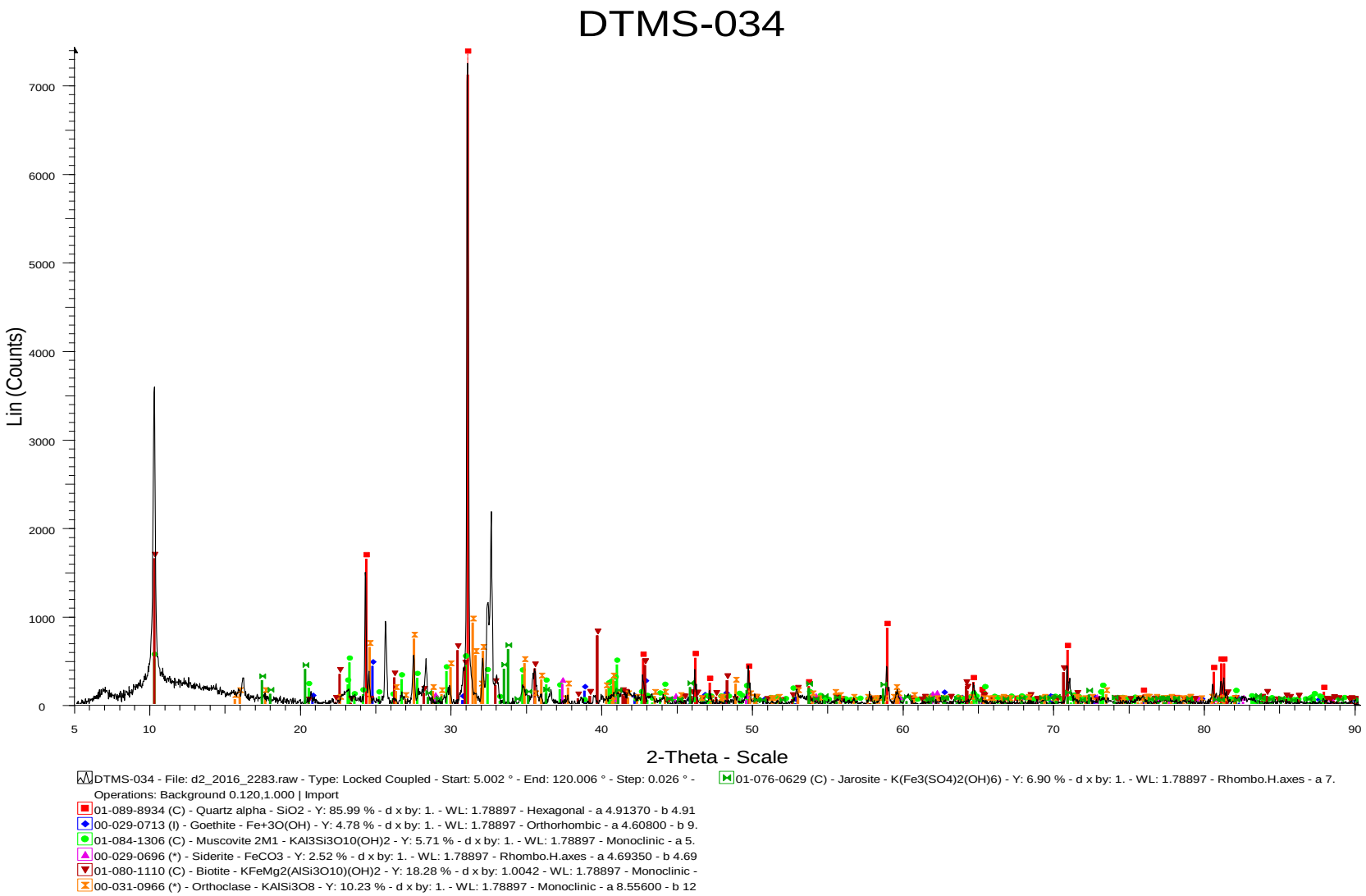

Figure 70: The result of sample DTMS-034 indicates the presents of silica, goethite, muscovite, siderite and biotite minerals.

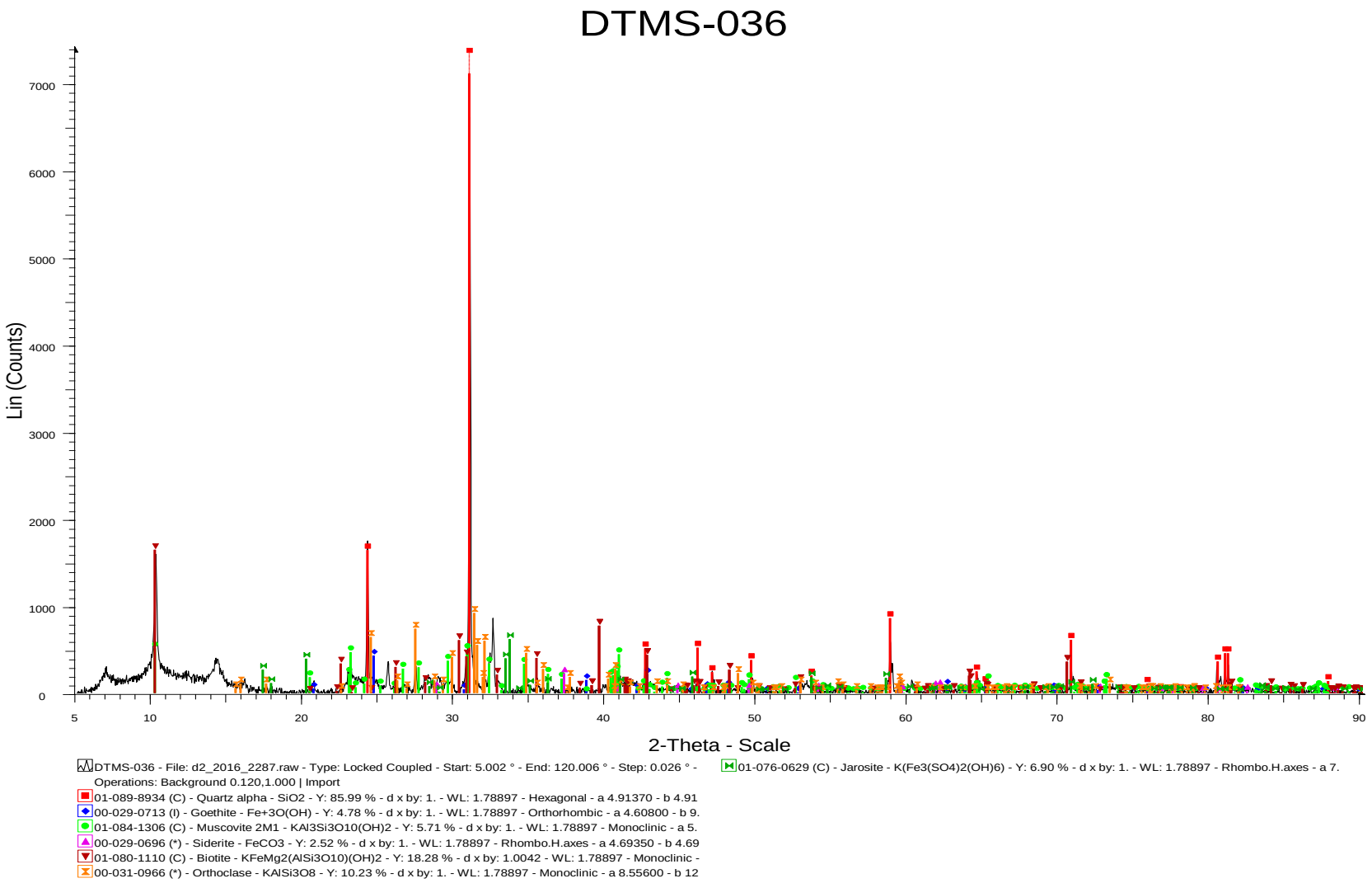

Figure 71: The result of sample DTMS-036 indicates the presents of silica, goethite, muscovite, siderite and biotite minerals.

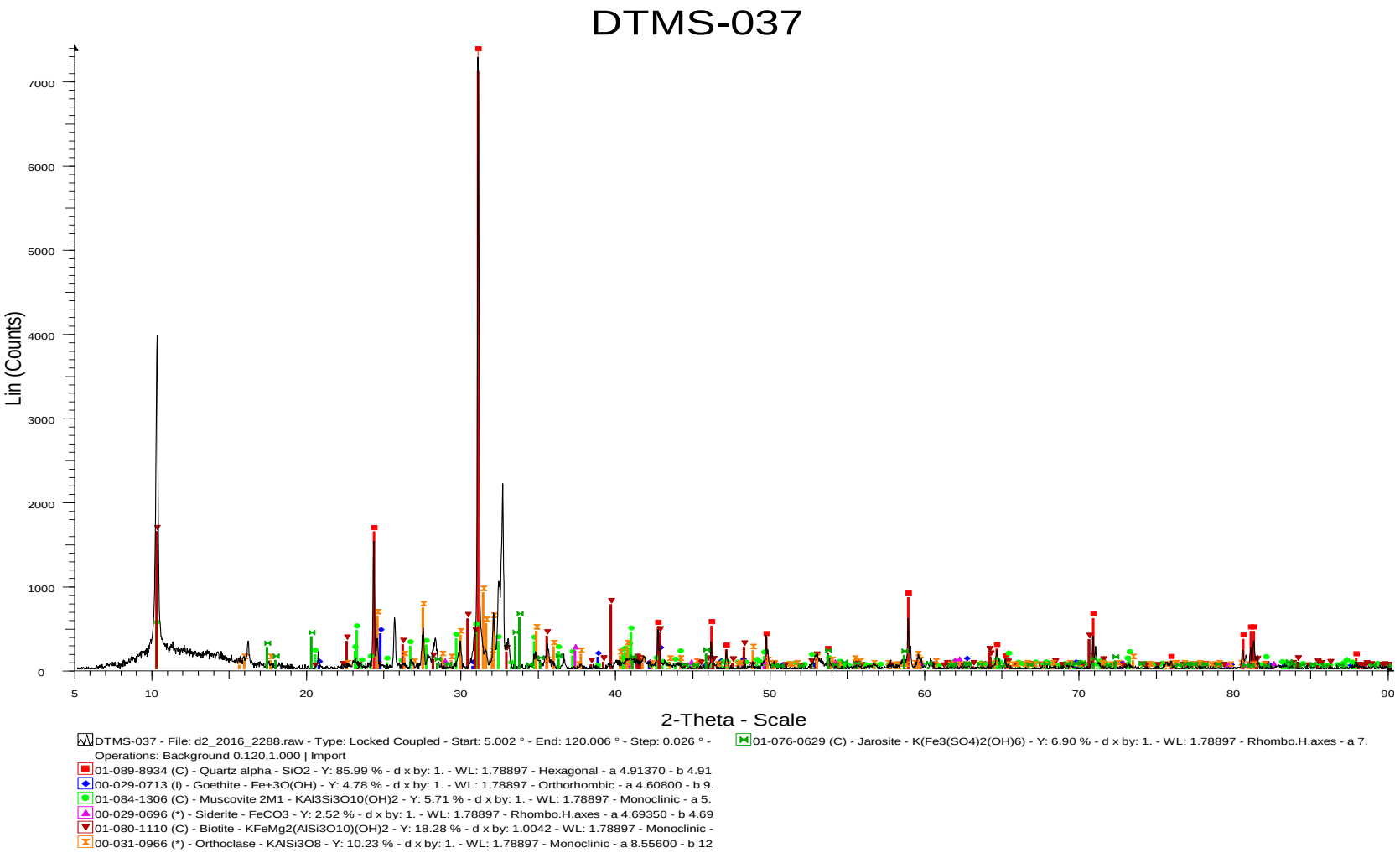

Figure 72: The result of sample DTMS-037 indicates the presents of silica, goethite, muscovite, siderite and biotite minerals.

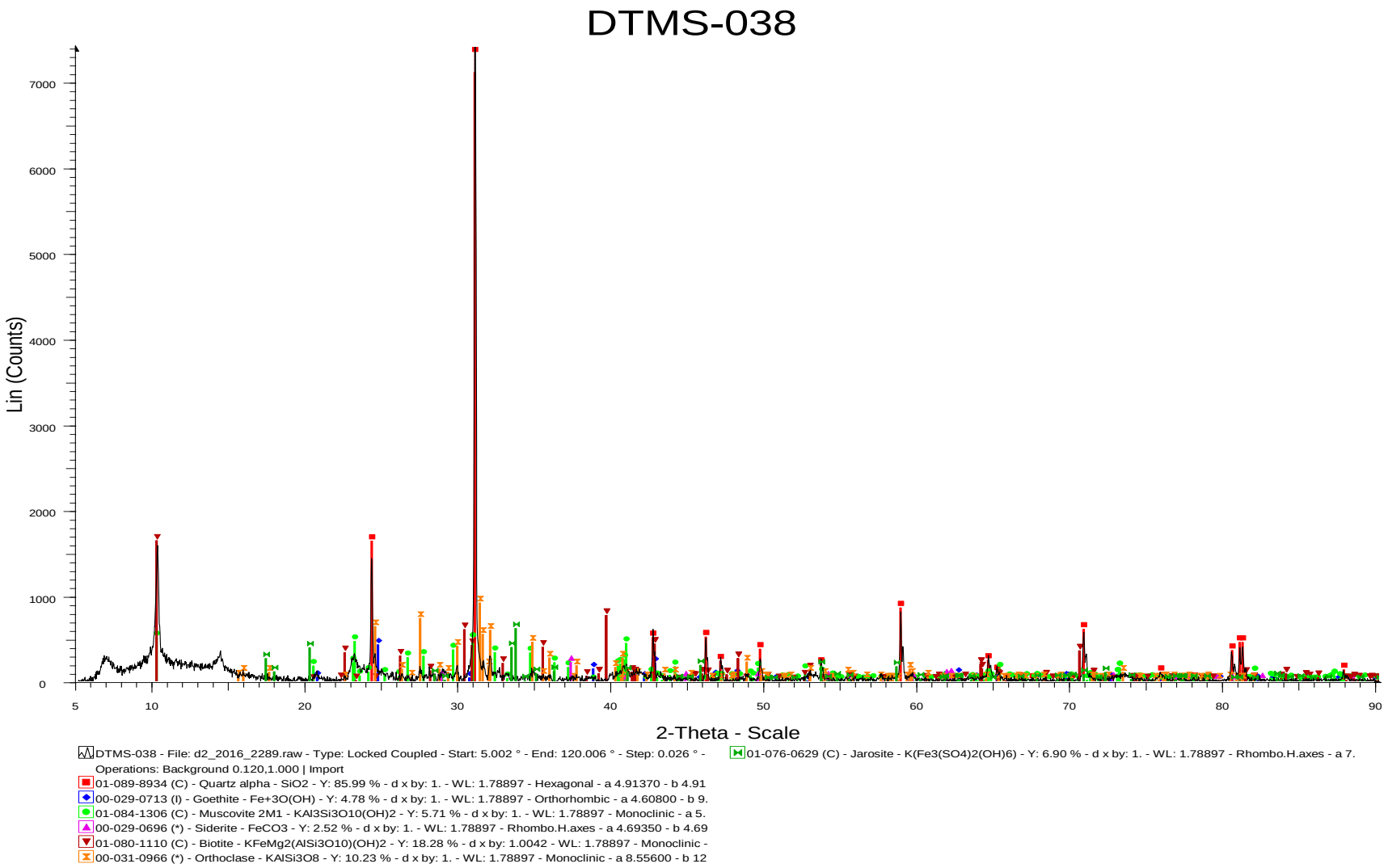

Figure 73: The result of sample DTMS-038 indicates the presents of silica, goethite, muscovite, siderite and biotite minerals.

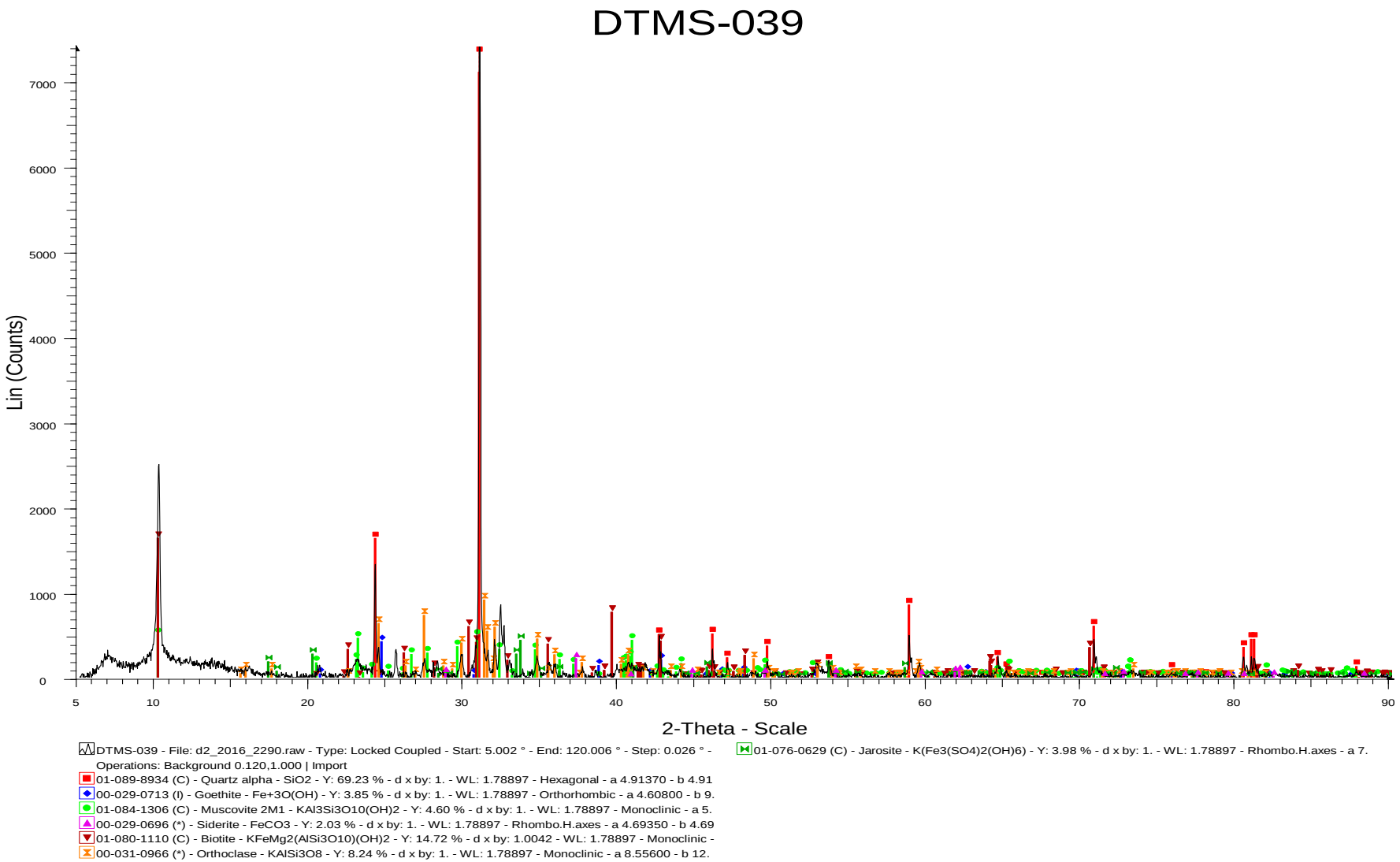

Figure 74: The result of sample DTMS-039 indicates the presents of silica, goethite, muscovite, siderite and biotite minerals.

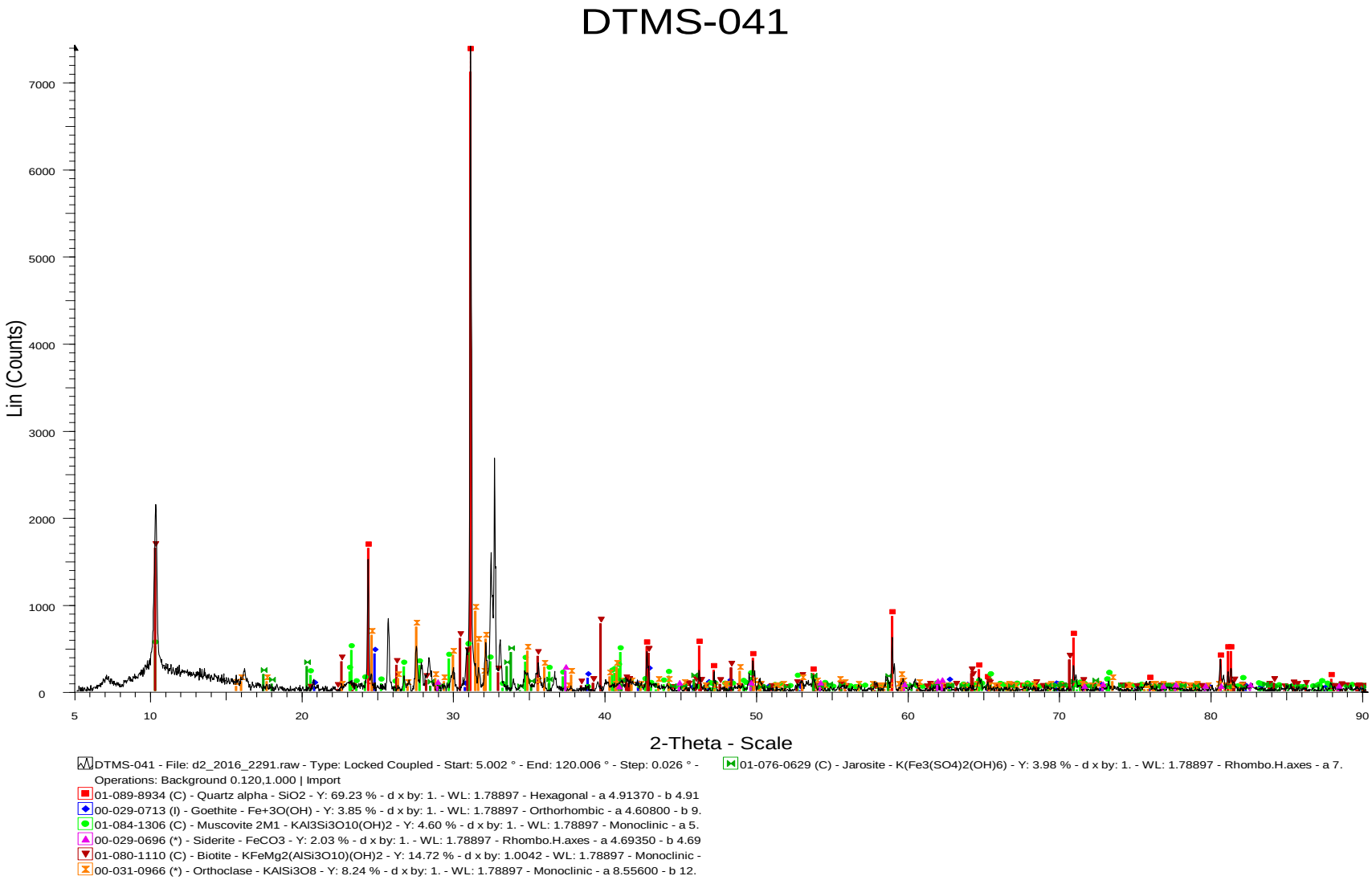

Figure 75: The result of sample DTMS-041 indicates the presents of silica, goethite, muscovite, siderite and biotite minerals.

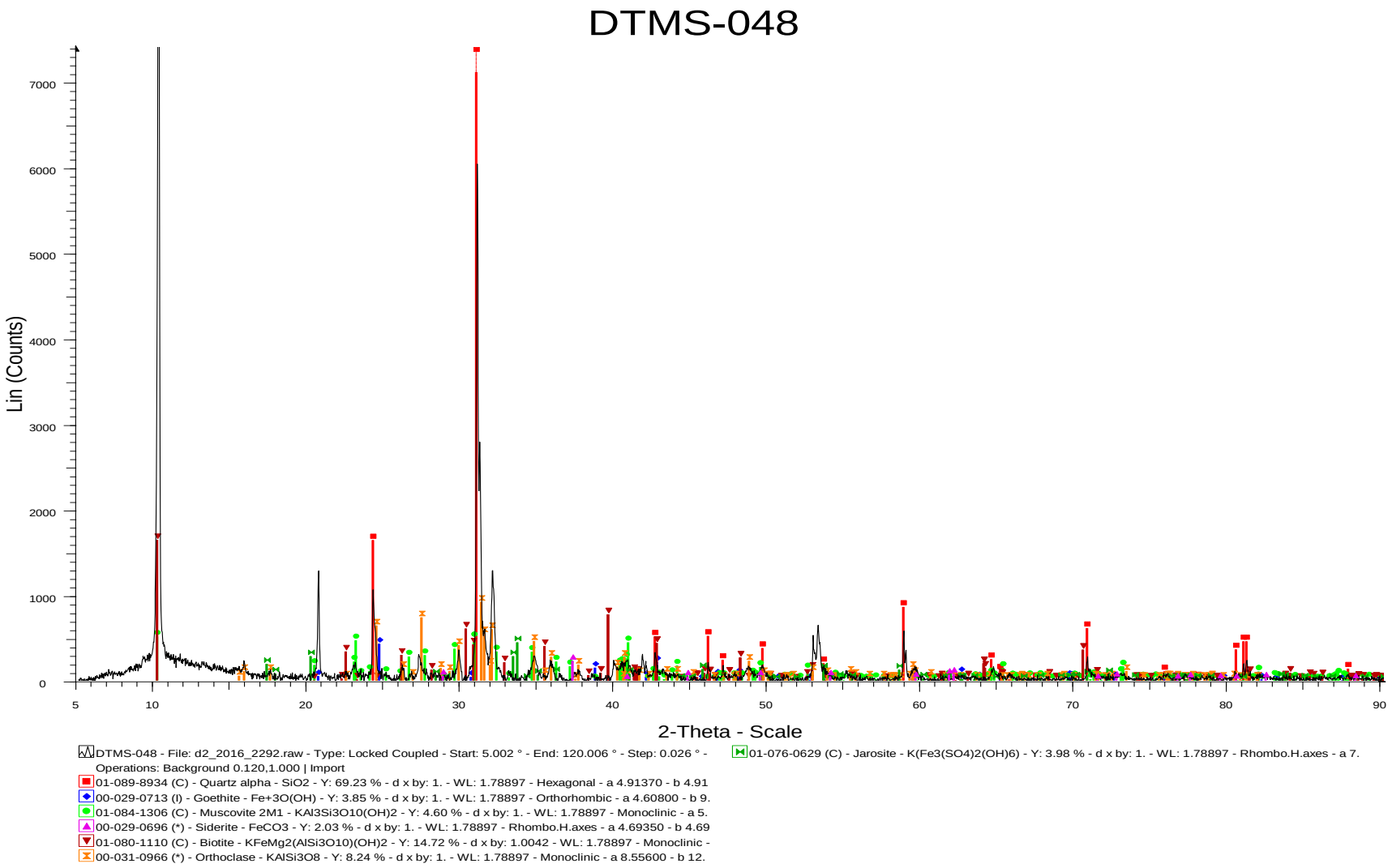

Figure 76: The result of sample DTMS-048 indicates the presents of silica, goethite, muscovite, siderite and biotite minerals.

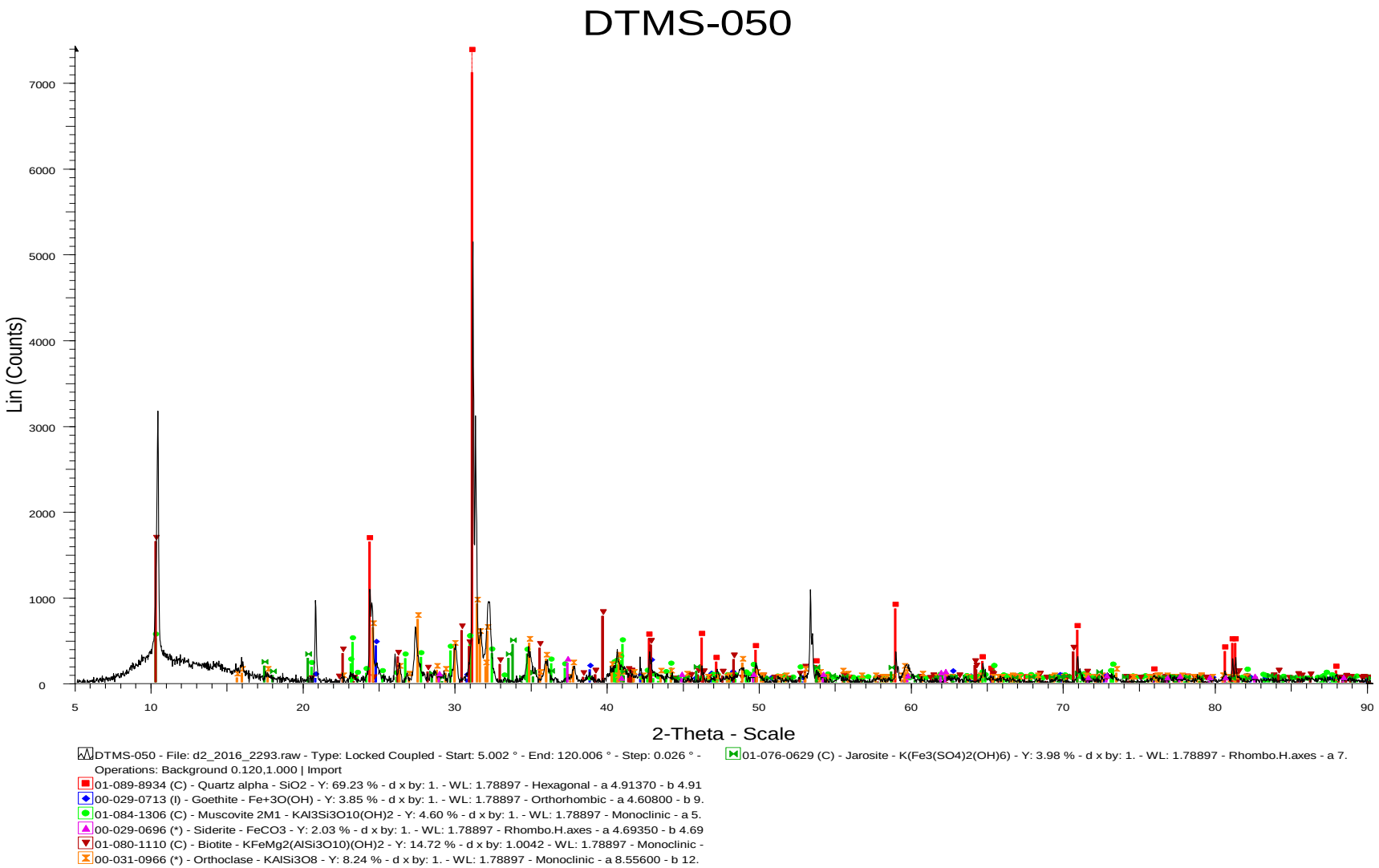

Figure 77: The result of sample DTMS-050 indicates the presents of silica, goethite, muscovite, siderite and biotite minerals.

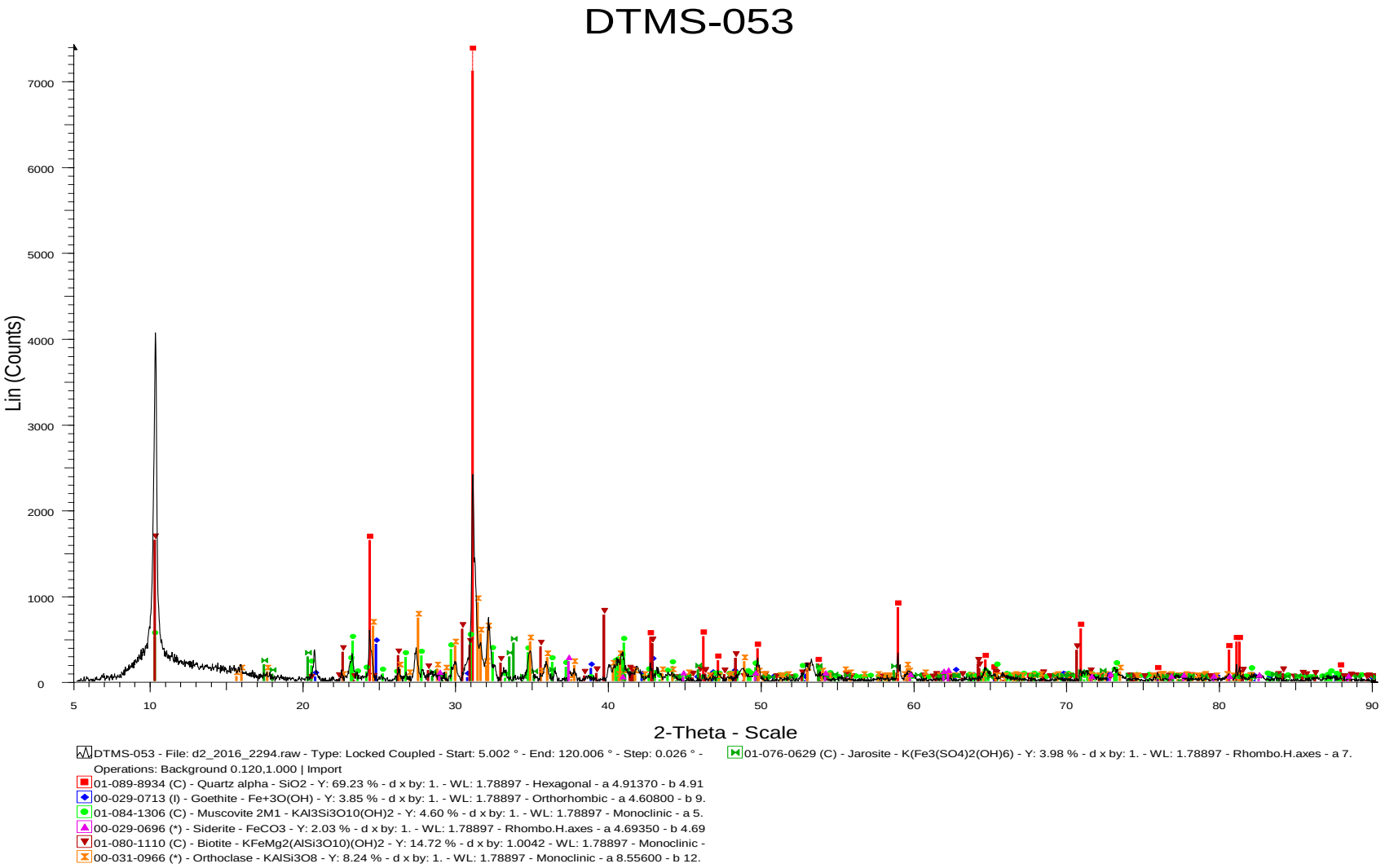

Figure 78: The result of sample DTMS-053 indicates the presents of silica, goethite, muscovite, siderite and biotite minerals.

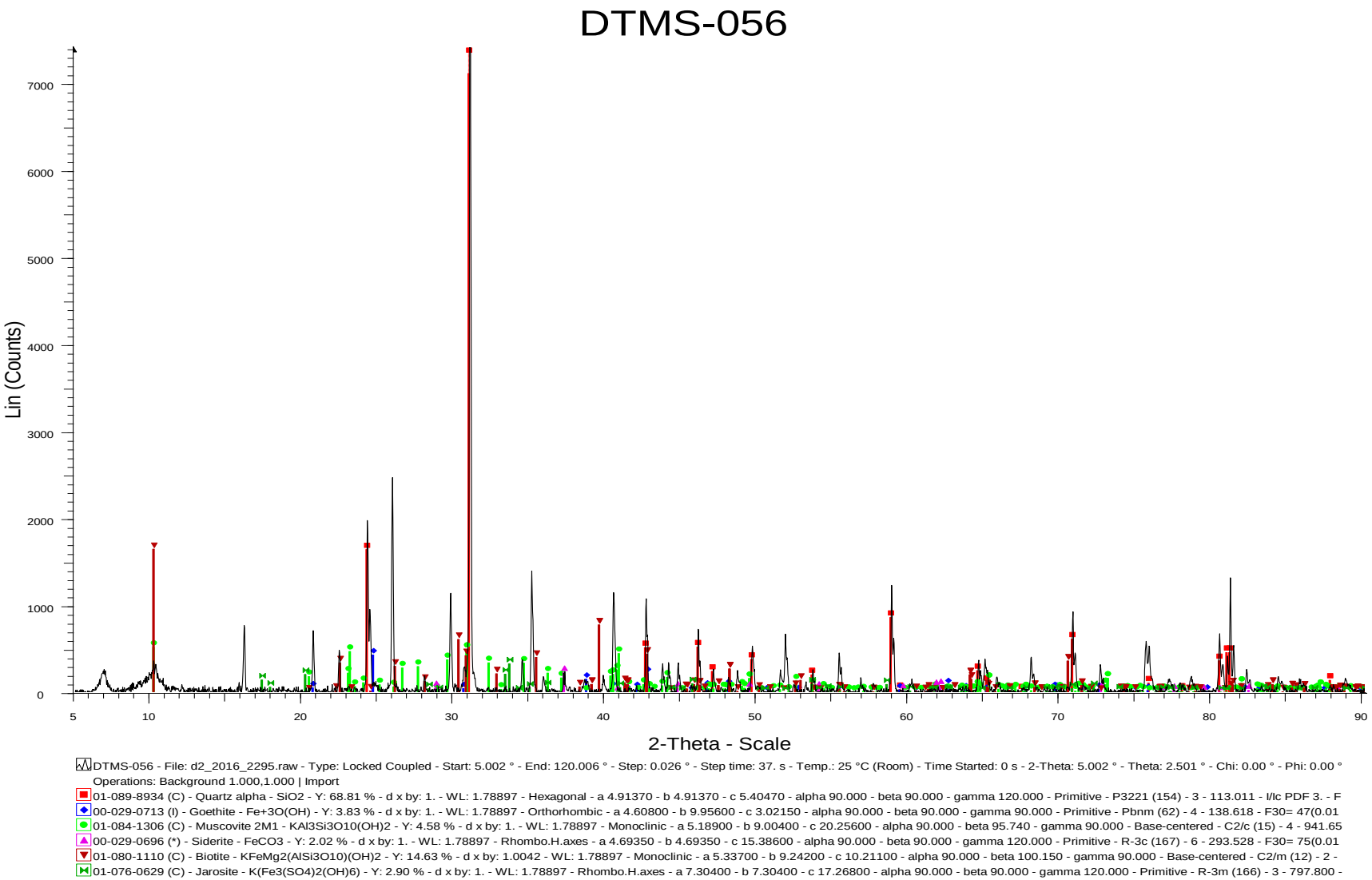

Figure 79: The result of sample DTMS-056 indicates the presents of silica, goethite, muscovite, siderite and biotite minerals.

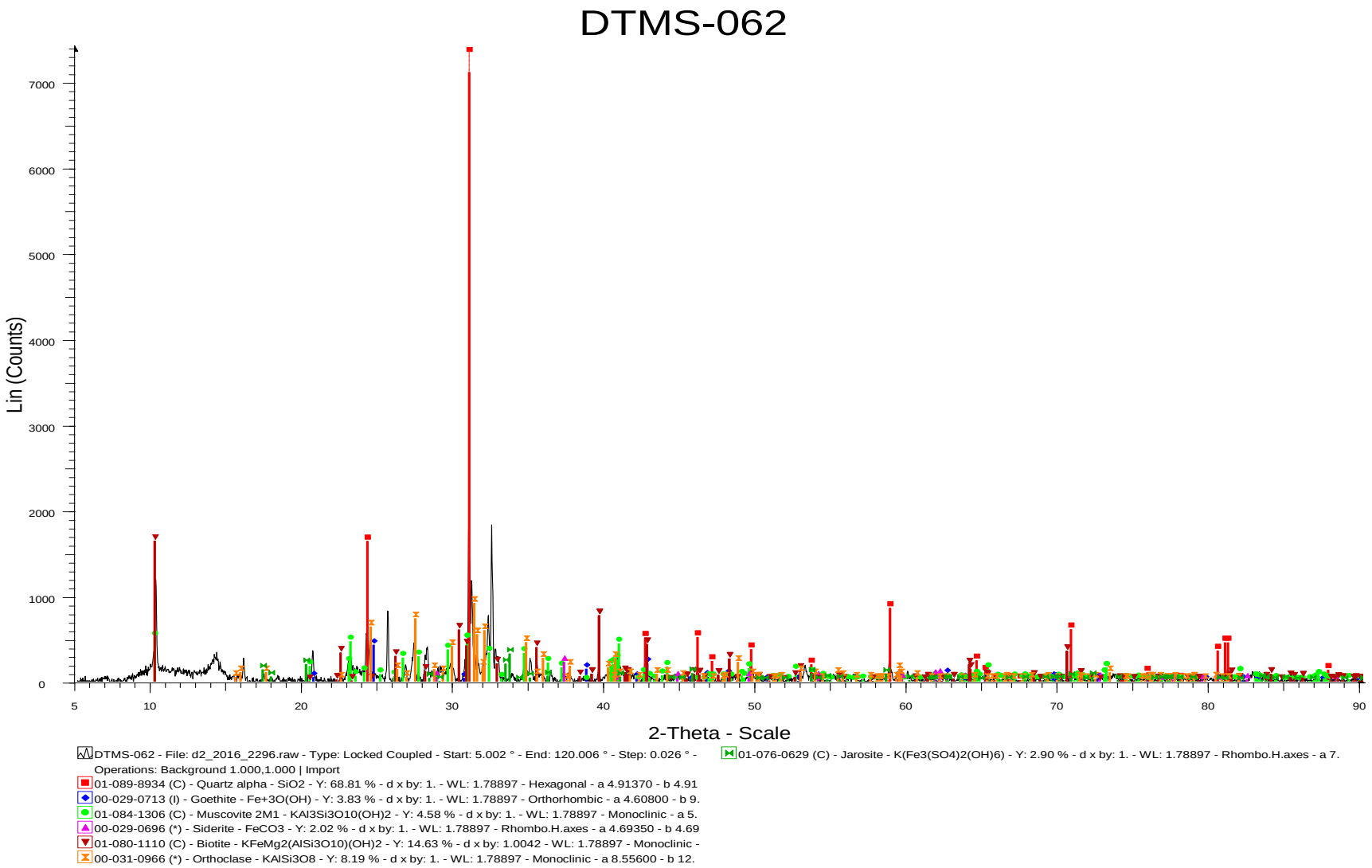

Figure 80: The result of sample DTMS-062 indicates the presents of silica, goethite, muscovite, siderite and biotite minerals.

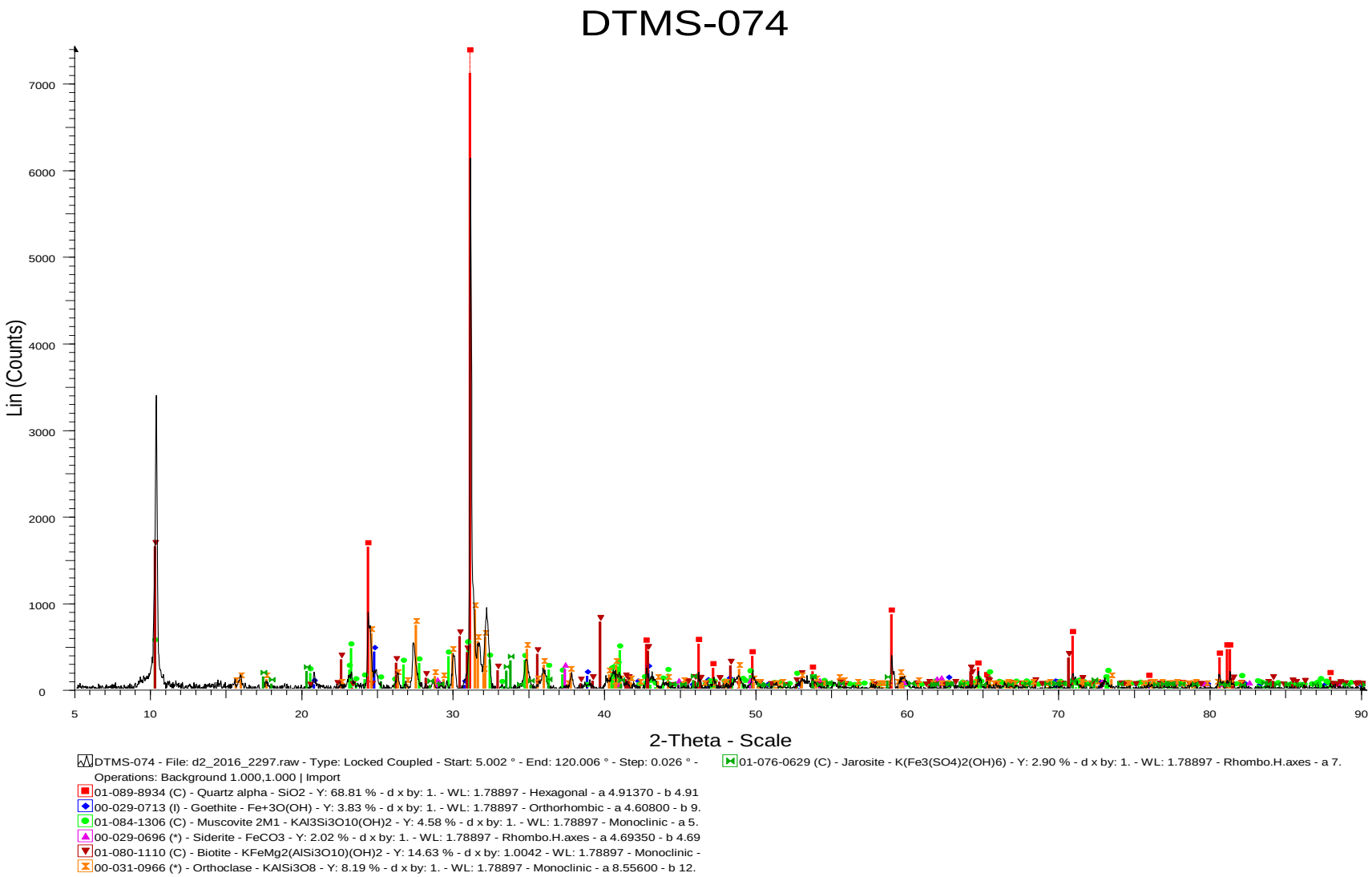

Figure 81: The result of sample DTMS-074 indicates the presents of silica, goethite, muscovite, siderite and biotite minerals.

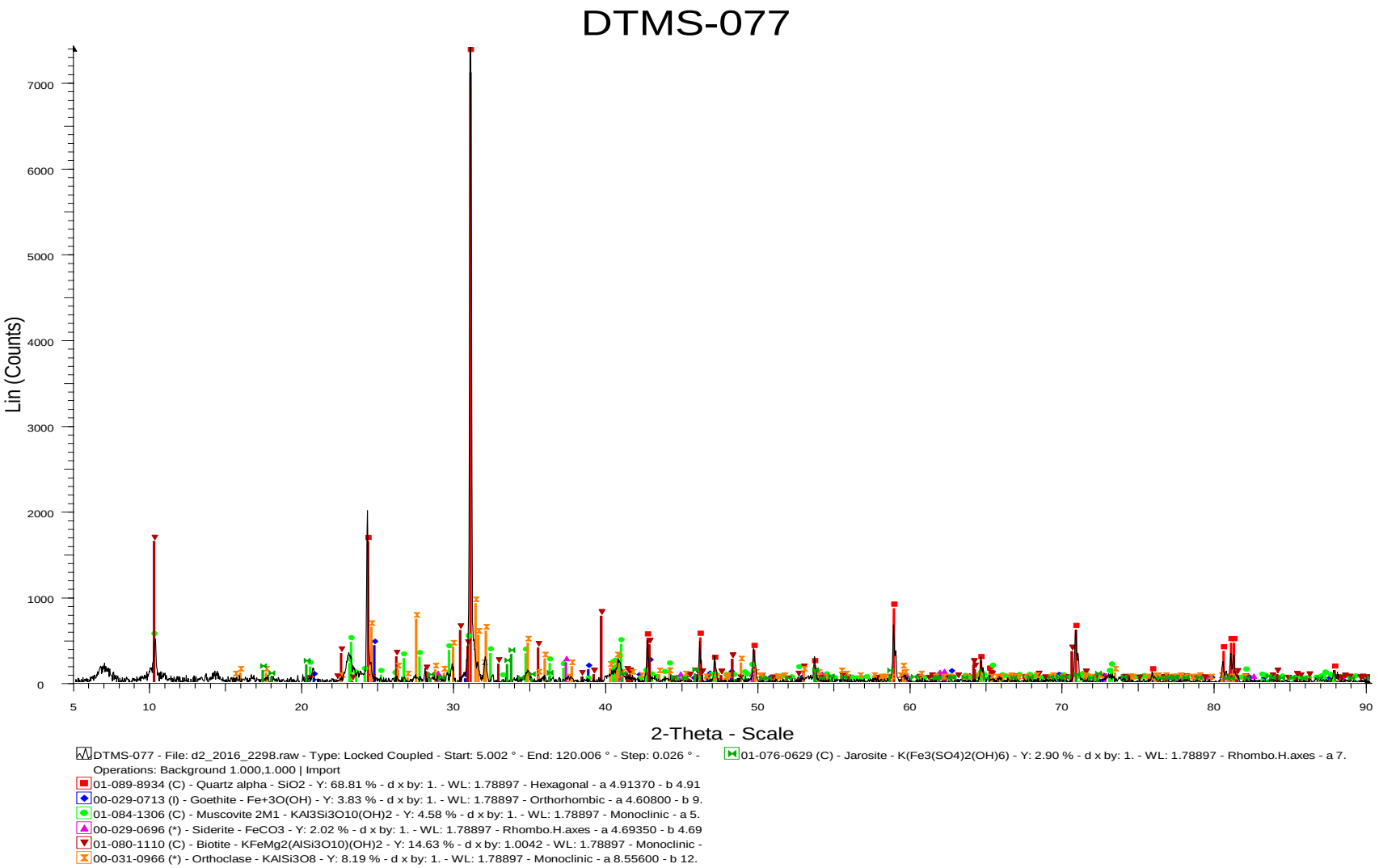

Figure 82: The result of sample DTMS-077 indicates the presents of silica, goethite, muscovite, siderite and biotite minerals.

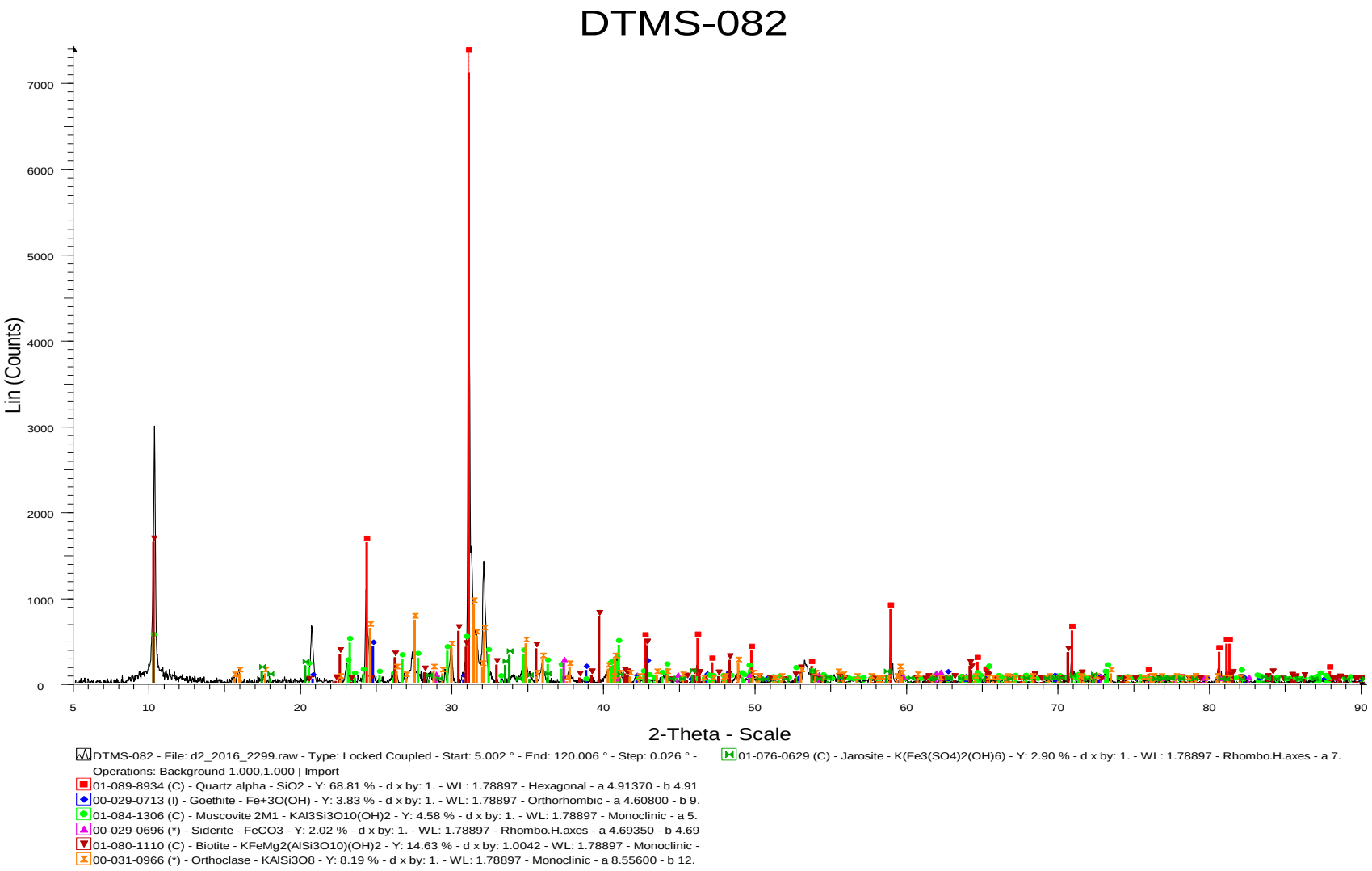

Figure 83: The result of sample DTMS-082 indicates the presents of silica, goethite, muscovite, siderite and biotite minerals.

4.3.5. Mineral separation

Minerals separation is a technique to separate heavy from light and magnetic minerals. The separation was conducted to identify each mineral content in the three-oxide development profile as well as to establish the relationship with gold mineralisation. The first mineral description was done in the field. The different minerals identified in the field are quartz, biotite, muscovite, sericite, and chlorite. Thirty samples were crushed, sieved to a fraction of < 500µm and separated into heavy and light minerals.

Two types of quartz were observed: type (1) showing dissolution holes, and another type (2) Sub-rounded to angular, which is less abundant. The colour of the quartz is white, yellow and red. The minerals observed under the binocular microscope are quartz, biotite, muscovite, chlorite, tourmaline, feldspar potassic, tourmaline, and jarosite. Some of those minerals were confirmed by the XRD analysis presented in Section 4.3.4.

From the gold shape, three types of gold mineralisation can be established that is; in situ gold, transported and hydrothermal.

4.3.6. Summary

The highest gold grades are associated with iron (Fe) and potassic (K) alteration. The XRF analysis conducted on the pulp samples, which were analysed for gold by fire assay confirm the relationship between gold mineralisation and potassic alteration, which has been previously established by Cameron (2010) and Masurel et al. (2014).

The silica is a product of calc-silicate weathering, the presence of 60% of silica (quartz) in the results analysed by XRF indicates that there is a relationship between calc-silicate alteration and gold mineralisation.

The relationship of the oxide jarosite alteration with gold mineralisation has been proved by the gold analysis results from SEMOS laboratory. The result of XRF and XRD analysis and the description of mineral separates were useful to determine the shape of gold and quartz. The shape of gold and quartz are an indicator of their origin. The presence of the minerals, such as alunite (K_2A_{l6} $(SO_4)_4(OH)_{12}$) and jarosite (K_2Fe_{63}+ $(SO_4)_4(OH)_{12}$) highlight a highly acidic environment and acid supergene conditions (Hein, 2008). The bernalite mineral can be found from the surface oxidation zone. Alunite and jarosite formed deeper in the oxidation zone.

The significant presence of the gold grade in the unweathered calc-silicate can be explained by one or both hypothesis: (1) As Thermal Aureole Gold Deposit (TAGD) as proposed by Hein (2007), and (2) as hydrothermal mineralisation proposed by Masurel et al. (2017), although in the latter study

the origin of fluid and metals are unspecified. The concentration of the gold in the weathered calc-silicate can be due to the loss of volume and density as a consequence of the oxidation.

Chapter 5

Discussion

The combination of mapping and drilling data in the building of the 3D model and analysing gold XRF and XRD bring a new understanding of Sadiola goldfield model. According to the project, three oxide profiles were found, and three types of gold mineralisation were established in the Sadiola goldfield. Two types of quartz were observed in the study area, and seven minerals detected in XRF and XRD. The similarity between the stratigraphy in the Sadiola Hill opencast and FN3 opencast pits has been established and five profiles were identified from top to bottom, while seven profiles were identified in Tambali opencast pit. Three layers of ferricrete were observed. Oxidation resulting in the collapses of the oxide profile caused several events in the goldfield. Five lithologies and six sub-facies of the calc-silicate were established. The oxide profiles were found along the SFZ and the northeast trending faults.

5.1. Oxide profile development

The Sadiola gold mine in western Mali develops different profiles, which are different from other mines in the region. In the Sadiola goldfield, the oxide profile developed includes saprolite and transitional zones. These profiles are composed of three-oxide facies developed namely: Type 1, decarbonated calc-silicate alteration; Type 2, Fe alteration (oxide-jarosite-siderite); and Type 3, potassic clay alteration. This study established a relationship between the gold mineralisation and type 2 and 3 of oxides developed. The colour of type 2 is red and, defined as oxide-jarosite-siderite, while the type 3, colour is pink and, defined as potassic clay alteration. However, Strydom and Rompel (1997) defined their type (ii) like yellowish stained marble as limonite mineralised, and type (iii) like brown to red stained as goethite and hematite mineralised. The three-oxide facies described in this study correspond to those defined by Strydom and Rompel (1997).

The Sadiola goldfield opencast pits mapping allowed the identification of five main lithologies: meta-sandstone, calc-silicate, siltstone-shale-greywacke, diorite and quartz-feldspar porphyry, while Hein and Tshibubudze (2007) classified the lithologies of the Sadiola goldfield into greywacke, volcaniclastic, volcaniclastic-greywacke, carbonaceous siltstone, marble, carbonaceous greywacke, BIF, shale and graphitic shale. The difference appears in the presence of intrusion, grouping of the siltstone-shale-greywacke in the present study. Hein and Tshibubudze (2007) present a more detailed classification with less grouping.

The calc-silicate study conducted in the Sadiola goldfield establish the following sub-facies of the calc-silicate (1) very thick (more than 1 cm) to thick-bedded (0.5-1 cm) marble (with alternate of white and black layers), (2) thin (3-5 mm) to very thin-bedded (1-3 mm) marble, (3) massive marble,

(4) slump-folded marble, (5) carbonaceous siltstone and (6) pure marble, while Hein (2008) identified five calc-silicate sub-facies (1) massive greywacke facies, (2) carbonate greywacke-siltstone facies, (3) massive carbonate facies, (4) bedded carbonate, and (5) slump facies to massive carbonate facies. The similarity could be found in the massive to bedded and slump-folded sub-facies. Much of those calc-silicate sub-facies are probably formed because of the oxide profiles collapsing.

The weathering process of the calc-silicate resulted in a concentration of the quartz in the oxide profile. Two types of quartz were observed: quartz type (1) with dissolution holes, a lot of the quartz is presented like that, this quantity is probably due to the sulfidation of the calc-silicate rock. (2) Sub-rounded to angular quartz. This type of quartz can be explained by transport.

The colour of the quartz is white, yellow and red. The different colours could relate to the different style of oxidation, like white related to (Type 1) decarbonated calc-silicate alteration, then the red could be related to the (Type 2) Fe alteration (oxide-jarosite-siderite), and finally, the yellow can be related to the (Type 3) potassic clay alteration.

There is two types of gold mineralisation in the oxide phase, and one in the sulphides. The gold mineralisation in the oxide phase is composed of gold in ferricrete (Eocene-Miocene age), and the gold mineralisation in the oxide profile (oxide saprolite and transitional) with unknown age. The gold mineralisation found in the hard rock is from Birimian age, probably related to the Eburnean Orogeny at 2.1 Ga. At Sadiola goldfield opencast pits the study of oxide profiles allowed to identify different types of gold shape, suggesting that the source of the gold mineralisation could be variable: (1) transported gold hosted in ferricrete, (2) as Thermal Aureole Gold Deposit defined by Hein (2007), and (3) as hydrothermal gold proposed by Masurel et al. (2017), although in the latter study the origin of fluids and metals as remain unspecified. Sadiola gold mineralisation is mined in the oxide phases and the ferricrete units. The three units which host gold mineralisation are as following: (1) ferricrete, (2) oxide phases and (3) hard rocks (calc-silicate and/or siltstone-shale-greywacke). It appears that the oxide profile gold has not been mentioned by Hein 2007), and Masurel et al. (2017).

The different minerals detected by XRD are: (1) Silica or quartz (SiO_2), (2) Goethite (Fe+ 3O.OH), (3) Muscovite ($KAl_3Si_3O_{10}$ $(OH)_2$), (4) Siderite ($FeCO_3$), (5) Biotite $KFeMg_2$ $(AlSi_3O_{10})(OH)_2$, (6) Bernalite (Fe $(OH)_3$), (7) Orthoclase ($KAlSi_3O_8$). The calc-silicate skarnification was conducive to the formation of variable minerals such as diopside, actinolite, chlorite, epidote, dravitic tourmaline (Sillitoe, 1994) scapolite, vesuvianite and fluorite (Boshoff et al., 1998). The minerals observed under the binocular microscope are quartz, biotite, muscovite, chlorite, tourmaline, feldspar potassic, jarosite, limonite and hematite. Some of those minerals were confirmed by the XRD analysis result. The condition of formation of the different minerals identified helped to understand the condition of the oxide formation. The presence of alunite (K_2A_{l6} $(SO_4)_4(OH)_{12}$) and jarosite (K_2Fe_{63}+ $(SO_4)_4(OH)_{12}$) highlight a highly acidic environment and acid supergene conditions.

Gold is observed in some samples under the binocular microscope. The shapes are variable: (1) sub-rounded to rounded, (2) oval and (3) sub-angular to angular. The gold shape can explain the different type of gold mineralisation within the goldfield. These different types of gold shapes could be related to the units, which host the gold mineralisation. Hein et al. (2015) established the following gold grain shapes: rounded to oval, curved, irregular (abundant), rod-shaped, tabular gold, wire to tangled wire type gold, broken hexagonal and rare pseudo-crystalline gold.

The stratigraphic columns for Sadiola Hill opencast, and FN3 opencast pits are similar, based on the mapping of the lithologies, and comprise the following, from top to bottom: (1) soil profile that is brown in colour with a significant amount of organic material, (2) a ferricrete horizon that is red in colour with coarse pisolitic gravel and sometimes clasts of quartz. The ferricrete is present in two or three distinct levels that are separated by aeolian sand or bauxite clay. (3) Aeolian sand horizon, very fine grained and yellow to red in colour, encrusted with kaolinite and limonite; (4) weathered calc-silicate (decarbonated) composed of very fine-grained sandy clay. (5) Massive to bedded hard calc-silicate rocks, and moderately silicified, bedded siltstone-shale-greywacke that is moderately silicified. The Tambali opencast pit stratigraphic column comprises of (1) a soil layer that is brown in colour with the significant organic material, (2) a ferricrete horizon that is red in colour with coarse pisolitic gravel and sometimes clasts of quartz, (3) red to yellow sandstone horizon that is very fine to medium grained. This sandstone is friable and encrusted with kaolinite, limonite to hematite alteration. (4) Siltstone-shale-greywacke that is moderate to strongly silicified. (5) Calc-silicate rock that is massive. (6) Quartz-feldspar porphyry dykes oriented north-northeast crosscut all the sediments and (7) diorite dykes intruded the quartz-feldspar porphyry and the sediments. While Hein (2008) established a stratigraphic column for Sadiola Hill opencast and FE3 opencast pits such as (1) laterite, (2) sand, and brown clay soil in paleochannels, (3) granodiorite, (3) siltstone-shale ± greywacke sequence, (4) slump-turbidite sequence, (5) mass-wasting sequence (MWS), (6) paleo regolith, (7) marble sequence.

According to Masurel et al. (2017), the metasedimentary rocks mapped in the Sadiola Hill opencast pit are intruded by two generations of diorite and one generation of quartz-feldspar porphyry. According to Theron (1997), in the Sadiola Hill opencast pit, the intrusions are trondhjemitic diorite-quartz dioritic to granodioritic in composition. Calcite is present in all rock types as an alteration product. The sedimentary rock displays a strong to weak weathering profile in appearance. A diorite dyke is situated at the contact between siltstone-shale-greywacke and calc-silicate rock in the Sadiola Hill opencast pit. These dykes were emplaced after deposition of the metasedimentary rocks based on crosscutting relationships.

XRF results allowed establishing the proportionality between the gold mineralisation and silica, potassium, and iron. There is a strong correlation between the gold mineralisation, potassium (K), and iron (Fe) alteration. In the Sadiola goldfield, the potassium and iron alteration are hosted in the

decarbonated calc-silicate and are related to the three-oxide developed in the oxide profiles. Cameron (2010) and Masurel et al. (2017) have also shown the relationship between gold and potassium and iron (Fe).

The more important consequence of the calc-silicate oxidation in terms of mine benefit is the concentration of gold mineralisation in the altered calc-silicate (oxide saprolite and oxide transitional). The circulation of cool and hydrothermal fluids allowed mobilization of all the types of gold in the oxide phases. The significant gold mineralisation is found and mined from the oxide profile, which is not carbonated, but represents a calc-silicate alteration product. The Sadiola Hill oxide gold mineralisation can't be classified as carbonate-hosted due to the absence of the carbonate in the oxide profile. In the light of this work, the Sadiola gold mineralisation can be classified as an oxide gold enrichment deposit, similar to the Siguiri Gold deposit proposed by Robertson and Peter (2002) in Guinee Conakry and Carlin-style in Nevada (Maroun et al, 2017). Gold mineralisation in the Yatela Main gold mine is hosted in a saprolitic residuum situated above Birimian supracrustal rocks (Hein et al, 2015). Robertson and Peter (2002) identified supergene or oxidised gold deposits in the West African Craton, e.g. at Yatela and Siguiri.

Traoré and Samaké (2010) reported that the Sadiola ore body displacement was only due to this west-east trending faults. According to this research, the displacement of the Sadiola ore body is significantly due to the collapses of the oxide profile. The oxide profiles collapses can be explained by the diminution of the volume of oxide. The pit mapping data interpretation can explain that these collapses caused the displacement of the orebody in the oxide phases. The loss of volume and density resulted in the concentration of the gold mineralisation in the oxide profile. SFZ attributed to collapse of a contact in this study, while Masurel et al. (2017) and other previous workers relate this structure to local and regional deformation.

Three ferricrete layers were observed on the decarbonated calc-silicate, while it is one (1) on the siltstone-shale-greywacke. The differences in the number of the ferricrete layers above the decarbonated calc-silicate can be explained by the collapses of the oxide profiles because of its diminution of the volume. This difference of ferricrete layers can be explained by the collapses of decarbonated calc-silicate because of oxidation of the calc-silicate. When the decarbonated calc-silicate collapsed, aeolian sand was deposited and the ferricrete layer formed. According to Grimaud (2014), the ferricrete formation began in the Eocene-Miocene, with the development of three distinct glaciations across West Africa Craton. The lower glaciation is generally an infill of deep palaeochannels as this can be seen in the highwall adjacent to the ramp in the FE4 opencast pit.

This study established three types of gold, with two types of gold mineralisation in the oxide phase, and one in the sulphides. The different types of gold were established according to the age of the host rock, while Strydom and Rompel (1997) established four types of mineralisation (1) pelites layer, (2) cross pelites and folded, (3) extension vein of quartz and calcite vein, and (4) yellow and red Fe-hydroxide mineralisation.

5.2. Genetic Model hypothesis

The Sadiola Hill oxide zone study conducted to establish a genetic model as follows. The genetic model has been modified from Hein (2007; 2008) as follows:

1) Deposition of metasedimentary sequences in shallow marine deltaic to the pro-deltaic environment (horizontal contact between siltstone-shale-greywacke on top and calc-silicate in the bottom).

2) Deformation with an oriented NW-SE compression, probably associated, with the Eburnean orogeny, produced an effect on the SFZ, and northeast trending faults. The SFZ and north-northeast faults seem to be syn-genetic because of the NE faults always start from the SFZ outward.

3) The meteoric fluids penetrated the calc-silicate rock through the SFZ and northeast trending faults. The fluids circulation in calc-silicates facilitated its oxidation. According to Keita (2003) oxidation and hydrolysis reactions occurred. The most important reaction was oxidation and change in pH towards acidic conditions. At Sadiola Hill opencast pit, pyrite is the most important sulphide in terms of quantity. Pyrite in the presence of H_2O and O_2 was involved in the following reactions.

Oxidation, the formation of acid, referring to Blanchard (1966)

(1) $2FeS_2 + 7O_2 + 2H_2O \longrightarrow 2FeSO_4 + 2H_2SO_4$

(2) $12FeSO4 + 3O_2 + 6H_2O \longrightarrow 4Fe2\,(SO_4)_3 + 4Fe\,(OH)_3$

Or

(2) $4FeSO_4 + O_2 + 2H_2SO_4 \longrightarrow 2Fe_2\,(SO_4)_3 + 2H_2O$

(3) $Fe_2\,(SO_4)_3 + 6H_2O + 6H_2O \longleftrightarrow 2\,Fe\,(OH)_3 + 3H_2SO_4$ (sulphuric acid)

Limonite could be formed as a result of the oxidation reaction. Limonite composition is $2Fe_2O_3.nH_2O$ and composed of goethite (FeO. OH), hematite (Fe_2O_3) and scarce magnetite, jarosite and siderite and impurity as silica, and different types of carbonate. The first process of the formation of limonite is that of the dilution of solutions resulting from the oxidation of pyrite Blanchard (1966). The second process of precipitation of limonite is the one demonstrated by reactions (3) and (4).

The sulphates oxidize other sulphide as follows:

(4) $M^{++}S + 4Fe_2\,(SO_4)_3 + 4H_2O \longrightarrow M^{++}SO_4 + 8FeSO_4 + 4H_2SO_4$

Hydrolysis and hydroxide formation (OH^-) and bases.

a) $FeSiO_4 + 4H_2O \longrightarrow 2Fe^{2+} + 4OH^- + H_2SiO_4$

(Fayalite)

b) $2KAlSi_3O_8 + 3H_2O \longrightarrow Al2Si_2O_5\,(OH)_4 + 4Si_2O_5\,(OH)_4 + 4SiO_2 + 2\,KOH$

(Orthoclase) (Kaolinite)

c) $MgCO_3 + H_2O \longrightarrow Mg^{2+} + OH^- + HCO^-_3$

(Anklesite)

In the Sadiola goldfield, the gold mineralisation is associated with the major sulphides, namely arsenopyrite, pyrrhotite, and pyrite (Masurel et al. 2017). The water in contact with the sulphide under appropriate temperature and pressure conditions could activate reactions which can create minerals like siderite, and jarosite.

4) The calc-silicate, which was oxidized, led to formation of decarbonated calc-silicate, resulting in a decrease in volume of the decarbonated calc-silicate and concentration of gold content in the decarbonated calc-silicate.

5) Formation of the first layer of ferricrete above the meta-siltstone shale greywacke and decarbonated calc-silicate rock.

6) The decrease in the volume of the decarbonated calc-silicate caused a collapse of oxide. Then, SFZ collapsed. The sudden and slow collapse of the SFZ can be explained by the diminution of the volume of the oxide profile added to the charge of above lithologies, like the siltstone-shale-greywacke and ferricrete. Subsequently, the aeolian sand was progressively deposited on the ferricrete unit, which resides on top of the decarbonated calc-silicate unit.

7) Formation of the second layer of the ferricrete on the decarbonated calc-silicate on the aeolian sand.

8) The second collapse of decarbonated calc-silicate resulted in another collapse of SFZ, then another period of filling by aeolian sand occurred on the second layer of ferricrete.

9) Formation of the third layer of ferricrete on the decarbonated calc-silicate. These different stages of collapsing occurred globally within the decarbonated calc-silicate.

10) Formation of regolith profile, with the final position of Sadiola Hill opencast pit.

The oxidation is the source of the concentration of the gold grade. The oxidation profile follows the SFZ and the north-northeast structures, which explain the reason why many researchers relate the gold mineralisation to the structures. In the Sadiola goldfield, the gold mineralisation is hosted in each lithology, but the gold concentration varies in the various rock units. Many factors could be the source of gold concentration: (1) the chemistry of the calc-silicate, (2) the density of the gold in a relationship with the meteoric fluid circulation. The Sadiola gold mineralisation can be classified as oxide gold enrichment deposit.

Chapter 6
Conclusions and Recommendation

This research study on the Sadiola goldfield was aimed at improving current understanding of the Sadiola Hill oxide zone, in particular, the geochemical complexities and alteration signatures. Examination of the oxide saprolite and transitional profile allowed establishing three-oxide facies: (Type 1) decarbonated calc-silicate alteration, (Type 2) Fe-alteration (oxide-jarosite-siderite) and (Type 3) potassic clay alteration. The lithological mapping established the following: calc-silicate or marble sub-facies as (1) very thick (more than 1cm) to thick-bedded marble (0.5-1 cm) (with alternate of white and black layers), (2) thin (3-5 mm) to very thin-bedded (1-3 mm) marble, (3) massive marble, (4) slump-folded marble, (5) carbonaceous siltstone and (6) pure marble.

All these marble sub-facies hosts gold mineralisation, but significant gold mineralisation was found in thick-bedded marble with an alternating of white and black layers associated with biotite alteration within the dark layers. The carbonaceous siltstone marble sub-facies, without significant structural features or alteration signatures are not mineralised.

The key minerals identified by XRD are alunite (K_2A_{l6} $(SO_4)_4(OH)_{12}$) and jarosite (K_2Fe_{63}+ $(SO_4)_4(OH)_{12}$). The mineral association suggests a highly acidic environment and acidic supergene conditions. The examination of oxides also allowed distinguishing the different ferricrete horizons in the Sadiola goldfield. Significant gold mineralisation is hosted in the oxide profile (weathered calc-silicate) in the Sadiola Hill opencast pit.

The relative age of the Sadiola oxide profile could be established between the ferricrete unit, Miocene-Eocene age and the hard rock which is Birimian age (2200-2100 Ma). The consequences of the oxidation are variable: (1) diminution of the volume of the decarbonated calc-silicate, (2) concentration of gold mineralisation, (3) collapse of the lithological contact between calc-silicate and the siltstone-shale-greywacke, (4) formation of several discontinuous pieces of diorite units in the oxide unit, (5) formation of several discontinuous pieces of the quartz-feldspar porphyry observed in the south-east of the Sadiola Hill opencast pit, and (6) brittle and ductile deformation observed through the SFZ.

The 3D oxide and hard rock modelling defined three types of gold mineralisation according to the age of the host rock. The young gold is found in the ferricrete (Eocene-Miocene age), the second gold type is found in the oxide profile (oxide saprolite and transitional), with unknown age and the third gold is found in the hard rock that is Birimian age.

Formation of the three layers of ferricrete occurred on the decarbonated calc-silicate.

Combining all above observations, the Sadiola Hill opencast pit can be classified as an oxide gold enrichment deposit.

References

AAOA, 2000. The trans-Saharan Gold Trade (7th-14th century). In Heilbrunn Timeline of Art History. New York: The Metropolitan Museum of Art, Department of Arts of Africa, Oceania, and the Americas. 2000-. http://www.metmuseum.org/toah/hd/gold/hd_gold.htm (October 2000).

Abouchami, W., Boher, M., Michard, A. and Albarede, F. 1990. A major 2.1 Ga old event of mafic magmatism in West Africa: An Early stage of crustal accretion. Geophysical Research 95, 17605-I 7629.

Anonymous, 1994. Geology of the Sadiola Hill orebody near Kayes, Mali - some preliminary observations. Unpublished, Field workshop for ANMERCOSA Exploration (Mali) Limited, 17p.

Bassot, J.P., 1966. Etudes géologique du Sénégal Oriental et de ses confins guinéo-maliens. Mémoires BRGM 40, 322p.

Bassot, J.P., 1987. Le complexe volcano-plutonique calco-alcalin de la rivière Daléma (Est Sénégal): discussion de sa signification géodynamique dans le cadre de l'orogène éburnéenne (Protérozoïque inférieur). Journal of African Earth Sciences 6 (4): 505-519.

Bassot, J.P., and Dommanget, A., 1986, Mise en évidence d'un accident majeur affectant le Protérozoïque inférieur des confins sénégalo-maliens: Comptes Rendus Géosciences, v. 302, p. 1101–1106.

Baratoux, L., Ouiya, P., Siebenaller, L., Salvi, S., Béziat, D., Naba, S., Naré, A., Franceschi, G., 2016. The Nassara gold prospect, Gaoua District, southwestern Burkina Faso. Ore Geology Reviews. Doi: 10.1016/j.oregeorev.2015.11.026

Blanchard, R., 1966. Interpretation of leached outcrops. Nevada Bureau of Mines. Bulletin 66: 196

Boher, M., Abouchami, W., Michard, A., Albarede, F., Arndt, N.T., 1992. Crustal Growth in West Africa at 2.1 Ga. Journal of Geophysical Research 97 (B1); 345-369.

Boshoff, F., Hanssen, E., Hill, J.V., Jones, D., Kaisin, J., Traore, S., Voet, H.W., 1998. The Sadiola Hill Mine: A lower Proterozoic gold deposit in the Kéniéba window - Mali, West Africa. In: Pathways 98, Exploration Symposium, and Vancouver, Canada, 6p.

Cameron, G.H., 2010. A review and investigation into the controls of deep sulphide mineralisation at the Sadiola and Gold Deposit Mali - West Africa. Unpublished report prepared for SEMOS S.A., 33p.

Charbon, D., Grimaud, J.L., Metelka., V, Beauvais., A, Bamba, O., 2015. Neogene cratonic erosion fluxes and landform evolution processes from regional regolith mapping (Burkina Faso, West Africa). Geomorphology, 241, 315-330.

Dabo, M., Aïfa, T., 2010. Structural styles and tectonic evolution of the Kolia-Boboti sedimentary basin, Kédougou-Kéniéba Inlier, eastern Sénégal. Comptes Rendus Geosciences 342, 796-805.

Debat, P., Diallo, D.P., Ngom, P.M., Rollet, M., and Seyler, M., 1984, La série de Mako dans ses parties centrale et méridionale (Sénégal Oriental, Afrique de l'ouest). Précisions sur l'évolution de la série volcanosédimentaire et données géochimiques préliminaires sur les formations magmatiques posttectoniques: Journal of African Earth Sciences v. 2, p. 71–79.

Debat, P., Nikie´ma, S., Mercier, A., Lompo, M., Be´ziat, D., Bourges, F., Roddaz, M., Salvi, S., Tollon, F., Wenmenga, U., 2003. A new metamorphic constraint for the Eburnean orogeny from Palaeoproterozoic formations of the Man shield (Aribinda and Tampelga countries, Burkina Faso). Precambrian Res. 123, 47–65.

Dia, A., 1988, Caractéres et signification des complexes magmatiques et métamorphiques du secteur de Sandikounda-Laminia (Nord de la boutonnière de Kédougou, Est du Sénégal) : un modèle géodynamique du Birimien de l'Afrique de l'Ouest: Ph.D. thesis, Sénégal, Université de Dakar, 350 p.

Dia, A., 1993a. Nd and Pb isotopic constraints on the evolution of the Early Proterozoic magmatism episod in the Kedougou Inlier, East Senegal: implications for the timing of the Early Proterozoic crustal growth event. In: Dia, A. (Ed.), Early Proterozoic: Geochemical and Structural Constraints- Metallogeny-Atmosphere. International Symposium, January 1993, vol. 23. CIFEG Occas. Publ., Dakar/Senegal, pp. 16-19.

Dia, A.,1993b. Geochemical constraints and tectonic significance of amphibolite-gneiss xenoliths in an Early Proterozoic arc complex (2.1 Ga) in the Mako area, Kedougou Inlier, eastern Senegal. In: Dia, A. (Ed.), Early Proterozoic: Geochemical and Structural Constraints-Metallogeny-Atmosphere. International Symposium, January 1993, vol. 23. CIFEG Occas. Publ., Dakar/Senegal, pp. 20-23.

Dia, A., Rocci, G., Bassot, J.P., Albarede. F., Dioh, E., Diallo, D.P., Ngom, P.M. and Sylla, M., 1993. The Early Proterozoic magmatism of the Mako Supergroup area, eastern Senegal-characteristics of new crust. In: Dia, A. (Ed.), Early Proterozoic: Geochemical and Structural Constraints-Metallogeny- Atmosphere. International Symposium, January 1993, vol. 23. CIFEG Occas. Publ., Dakar/Senegal, pp. A19-A22.

Dia, A., Van Schmus, W.R., Kroner, A., 1997. Isotopic constraints on the age and formation of a Paleoproterozoic volcanic arc complex in the Kédougou Inlier, eastern Senegal, West Africa. Journal of African Earth Sciences 24 (3), 19-213.

Diene, M., Gueye, M., Diallo, D.P., Dia, A., 2012. Structural evolution of a Precambrian segment: example of the Palaeoproterozoic formations of the Mako belt (eastern Senegal, West Africa). International Journal of Geosciences 3, 153-165.

Dioh, E., Béziat, D., Debat, P., Grégoire, M., Ngom, P.M., 2006. Diversity of the Palaeoproterozoic granitoids of the Kédougou inlier (eastern Senegal): Petrographical and geochemical constraints. Journal of African Earth Sciences 44, 351-371.

Grimaud, J. L., 2014. Dynamique long-terme de l'érosion en contexte cratonique : l'Afrique de l'Ouest depuis l'Eocène. Earth Sciences. Université Paul Sabatier - Toulouse III, 2014. French. <tel-00982077>

Hanssen, E., Kaisin, J., Mounkoro, B., Hill, J., 1998. Sadiola sulphide drilling project. Unpublished, report to IAMGOLD Corporation on behalf of SEMOS, November 1998, 87p.

Hein, K.A.A., 2007. Sadiola & Yatela opencasts and satellite pits, Alamoutala opencast pit & the Dinnguilou prospect, Mali: notes on the geology, palaeogeography and gold metallogenesis. Report to Société D'Exploitation des Mines d'Or de Sadiola S.A, Sept 2007, 19p.

Hein, K.A.A., Tshibubudze, A., 2007. Sadiola Ore Genesis Model, Sadiola Mine and satellite pits, Mali. Unpublished report to Société Exploitation des Mines d'Or de Sadiola S.A. (SEMOS), 16p.

Hein, K.A.A., 2008. Geology of the Sadiola opencast pit and ancillary pits, Mali. (Draft) final report to SEMOS SA, Jan 2008, 18p.

Hein, K.A.A., Matsheka, I.R., Bruguier, O., Masurel, Q., Bosch, D., Caby, R.; Monié, P., 2015. The Yatela gold deposit: 2 Billion years in the making. Journal of African Earth Sciences Special Volume, 29p.

Hirdes, W., Davis D.W., 2002. U-Pb Geochronology of Palaeoproterozoic Rocks in the Southern Part of the Kédougou-Kéniéba Inlier, Senegal, West Africa: Evidence for Diachronous Accretionary Development of the Eburnean Province. Precambrian Research 118, 83-99.

Keita, M., 2003. Etude de la distribution qualitative et quantitative des sulfures et leur rapport lith-stuctural avec la minéralisation aurifère dans la mine d'or de Sadiola.

Keith, S. M., 2004. The systems engineering of automated fire assay laboratories for the analysis of the precious metals. Dissertation presented for the Degree of DOCTOR OF PHILOSOPHY (Extractive Metallurgical Engineering Science), 295p.

Klöckner Industries (1989) Notice explicative de la carte géologique du Mali occidental, Direction Nationale de la Géologie et des Mines, Ministère de l'industrie, République du Mali.

Lawrence, D.M., Treloar, P.J., Rankin, A.H., Harbidge, P., Holliday, J., 2013. The Geology and Mineralogy of the Loulo Mining District, Mali, West Africa: Evidence for Two Distinct Styles of Orogeny Gold Mineralisation. Economic Geology 108, 199–227.

Ledru, P., Pons, J., Milési, J.P., Feybesse, J. L, Johan, V., 1991. Transcurrent tectonics and polycyclic evolution in the lower Proterozoic of Senegal- Mali. Precambrian Research 50, 337-354.

Lompo, M., 2010. Paleoproterozoic structural evolution of the Man-Leo Shield (West Africa). Key structures for vertical to transcurrent tectonics, Feb 2010, 18p.

Milesi, J. P., Ledru, P., Dommanget, A., Johan, V. and Diallo, M. 1989. Lower Proterozoic succession in Senegal and Mali (West Africa): posrtion of sediment-hosted Au and Fe deposits of Loulo area and significance in terms of crustal evolution. Abstracts, 28th international Geological Congress Washington. July, 2-3, ~~353-357. Washington DC, USA.

Milési, J.P., Ledru, P., Feybesse, J.L., Dommanget, A., and Marcoux, E., 1992, Early Proterozoic ore deposits and tectonics of the Birimian orogenic belt, West Africa: Precambrian Research, v. 58, p. 305–344.

Maroun, J. S., Lindsey R. C., Cline, A. S., Page A., John M., 2017. High-Grade Gold Deposition and Collapse Breccia Formation, Cortez Hills Carlin-Type Gold Deposit, Nevada, USA. Bulletin of the society of economic geologists. June 2017, Vol. 112, 707-740. 34p

Masurel, Q., Thébaud, N., Miller, J., 2013. Controls on the genesis, geometry and location of the Sadiola gold system in Mali, West Africa. Quarterly Report October 2013. Unpublished report to SEMOS, Mali, 22p.

Masurel, Q., Thébaud, N., Miller, J., 2014. Controls on the genesis and location of the Sadiola gold system. Annual Report 2014, 1-41.

Masurel, Q., Miller, J., Hein, K.A.A., Hanssen, E., Thébaud, N., Ulrich, S., Kaisin, J., Tessougue, S., 2016, The Yatela gold deposit in Mali, West Africa: The final product of a long-lived history of hydrothermal alteration and weathering: Journal of African Earth Sciences, v. 113, p. 73–87.

Masurel, Q., Thébaud, N., Miller, J., Ulrich, S., Hein, K., Cameron, G., Davis, J., 2017. Sadiola Hill: A world-class carbonate hosted gold deposit in Mali, West Africa. Economic Geology Special Volume 112, 23-47.

Masurel, Q., Thébaud, N., Miller, J., Ulrich, S., Roberts, M.P., Béziet, D., 2017. The Alamoutala carbonate-hosted gold deposit, Kédougou-Kénieba Inlier, West Africa. Economic Geology 112, 49-72.

Ndiaye, P. M. 1994. Evolution au Protérozoïque inferieur de la région Est Saraya, Supergroupe de Dialé-Daléma, Sénégal oriental: tourmalinisation, altérations hydrothermales et minéralisations associées. Unpubl. Ph. D. thésis 372~. Université de Dakar, Sénégal.

Ndiaye, P.M., Dia, A., Vialette, Y., Diallo, D.P., Ngom, P.M., Sylla, M., Wade, S., Dioh, E., 1997. Données pétrographiques, géochimiques et géochronologiques nouvelles sur les granitoïdes du Paléoprotérozoïque du Supergroupe de Dialé Daléma (Sénégal Oriental) : implications pétrogénétiques et géodynamiques. Journal African Earth Sciences 25, 193–208.

Ngom, P.M., 1989. Caractères géochimiques des formations Birrimiennes du Supergroupe de Mako. (Sabadola et ses environs). J. Afr. Earth Sci. 8 (1), 91–97.

Pons, J., P. Debat, C. Oudin and J. Valero, 1991. Emplacement and evolution of a synkinematic Pluton (Saraya granite, Senegal, West Africa). Bull. Soc. Géol. Fr., 162: 1075-1082.

Pons, J., Pons, C., Oudin, J., Valero, 1992. Kinematics of large syn-orogenic intrusions: example of the Lower Proterozoic Saraya batholith (Eastern Senegal). Geologische Rundschau 81, 473-486.

Pons, J., Barbey, P., Dupuis, D., Leger, J.M., 1995. Mechanisms of pluton emplacement and structural evolution of a 2.1 Ga juvenile continental crust: the Birimian of southwestern Niger. Precambrian Research 70, 281-301.

Pawlig, S., Gueye, M., Klischies, R., Schwarz, S., Wemmer, K., and Siegesmund, S., 2006, Geochemical and Sr-Nd isotopic data on the Birimian of the Kedougou-Kenieba inlier (eastern Senegal): Implications on the Palaeoproterozoic evolution of the West African craton: South African Journal of Geology, v. 109, p. 411–427.

Robertson, M., Peter, L., 2016. West African goldfields. The MSA Group. 20B Rothesay Avenue, Craighall Park, 2196, South Africa. DOI 10.18814/epiiugs/2016/v39i2/95773, June 2016, Episodes Vol. 39 n0. 2:155-176.

Sarr, D., Fall, M., Ngom, P. M., Ndiaye, M., Kane, C.H., Ba, M., 2012. Geomechanical Characterization of Sandstones Cliffs of Segou (Senegal, West Africa) in the Madina Kouta Basin, February 2012, 9p.

Schwartz, M.O., and Melcher, F., 2004, The Falémé iron district, Senegal: ECONOMIC GEOLOGY, v. 99. p. 917–939.

Schwarnecki, M., 2014. Sadiola report. Sadiola goldfield regolith mapping, Mali. Unpublished report to Société Exploitation des Mines d'Or de Sadiola S.A. (SEMOS), 8p.

Sillitoe, R.H., 1994. Comments on mineralisation style and exploration approach at the gold prospects of Sadiola in Mali, Bambadji in Sénégal and Yako-Arbole in Burkina Faso, West Africa. Unpublished report to Anglo America Corporation S.A. Limited, July 1994, 17p.

Sillitoe, R. H., 2005, Supergene Oxidized and Enriched Porphyry Copper and Related Deposits: Economic Geology, 100th Anniversary Volume, p. 723-768.

Strydom, D., Rompel, A.K.K., 1997. Structural investigation of the Sadiola exploitation and exploration area in the Kéniéba Kédougou window, western Mali. Anglo American Corporation of South Africa Limited, Vol1, 4p.

Taylor, P.N., Moorbath, S., Leube, A., Hirdes, W., 1992. Early Proterozoic crustal evolution in the Birimian of Ghana: constraints from geochronology and isotope geochemistry. Precambrian Res. 56, 97–111.

Theron, S.J., 1997. Possible genetic model for gold mineralisation within the greater Sadiola Concession Area. Unpublished Memorandum to AARL Geology, Sadiola, 3p.

Traoré, S., Samaké, M., 2010. Sadiola monthly report. Sadiola Mine and satellite pits, Mali. Unpublished report to Société Exploitation des Mines d'Or de Sadiola S.A. (SEMOS), 12p.

Voet, H.W., 1996. The Sadiola Hill orebody in western Mali - A giant diorite gold porphyry deposit with Carlin-like characteristics. Unpublished report to Anglo American Corporation of South Africa Limited, 15p.

Voet, H.W., 1997. Cross folding at Sadiola Hill mine and the possible extent of the orebody to the south. Unpublished, report to Anglo American Corporation of South Africa Limited, File 13-147-500(a), 19 November 1997, 3p.

Villeneuve, M., 2008, Review of the orogenic belts on the western side of the West African craton: the Bassarides, Rokelides and Mauritanides: Geological Society of London Special Publication 297, p. 169–201.